Imagerie optique 3D multimodale : traitements spatio-temporels, correction du front d'onde et classification automatique.

Jules Scholler

▶ **To cite this version:**

Jules Scholler. Imagerie optique 3D multimodale : traitements spatio-temporels, correction du front d'onde et classification automatique.. Physique [physics]. Université Paris sciences et lettres, 2020. Français. NNT : 2020UPSLS007 . tel-03145406

HAL Id: tel-03145406
https://pastel.hal.science/tel-03145406

Submitted on 18 Feb 2021

PSL★
UNIVERSITÉ PARIS

THÈSE DE DOCTORAT
DE L'UNIVERSITÉ PSL

Préparée à l'ESPCI Paris

Imagerie optique 3D multimodale : traitements spatio-temporels, correction du front d'onde et classification automatique.

-

Multimodal 3D optical tomography: spatio-temporal processing, wavefront correction and automatic classification.

Soutenue par
Jules Scholler
Le 22 Juillet 2020

École doctorale nº564
Physique en Ile de France

Spécialité
Physique

Composition du jury :

Emmanuel Beaurepaire Dir. de recherche, École Polytechnique	*Président du jury*
Elsa Angelini Associate professor, Télécom Paris	*Rapporteure*
Christophe Moser Associate professor, EPFL	*Rapporteur*
Martin Booth Professor, University of Oxford	*Examinateur*
Katharine Grieve IR, Hôpital des 15-20	*Examinatrice*
Claude Boccara Professeur émérite, ESPCI Paris	*Co-directeur de thèse*
Mathias Fink Professeur, ESPCI Paris	*Directeur de thèse*

ESPCI ℮ PARIS | PSL★

Compiled August 26th, 2020.

Acknowledgements

This thesis would not have been possible without the help of my advisors **Mathias**, **Claude** and **Kate**. I am deeply grateful to you **Claude** for spending so much time answering my endless questions. When I started my PhD, I hadn't touched an optical bench and the wave equation for more than a year and you explained me pedagogically the principle of OCT. You came nearly everyday jovially to see if I was facing issues or to discover the latest results. Your scientific intuition led to numerous results and I really enjoyed working with you. I am also profoundly grateful to you **Kate** for your implication during these three years. You always found new samples to image, new ideas to try and new people to collaborate with. I lost count on the number of times you proofread preprints, papers, rebuttal letters and finally this thesis. I hope you will obtain your HDR before the end of the year so that other students could have the chance to work under your guidance.

These three years wouldn't have been the same without my closest friends, climbing companions, brewing partners and board games lovers **Maxime** and **Louis**. **Louis**, I forgive you for being a chemist. **Maxime**, please do not die from some random disease. I love you guys.

I would like to thank the members of the OCT team for the great all around atmosphere. **Kassandra**, you were there when I built my first OCT and you always agreed to help me. You followed me in many hikes around the world where I lied about the distance and elevation gain. You accepted to rent a Mustang in San Francisco and never grumbled even when I drifted corners and most of all you almost saved my life in Vancouver. **Leo**, you were a great hiking partner (and a great liar). I hope you succeed in starting a company with your Laser Doppler Holography technology. **Olivier**, I enjoyed working with you. You always have great ideas and know so much about microscopy, you taught me many things and part of this work was achieve owing to your guidance. **Egidijus**, you were always in the lab when I started my PhD. I didn't always understand what you told me at that time but I have learnt a lot from you! I spent the brightest moments with you wandering around in the exhibition hall looking for cameras. You showed me around Warsaw and brought me to the best bars (almost!). **Paul**, it's a shame you came this late to the lab (and that you have a degree in management). I really enjoyed working with you and hopefully some day we will start a company together. **Pedro**, you know the eye like no-one and you taught me so much on eye imaging. **Slava**, you are the only one I know who make such nice presentations and wash the skin of bananas.

I would like to thank all the members of the Institut Langevin, you are always happy to help and share your ideas. **Joris**, it's a shame you moved to Nation, I enjoyed our teeth brushing sessions after lunch and riding home with you. **Mons**, I don't understand what you are doing, but I like when you ask for my inputs. See you at the bar! Also, thank you

Acronyms

API: Application Programming Interface
BS: Beam Splitter
CPU: Central Processing Unit
D-FFOCT: Dynamic Full Field Optical Coherence Tomography
DOF: Depth Of Field
FF: Full Field
FFOCT: Full Field Optical Coherence Tomography
FOV: Field Of View
GPU: Graphics Processing Unit
HSV: Hue Saturation and Value
MTF: Modulation Transfer Function
NFL: Nerve Fiber Layer
NA: Numerical Aperture
PSD: Power Spectrum Density
PSF: Point Spread Function
PZT: Piezoelectric Translation
OCT: Optical Coherence Tomography
OTF: Optical Transfer Function
RAM: Random Access Memory
RFE: Random Fourier Expansion
SDK Software Development Kit
SIM: Structured Illumination Microscopy
SLM: Spatial Light Modulator
SNR: Signal to Noise Ratio
SH: Shack-Hartmann
SS: Swept Source
SVD: Singular Value Decomposition
TD: Time Domain
WFS: WaveFront Sensor

Contents

Introduction

Optical imaging is a vast and dynamic field, in which many groups and researchers are involved and develop brilliant ideas to push the limits of imaging ever further. Optical imaging systems can be gathered into different categories which helps to classify and understand them. They can first be separated into transmission and reflection devices[1]. In transmission systems, the illumination is on the opposite side of the detection whereas for reflective systems the illumination and detection are performed on the same side of the object. While the transmission configuration can be very interesting[2] (e.g. to measure optical absorption with X-rays) it would be invasive for most microscopy applications[3] so that usually reflection systems are preferred for diffraction limited imaging. Optical systems can then be separated into coherent and incoherent detection according to how the light field is measured. Coherent systems exhibit very interesting properties as they allow to access the complex nature of the light field, i.e. to measure both amplitude and phase[4] while incoherent system can only measure the squared amplitude of the light field, losing phase information. Finally, systems can be further separated into direct and indirect measurements depending on the way signals are probed. Indeed, some imaging systems such as MRI, X-ray bragg diffraction imaging or Fourier-transform spectroscopy do not acquire signals in the direct domain (i.e. in space or time) but in the Fourier (frequency) domain. Although indirect measurements often bring interesting properties, they usually all share the same drawback: the whole domain needs to be measured before the image can be retrieved by going from the probed space to the direct space. The common goal of all these imaging systems is to measure the optical properties of an object with the best image quality and resolution. Microscopists have many physical enemies[5] that deteriorates imaging performances and are working to overcome these by designing innovative methods that allows to recover and filter information even when it was supposedly lost. Such methods include filtering ballistic photons from scattered ones, matrix approaches and using multimodal systems that combines electromagnetic and acoustic waves. All of these methods are currently studied and developed in our lab in a very stimulating environment.

In this thesis, I was mostly involved in building and working with optical coherent tomography (OCT) systems which fall into reflection, coherent and direct[6] systems. Some

---

[1]There also exists hybrid systems where the illumination can be orthogonal to the detection such as light-sheet microscopy [Santi, 2011]

[2]Or even mandatory, e.g. in astronomy photons from a distant star are probed. Even if we could build a sufficiently powerful source to illuminate celestial objects, the time required to probe back the light would be too high to perform such experiments.

[3]Endoscopy in transmission would be dreadfully invasive because it would require to embed the detector in the patient tissue

[4]Phase information is useful e.g. to measure sub-wavelength axial displacements or to propagate the field to access other planes.

[5]Diffraction, shot noise, aberrations, scattering, and many more!

[6]There also exists indirect OCT system which work in the Fourier domain.

very interesting property of OCT are its ability to reject scattered photons and its optical sectioning capability. OCT is very close to holography, the difference being that holography uses monochromatic illumination whereas OCT uses broadband sources so that holography does not have direct optical sectioning capability. However, for weakly scattering objects, digital holographic microscopy[7] can reconstruct the object structure in 3D using light propagation models which typically fails when the object is a few cells in width. During my PhD, I also tried to combine OCT with fluorescence imaging in a reflection configuration. Fluorescence is a direct measurement which always falls into the incoherent category since fluorescence is a non-coherent process, even if the illumination used to generate fluorescence is coherent. The incoherent nature of fluorescence led to numerous attempts[8] to bring optical sectioning capability with smart illumination and detection schemes.

This manuscript is divided into five chapters. The first chapter introduces the concepts and challenges of imaging in scattering media. To that end, a brief introduction of light propagation in such media is given. Then, general concepts for filtering scattered photons are discussed and time gating is introduced with OCT. The first implementation of OCT[9] is presented with a physicist point of view before deriving mathematical concepts and equations that lead to the image formation on the detector. These mathematical models are applied on both time domain and Fourier domain OCT in order to show that they both measure the same physical quantity. I wanted to introduce these concepts because I think they are important for anyone who wants to build an OCT system. Even if the concept looks simple, there are many pitfalls and subtleties with OCT systems[10]. Also, these concepts are fundamental for understanding the latest research in OCT with its many branches, as we shall see at the end of this chapter. Then, with the complete description of OCT I derive the performances and limitations of scanning OCT before introducing full field OCT (FFOCT). There, the measurement is parallelized using a camera rather than a photo-diode, thus discarding the necessity of scanning. Many aspects of FFOCT are described to provide the reader with an overview of the different parameters and giving a utility guide for anyone who might want to build such a system. Finally, I compare our FFOCT approach, which is time domain and spatially incoherent, with the other most promising full field OCT approaches.

The second chapter introduces dynamic measurements with FFOCT by analyzing temporal fluctuations of the interferometric signal. In this chapter, I support the idea that dynamic FFOCT (D-FFOCT) is not suited to recover physical properties of local scatterers but can be used to generate quantitative images where cells are revealed with an excellent contrast and where the study of their dynamic profile can give interesting biological insights. An application of D-FFOCT is shown on imaging of retina organoids with an article integrated in this manuscript [Scholler et al., 2020].

The third chapter gathers the post-processing methods and frameworks that I developed during my PhD in order to improve (D-)FFOCT images. A particularly interesting section is the removing of motion artifacts from D-FFOCT acquisitions. Because D-FFOCT also

---

[7]Sometimes called optical diffraction tomography

[8]Such as confocal fluorescence microscopy which is based on a spatial filtering of scattered photons by illuminating and detecting through a pinhole, light-sheet microscopy where only a thin axial slice of the sample is illuminated and multiphotons fluorescence which is based on non-linear processes.

[9]Which is referred as scanning OCT

[10]Which makes them very interesting to work with.

probes the phase, tiny axial displacements create strong artifacts that masks the signal of interest and prevented the acquisition of D-FFOCT images in vivo. Removing these artifacts was a milestone in the development of D-FFOCT and the method is explained in detail in a paper integrated in this manuscript which was published in 2019 [Scholler, 2019b]. In this paper I also presented a different way to compute the dynamic images which improved the signal to noise ratio, hence allowing to image deeper inside tissues.

The fourth chapter gathers the hardware modifications and add-ons that I developed for both in vivo human retina imaging and microscopy. Regarding retina imaging, the presented work is a common effort with Pedro Mecê to make FFOCT a robust, high-resolution and consistent device to image the retina. The first step was to combine FFOCT with an axial tracking device in order to track the retina to automatically match the optical path length between the imaged retina layer and the reference mirror. The second step was then to manipulate the wavefront in order to maintain an optical symmetry between the eye and the reference arm. Without this symmetry, FFOCT images could only be acquired on a small patch rather than on the whole field of view. Finally the last step was to correct ocular aberrations with an efficient and low-cost approach, using an adaptive lens in order to improve the signal to noise ratio. To succeed in this last step, a great effort on understanding the theory behind the manifestation of aberrations in FFOCT was made by Victor Barolle during his PhD. Then, I experimentally demonstrated the validity of this theory during my PhD and presented at the end of this chapter.

Finally the fifth chapter gathers the numerous applications of (D-)FFOCT that were successfully carried out during my PhD. Motion tracking was used to monitor wound healing on D-FFOCT images and presented with an article published in 2019 [Scholler et al., 2019]. Motion tracking was also applied to compute in vivo angiography maps of blood flow in a human conjunctiva, in a second article published in 2020 [Mazlin et al., 2020]. Then, strategies to combine (D-)FFOCT with fluorescence imaging are described in order to gain more insight on the dynamic part of the signals (e.g. differentiate mitochondria from lysosomes), which will be useful for further developments and biological applications of D-FFOCT[11]. Finally, machine learning and deep learning approaches for retinal cell classification and breast cancer screening using (D-)FFOCT measurements are presented in appendix D.

This manuscript contains a few articles which I will introduce and where I will point the reader to the interesting parts. In order to avoid any confusions between the sections in this manuscript and the sections of the introduced papers I will use a capital S (e.g. **S**ection 2.1) to refer to an article section whereas I will use a lower s (e.g. **s**ection 5.4) to refer to a section belonging to the present manuscript[12].

---

[11]These aspects are currently investigated by Kassandra Groux in our team, especially on retinal samples.

[12]The digital version of this thesis contains hyperlinks to automatically reach the desired thesis section.

Chapter 1

3D optical imaging in scattering media

Contents

1.1 Imaging in 3D in scattering media

For many years, optical imaging has been the most important tool in biomedical research to observe specimen with a sub-micron resolution with minimum invasiveness [Hajdu, 2002]. However, the conditions required for diffraction limited performances are rarely gathered as both the resolution and the contrast drop when the imaging depth increases inside a biological tissue. This phenomenon is a consequence of the spatial variations of the specimen refractive index which creates wavefront distortions. When these variations exhibits low spatial frequencies these distortions are referred as *aberrations* and are usually described using orthogonal polynomials. On the other hand, when these variations are of higher frequencies, theses distortions are referred as *scattering*. Aberrations and scattering limit the use of conventional microscopy to shallow depths or to almost transparent specimens. Imaging deeper, hence achieving 3D imaging, requires to counteract these detrimental phenomena so that for deep imaging, a gating mechanism is generally used to reject scattered photons and capture only the ballistic light. Many methods have

been developed in the past years to achieve this goal by allowing a gating for ballistic photons. This gating can either be spatial as in confocal microscopy [Minsky, 1988] or temporal as in optical coherence tomography (OCT) [Huang et al., 1991]. Ballistic light is exponentially attenuated in biological tissues which means that the deeper one wants to images, the lower the probed signal and the lower the contrast.

In order to quantify how an optical system behave in different imaging conditions, it is useful to introduce two important notions that characterise light propagation: the scattering and transport mean free path.

1.1.1 Scattering mean free path

Fig. 1.1: Effects of scattering on photography. - **1**: Ballistic photons, these photons have not been scattered even once. **2**: Single scattered photons, these photons have been scattered once (on average). It is still possible to see through because part of the photons have not been scattered. **3**: Multiply scattered photons, these photons have been scattered multiple times and it is not possible to see through anymore with this conventional imaging technique. Photo: Yosemite valley (2018), iPhone 8.

The measured intensity I after a scattering layer of thickness L is the sum of ballistic intensity I_B (photons that have not been scattered) and scattered intensity I_S (photons that have been scattered at least once):

$$I = I_B + I_S \tag{1.1}$$

The scattering mean free path l_s is the average distance travelled by a photon between successive scattering events so that the ballistic component I_B of the total transmitted intensity decays exponentially across a scattering layer of thickness L [Akkermans and Montambaux, 2007]:

$$I_B = I e^{-\frac{L}{l_s}} \tag{1.2}$$

Conventional imaging using a microscope typically fails when the depth of imaging exceed l_s. In biological tissue l_s is on the order of 100 μm, which is typically the maximum

thickness of cryosections[1] used in histology and the sample thickness on microscope slides. To better illustrate the effect of scattering, Fig. 1.1 present the effect of light scattering by clouds on a photography without gating ballistic photons. Conventional imaging techniques will work best in the first case and will be limited in the second case by producing poorly contrasted images. In this work, my aim is to push the limit of full field optical coherent tomography (FFOCT) imaging in order to acquire signals in the third case in a microscopy setting for tissues and 3D cell cultures imaging and for retinal in-vivo imaging. I hope that the challenges of both these tasks will be clear throughout this manuscript. Note that the community tends to use the terminology OCT for in-vivo eye imaging while using optical coherent microscopy (OCM) for ex-vivo application of OCT. I won't use the latter and will stick with "OCT" to also refer about microscopy.

1.1.2 Transport mean free path

The second important scale to describe light propagation is the transport mean free path l_t. It represents the average length over which the direction of photon propagation is randomized. It is related to the scattering mean free path by the following equation:

$$l_t = \frac{l_s}{1 - g} \tag{1.3}$$

where $g = < cos(\theta) >$ is the asymmetry coefficient. The transport mean free path is useful to describe light propagation when multiple scattering dominates. The transport mean free path in biological tissue is on the order of 1 mm^2. For systems with gating strategies (confocal microscopy, OCT), the penetration depth is of the order of the transport mean free path[3]. Indeed, if photons have traveled a distance corresponding to the transport mean free path, then the backscattered field is completely random and it is not possible to get an image of the object. In this regime one can still obtain an image with a conventional method but the resolution will be of the order of the depth[4] which is tremendously low compared to the diffraction limit. However in this regime, the light propagation can be described by the radiative transfer equation [Yoo et al., 1990]. Some imaging modalities[5] rely on several measurements to solve the back-propagation of the radiative transfer equation. These modalities allow to image several order of magnitude deeper (several centimeters) in biological tissues with a maximal theoretical[6] resolution of l_t which is worse than what is achievable by a diffraction limited technique but far better than the penetration depth [Domínguez and Bérubé-Lauzière, 2013]. These techniques are widely used for clinical imaging for medical applications. Their poor resolution does not allow to resolve cellular features and are therefore not in the scope of this work which aims at probing cellular mechanisms and organisation. Finally, recent advances in reflection-matrix approaches [Badon et al., 2016, Yoon et al., 2020] which record and process multi-scattered photons enables to image deeper while keeping the diffraction limited resolution. These methods

---

[1]Usually cryosection have a thickness of 10 μm to 50 μm.

[2]The transport mean free path (hence g) value vary greatly for biological tissues, a table is available in [Ntziachristos, 2010] and [Jacques, 2013].

[3]Here you might be wondering why OCT is performing better than confocal microscopy. In confocal microscopy, spatially filtered photons are simply lost. In OCT however, the sample field is correlated with the reference field (not scattered/attenuated) which act as an amplifier. This will become clear with Eq. 1.8 in the following and is explained in more detail in [Badon et al., 2016].

[4]If a source is embedded inside a scattering medium at depth d, then the cone of diffusion on the medium surface will have a width of around d and depend on the diffusion angle.

[5]Such as diffuse optical tomography [Yoko and Yukio, 2016] and computed tomography.

[6]In practice the resolution is of the order of the third of the depth.

are still proof-of-concepts that are not yet applicable to in-vivo imaging but will surely pave the way to very interesting results in the near future.

1.2   3D imaging with scanning OCT

As mentioned in the previous section, OCT can distinguish between scattered and ballistic photons owing to a time gating. In this part I will explain the principle and performances of scanning OCT, which is essentially declined in two different approaches: time domain (TD) and spectral domain (SD). Then I will highlights the main drawbacks of both time domain OCT (TD-OCT) and spectral domain OCT (SD-OCT) design before introducing the FFOCT approach that we develop in our group [Beaurepaire et al., 1998] (which was the first full field approach for OCT). Since then, many approaches using full-field rather than scanning approaches have been developed and I will present two of them which I think are the most promising, should the hardware becomes faster and cheaper these full field techniques may completely replace actual clinical and commercial implementations of scanning OCT.

1.2.1   Scanning OCT in a nutshell

When a light pulse travels in a scattering medium, a fraction of the incoming photons will be backscattered. Nevertheless, due to the scatterers spatial distribution and to multiple scattering, the backscattered signal is temporally broadened. Neglecting multiple scattering, the first photons to impinge the photodetector are photons that have been backscattered at shallow depth whereas later photons have been scattered inside the bulk. Indeed, the longer time it takes for the photons to impinge the photodetector, the deeper they have propagated inside the sample. So by selecting photons by their arrival time it should be possible to reconstruct the backscattering properties of the sample (note that this is what is done in ultrasound, the difference being that they typically use several focusing law for different depth of focalisation to reconstruct the entire sample depth). In optics, because the celerity of light is so high, there is yet no photodetector which could electronically differentiate the arrival times of these photons. Indeed, if one wanted to have a 1 μm axial resolution in a tissue of refractive index $n = 1.4$ it would require a time resolution of $\delta_t = 2.4 \times 10^{-15}$ s, i.e. a minimum bandwidth of $\Delta_f = 2.1 \times 10^{14}$ Hz which is far from the faster electronic we have nowadays (and which will probably never be achieved because of quantum effects arising when shrinking transistor size required for increasing the clock speed of micro-processors). Rather than relying on a very fast photodiode, the time arrival of photons can be measured using low coherence interferometry. Low-coherence interferometry measures the echo time delay and intensity of backscattered light by comparing it to light that has traveled a known reference pathlength and time delay. Measurements are performed using an interferometer in a Michelson like configuration, see Fig. 1.2. Light from a source is directed onto a beam splitter (BS), one of the beams is incident onto the sample to be imaged, while the second beam travels a reference path with a variable pathlength and time delay and is reflected by a mirror. The backscattered light from the sample interfere with the reflected light from the reference arm on a photodetector at the output of the interferometer. If low-coherence or short pulse light (less common because more expensive) is used, then interference of the light reflected from the sample and reference path can occur only when the two pathlengths match to within the coherence length. The echo time delay and amplitude of backscattered light from features inside the sample can be measured by detecting and demodulating the interference

measured by the photodetector while scanning the reference pathlength. Finally, in order to make a 3D image of the sample, scanning galvanometer mirrors are used to scan the beam across the sample surface.
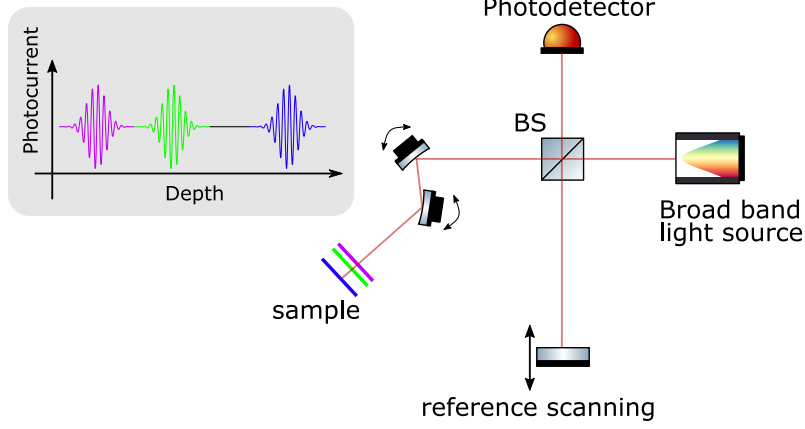
Fig. 1.2: TD-OCT simplified experimental setup. The sample is composed of 3 different reflective layers with the same reflectance.

At large depth, because of multiple scattering, the time information is not sufficient to discriminate between deep ballistic photons and shallow depth multiply scattered photons which in practice will limit the maximal depth of OCT imaging to around 10 scattering mean free path [Badon et al., 2016], i.e. around 1 *mm* in biological tissue.

1.2.2 OCT mathematical model

In this section, I derive a simple mathematical model to explain how OCT signals arise on the photodetector and the steps required to reconstruct the complex features of the imaged sample. This is greatly inspired from [Fuji et al., 1997] and [Mertz, 2019], which I recommend to read as the explanations are more thorough with use case examples. Let us consider the propagation of light in the scalar approximation. In the case of a Michelson interferometer, such the one presented Fig. 1.2, the light field E_D at the detector plane can be written:

$$E_D(t) = \underbrace{E_i(t - \frac{2}{c}z_r)}_{\text{reference mirror}} + \underbrace{\int_{z_0 \in L} \rho_z(z_0)E_i(t - \frac{2}{c}z_0)dz_0}_{\text{backscattering inside sample}} \tag{1.4}$$

where E_i is the incident field after the beam splitter (assuming a 50/50 beam splitter), z_r is the axial position of the reference mirror, z_0 is the axial coordinate scanned along the sample domain L, $\rho(z_0)$ is the sample reflectivity at coordinate z_0, c is the average light celerity in the sample[7]. The total intensity $I_D = |E_D|^2$ measured by the photodetector can therefore be written:

$$I_D = I_{rr} + I_{ss} + I_{sr}(z_r) + I_{sr}^*(z_r) + I_{incoh} \tag{1.5}$$

---

[7]For the sake of simplicity I considered an average velocity for the light celerity and I neglected dispersion effects. However one can write the light field on the detector by explicitly injecting an axial and frequency dependence on the celerity c but it is not of interest here.

with:

$$I_{rr} = |E_i|^2 \tag{1.6}$$

$$I_{ss} = \iint_{(z_0, z_0') \in L^2} \rho_z(z_0)\rho_z^*(z_0')E_i\left(t - \frac{2}{c}z_0\right)E_i^*\left(t - \frac{2}{c}z_0'\right)dz_0 dz_0' \tag{1.7}$$

$$I_{sr}(z_r) = \int_{z_0 \in L} \rho_z(z_0)E_i\left(t - \frac{2}{c}z_r\right)E_i^*\left(t - \frac{2}{c}z_0\right)dz_0 \tag{1.8}$$

where z_r is the position of the reference mirror. I_{rr} is a constant term arising from the reference alone, representing the source power. I_{ss} is a term arising from the sample alone and is usually small compared to the other terms because the mirror reflectivity is much higher than the sample reflectivity. $I_{sr}(z_r)$ and $I_{sr}^*(z_r)$ are the complex conjugate interference terms. Finally I_{incoh} corresponds to the light that will not interfer and which will create a uniform background. We can further take into account the temporal coherence of the illumination $\gamma(\tau)$ defined as:

$$\gamma(\tau) = \hat{\gamma}(\tau)e^{-i2\pi c\kappa_c \tau} \tag{1.9}$$

where $\hat{\gamma}$ is the coherence function envelop, $\kappa_c = \frac{1}{\lambda_c}$ is the mean wavenumber of the illumination beam. The time delay between $E_i\left(t - \frac{2}{c}z_r\right)$ and $E_i\left(t - \frac{2}{c}z_0\right)$ is $\tau = \frac{2}{c}(z_0 - z_r)$ therefore Eq. 1.8 can be recast in the equivalent form:

$$I_{sr}(z_r) = \int_{z_0 \in L} \rho_z(z_0)\hat{\gamma}\left(\frac{2}{c}(z_0 - z_r)\right)e^{i4\pi\kappa_c(z_0 - z_r)}dz_0 \tag{1.10}$$

In many applications, the sample reflectivity $\rho(z_0)$ is sought, mainly because it gives a 3D representation of the sample structure. In this case the goal is to extract $\rho(z_0)$ from Eq. 1.10. Notice that before extracting $\rho(z_0)$ from Eq. 1.10 the interference term $I_{sr}(z_r)$ must be isolated from the other term in Eq. 1.5. To do so, several approaches exist such as using phase stepping scheme or by using an off-axis configuration to spatially separate each term as first shown in [Leith and Upatnieks, 1962] and then successfully used in [Schnars and Jüptner, 2002, Kim, 2010].

Time domain OCT

Time Domain OCT (TD-OCT) is based on low temporal coherence illumination so that $\gamma(\tau)$ is tightly localized in time around $\tau = 0$. This coherence function therefore serves as the temporal gate and provides optical sectioning. Let us consider a distribution of N scatterers along the scanned axis (Fig. 1.2 presents a visual example with 3 scatterers), so that the axial reflectivity can be written:

$$\rho(z) = \sum_{i=1}^{N} \rho_i \delta(z_0 - z_i) \tag{1.11}$$

where ρ_i is the i-th scatterer reflectance and $\delta(z - z_i)$ is the Dirac distribution centered on z_i, the axial position of the i-th scatterer. Inserting this in Eq. 1.10 boils to:

$$I_{rs}(z_r) = \sum_{i=1}^{N} \rho_i \hat{\gamma}\left(\frac{2}{c}(z_i - z_r)\right)e^{i4\pi\kappa_c(z_i - z_r)} \tag{1.12}$$

In TD-OCT the reference mirror is axially scanned so that the coherence function is peaked at each z_i, then by taking the magnitude of $I_{rs}(z_r)$:

$$|I_{rs}(z_r)| = \sum_{i=1}^{N} |\rho_i| |\hat{\gamma}\left(\frac{2}{c}(z_i - z_r)\right)| \tag{1.13}$$

one can extract the position z_i of the scatterer with a resolution given by half (because of the round trip) of the coherence function γ width, given for a Gaussian source by Eq. 1.18. In order to obtain the exact phase of ρ_i, the phase of the coherence function must be known, i.e. the frequency spectrum of the source must be characterized beforehand. In many applications, only phase differences matter and computing the argument of $I_{rs}(z_r)$ will therefore suffice. Such applications include measuring a nanometric distance between ρ_i and ρ_{i+1} or track the axial nanometric displacement of $\rho_i(t)$ over time, which was done to see the elongation of photorecptors after visual stimulation in [Pfäffle et al., 2019]); or recovering diffraction limited measurement by performing computational aberration correction by propagating the complex field ρ_i and applying phase law to compensate aberrations effect [Hillmann et al., 2016]. Note that the latter requires phase stability during the 3D volume acquisition, which is usually not the case with scanning OCT for in vivo retina imaging.

Fourier domain OCT

Fourier Domain OCT (FD-OCT) rely on the Fourier analysis of the broadband source and was first introduced in [Fercher et al., 1995]. There are basically two approaches:

- Spectral Domain OCT (SD-OCT) where a broadband spatially coherent source (laser, SLD) is used as illumination in combination with a spectrometer at the interferometer output (typically a prism or grating which decompose the light onto a line camera). Each pixel of the spectrometer probing a narrow frequency band, corresponding to a long temporal coherence.

- Swept Source OCT (SS-OCT) where a tunable laser is used as illumination, the narrow-band illumination is tuned over a wide spectrum. The photodetector is synchronised with the source so that each exposure corresponds to a narrow-band illumination during the sweep.

The experimental setups for both these techniques is depicted Fig. 1.3. In these two approaches, the axial scan is performed optically, rather than mechanically for TD-OCT, which is beneficial for both speed and sensitivity [Kishi, 2016]. Because the frequency band is narrow in FD-OCT the coherence function envelop is very large. Therefore it is possible to approximate the coherence function to a constant over the probed axial extension: $\hat{\gamma}(\tau) \approx 1$, giving for Eq. 1.10:

$$\tilde{I}_{sr}(\kappa, z_r) = e^{-i4\pi\kappa z_r} \int_{z_0 \in L} \rho_z(z_0) e^{i4\pi\kappa z_0} dz_0 \tag{1.14}$$

Note that the wavenumber κ is well defined here since the illumination or detection bandwidth is narrow for each measurement $\tilde{I}_{sr}(\kappa, z_r)$. In FD-OCT, this measurement is performed for $\kappa \in [\kappa_c - \Delta\kappa/2, \kappa_c + \Delta\kappa/2]$ so that κ plays the role of a Fourier variable. An

inverse Fourier transform allows to recover $I_{rs}(z_r)$ from $\tilde{I}_{sr}(\kappa, z_r)$:

$$I_{rs}(z_r) = \frac{1}{\Delta\kappa} \int_{\kappa=\kappa_c-\Delta\kappa/2}^{\kappa_c+\Delta\kappa/2} \tilde{I}_{sr}(\kappa, z_r) e^{i2\pi\kappa z_\kappa} d\kappa \tag{1.15}$$

$$= e^{-i4\pi\kappa_c\left(z_r-\frac{z_k}{2}\right)} \int_{z_0\in L} \rho_z(z_0) sinc\left(2\Delta\kappa\left(z_0 - z_r + \frac{z_k}{2}\right)\right) e^{i4\pi\kappa_c z_0} dz_0 \tag{1.16}$$

Eq. 1.16 is similar to Eq. 1.10, the coherence function being replaced by the inverse Fourier transform of the constant we considered giving a cardinal sinus with a width inversely proportional to the frequency bandwidth $\Delta\kappa$. Inserting Eq. 1.11 in Eq. 1.16 yields:

$$I_{rs}(z_r, z_\kappa) = \sum_{i=1}^{N} \rho_i sinc\left(2\Delta\kappa\left(z_i - z_r + \frac{z_k}{2}\right)\right) e^{i4\pi\kappa_c z_i - z_r + \frac{z_\kappa}{2}} \tag{1.17}$$

where z_r is the fixed position of the reference mirror. $I_{rs}(z_r, z_\kappa)$ is therefore a function of z_κ only which corresponds to the optical scanning of the sample in the Fourier domain. In FD-OCT $I_{rs}(z_r, z_\kappa)$ is peaked around $\frac{z_k}{2} = z_r - z_i$. In the same manner as in TD-OCT, the reflectances $|\rho_i|$ can be obtained by computing the magnitude of $I_{rs}(z_r, z_\kappa)$. Note that in practice the computation of the Fourier transform can be done directly on I_D to avoid phase stepping scheme or off-axis configurations (but this requires a particular position of the reference mirror), but the axial FOV will be reduced by a factor of 2 because of the mirror image $I_{rs}^*(z_r, z_\kappa)$. Not only FD-OCT is faster than TD-OCT because it does not require any axial mechanical translation of the reference arm but also has greater sensitivity. Indeed, the noise is spread on each of the N measured wavelengths[8] so that the SNR is increased by $\sqrt{N}$ [Mertz, 2019]. Nowadays, SS-OCT are privileged over SD-OCT because they offer higher scanning speeds with an A-scan rate of up to 6 MHz while SD-OCT are limited to around 100 kHz (mainly limited by line camera technology). More details about SD-OCT implementations can be found in [Drexler et al., 2014].
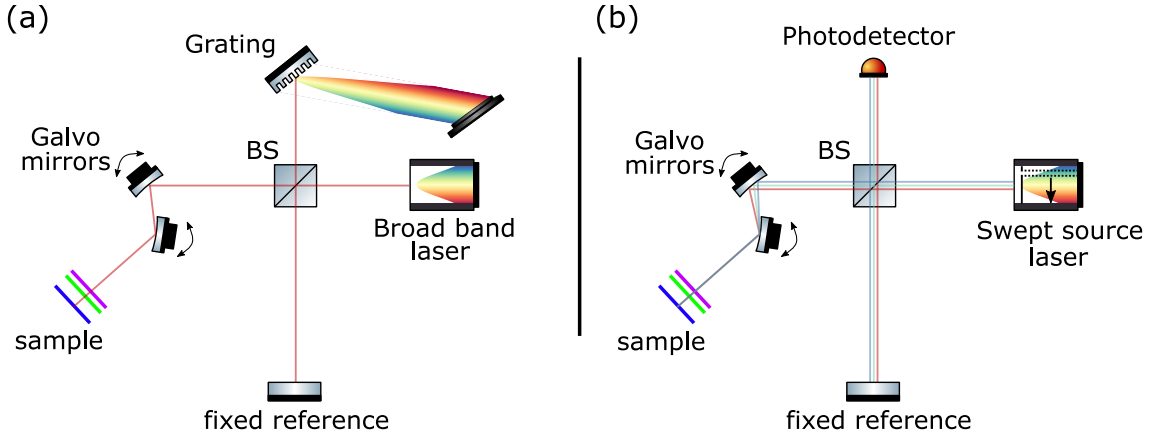
Fig. 1.3: FD-OCT simplified experimental setup. (a) SD-OCT setup: a broadband laser is used as illumination. The intensity is measured for each wavenumber κ and an inverse Fourier transform allows to obtain the axial distribution of reflectance R without mechanical scanning. **(b)** SS-OCT setup: a tunable laser is swept across the range of wavenumbers $\Delta\kappa$. The intensity is recorded for a collection of κ and the axial reflectance of the sample can again be obtained by an inverse Fourier transform.

---

[8]In SD-OCT, the power is divided onto the N pixels of the detector but the exposure time is considered to be N times longer to reach similar A-scan rates between SD-OCT and TD-OCT. Therefore, the measured optical power is similar between both configurations but the noise is equally distributed over N pixels in SD-OCT as opposed to TD-OCT

FD-OCT can also be seen as a manifestation of the Wiener-Khinchin theorem: by scanning the whole reference pathlength axially, the measured intensity corresponds to the axial cross-correlation of the sample and the reference fields. Because each axial position z correspond to a time delay dt, the measured intensity also corresponds to a temporal cross-correlation between the reference and sample fields. Wiener-Khinchin theorem states that the cross-correlation of the electric field is proportional to the Fourier transform of the power spectrum density [Goodman, 1985] so that taking the correctly scaled Fourier transform of the power spectrum density gives the cross-correlation of the electric-field, which is precisely what is measured by TD-OCT in Eq. 1.8. So rather than mechanically scanning the reference pathlength, it is possible to acquire the power spectrum density either by scanning the wavelength at the interferometer input (SS-OCT) or by using a broadband source and measure the spectrum at the output using a spectrometer (SD-OCT).

1.2.3 Performances and limitations of scanning OCT

Axial resolution

Axial resolution depends on the illumination properties and more precisely on the temporal coherence length l_γ. In traditional microscopy techniques, both axial and lateral resolution are linked to the NA of the optical system. In OCT, the axial resolution is independent of the NA (except when the depth of focus is smaller than half of the coherence length, which is rarely the case for scanning OCT). For a source with a Gaussian spectral distribution, the axial resolution δ_z can be written [Goodman, 1985]:

$$\delta_z = \frac{l_\gamma}{2} = \frac{2ln(2)}{\pi} \frac{\lambda_c^2}{\Delta\lambda} \tag{1.18}$$

where l_γ is the coherence length of the illumination, $\Delta\lambda$ is the full width at half maximum of the source power spectrum and λ_c is the source center wavelength in the sample. The axial resolution is inversely proportional to the bandwidth of the light source, and thus high resolution can be achieved by using broadband optical sources. Note that this equation is valid for both TD-OCT and FD-OCT.

Transverse resolution

Transverse resolution is determined by the diffraction limited spot size on the focus plane that is proportional to the center wavelength and inversely proportional to the NA of the system and can be written:

$$\delta_{x,y} = \frac{2\sqrt{ln(2)}}{\pi} \frac{\lambda_c}{NA} \tag{1.19}$$

For fiber-based OCT systems, the thin fiber aperture works as a pinhole in the same manner as confocal microscopy to reject part of out-of-focus light and scattered photons. In this case, the lateral resolution is improved by a factor $\sqrt{2}$.

Depth of focus

The depth of focus (DOF) is related to the Rayleigh range, i.e. the distance from the focal plane to the point where the light beam diameter has increased by a factor $\sqrt{2}$. As in conventional microscopy, the depth of focus in OCT is linked to the transverse resolution:

$$DOF = \frac{\pi}{4} \frac{\delta_{x,y}^2}{\lambda_c} = \frac{ln(2)}{\pi} \frac{\lambda_c}{NA^2} \tag{1.20}$$

Given that the depth of focus decreases when the transverse resolution increases, it is clear that there is a trade-off in scanning OCT. Indeed, by improving the lateral resolution and so decreasing $\delta_{x,y}$ in Eq. 1.19, then the DOF will dramatically decreases. In biological tissue, OCT can typically acquire signals up to 1 mm deep so that the DOF should be greater than 0.5 mm which lead to a maximum transverse resolution of $\delta_{x,y} = 20 \ \mu m$ which corresponds to $NA = 0.015$. Compared to classical microscopy techniques where the NA can be as high as 1.5, this result for OCT was limiting its extensive use in microscopy. Nonetheless, because the axial resolution was decoupled from the NA and could reach $\delta_z = 1 \ \mu m$ OCT found applications in ophthalmology for retina imaging where the retinal layers are separated by a few microns, hence OCT was able to resolve retinal structures for diagnostics. To overcome this trade-off limitation, it is possible to translate the sample in TD-OCT synchronously with the reference mirror so that the probed depth remains in focus so that it becomes possible to use higher NA systems. This adds another complexity and leads to very slow scanning that are not used in practice. It is also possible to use Bessel beams to obtain a larger depth of field with a higher NA [Leitgeb et al., 2006]. This leads to a DOF 10 times greater than with Gaussian beam, leading to a gain of $\sqrt{10}$ in transverse resolution, i.e. $\delta_{x,y} = 6.3 \ \mu m$ (NA = 0.15) for a DOF of 1 mm which is still low compared to traditional microscopy. Note that this drawback can be mitigated with FD-OCT by refocusing the complex field in post processing in order to recover the resolution in out-of-focus planes. Nonetheless, this is only possible for a few depth of focus distance and it is sensitive to multiple scattering and speckle which will deteriorate image quality [Hillmann et al., 2016]. This also requires phase stability and is therefore not always possible in-vivo [Borycki et al., 2019].

In order to mitigate these drawbacks, i.e. improving the resolution and speed, full field techniques were developed by several groups.

1.3 Spatially incoherent time domain FFOCT

Full-Field OCT (FFOCT) refers to OCT techniques where the whole en face slice of a sample volume is acquired simultaneously by using a two-dimensional array camera as the detector in a wide-field interferometer. The expressions derived for lateral resolution and axial FOV for scanning implementation of OCT are also applicable for FFOCT. FFOCT has many advantages over scanning OCT, such as improvement in speed, lateral resolution and aberration compensation for in-vivo acquisitions due to the phase stability. During my PhD I used a spatially incoherent time domain implementation of FFOCT [Dubois et al., 2004]. There also exist:

1. A spatially coherent time domain implementation of FFOCT [Považay et al., 2006, Choi et al., 2012, Hillmann et al., 2016].

2. A spatially coherent off-axis swept-source implementation of FFOCT [Hillmann et al., 2017].

3. A spatially coherent swept-source implementation of FFOCT [Sarunic et al., 2006, Auksorius et al., 2019, Stremplewski et al., 2019].

that I will briefly detail in section 1.4. Spectral domain FFOCT has never been demonstrated since a three-dimensional camera would be necessary to obtain the two spatial and one spectral dimensions that would be required to reconstruct a 3D volume.

During my PhD I designed several experimental setups which I will introduce throughout the following chapters when needed. In this section I want to introduce the original design and highlight the many subtleties and design choice we face when building a FFOCT setup. In order to alleviate the cumbersome notation, I will refer to our spatially incoherent time domain FFOCT as simply FFOCT in the rest of this manuscript.

1.3.1   Basic experimental setup

The basic layout of a FFOCT setup is composed of 4 arms:

1. An illumination arm. We typically use a Köhler illumination with an LED or a thermal source in order to obtain an homogeneous illumination of the sample. In order to obtain the best performances, LED with higher optical power are used (maximal power are not used for eye imaging in order to respect eye safety regulation).

2. A reference arm mounted on a translation stage. This translation stage allows to modify the optical pathlength between both arm in order to match the focal plane and the coherence plane, see section 1.3.3. The reference mirror is mounted on a piezoelectric translation (PZT) in order to apply phase-shifts to demodulate the interference signals. The PZT is controlled by applying a voltage waveform which depends on the phase shifting algorithm (see section 1.3.2). In order to go as fast as possible, the PZT can be driven at several hundreds Hz with abrupt changes in voltage. In order to follow the applied waveform, the current fed to the PZT must be high enough and often requires a current amplification stage between the digital to analog converter (which has limited current output) and the PZT.

3. A sample arm where only the sample is mounted on a translation stage to shift the plan of imaging in order to select the depth we want to image and make 3D volume images. Because there is no trade-off between axial FOV and transverse resolution, we typically use high NA objectives to obtain resolutions around $\delta_{x,y} = 0.5\ \mu m$. The sample arm is usually built strongly mechanically coupled with the reference arm, especially for dynamic acquisition. Indeed, mechanical vibration between the interferometer and the camera would hardly be visible because nanometer displacement remains in the depth of focus of the tube lens. But nanometric displacement inside the interferometer cause the phase to shift and can be detrimental for dynamic measurement, see chapter 3.

4. A detection arm where a tube lens focus the light field on a CMOS camera. This is probably the most important arm because FFOCT sensitivity is strongly dependant on the camera technology. Indeed, the signal to noise ratio (SNR) is linked to the full well capacity (FWC) [Scholler et al., 2019], i.e. the number of photo-electron the camera can probe per pixel. For many applications the number of probed photons is low (fluorescence, astronomy, etc.) and a good camera must provide a low dark noise to probe a few photons. In FFOCT it is completely the opposite: we need to probe a very large amount of photons and we care less about dark noise because we are always shot noise limited in our experiments, i.e. we are limited by the Poisson nature of photons arrival and not by the electronic noise of the camera. A great advance in FFOCT was born with the development of a new camera (Quartz 2A750, ADIMEC, Netherlands) which made FFOCT a promising approach. The best camera on the market before ADIMEC was a PhotonFocus (MV-D1024E-160-CL-12, Switzerland) which could probe 2×10^5 photo-electrons at 150 frames per second

(fps) giving a photo-electron throughput of $f_{PF} = 3 \times 10^7$ photo-electron/s. Compared to ADIMEC camera (which also has more pixels) which can probe 2×10^6 photo-electrons at 720 fps giving a photo-electron throughput of $f_A = 1.44 \times 10^9$ photo-electron/s. This represents a gain of almost 7 in SNR.

This arm is linked to the computer which I had the chance to design (see appendix A) and built myself for our experiment requirements. At the beginning of my thesis I designed the software used for my experiments which I later published [Scholler, 2019a]. This is the only piece of code written using non-open source programming language that I coded during my PhD, in the aim that it could benefit for other researcher in our group (MatLab is still more popular). I developed with versatility, speed and re-usability in mind and it is the same software that controls our FFOCT setups for ex-vivo experiments (FFOCT, FFOCT combined with fluorescence, FFOCT combined with adaptive optics) and in-vivo experiments (retinal imaging).
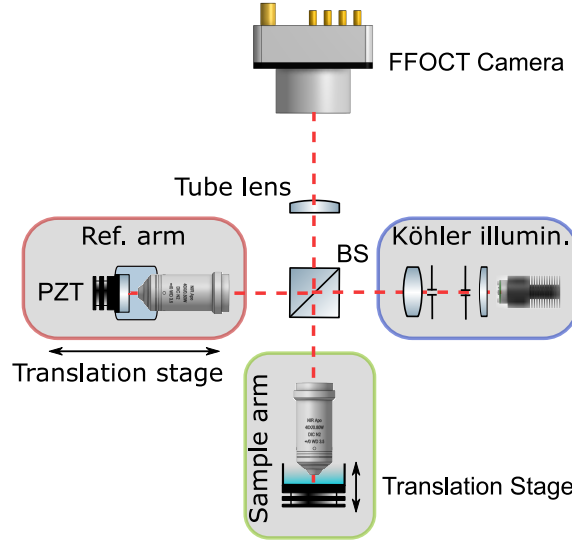
Fig. 1.4: FFOCT simplified experimental setup.

1.3.2 Phase shifting interferometry

The intensity recorded by the FFOCT camera is the sum of the backscattered light from both the sample and the reference arm, Eq. 1.5 can be recast for FFOCT and taking the 2D detection into account:

$$I_D(\boldsymbol{r}) = \eta \frac{I_0}{4} \left(\rho_s^2(\boldsymbol{r}) + \rho_{inc}^2 + \rho_{ref}^2 + \underbrace{2\rho_s(\boldsymbol{r})\rho_{ref} cos\left(\Delta\phi(\boldsymbol{r})\right)}_{\text{interference term}} \right) \qquad (1.21)$$

where $I_D(\boldsymbol{r})$ is the intensity recorded at position $\boldsymbol{r} = (x, y)$, η is the camera quantum efficiency, I_0 is the power LED output impinging on the interferometer considering a 50/50 beam-splitter, ρ_{ref} is the reference mirror reflectivity in amplitude, $\rho_s(\boldsymbol{r})$ is the sample reflectivity in amplitude at position $\boldsymbol{r}$, $\Delta\phi(\boldsymbol{r})$ is the phase difference between the reference and sample back-scattered signals at position $\boldsymbol{r}$, $I_{inc} = \rho_{inc}I_0/4$ is the incoherent light back-scattered by the sample on the camera, mainly due to multiple scattering and reflections out of the coherence volume. From Eq. 1.21 it is clear that processings must be applied to recover the interference term from the measured intensity. To do so, we use phase shifting algorithms which are detailed in the following sections.

2 phases demodulation

To perform 2 phases demodulation, two frames are recorded with a π-shift phase difference. The intensity recorded on a camera pixel is the coherent sum of the reference and sample beams and can be written using Eq. 1.21:

$$I_{\Phi=0} = \eta \frac{I_0}{4}(\rho_s^2 + \rho_{inc}^2 + \rho_{ref}^2 + 2\rho_s\rho_{ref}cos\left(\Delta\phi(\boldsymbol{r})\right)) \tag{1.22}$$

$$I_{\Phi=\pi} = \eta \frac{I_0}{4}(\rho_s^2 + \rho_{inc}^2 + \rho_{ref}^2 - 2\rho_s\rho_{ref}cos\left(\Delta\phi(\boldsymbol{r})\right)) \tag{1.23}$$

where $I_{\Phi=0}$ is the intensity recorded without phase shift, $I_{\Phi=\pi}$ is the intensity recorded for a π phase shift. The 2 phases image $I_{2-phases}$ is formed by subtracting $I_{\Phi=\pi}$ from $I_{\Phi=0}$ and taking the modulus:

$$I_{2-phases} = \eta I_0 \rho_s \rho_{ref} |cos(\Delta\phi)| \tag{1.24}$$

As shown by Eq. 1.24, it is not possible to un-mix phase and amplitude by using a 2 phases scheme. This imaging mode is nonetheless interesting because it is the fastest and when phases are randomly distributed[9] (e.g. in biological tissue), one might be interested to go faster and average many 2 phases images rather than using more complex phase shifting techniques.

4 phases demodulation

If we could theoretically isolate the interference term and un-mix phase and amplitude using only three phases, the 4 phases scheme is preferred as it allows an easier and more robust computation [Dubois et al., 2002]. This scheme consists of acquiring four images $I_{i\in[1,4]}$ with phase difference of $[3\pi/2, \pi, \pi/2, 0]$. Then amplitude and phase are reconstructed using the following equations:

$$A = \frac{1}{2}\sqrt{(I_4 - I_2)^2 + (I_3 - I_1)^2} \tag{1.25}$$

$$\phi = tan^{-1}\left(\frac{I_3 - I_1}{I_4 - I_2}\right) \tag{1.26}$$

Note that in practice we compute $arg((I_4 - I_2) + i(I_3 - I_1))$ which is numerically more stable against noise than computing the tan^{-1}. The main drawback of the 4 phases demodulation is that it works only for quasi monochromatic illumination. With a broadband illumination, the phase shift applied by translating the reference mirror differs for each wavelength and artifacts arise: amplitude and phase are not correctly demodulated.

5 and 10 triangular phases demodulation

To perform triangular phase demodulation, a triangular modulation is imposed onto the PZT. During both the increasing and decreasing part 5 images are taken, see Fig. 1.5(a) for notations. Then amplitude and phase are computed as follows [Larkin, 1996] for the 5 phases image:

$$A = \sqrt{4(I_2 - I_4)^2 + (-I_1 + 2I_3 - I_5)^2} \tag{1.27}$$

$$\phi = -tan^{-1}\left(\frac{2(I_2 - I_4)}{-I_1 + 2I_3 - I_5}\right) \tag{1.28}$$

---

[9]If phases are randomly distributed then fringes artifacts are not presents.

For such triangular demodulation, there are several ways to compute the amplitude and phase, i.e. different possibilities to choose $I_{i\in[1,5]}$. For each triangle it is possible to construct 2 images, the first by taking $I_{i\in[1,5],a}$ and the second by taking $I_{i\in[1,5],b}$. The problem with doing so is that it requires a perfect synchronization between the piezo and the camera, which was nearly impossible to obtain in practice as the calibration depends on the camera frame-rate[10]. Another possibility is to average a and b images before computing the amplitude and phase maps, leading to only one image per triangle and effectively using 10 phases per FFOCT image. This method is much more stable, see Fig. 1.5(b-e). When the synchronization is perfect, 5 and 10 phases images are identical. I acquired a stack of 20 amplitude and phases map on a silicon mirror using 4,5 and 10 phases algorithm. I then computed the phase map RMS error Fig. 1.5(b-d) using the following expression to avoid phase wrapping:

$$RMSE_{phase} = RMSE(e^{i\phi}) = \sqrt{\sum_i |\phi_i - \bar{\phi}|^2} \qquad (1.29)$$

where ϕ_i is the computed phase at time sample i, and $\bar{\phi}$ is the average phase. One can see on Fig. 1.5(b-g) that there are phase modulations remaining. Indeed, because we are using polychromatic sources the 4 phases reconstruction algorithm perfectly demodulates for the central wavelength but artifacts arise for other wavelengths. It has been shown that triangular 5 phases algorithm allows to cancel first order errors for polychromatic interference patterns [Larkin, 1996]. Triangular phase shifting algorithm is better at un-mixing phase and amplitude in FFOCT than 2 and 4 phases, see Fig. 1.5(f,g). The drawback would be the acquisition speed 10 times slower if we compute amplitude and phase maps using 10 frames.
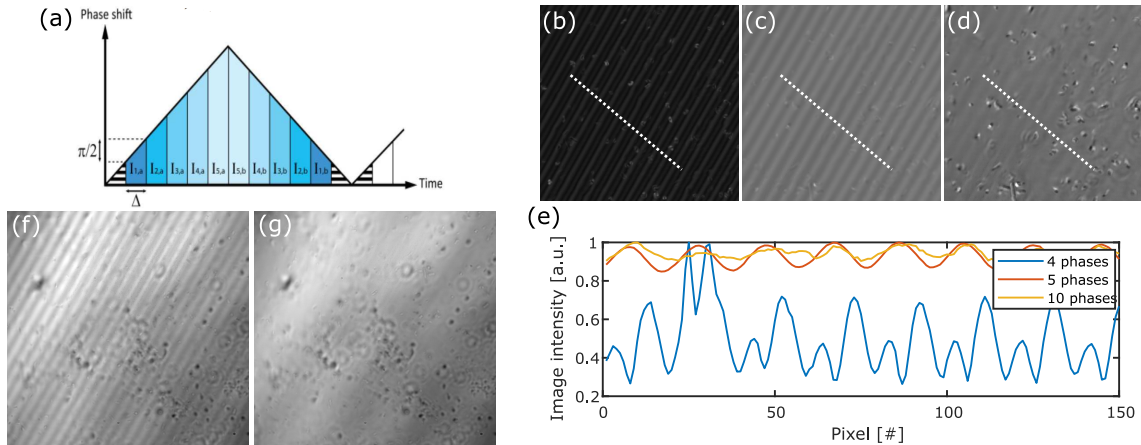
Fig. 1.5: 5 and 10 phases demodulation. (a) A triangular phase shift is applied on the PZT and 5 images are recorded during the rising phase and then 5 images are recorded during the decreasing phase. **(b,c,d)** are respectively the phase standard deviation for a 20 frames acquisition with 4 phases, 5 phases and 10 phases with **(e)** the profile to compare the phase stability. **(f,g)** are respectively the amplitude obtained with a 4 phases and a 10 phases scheme. 10 phases scheme allow to better un-mix the amplitude and phase, resulting in less fringes artifacts on the amplitude image.

---

[10]When the camera is triggered there is a delay before it starts to acquire. This delay varies with the frame-rate and other parameters so that it was not possible to calibrate it in practice.

Other demodulation techniques

There are other demodulation schemes that I haven't used during my PhD. A popular one is a sinusoidal modulation of the PZT [Dubois et al., 2002] that allows to use the piezo at very high frame rate which can be useful for elastography imaging [Nahas et al., 2013a, Nahas et al., 2013b]. I did not need such acquisition frame rate so I never use this approach which requires a good synchronisation between the camera and the piezo.

1.3.3 Differences that matters with FFOCT

Even if the principles of FFOCT are very close to scanning OCT, in practice there are slight differences that needs to be tackled in order to obtain good performance for imaging. These differences are gathered and explained in this section.

High NA: depth of focus lower than coherence length
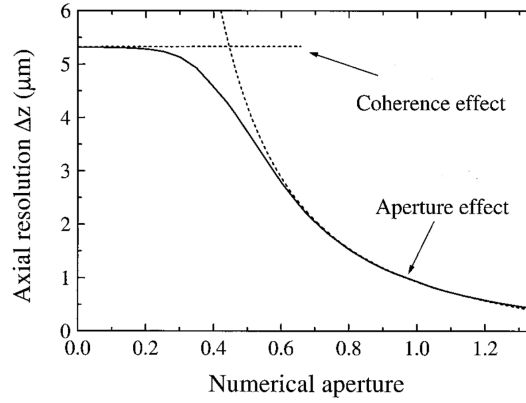
Fig. 1.6: Axial resolution in FFOCT. For low NA the axial resolution is fixed by the illumination coherence length. For higher NA, the depth of focus can become smaller than the coherence length, hence reducing the axial resolution. Figure adapted from [Dubois et al., 2002].

Because the trade-off between the DOF and the transverse resolution does not exist in FFOCT. High NA objectives are typically used in order to get the best possible transverse resolution and to resolve the smallest possible features, especially where cellular resolution is required. While for low NA the axial resolution given by Eq. 1.18 is still valid, for higher NA the depth of focus will be shorter than the coherence length so that interferences happening outside of the depth of focus are blurred and therefore damped. For high NA the axial resolution is given by:

$$\delta_z^{\text{high NA}} = \underbrace{\frac{n\lambda_c}{NA^2}}_{\text{diffraction}} + \underbrace{\frac{n}{NA}\frac{l_{pixel}}{M}}_{\text{geometry}} \tag{1.30}$$

where n is the imaging medium refractive index, l_{pixel} is the pixel size and M is the system magnification so that l_{pixel}/M is the size of the pixel imaged onto the imaged sample. The transition from Eq. 1.18 to Eq. 1.30 is smooth and represented Fig. 1.6. The geometry effect arises from discrete pixel sampling on the camera and is usually (for correctly designed systems) not the limiting term as opposed to the diffraction. In practice the axial resolution in my experiment in microscopy was always set by the aperture, the exception being in-vivo retinal imaging, where the NA of the eye is lower.

Mismatch between focal plane and coherence plane

In order to acquire in depth en-face images of a sample, we translate the sample using a motorised sample stage shown Fig. 1.4 illustrated with water-immersion objectives. In general, samples have different refractive index than the immersion medium (water or oil), so that the focus position will shift inside the sample because of the refractive mismatch, see Fig. 1.7. When the refractive index of the sample is higher than the immersion medium, then the focus shifts downwards. The reference arm is built with the right immersion medium in order to lower aberrations and because it is easier in practice. Now, the beam will travel slower in the sample than in the immersion medium in the reference arm, this means that the illumination beam will travel less distance in the sample that in the reference arm, effectively shifting the coherence gate position upwards, in the opposite direction of the focus. This lead to a mismatch between the coherence plane and the focal plane, which dampen the interferometric signal. In order to be able to image in-depth we need to compensate the mismatch by shifting the whole reference arm to shift only the coherence gate inside the sample, so that it matches back the focal plane. The same phenomenon happens if the refractive index of the sample is lower than the refractive index of the immersion medium.
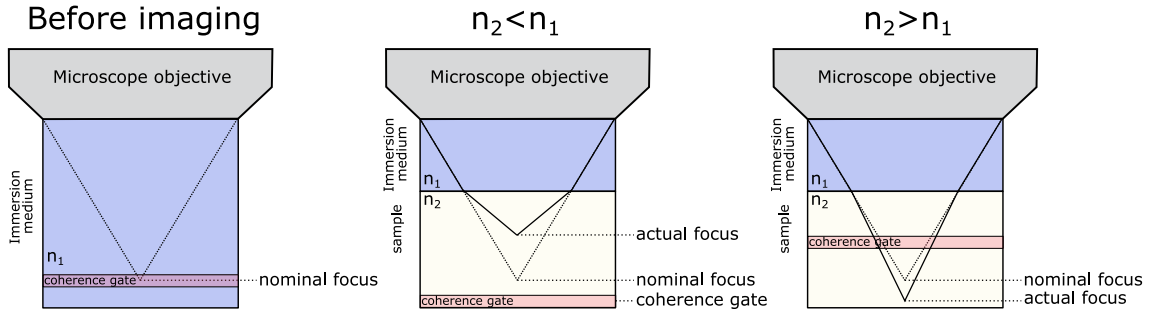
Fig. 1.7: Focus and coherence mismatch. Refractive index changes in the sample arm due to the sample shifts the focus plane. In addition, the light travels at a different speed and therefore the coherence plane position also shifts. Because these two shifts happen in opposite direction, the coherence plane position must be compensated by moving the reference arm.

There exists closed form computation in the paraxial approximation [Labiau et al., 2009, Binding et al., 2011] of the reference arm translation needed to perfectly compensate for the refractive mismatch. In practice it requires to know precisely the refractive index (or refractive index distribution) of the sample and to control the motor with micrometric precision so that it becomes cumbersome to apply the correction with the analytic formula. In my experiments, I can automatically move the reference arm to maximize the FFOCT signal and correct for the mismatch which takes times because it is an optimization process. Another strategy is possible owing to the linearity of the mismatch with respect to the depth of imaging. If I want to image up to a depth d, then I optimize the reference arm at this depth and at the sample surface. Because the mismatch is linear with depth I just need to interpolate between the two optimal position during the imaging procedure. To grasp the scale involved in the refractive mismatch we can compute the spatial mismatch $\delta_{mismatch}$ between the focal plane and the coherence plane:

$$\delta_{mismatch}(z) = 2n_s z \left(\underbrace{\frac{tan\left(sin^{-1}\left(\frac{n_m}{n_s} sin\left(cos\left(sin^{-1}\left(\frac{NA}{n_m}\right)\right)\right)\right)\right)}{tan\left(sin^{-1}\left(\frac{NA}{n_m}\right)\right)}}_{\text{focus shift}} - \underbrace{\frac{n_m}{n_s}}_{\text{coherence shift}} \right) \quad (1.31)$$

This equation can be simplified when using low NA in the paraxial approximation:

$$\delta_{mismatch}^{paraxial}(z) = 2n_s z \left(\frac{n_s}{n_m} - \frac{n_m}{n_s} \right) \quad (1.32)$$

where z is the depth of imaging, n_s and n_m are the sample and immersion medium refractive index, respectively. For $NA = 0.8$ in water ($n_m = 1.33$) with $n_s = 1.4$ we have $\delta_{mismatch}(z) = 0.52z$. In practice this needs to be compared with the coherence length, when the mismatch is bigger than the coherence length then FFOCT signals start to be damped.

1.4   Other FFOCT systems

The spatial coherence of the illumination has a strong impact on imaging performances in full field configurations. Indeed, with spatially coherent illumination, artifacts are present due to multiple scattering and cross talk [Karamata et al., 2005a, Karamata et al., 2005b]. Cross talk originates in scattering samples when multiply scattered photons with the same pathlength interfere on the camera. Because there is no spatial filtering, photons from different transverse position can interfere on the camera. In scanning OCT, the confocal aperture of the fiber rejects most of the multiply scattered light. However, FFOCT systems lack this confocal aperture and therefore, multiply scattered photons propagates back to the camera. Using an incoherent illumination in our TD-FFOCT system we prevent multiply scattered photons from interfering, effectively creating a spatial coherence gate that serves the same function as the confocal pinhole in scanning OCT. For spatially coherent FFOCT there are essentially two strategies:

1. Tilting the reference arm. Indeed, most of the multiple scattering is happening inside the sample and is therefore contained in I_{ss} in Eq. 1.5. Tilting the reference allow to spatially separate the self interference of the sample (cross talk) from the cross-interference between the reference and the sample, which greatly limits artifacts.

2. Breaking the spatial coherence of a swept-source laser by rapidly changing the phase, i.e. deccorelating the speckle in the sample, during the exposure time of the camera.

These two approaches are briefly discussed in this section.

1.4.1   Off-axis FFOCT

Off-axis spatially coherent time domain FFOCT as been demonstrated for low cost hand-held retina imaging [Sudkamp et al., 2016], and is currently being engineered for commercial application. The setup is depicted Fig. 1.8(a). Advantages of this approach is that computational aberrations correction is possible in post-processing [Sudkamp et al., 2018] owing to the coherent illumination, allowing diffraction limited imaging in the eye without

the need for costly and cumbersome adaptive optics hardware. Together with the cheap superluminescent diode (SLD) illumination, this low cost approach is very promising for medical application (a patient could borrow a device and use it alone to remotely monitor its retina). The second approach that successfully uses the off-axis configuration is based on a swept source illumination [Hillmann et al., 2017], depicted Fig. 1.8. This approach is faster (ultra-fast camera and swept source) but it also a lot more expensive, making it an interesting approach more suited for research.
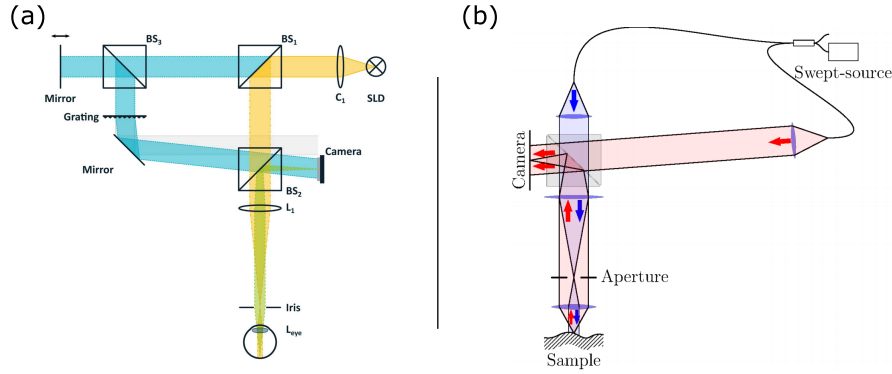
Fig. 1.8: Off-axis FFOCT. (a) Time domain implementation where a spatially coherent superluminescent diode (SLD) is used for illumination. The reference beam is tilted for suppressing the cross-talk inside the sample. **(b)** Swept source implementation where the reference beam is also tilted for the same purpose. This figure is adapted from [Sudkamp et al., 2016] and [Hillmann et al., 2017].

1.4.2   Phase decorrelated swept-source FFOCT

Rather than tilting the reference beam to remove cross-talk, it is possible to rapidly (during the exposure time of the camera) shuffle the phases to simulate an incoherent acquisition. First demonstrated using a spatial light modulator (SLM) [Borycki et al., 2019] it has been applied in-vivo for skin imaging [Stremplewski et al., 2019] and for retinal imaging [Auksorius et al., 2019] using a deformable membrane which is much faster than an SLM. The experimental setup is shown Fig. 1.9. With this approach, it is also possible to perform computational aberration correction [Borycki et al., 2019, Borycki et al., 2020] even if the coherence of the illumination is broken by the phase shuffling. In term of acquisition time, this is the fastest FFOCT system for volumetric imaging to this day[11] with 15.7×10^9 voxel per second leading to 116 volume per second. In comparison our FFOCT approach with 2 phases demodulation gives 0.75×10^9 voxel per second leading to 0.7 volume per second with 512 en-face images. The difference being that our en-face images have 1440×1440 pixels compared to 512×512 for their ultra-fast camera, so that we can have a greater field of view.

---

[11]Note that the aberration correction is done before averaging so the computing time required for getting a 3D volume must be very high. Even if the acquisition takes a few milliseconds, the time required before getting and being able to see the object in 3D is at least a few hours.
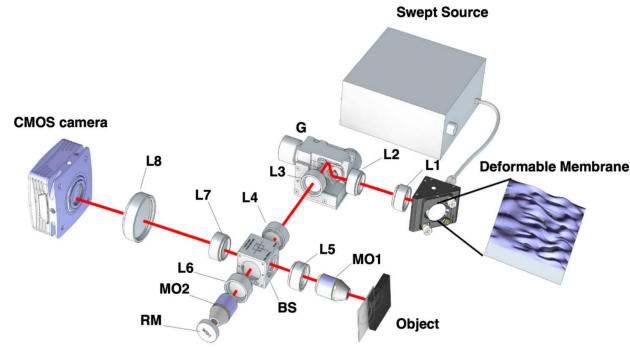
Fig. 1.9: Phase decorrelated SS-FFOCT. L1-L8: achromatic doublet lenses - G: galvo scanner introducing additional angular compounding; MO1 and MO2: 10x Olympus objectives with 0.3NA - RM: reference mirror - BS: beam splitter. This figure is adapted from [Stremplewski et al., 2019]

Chapter 2

New contrast for live cell and tissue imaging: D-FFOCT

Contents

2.1 D-FFOCT: new contrast to reveal cells

Dynamic full-field optical coherence tomography (D-FFOCT) was first proposed by Clément Apelian [Apelian et al., 2016] as a novel technique to image the intra-cellular dynamic of living cell in fresh ex-vivo tissues. The primary idea was to reveal cells inside scattering tissue, indeed cells are mostly transparent and homogeneous which make them challenging to image, especially in tissue where they are mixed with very reflective collagen fibers that have very reflective properties. Cells are essentially phase object and Zernike originally proposed in 1942 [Zernike, 1942] a phase contrast to statically enhance cell contrast. Using the same idea D-FFOCT uses interferometry to probe phase changes in order to enhance cell contrast and allow to probe intra-cellular motility. The metabolic index was first proposed to be computed as the temporal running standard deviation averaged for several hundreds frames [Apelian et al., 2016, Thouvenin et al., 2017a]. We will see that several features can be computed on top of the metabolic index in order to generate colored images and that these features carry limited physical information about scatterers but allow to differentiate between cells by looking at their dynamic profile[1].

Initially, D-FFOCT phenomenological description was that the display of the amplitude of fluctuations enhances the signal from cells while reducing the signal from stationary structures. Moreover, the dynamic contrast is not observed in fixed samples (retina organoids, cell cultures and mice liver) suggesting that the origin of D-FFOCT signals is linked to metabolic activity. Previous experiments [Apelian et al., 2016] shown that blocking the

---

[1]The distribution of metabolic index and the distribution of fluctuations frequencies.

energy production[2] inside cells with 2-deoxy-D-glucose rapidly leads to a decrease in D-FFOCT signals. This experiment shows that signal fluctuations mostly depend on active processes inside cells and that confined Brownian diffusion probably does not lead to enough fluctuations to create a significant D-FFOCT signal.

2.2 D-FFOCT: amplitude or phase fluctuations?

One may wonder what is the origin of the dynamic signals being probed and what physically leads to these fluctuations. Let us assume that we have a single scatterer in the coherence volume, which roughly have a transverse size of 0.5 μm and an axial size of 1.5 μm for most of our experiments[3]. The first thing to note is that a π phase shift (equivalent to an axial displacement of $\lambda/4$) produces a fluctuation twice as big as a scatterer going from the center of the voxel to outside of the voxel. The latter is equivalent to a lateral displacement of $\lambda/NA \approx \lambda$ so that phase sensitivity is around 10 times higher than amplitude sensitivity. This means that for small displacement D-FFOCT fluctuations are mainly phase fluctuations. For longer displacement, e.g. for active transport in cells, then amplitude fluctuations needs to be considered. Let us consider a mitochondria which can be in two states [Saunter et al., 2009]: Brownian diffusion or motor-driven motion whose duration are stochastically determined with speeds that can reach 300 $nm.s^{-1}$. The typical size of mitochondria ($\sim 1 \ \mu m$) allows to have only one scatterer per voxel so that we can simply simulate both states of the mitochondria to illustrate phase and amplitude fluctuations. The interferometric signal is modeled for a mitochondria at position (x, y, z) (the origin is taken in the center of the voxel) with the following equation:

$$I_D(t) = \underbrace{A_t(x(t), y(t))A_a(z(t))}_{\text{amplitude}} \underbrace{cos\left(\frac{4n\pi}{\lambda}z(t)\right)}_{\text{phase}} \tag{2.1}$$

where $A_t(x, y)$ is the transverse amplitude function[4], $A_a(z)$ is the axial amplitude function[5], n is the sample refractive index, λ_c is the source central wavelength and $z(t)$ is the mitochondria axial position. I simulated both mitochondrial state with the parameters measured by [Saunter et al., 2009]. The results are shown Fig. 2.1(a,b) for the Brownian diffusion where the displacements are small and the fluctuations can mostly be associated with phase fluctuations. On the contrary, for active transport where the displacements are much longer Fig. 2.1(c,d) then the dynamic fluctuations are from both amplitude and phase fluctuations[6]. From this simple experiment one can already see that even in the strong hypothesis that there is only one scatterer per voxel the inverse problem of recovering some physical parameter such as the scatterer speed or diffusion coefficient given the dynamic signal is impossible. Indeed, we only have one equation but many unknowns (initial position, direction of motion, etc.). Adding more scatterers create an average effect that

---

[2]2-deoxy-D-glucose blocks glycolysis inside cells, but glycolysis also produces pyruvate, which is essential for aerobic ATP production of the cells. Therefore, injecting 2-deoxy-D-glucose without adding pyruvate provoke a disruption of ATP production and stops most active processes of the cells, including active transport.

[3]I only used high NA objectives where the optical sectioning and therefore the axial resolution was set by the depth of focus rather than the coherence length.

[4]Approximated as a 2D Gaussian with standard deviation $\sigma_{x,y} = \frac{\lambda_c}{NA}$.

[5]Given by the depth of field and approximated as a Gaussian with standard deviation $\sigma_z = \frac{\lambda_c}{NA^2}$

[6]Transverse displacements only acts on amplitude fluctuations, whereas axial displacement acts on both.

tends to increase the phase fluctuations influence over the amplitude fluctuations because on average the number of scatterer per volume should remain the same. Even if one scatterer leave the coherence volume, its influence on the dynamic signals is less important than in the single scatterer case, see Fig. 2.1(e,f) where I simulated 10 scatterers in the coherence volume with the same backscattering properties. The measured fluctuations come almost exclusively from phase fluctuations. Note that my simple model considered that the scatterers orientations were constant, in practice scatterers probably rotate and this adds another unknown preventing us to extract physical properties. Finally, in this simulation I neglected the shot noise but even if the inverse problem was tractable, the uncertainties associated with the computed physical parameters would probably prevent us from drawing a conclusion on what was in fact giving such fluctuations. Even if we cannot extract quantitative physical properties, it is possible to compute numerous features on these dynamic signals to generate dynamic images. These features are usually the amplitude of the fluctuations, the dynamic mean frequency or the decorrelation time[7] which are then associated using the HSV method, see appendix B. The aim being to create a contrast that can be useful to interpret images and get biological insight on live cell cultures.

---

[7]Interestingly the mean frequency and the decorrelation time computed as the width at half maxima of the autocorrelation of dynamic signals gives similar contrasts.
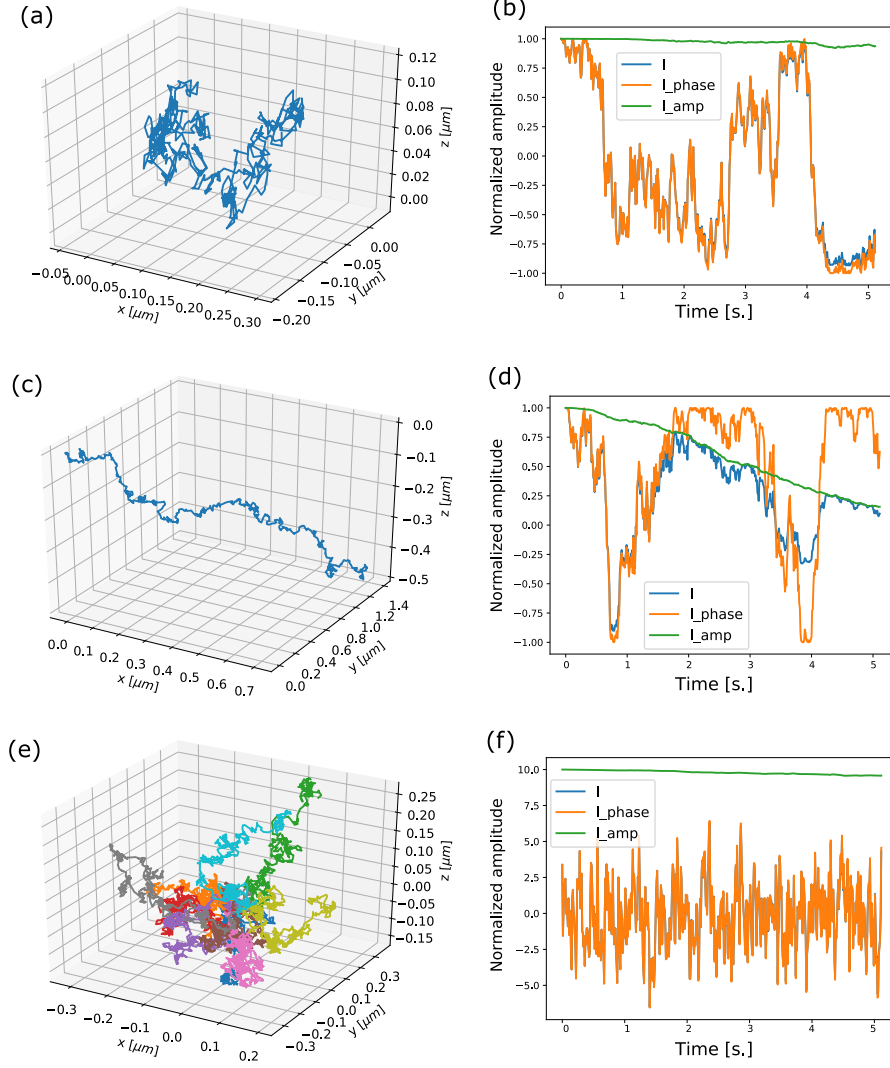
Fig. 2.1: Dynamic simulations of single mitochondria. (a,b) Simulations for Brownian diffusion state, mitochondria's position is shown in **(a)**. **(c,d)** Simulations for active transport state, mitochondria's position is shown in **(c)**. **(e,f) Simulation with 10 scatterers.** Scatterers position are shown in **(e)**. The measured intensity on the detector is depicted in **(b,d,f)** for amplitude fluctuations, phase fluctuations and both. For Brownian diffusion of single scatterer **(b)** the fluctuations are dominated by phase fluctuation, whereas for active transport greater displacements lead to both phase and amplitude fluctuations **(d)**. The more scatterers the more dynamic fluctuations arise from phase fluctuations only **(f)**.

2.3 Interferometric amplification

Signals probed by D-FFOCT are tiny and are close to the detection limit which is approximately 83 dB for our setups [Scholler et al., 2019]. We can therefore detect a sample with reflectivity $\rho_s \approx 10^{-8.3}$, i.e. when only 1 photon amongst 200 millions is backscattered it is still possible to probe it. This high sensitivity is due to the interferometric amplification, indeed by looking at the detected intensity on the detector (Eq. 1.21 given again below

for convenience):

$$I_D(\boldsymbol{r}) = \eta\frac{I_0}{4}\left(\rho_s^2(\boldsymbol{r}) + \rho_{inc}^2 + \rho_{ref}^2 + \underbrace{2\rho_s(\boldsymbol{r})\rho_{ref}cos\left(\Delta\phi(\boldsymbol{r})\right)}_{\text{interference term}}\right) \qquad (2.2)$$

one can see that the sample reflectivity ρ_s is amplified by the reference reflectivity ρ_{ref}. We can wonder how ρ_{ref} must be chosen in order to maximize the SNR when we are shot noise limited (which is always the case in practice as we work close to the camera saturation). If we suppose that dynamic signals are created by phase fluctuation alone, the maximal intensity change when scatterers have time to explore more than half the central wavelength can be written:

$$\Delta I_{max}(\boldsymbol{r}) = \eta\frac{I_0}{2}\rho_s(\boldsymbol{r})\rho_{ref} \qquad (2.3)$$

The maximal SNR can then be computed:

$$SNR_{max}(\boldsymbol{r}) = \frac{\Delta I_{max}}{\sqrt{I_D(\boldsymbol{r})}} \qquad (2.4)$$

$$= \sqrt{\eta I_0}\frac{\rho_s(\boldsymbol{r})\rho_{ref}}{\sqrt{\rho_s^2(\boldsymbol{r}) + \rho_{inc}^2 + \rho_{ref}^2 + 2\rho_s(\boldsymbol{r})\rho_{ref}}} \qquad (2.5)$$

I simulated $SNR_{max}/\sqrt{\eta I_0}$ for various ρ_s and ρ_{ref} with $\rho_{inc} = 0$[8], Fig. 2.2(a), where the black dashed lines correspond to a constant intensity I_D on the camera. For a given I_D (ideally close to the camera saturation to maximize the SNR [Scholler et al., 2019]) one can see that the best SNR is always obtained when $\rho_s = \rho_{ref}$ which is what we can analytically find by maximizing the SNR under the constraint of constant I_D using Lagrange multipliers. Now, if we consider that ρ_{inc} is a function of ρ_s the analytical solution is much harder to find but the simulation remains tractable. If we consider ρ_{inc} proportional to ρ_s, then we obtain Fig. 2.2(b) where I considered that $\rho_{inc} = 1000 \times \rho_s$. This time one can see that the reference needs to be stronger (more reflective) than the sample in order to lower the incoherent part and amplify the sample signals without increasing the incoherent part. The optimal SNR curve is still a line with the same slope but shifted towards the reference[9].

---

[8]In this case $SNR_{max}/\sqrt{\eta I_0} = 0.5$ (due to the 50/50 beam splitter half of photons are lost) for $(\rho_s, \rho_{ref}) = (1, 1)$. The shape of $SNR_{max}/\sqrt{\eta I_0}$ would not change by taking ρ_{inc} for another constant but will lower the SNR because some photons will not be backscattered

[9]There are also settings where the power send inside the sample must be low (e.g. in vivo retina imaging) and where the reference can be increased to improve the SNR without damaging the sample. This gives (D-)FFOCT an important degree of liberty regarding SNR and power distribution.
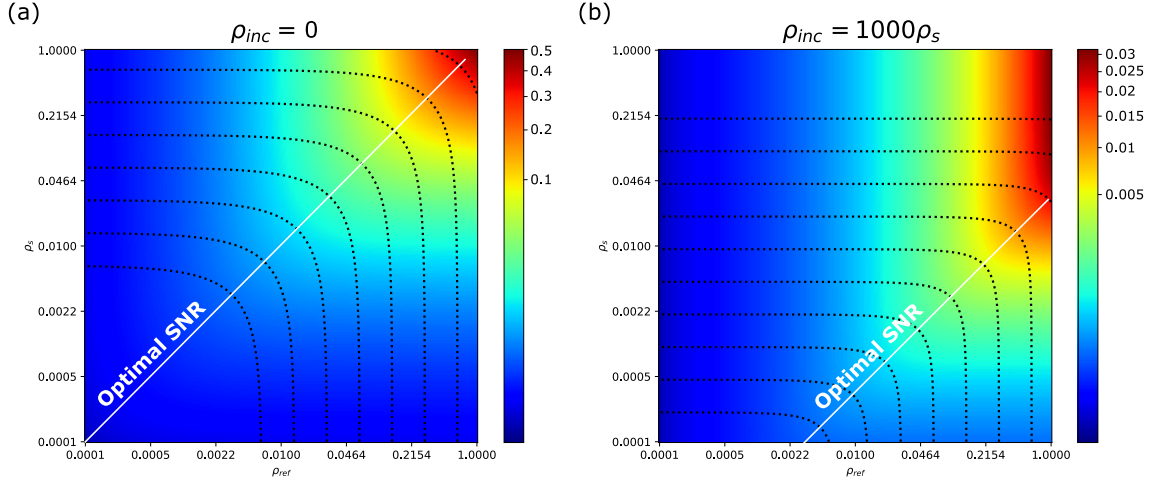
Fig. 2.2: SNR in FFOCT for various conditions. (a) When the incoherent part ρ_{inc} is set to 0 and **(b)** when the incoherent part ρ_{inc} is proportional to the sample part ρ_s.

Now if we compare to a conventional system which can filter out out-of-focus photons in post processing (e.g. [Mecê et al., 2020]) the SNR will be:

$$SNR_{conv} \propto \frac{\rho_s^2}{\sqrt{\rho_s^2 + \rho_{inc}^2}} \approx \frac{\rho_s^2}{\rho_{inc}} \tag{2.6}$$

whereas for D-FFOCT if $\rho_s \ll \rho_{inc}$ and $\rho_s \ll \rho_{ref}$ the SNR writes:

$$SNR_{FFOCT} \propto \frac{\rho_s \rho_{ref}}{\sqrt{\rho_{ref}^2 + \rho_{inc}^2}} \tag{2.7}$$

If we consider that $\rho_{ref} \approx \rho_{inc}$ it yields:

$$\frac{SNR_{FFOCT}}{SNR_{conv}} = \frac{\rho_{ref}}{\sqrt{2}\rho_s} \tag{2.8}$$

Considering typical values $\rho_s = 10^{-6}$ and $\rho_{ref} = 0.5$ we obtain $SNR_{FFOCT}/SNR_{conv} = 3.5 \times 10^5$. One can see that owing to the interferometric amplification, D-FFOCT is tremendously more sensitive to probe tiny variations of sample reflectivity, hence its ability to probe motility signals from small scatterers inside scattering samples.

2.4 Article: Dynamic full-field optical coherence tomography: 3D live-imaging of retinal organoids

In this article, we take advantage of the high sensitivity and high contrast of D-FFOCT and demonstrate its ability to image non-destructively retina organoids. The method to generate quantitative colored images and volumes is presented and compared with existing imaging modalities. In addition to produce high-resolution volumetric data, we show that D-FFOCT is the only existing method that combines both spatial and temporal high resolution. Supplementary videos can be found at `https://www.nature.com/articles/s41377-020-00375-8`.

Dynamic full-field optical coherence tomography: 3D live-imaging of retinal organoids

Jules Scholler[1], Kassandra Groux[1], Olivier Goureau[2], José-Alain Sahel[2,3,4,5], Mathias Fink[1], Sacha Reichman[2], Claude Boccara[1] and Kate Grieve[2,3]

Abstract
Optical coherence tomography offers astounding opportunities to image the complex structure of living tissue but lacks functional information. We present dynamic full-field optical coherence tomography as a technique to noninvasively image living human induced pluripotent stem cell-derived retinal organoids. Coloured images with an endogenous contrast linked to organelle motility are generated, with submicrometre spatial resolution and millisecond temporal resolution, creating a way to identify specific cell types in living tissue via their function.

The comprehension of the human body and its mechanisms at the subcellular scale is still an open area of research. During the seventeenth century, the first examinations of life under the microscope were conducted directly on humans, animals and bacteria[1]. Then, at the end of the nineteenth century, cell culture studies began to replace in vivo studies, as this allows the creation of in vitro models beneficial for the comprehension of biological phenomena in different environments[2,3]. Because of the two-dimensional nature of early cell cultures, the possibilities of understanding tissues and organs as a whole were limited. Recently, three-dimensional (3D) cultures have been developed from stem cells to generate organoids that mimic a variety of tissues and serve as models of human development[4] and disease studies[5–7]. Organoids could also serve as sources of human tissues for transplantation and as platforms for drug screening[8–10]. These self-organizing structures develop cellular compositions and architectures similar to in vivo tissues, thereby replicating biologically relevant intercellular phenomena in vitro[11,12].

For each biological trend, optical imaging devices have been developed and optimized to image tissues, cell cultures and, recently, organoids, which are one of the most fundamental tools in biology, clinical pathology and medical diagnosis[13]. There are many challenges in imaging 3D structures: due to their relatively transparent nature, it is difficult to obtain contrast on specific structures without staining. Moreover, 3D samples require optical sectioning to discriminate the layer in focus from out-of-focus layers. In this study, we present dynamic full-field optical coherence tomography (D-FFOCT) as a technique to image retinal organoids derived from human induced pluripotent stem cells (hiPSCs)[14], which are a major breakthrough in the study of the retina and retinal diseases[15–17]. These hiPSC-derived retinal organoids are routinely imaged with various techniques (see Supplementary Table 1). However, each of the existing methods presents major drawbacks, such as the need for fixation or mechanical sectioning, rendering the study of dynamic phenomena impossible; the need for labelling, requiring cumbersome and costly preparation; or a lack of functional contrast, indicating only cell presence and not cell health or behaviour[18–20]. Optical coherence tomography (OCT) is commonly used in biology and medicine to obtain 3D images of microstructures in tissue. OCT contrast arises from the local endogenous optical backscattering level[21]. The main drawback of traditional OCT

Correspondence: Kate Grieve (kategrieve@gmail.com)
[1]Institut Langevin, ESPCI Paris, PSL University, CNRS, 10 rue Vauquelin, Paris, France
[2]Institut de la Vision, Sorbonne Université, INSERM, CNRS, F-75012 Paris, France
Full list of author information is available at the end of the article.
These authors contributed equally: Jules Scholler, Kassandra Groux

Fig. 1 Experimental setup and post-processing schematic. Acquisition of images a, Full-field OCT setup combined with wide-field fluorescence microscopy (side view). PZT piezoelectric translation, TS translation stage, BPF bandpass filter, HPF high pass filter. As fluorescence is recorded in the same spectral range as that used for D-FFOCT, D-FFOCT and fluorescence images could not be recorded at the same time; for this purpose, a flip mirror was added to switch from one modality to another. **b** 3D cube of data (*x*, *y*, *t*) acquired before processing. Each time evolution of a pixel is processed independently. **c** An intensity trace is plotted for a pixel inside a living retinal organoid. **Post-processing steps d–f**. Dynamic images are computed in the HSV colour space. **d** Hue is computed with the mean frequency, from blue (low temporal frequencies) to red (high temporal frequencies). **e** Saturation is computed as the inverse of the frequency bandwidth; as a consequence, a signal with a broader bandwidth (e.g., white noise) appears dull, whereas a signal with narrow bandwidth appears vivid. **f** The value is computed as the running standard deviation[23]. Bottom row is a D29 retinal organoid. **g** Computation of the mean frequency (hue); **h**, frequency bandwidth (saturation); and **i**, dynamic (value) before **j**, reconstruction. Scale bar: 50 μm

is the trade-off between imaging depth and resolution. To increase the lateral resolution, the numerical aperture of the system must be increased. As a consequence, the depth of field decreases, and only a small layer of the sample can be imaged. Current OCT systems therefore have a lateral resolution on the order of 10 μm, which is insufficient to resolve cell structures laterally. Using an incoherent light source and a camera, time domain full-

field OCT (FFOCT) is an en face variant of OCT with a higher spatial and temporal resolution than OCT in the en face plane[22]. As FFOCT acquires an entire en face plane rather than a line in the depth dimension, the numerical aperture can be arbitrarily increased without any imaging depth trade-off. Using the FFOCT experimental setup shown in Fig. 1(a) and detailed in the Methods section, a novel contrast mechanism has recently

been exploited by measuring temporal fluctuations of back-scattered light in a technique called dynamic FFOCT (D-FFOCT)[23]. By revealing sub-cellular structures that have very weak back-scattering, these dynamic measurements provide contrast based on local intra-cellular motility[24,25] with sub-micrometre resolution, and can achieve millisecond temporal resolution to study fast phenomena.

In FFOCT, light coming back from the sample slice of interest interferes with light coming back from the reference mirror and is projected onto the camera (Fig. 1 (a)). To compute a D-FFOCT image, a movie (typically 512 frames) of the interferogram pattern is recorded and processed (see Methods) to extract local fluctuations and render them coloured (Fig. 1(b–j)). Using the hue-saturation-value (HSV) colour space, image brightness is linked to fluctuation amplitude, whereas colour is linked to fluctuation speed, from blue (slow) to red (fast) through green (in between). By translating the sample in the axial direction to acquire a stack of planes, see Supplementary Vid. 1, a 3D volume can be reconstructed (see Methods). Alternatively, a series of dynamic images may be acquired in the same plane to follow the evolution of activity over several hours in a time-lapse fashion with a temporal resolution of up to 20 ms (see "Methods").

A 3D reconstruction of a 28-day-old (D28) retinal organoid is depicted in Fig. 2(a), corresponding to an optic vesicle stage during retinogenesis[9,10,15,16], along with a sub-volume in Fig. 2(b), highlighting the layered internal retinal progenitor cell organization. A cross-section is shown in Fig. 2(c), in which the elongated shape of cells is seen. A time-lapse video at 50 μm depth was acquired on the same organoid to study its temporal evolution over three hours (see Fig. 2(d) and Supplementary Video 2 for the full recording). In these acquisitions, different dynamic profiles of cells can be observed: surface cells exhibit faster dynamics than those inside the sample volume. This could be explained by the fact that at the surface of the organoid, the cells are in contact with the external environment, making them more vulnerable to change and often leading to their death. In Fig. 2(d), cells in the centre of the organoid exhibit fast and intense activity until their disappearance, possibly indicating that they are undergoing apoptosis. Evolution of cell dynamics near a clear boundary between two distinct types of cells is also visible. On one side of the boundary, cells exhibit faster and stronger dynamics, suggesting a differentiation process towards specific retinal lineages[15], and on the other side, small rounded progenitor cells have slower activity. These two cell types are therefore distinguishable by their dynamic profile alone. Generated D-FFOCT images present a consistent colormap in which each frequency is continuously represented by the same colours; therefore, similar results are obtained for different retinal

organoids at the same developmental stage. Supplementary Video 3 shows a time-lapse movie of the D28 retinal organoid shown in Fig. 2(a–c) alongside a D29 retinal organoid. The same clear boundary between distinct types of cells is present for both. By processing the data contemporaneously on the GPU using a modified version of Holovibes software[26], an enhanced temporal resolution of 20 ms was achieved, which represents a 500-fold improvement without the need to store the raw data (up to $4\,\mathrm{Go.s^{-1}}$). The price paid for this improvement is the use of an alternative version of the dynamic computation, which is noise-sensitive and non-quantitative (see "Methods"). Figure 2(f–h) shows high temporal resolution (20 ms) images of a D147 retinal organoid. The typical rosette organization of retinal cells, previously described[14,15], is visible in the centre, i.e., photoreceptors (seen from the side) in the inner part of the rosette centre with emerging outer segments (indicated by white lines on Fig. 2(h)), and other surrounding retinal cells are evident. Photoreceptor nuclei exhibit different dynamic profiles (Fig. 2(g))—either compact and uniform, inflated, or absent—which may correspond to the nuclear G0/G1, dying and M states, respectively. The gain in temporal resolution allows the study of fast biological processes such as organelles moving inside the cytoplasm (see Supplementary Video 4). A series of retinal organoids imaged by D-FFOCT at consecutive steps of development showed the gradual differentiation of retinal cell progenitors into neural cells and photoreceptors (Supplementary Fig. 2), as validated by comparison with a similar organoid series imaged with immunofluorescence on a confocal microscope[14].

To further validate the D-FFOCT signal origin via direct comparison between D-FFOCT and specific fluorescence labelling in the same organoids, a multimodal setup was developed that combines D-FFOCT and fluorescence channels to allow a pixel-to-pixel overlay of D-FFOCT and fluorescence images. A D29 retinal organoid was labelled with a dye targeting the nuclei of dead cells (see "Methods"). D-FFOCT images overlaid with fluorescence wide-field images are shown Fig. 3(a–d). Two fluorescent red spots are clearly visible (Fig. 3(a)) and correspond to very weak dynamic signals in the D-FFOCT image, confirming that dead cells exhibit low activity and that the contrast revealed by D-FFOCT is metabolic. These two areas are magnified in Fig. 3(c, d), and dark zones are encircled by a white dotted line. A retinal organoid was imaged with the combined D-FFOCT-fluorescence system at D126, via which a large number of differentiating photoreceptors can be detected in rosette-like configurations (Fig. 3(e, f)). A red fluorescent zone corresponding to photoreceptors is visible in Fig. 3(e), whereas in the D-FFOCT image (Fig. 3(f)), the different activity level in photoreceptors compared to surrounding cells is
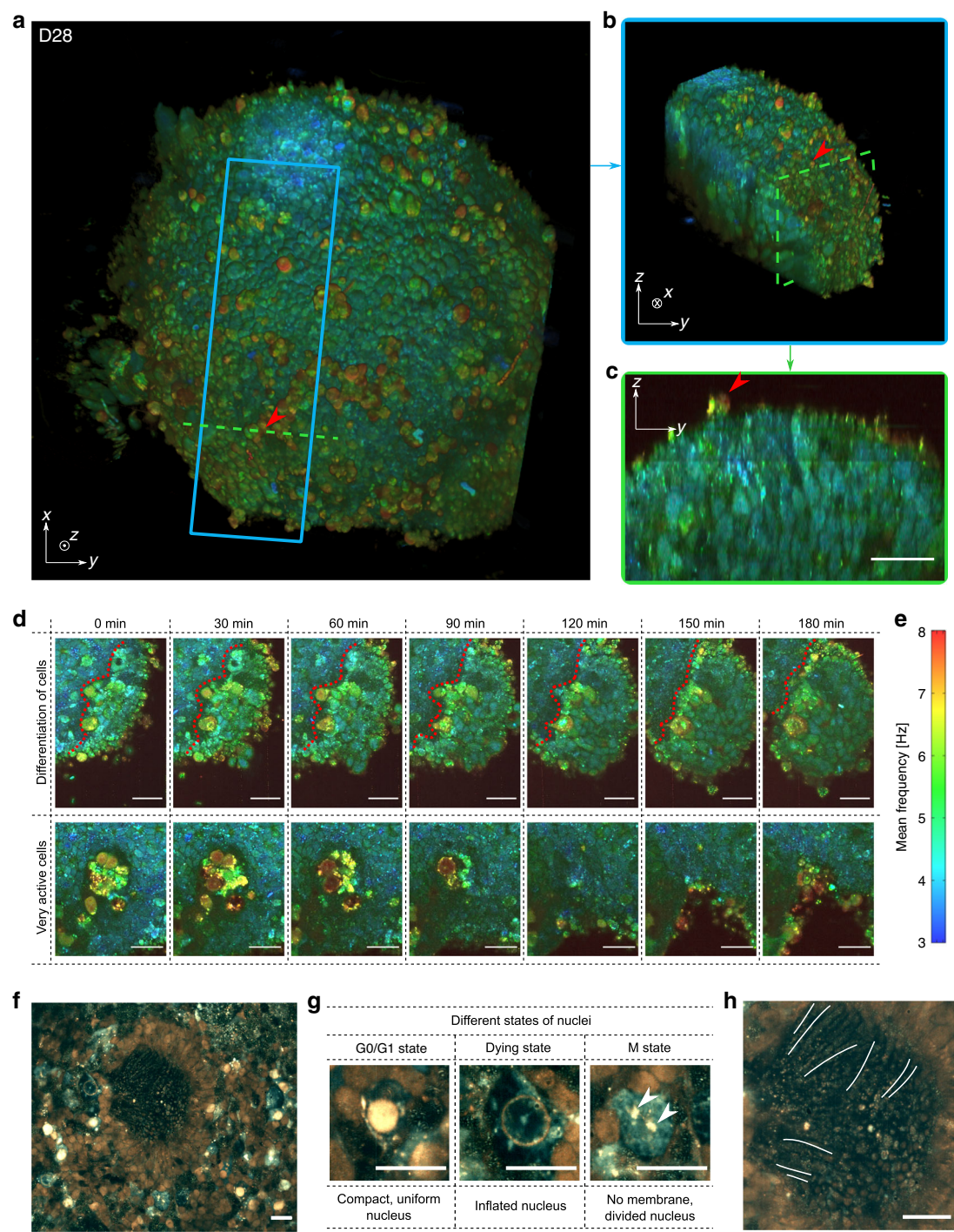
Fig. 2 (See legend on next page.)

sufficient to provide distinction of the cell type through the dynamic signal alone, across a region that is coincident with the fluorescently labelled zone. Underlying biological processes responsible for the dynamic contrast, which has been shown to be linked to cell metabolism[23], could include movement of organelles. Preliminary experiments suggest mitochondrial contribution, but other potential contributors, such as Golgi bodies,

(see figure on previous page)
Fig. 2 Imaging hiPSC-derived retinal organoids with D-FFOCT. a 3D reconstruction of the spherical D28 retinal organoid, composed of cells ~5 μm in diameter. Red arrows highlight surface cells exhibiting fast dynamics. **b** Image represents a sub-volume of **a** (blue square). **c** Image represents a cross-section in (**a**) (green dashed line) in which one can see the organization of the layers inside the retinal organoid. **d** High-magnification images of two different areas of the organoid during a 3h time-lapse acquisition: magnified images in the top row show the change in dynamic profile that could reflect a differentiation process (the boundary between the two types of cells is represented by a red dotted line); images in the bottom row show a very active zone composed of cells exhibiting fast and high dynamics, possibly undergoing apoptosis, in the centre of the organoid. **e** Colour bar of the D-FFOCT images for the 3D and time-lapse acquisitions with a consistent colormap for (**a–d**). High-temporal-resolution imaging performed on a D147 retinal organoid. **f** Part of the retinal organoid revealing fusiform structures corresponding to emerging photoreceptor outer segments in the centre of the rosette. **g** Magnified view of nuclei in three different states around the rosette: (i) a nucleus in a normal state with a compact, uniform shape and is very bright (i.e., exhibiting a high activity); (ii) an seemingly dying, inflated nucleus, exhibiting almost no activity; and (iii) a nucleus undergoing division with no defined nuclear membrane in the cytoplasm, and two distinct parts (white arrows) of the content of a nucleus (suggesting mitosis of the nucleus with chromosomes already divided, with the same subcellular activity level as the "normal" nucleus). **h** Magnified image of the photoreceptor outer segment-like structures imaged side-on; three of them are marked with a white line. Scale bar: 20 μm

lysosomes, vesicles, and pigments, have not yet been discarded.

With D-FFOCT, once installed in the culture lab under controlled environmental conditions, we anticipate being able to follow retinal organoid developmental processes that have been documented by traditional methods[14,19], such as the quantification of cells exhibiting the same dynamic profile at multiple time points. In addition, we should also gain additional biological insights owing to the non-invasive nature of our imaging method, as it provides access to the time course of continuous processes such as progenitor cell proliferation and migration, cell type differentiation including evolution of the boundary between neural and non-neural retinal cells (Fig. 2(d)) and evolution of the organoid into layered retina. Interestingly, combining D-FFOCT and a 3D organoid-based model of retinal dystrophies due to patient-specific iPSCs offers the opportunity to understand fundamental subcellular processes leading to diseases in a way that was not previously possible.

Dynamic FFOCT imaging creates a new label-free non-invasive contrast for imaging retinal organoids. As this technique does not damage the samples, it complements and could potentially replace the imaging modalities traditionally used. D-FFOCT allows imaging of different layers at multiple depths while preserving the sample integrity, i.e., using neither exogenous labelling nor destructive methods, and is therefore suitable to follow the evolution of the same organoid at different stages of its development. The high dimensionality of the probed signals (512 interferograms per pixel) is useful for developing statistical approaches such as automated classification and clustering, and we are working towards the identification of cells via their D-FFOCT contrast alone using machine learning algorithms, with the ultimate goal of removing the need for markers entirely. The only missing part, for now, is the lack of ground truth validation data (e.g., segmented cells with labels that could be generated by fluorescence or by annotating experts), which will be a milestone in the further development of this technique.

Methods

Human iPSC maintenance and retinal differentiation

Two established human iPSC lines, hiPSC line-5f[17] and fluorescent reporter AAVS1::CrxP H2BmCherry hiPSC line[27], both derived from retinal Müller glial cells, were cultured as previously described[14]. Briefly, hiPSC lines were cultured on truncated recombinant human vitronectin-coated dishes with Essential 8TM medium (Thermo Fisher Scientific, Les Ulis, France). For retinal differentiation, adherent hiPSCs were expanded to 70–80%, and FGF-free (fibroblast growth factor) medium was added to the cultures for 2 days, followed by a neural induction period allowing retinal structures to appear. Identified retinal organoids were manually isolated and cultured as floating structures for several weeks to follow retinal cell differentiation as previously described[14,28].

Sample preparation for D-FFOCT imaging

Retinal organoids were placed in CO_2-independent medium (Gibco^{TM}, Thermo Fisher Scientific) in a Petri dish and kept close to 37 °C during imaging. Samples were mounted on a 3-axis translation stage under the sample arm objective and imaged directly after mounting. After imaging, each organoid was either cultured again for further D-FFOCT imaging or fixed using a solution of paraformaldehyde (PFA) for 15 min at 4 °C followed by three rinses and stored in a sucrose solution for further traditional imaging. For dead cell labelling (LIVE/DEAD Viability/Cytotoxicity Kit for Mammalian Cells, Thermo Fisher Scientific), organoids were incubated with 10 μM EthD-1 at 37 °C for 20 min before imaging and were mounted immediately after incubation and imaged within 10 min.

Immunostaining and imaging of retinal sections

For cryosectioning, retinal organoids were fixed for 15 min in 4% PFA at 4 °C and washed in phosphate-buffered saline (PBS). Structures were incubated at 4 °C in PBS/30% sucrose (Sigma Aldrich, Saint-Quentin-Fallavier, France) solution for at least 2 h and embedded in a
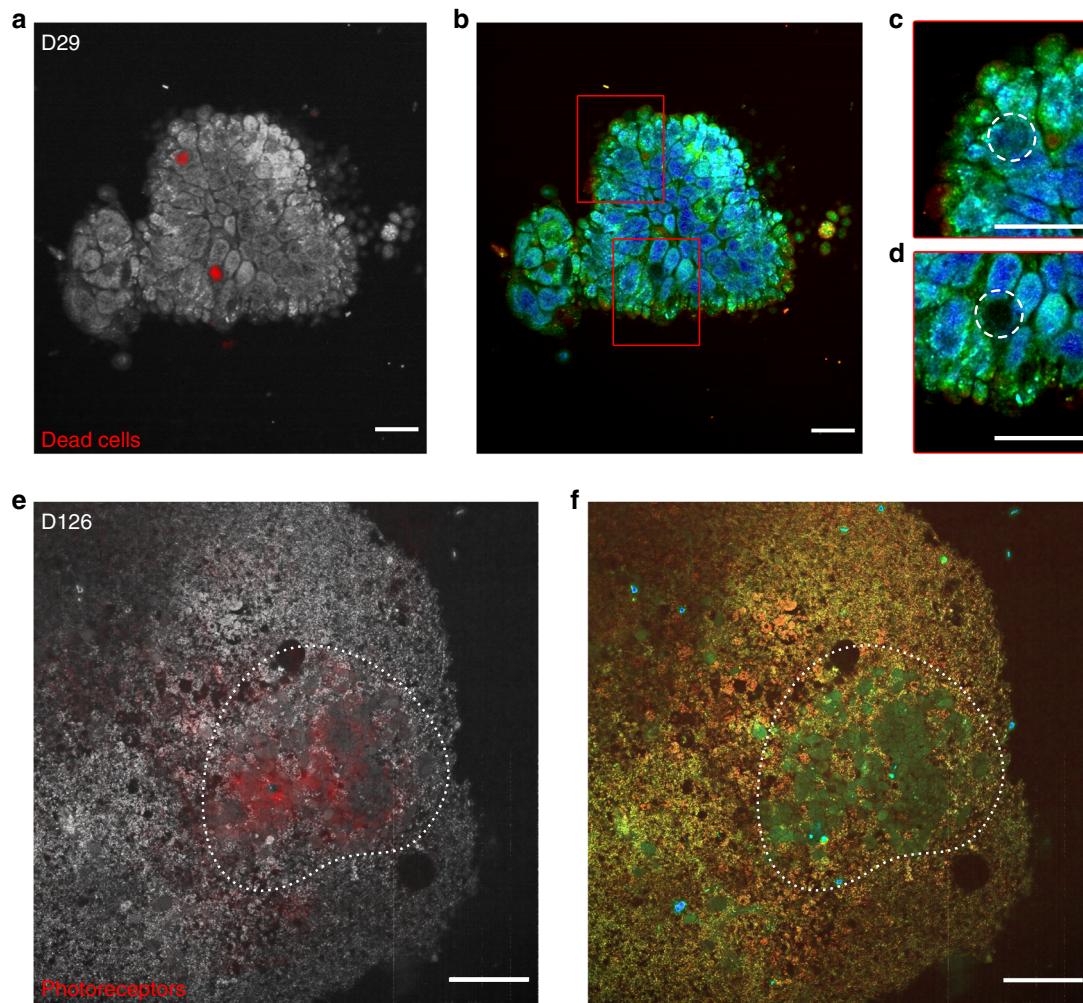
Fig. 3 Fluorescence validation of D-FFOCT imaging. D-FFOCT images are depicted in colour (**b–d**, **f**), D-FFOCT images overlaid with wide-field fluorescence images are depicted in greyscale (D-FFOCT) and red (fluorescence) (**a**, **e**). **a–d** D29 retinal organoid labelled with dye targeting the nuclei of dead cells. **a** One can see two dead cells marked by the red spots, corresponding to the two dark zones on (**b**), the D-FFOCT image, in which there is no dynamic signal in these zones. **c**, **d** Magnified images of the two dark zones (highlighted by a white dashed line, corresponding to the two red spots of fluorescence). **e**, **f** D126 retinal organoid derived from a fluorescent cone rod homeobox (CRX) reporter iPSC line exclusively labelling photoreceptors in red (mCherry). **e** Overlaid image on which the photoreceptor fluorescence matches the blue-green cells of (**f**), the D-FFOCT image. These areas are highlighted by a white dotted line. These precursors of photoreceptors have their own particular dynamic signature, which allows them to be distinguished from the surrounding cells by D-FFOCT alone. Scale bar: (**a–d**) 10 μm, (**e**, **f**) 50 μm

solution of PBS, 7.5% gelatine (Sigma Aldrich, Saint-Quentin-Fallavier, France), and 10% sucrose and frozen in isopentane at −50 °C. Ten-micrometre-thick cryosections were collected in two perpendicular planes. Sections were washed with PBS, nonspecific binding sites were blocked for 1 h at room temperature with a PBS solution containing 0.2% gelatine and 0.1% Triton X100 (blocking buffer) and then overnight at 4 °C with the primary antibodies VSX2 (goat, 1:2000, Santa Cruz Biotechnology, Clinisciences, Nanterre, France), CRX (mouse, 1:5000, Abnova, Clinisciences) and RHODOPSIN (mouse, 1:500, Merck, Guyancourt, France) diluted in blocking buffer. Slides were washed three times in PBS with 0.1% Tween

and then incubated for 1 h at room temperature with appropriate secondary antibodies conjugated with either Alexa Fluor 488 or 594 (Jackson ImmunoResearch Lab., Interchim, Montluçon, France) diluted at 1:600 in blocking buffer with 4′,6-diamidino-2-phenylindole diluted at 1:1000 to counterstain nuclei. Fluorescent staining signals were captured with an Olympus FV1000 confocal microscope.

Experimental setup

Time-domain FFOCT[22,29] is a variant of scanning OCT[21] in which two-dimensional en face images are captured using a CMOS camera. Three-dimensional

images can be acquired and reconstructed by scanning in the depth dimension with high precision motors. This configuration, together with the use of a broad-band LED source, allows for higher axial and en face resolution than conventional OCT and can perform micrometre resolution 3D imaging noninvasively in both fresh and fixed ex vivo tissue samples. For the D-FFOCT imaging of retinal organoids, a laboratory setup was designed with a 0.5 μm lateral resolution using high-magnification water-immersion objectives (Nikon NIR APO 40x 0.8 NA), for a field of view of ~$320 \times 320 \, \mu m^2$. Because of the high numerical aperture, an axial resolution of 1.7 μm was also obtained by the microscope objectives in this particular configuration in which the coherence length of the source is larger than the depth of focus. The light source used for the FFOCT system was an LED with a central wavelength of 660 nm (M660L3, Thorlabs, Newton, NJ, USA). The choice of the light source for an FFOCT system is one of the most important parameters. First, it needs to be spatially incoherent to avoid cross-talk artefacts due to multiple scattering. The optical power must be high enough to image close to camera saturation to maximize the signal-to-noise ratio. The central wavelength was chosen to be as close as possible to near-infrared to maximize the penetration depth while remaining in the visible spectrum (as fluorescence measurements were done in the visible spectrum and some optical components were coated only for the visible spectrum). Finally, the LED coherence length (computed as the width at half maxima of the axial fringe pattern) was 13.28 μm in water, which allowed a robust 3D alignment between the coherence plane and the focal plane, therefore allowing a homogeneous contrast over the whole field of view. The FFOCT signal was recorded on a custom camera (Quartz 2A750, Adimec). For validation purposes, this FFOCT setup was combined with a fluorescence microscope using an LED source centred at 565 nm (M565L3, Thorlabs, Newton, NJ, USA) for excitation and filtered with a bandpass filter centred on 562 nm with a bandwidth of 40 nm (Semrock FF01-562/40-25). The emitted fluorescence was filtered with another bandpass filter centred on 624 nm (Semrock FF01-624/40-25) and then imaged using a sCMOS camera (PCO Edge 5.5). The excitation and fluorescence wavelengths were separated by a dichroic mirror at 593 nm (Semrock FF593-Di03-25).

Data acquisition and processing

Producing each dynamic image slice required the acquisition of many (typically 512) direct images without modulating the piezo position. As opposed to static FFOCT acquisition, the measured fluctuations in D-FFOCT arise from subcellular motion. In this study, the frame rate was set to 100 Hz, which was a good trade-off between acquisition speed and signal-to-noise ratio (see

the following section). For a given acquisition, we typically obtain a (1440,1440,512) tensor in which 1440×1440 is the number of sensor pixels and 512 is the number of recorded frames. After acquiring data, the first step is to correct for the camera frame-to-frame instability by normalizing each frame to compensate for exposure time variations. Previously, we showed colour images that were constructed by integrating signals in the Fourier domain for three frequency ranges[30]. Here, we propose a new scheme wherein colour images are computed in the HSV colour space in which, contrary to the red-green-blue (RGB) colour space, it is possible to assign a physical property to each of the three channels for quantitative visual interpretation. The idea is then to attribute a colour for each pixel depending on the characteristic time period or frequency of the dynamic signal. Each individual pixel can be thought of as a sum of subcellular random walks with a typical covariance function depending on the motion type (e.g., diffusive, hyperdiffusive). To distinguish between several dynamic profiles, we performed power spectrum analysis. Note that a correlation analysis could also be performed and gives similar results but requires more computing time. We started by computing the power spectrum density (PSD) using Welch's method for each pixel and then used an L1 normalization on each PSD as if it were a probability distribution. Then, the hue channel, was computed as the mean frequency (which is simply the dot product between the normalized PSD and the frequency array). The values were then inverted and rescaled between 0 and 0.66 to go from blue (low frequencies) to red (high frequencies). We observed that two successive acquisitions could lead to different perceptual colour maps. We found that the lowest frequencies were slightly unstable (either due to sensor or mechanical instabilities as described in[31]). We removed this artefact by removing 3% of the lowest frequencies in the PSD. Then, the value (which corresponds to the perceived pixel intensity) was computed as the average of the temporal standard deviation with a window size of 50 samples. We saturated 0.1% of the highest value pixels to improve the contrast. For 3D stacks, the saturation threshold value was kept constant throughout the stack to obtain a consistent colour map. Finally, saturation was computed as the inverse of the normalized PSD bandwidth. As a consequence, the saturation channel carries the frequency bandwidth information. In practice, it is computed as the standard deviation of the frequencies (i.e., it corresponds to the frequency histogram width) as:

$$S = P.f^2 - (P.f)^2 \tag{1}$$

where P is the normalized PSD array, f is the frequency array and "." is the dot product. The saturation map is then inverted and rescaled between 0 and 0.8 to obtain a

visually pleasing output. The broader the spectrum, the lower the saturation. White noise has a broader bandwidth and will therefore appear greyish instead of coloured. Finally, the dynamic image is transformed in the RGB colour space for display purposes. A (1440, 1440, 512) stack is processed in less than 10 s by the GPU (Nvidia Titan V) using MATLAB (MathWorks) and our custom software[32], hence limiting temporal resolution by processing the data after each acquisition. To improve temporal resolution, we also used a modified version of a previous method[26], which computes real-time dynamic images on the GPU. In this case, the algorithm used to generate dynamic images is no longer quantitative and is subject to more noise. The 3D cube of data is first Fourier transformed; the Fourier transform magnitude of each temporal signal is then integrated into three bands to reconstruct an RGB image in which the band corresponding to lower frequencies is coded in the blue channel, the band corresponding to medium frequencies is coded in the green channel and the band corresponding to high frequencies is coded in the red channel. The processing power of the GPU allowed us to process a new cube of data every 2 frames, leading to a D-FFOCT frame rate of 50 Hz in practice and a temporal resolution of 20 ms. For 3D volumes, the temporal resolution depends on the number of planes per volume. In practice, the final plane is delayed by several minutes compared with the first acquired plane. However, as the biological changes being evaluated are on time scales slower than minutes, this lag was not an issue (see Supplementary Video 2). For 3D stacks, each plane is registered during post-processing using a feature-based method (rigid registration using SIFT features and RANdom SAmple Consensus algorithms to find correct matches) to compensate for the sample lateral drift. Stacks are then interpolated in the depth dimension using bicubic interpolation to obtain a square voxel edge size of 220 nm. For 3D display purposes, a nonlocal mean filter[33] can be applied to remove granularity.

Choosing the frame rate for D-FFOCT

The choice of 100 Hz for the camera frame rate is the result of the optimization between the acquisition speed and the signal-to-noise ratio. For a given number of frames, the signal-to-noise ratio increases in D-FFOCT when the frame rate decreases because scattering structures have more time to move and a greater volume can be explored, therefore leading to higher phase shifts and higher intensity fluctuations on the camera. For 512 frames, the signal-to-noise ratio starts decreasing when going faster than 100 Hz, so this value was chosen to maximize both the acquisition speed and signal-to-noise ratio.

Correcting for sample drift

Due to thermal effects, we observed a slow mechanical drift (on the order of 5 μm.h^{-1}), which could prevent us from measuring dynamic images in the same plane over several hours (axial resolution is 1.7 μm). To compensate for this drift, we developed a correlation-based method called the plane locking procedure[25]. This procedure was utilized when the cross-correlation between the current image and the target image was below a threshold (typically between 0.2 and 0.4). In this case, FFOCT images were acquired over an axial extent of 10 μm, with 0.5 μm steps using the sample translation stage and were then cross-correlated with the target image. The sample was then axially translated to the position corresponding to the maximum of the cross-correlation, which was typically between 0.5 and 0.8. After each plane correction procedure, a new FFOCT image was chosen as the target for the next correction to account for evolution in the sample position.

Combining FFOCT and fluorescence microscope channels

The FFOCT and fluorescence cameras do not share the same sensor size and resolution, so to construct overlays, FFOCT images were registered onto fluorescence images using a projective transformation. The projective transformation was calibrated using a deformation target (R1DS1N, Thorlabs, Newton, NJ, USA) before experiments. The final overlays were constructed in RGB colour space, the value channel corresponding to dynamic amplitude was inserted into every channel (R, G, and B), and a fluorescence image was added only to the R channel. In this way, the dynamic image appeared in greyscale with the fluorescence superimposed in red.

Author details
[1]Institut Langevin, ESPCI Paris, PSL University, CNRS, 10 rue Vauquelin, Paris, France. [2]Institut de la Vision, Sorbonne Université, INSERM, CNRS, F-75012 Paris, France. [3]Quinze-Vingts National Eye Hospital, 28 Rue de Charenton, Paris 75012, France. [4]Fondation Ophtalmologique Rothschild, F-75019 Paris, France. [5]Department of Ophthalmology, The University of Pittsburgh School of Medicine, Pittsburgh, PA 15213, United States

References
1. Hajdu, S. I. The first use of the microscope in medicine. *Ann. Clin. Lab. Sci.* **32**, 309–310 (2002).
2. Mazzarello, P. A unifying concept: the history of cell theory. *Nat. Cell Biol.* **1**, E13–E15 (1999).
3. Jedrzejczak-Silicka, M. History of cell culture in New Insights into Cell Culture Technology. ed. Sivakumar Joghi Thatha Gowder, IntechOpen, (2017).
4. Hynds, R. E. & Giangreco, A. Concise review: the relevance of human stem cell-derived organoid models for epithelial translational medicine. *Stem Cells* **31**, 417–422 (2013).
5. Lancaster, M. A. & Knoblich, J. A. Organogenesis in a dish: modeling development and disease using organoid technologies. *Science* **345**, 1247125 (2014).
6. Clevers, H. Modeling development and disease with organoids. *Cell* **165**, 1586–1597 (2016).
7. Hartogh, S. C. D. & Passier, R. Concise review: fluorescent reporters in human pluripotent stem cells: contributions to cardiac differentiation and their applications in cardiac disease and toxicity. *Stem Cells* **34**, 13–26 (2016).
8. Fatehullah, A., Tan, S. H. & Barker, N. Organoids as an in vitro model of human development and disease. *Nat. Cell Biol.* **18**, 246–254 (2016).
9. Gagliardi, G., M'Barek, K. B. & Goureau, O. Photoreceptor cell replacement in macular degeneration and retinitis pigmentosa: a pluripotent stem cell-based approach. *Prog. Retinal Eye Res.* **71**, 1–25 (2019).
10. Llonch, S., Carido, M. & Ader, M. Organoid technology for retinal repair. *Developmental Biol.* **433**, 132–143 (2018).
11. Rossi, G., Manfrin, A. & Lutolf, M. P. Progress and potential in organoid research. *Nat. Rev. Genet.* **19**, 671–687 (2018).
12. Lancaster, M. A. & Huch, M. Disease modelling in human organoids. *Dis. Models Mechanisms* **12**, dmm039347 (2019).
13. Yuste, R. Fluorescence microscopy today. *Nat. Methods* **2**, 902–904 (2005).
14. Reichman, S. et al. Generation of storable retinal organoids and retinal pigmented epithelium from adherent human iPS Cells in Xeno-free and feeder-free conditions. *Stem Cells* **35**, 1176–1188 (2017).
15. Reichman, S. et al. From confluent human iPS cells to self-forming neural retina and retinal pigmented epithelium. *Proc. Natl Acad. Sci. USA* **111**, 8518–8523 (2014).
16. Zhong, X. F. et al. Generation of three-dimensional retinal tissue with functional photoreceptors from human iPSCs. *Nat. Commun.* **5**, 4047 (2014).
17. Slembrouck-Brec, A. et al. Reprogramming of adult retinal müller glial cells into human-induced pluripotent stem cells as an efficient source of retinal cells. *Stem Cells Int.* **2019**, 7858796 (2019).
18. Browne, A. W. et al. Structural and functional characterization of human stem-cell-derived retinal organoids by live imaging. *Investigative Ophthalmol. Vis. Sci.* **58**, 3311–3318 (2017).
19. Capowski, E. E. et al. Reproducibility and staging of 3D human retinal organoids across multiple pluripotent stem cell lines. *Development* **146**, dev171686 (2019).
20. Cora, V. et al. A cleared view on retinal organoids. *Cells* **8**, 391 (2019).
21. Huang, D. et al. Optical coherence tomography. *Science* **254**, 1178–1181 (1991).
22. Dubois, A. et al. Ultrahigh-resolution full-field optical coherence tomography. *Appl. Opt.* **43**, 2874–2883 (2004).
23. Apelian, C. et al. Dynamic full field optical coherence tomography: subcellular metabolic contrast revealed in tissues by interferometric signals temporal analysis. *Biomed. Opt. Express* **7**, 1511–1524 (2016).
24. Thouvenin, O. et al. Cell motility as contrast agent in retinal explant imaging with full-field optical coherence tomography. *Investigative Ophtalmol. Vis. Sci.* **58**, 4605–4615 (2017).
25. Scholler, J. et al. Probing dynamic processes in the eye at multiple spatial and temporal scales with multimodal full field OCT. *Biomed. Opt. Express* **10**, 731–746 (2019).
26. Atlan, M. Holovibes: hologram rendering made easy. at http://holovibes.com. (2014)
27. Gagliardi, G. et al. Characterization and transplantation of CD73-positive photoreceptors isolated from human iPSC-Derived retinal organoids. *Stem Cell Rep.* **11**, 665–680 (2018).
28. Slembrouck-Brec, A. et al. Defined xeno-free and feeder-free culture conditions for the generation of human iPSC-derived retinal cell models. *J. Vis. Exp.* **139**, e57795 (2018).
29. Beaurepaire, E. et al. Full-field optical coherence microscopy. *Opt. Lett.* **23**, 244–246 (1998).
30. Apelian, C., Gastaud, C. & Boccara, A. C. Extracting relevant information for cancer diagnosis from dynamic full field OCT through image processing and learning. Proceedings of SPIE 10053, Optical Coherence Tomography and Coherence Domain Optical Methods in Biomedicine XXI. San Francisco, California, United States: SPIE, 2017.
31. Scholler, J. Motion artifact removal and signal enhancement to achieve in vivo dynamic full field OCT. *Opt. Express* **27**, 19562–19572 (2019).
32. Scholler, J. Jules Scholler/FFOCT: FFOCT_v0.1. (2019). at https://zenodo.org/record/3137246#.Xuxc8fk6veQ.
33. Buades, A., Coll, B. & Morel, J. M. A non-local algorithm for image denoising. Proceedings of 2005 IEEE Computer Society Conference on Computer Vision and Pattern Recognition (CVPR'05). San Diego, CA, USA: IEEE (2005).

Integrated supplementary information for

Dynamic full-field optical coherence tomography: 3D live-imaging of retinal organoids

Jules Scholler[1,†], Kassandra Groux[1,†], Olivier Goureau[2], José-Alain Sahel[2,3,4,5], Mathias Fink[1], Sacha Reichman[2], Claude Boccara[1] and Kate Grieve[2,3,*]

[1]Institut Langevin, ESPCI Paris, PSL University, CNRS, 10 rue Vauquelin, Paris, France
[2]Institut de la Vision, Sorbonne Université, INSERM, CNRS, F-75012, Paris, France
[3]Quinze-Vingts National Eye Hospital, 28 Rue de Charenton, Paris, 75012, France
[4]Fondation Ophtalmologique Rothschild, F-75019 Paris, France
[5]Department of Ophthalmology, The University of Pittsburgh School of Medicine, Pittsburgh, PA 15213, United States
†These authors contributed equally to this work
*kategrieve@gmail.com

		Imaging techniques			
		FFOCT/D-FFOCT	OCT	Conventional microscopy	Confocal, multiphoton or light sheet microscopy
Resolution (µm)	Lateral	0.5	10	0.5	0.5
	Axial	1.4	1	-	1.9
	Depth penetration	1000 / 150	1000	-	150 - 1000 (clearing)
Aquisition	3D	✓	✓	-	✓
	Live imaging	✓	✓	✓	✓
	Time	s / min	s	s	min - h
Sample preparation	Preparation time	s	s	h - d	h - d
	Clearing	-	-	-	✗
	Fixation	-	-	✗	✗
	Labeling	-	-	✗	✗
	Sectioning	-	-	✗	✗
Biological insights	Dynamic profile	✓	-	-	-
	Tissue development	✓	-	-	-
	Cell motility	✓	-	-	-
	Tissue organisation	✓	✓	✓	✓
	Specific protein distribution	-	-	✓	✓

− (not required/possible); ✓ (possible); ✗ (required); s (second); min (minute); h (hour); d (day)

Table 1: Comparison of the different techniques that can be used to image hiPSC-derived retinal organoids. Lateral resolution computed for the same microscope objective (Nikon NIR APO 40x 0.8 NA) is diffraction-limited for all methods aside from OCT, wherein the need for a large depth of field limits the lateral resolution to 10 μm. Axial resolution in (D-)FFOCT is determined by the depth of field of the objective rather than the coherence length in the current configuration as high NA objectives are used (i.e., as the depth of field is smaller than the coherence length, the axial resolution is limited by the numerical aperture). Confocal, multiphoton, and light sheet immunohistochemistry methods achieve the same axial resolution at shallow depths as (D-)FFOCT but usually require invasive tissue clearing procedures to maintain the resolution at greater depths. The lower penetration depth of D-FFOCT than that of FFOCT comes from the low reflectivity of the moving organelles [31] that produce the dynamic signals. No method can currently penetrate the full organoid depth with submicrometre resolution without sectioning. However, imaging of the entire organoid is not always necessary because with an imaging depth of 150 μm, part of the organoid that is representative of the entire structure can be successfully imaged even in the largest organoids, thanks to their spherical organization. Should 3D imaging of entire organoids prove worthwhile, aberration correction methods could be utilized with FFOCT to reach greater penetration depths, combined with organoid rotation and additional postprocessing. Immunohistochemistry methods rely either on staining, which adds specific colour contrast and in which the sample is mechanically sliced to provide sectioning (immunohistology), or with targeted dyes, wherein various techniques (confocal illumination/detection, light-sheet illumination, etc.) provide optical sectioning. Relying on

exogenous contrasts for imaging at specific time points greatly limits the structures or events that can be seen in samples and ultimately leads to the destruction of the sample, as these techniques all require sectioning, clearing or fixation steps that preclude live imaging and, therefore, monitoring of the development of the same sample over a long period of time. D-FFOCT is not only a unique technique that combines high spatial and temporal resolution but also a non-destructive approach that provides the possibility of following the development of the same organoids over time throughout development. This process could be automated by integrating the D-FFOCT setup directly inside a cell culture incubator under a CO_2 atmosphere. D-FFOCT can therefore offer new biological insights such as cellular motility, tissue development and organization and dynamic profile evolution and comparison.
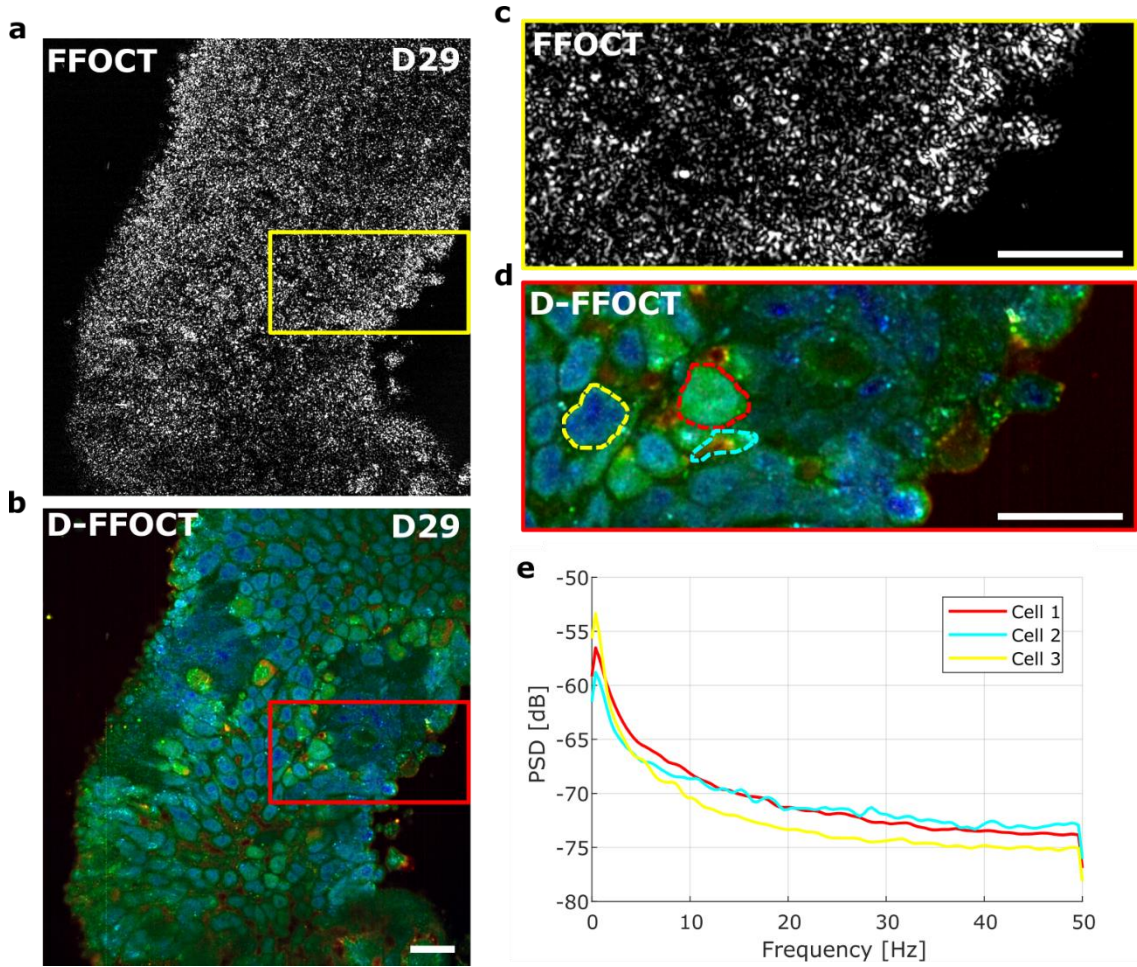
Figure 1: Comparison between FFOCT and D-FFOCT images on a D29 organoid. (a) FFOCT image of a D29 retinal organoid with (b) the corresponding D-FFOCT image. The FFOCT image was acquired using a 2-phase bucket scheme using a piezoelectric actuator to move the reference mirror [25] and extract the interferometric signal. 256 FFOCT amplitude images (corresponding to a total of 512 acquired images with 256 images for each phase) were averaged to obtain the final output. The D-FFOCT image was acquired with 512 direct images (without using piezoelectric modulation) and exhibits much higher contrast on cells. (c) Magnification of the FFOCT image (a) with the corresponding magnification of the D-FFOCT image (d). The mean power spectrum density was computed using Welch's method on the 3 cells drawn with the dashed line in (d) on graph (e). Scale-bar: 20 μm.
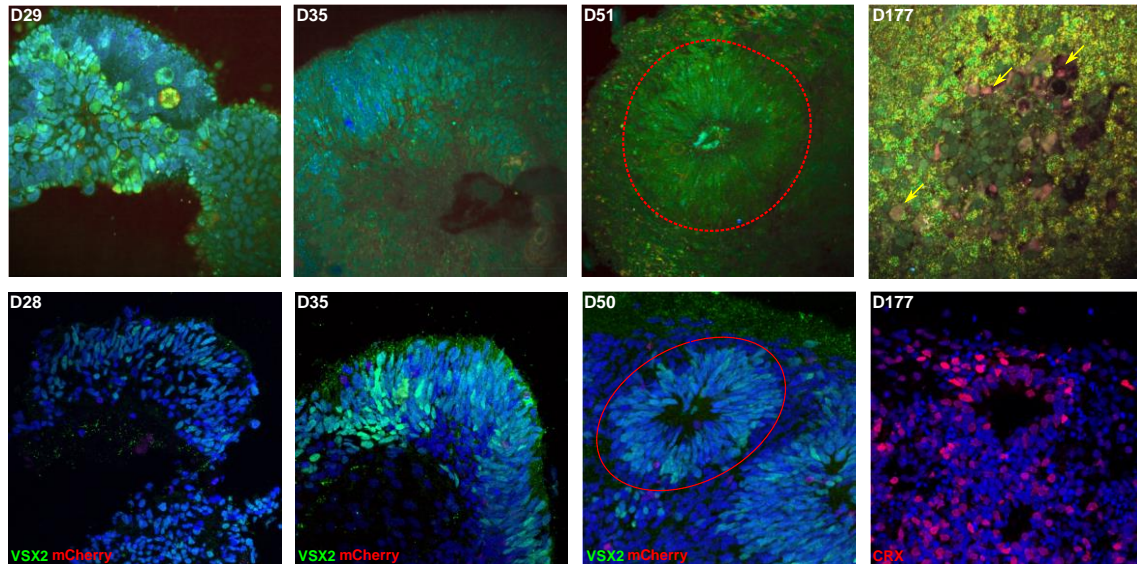
Figure 2: D-FFOCT imaging (top) and immunohistochemistry images acquired with confocal microscopy (bottom) of distinct retinal organoids at four equivalent stages of development. On D29 and D35, organoids are mainly composed of multipotent retinal progenitor cells expressing the Visual System Homeobox 2 (VSX2) transcription factor (green). At D51, rosette formation observed by D-FFOCT was confirmed by immunohistochemistry with differentiation of progenitor cells (red dotted lines). Photoreceptors can be identified in immunohistochemistry by CRX expression in rosette structures at D177 and are seen in DFFOCT as blue-green cells in the rosette centre (white arrows). In addition, the D-FFOCT image shows putative inner retinal neurons (identified due to their position around the edge of the rosette [15]) in red (yellow arrows). Nuclei are counterstained with DAPI (blue). The field of view of D-FFOCT images has been reduced to correspond to the field of view of the confocal images. Scale bar: 50 μm.
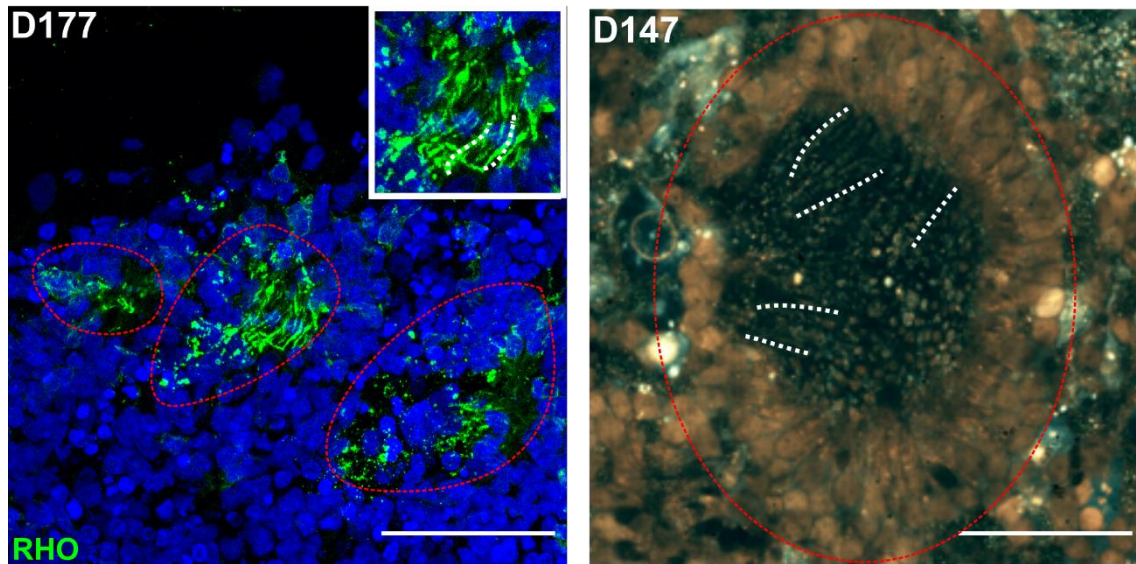
Figure 3: Immunohistochemistry image (left) acquired with a confocal microscope of a D177 retinal organoid wherein photoreceptor outer segments containing rhodopsin (green fluorescent label) are visible inside rosettes (red dotted lines). The magnified image in the top right corner highlights photoreceptor outer segments (green filaments, annotated with white dotted lines). Nuclei are counterstained with DAPI (blue). D-FFOCT image (right) of a similar retinal organoid at D147 showing a rosette (red dotted line) containing photoreceptor outer segments (white dotted lines), similar to those in the immunohistochemistry image. Rosette sizes can vary greatly and happen to be smaller in the organoid on the left than in the organoid on the right. The D-FFOCT field of view has been cropped to match the immunohistochemistry image; see Supplementary Vid. 4 for the whole field of view. Scale bar: 50 μm.

Supplementary files information

Video 1:

Depth stack of the D28 hiPSC-derived retinal organoid shown in Fig. 2(a-c). Planes from top $0 \ \mu m$ to approximate center of the organoid $101 \ \mu m$, in $1 \ \mu m$ steps are shown revealing the internal structure of the organoid.

Video 2:

Time-lapse video with 1 min temporal resolution of the evolution of the D28 hiPSC-derived retinal organoid shown in Fig. 2(d). Video shows the evolution of the whole organoid over three hours of imaging, with three magnifications corresponding to the zones depicted in Fig. 2(d).

Video 3:

Time-lapse video with 1 min temporal resolution of the evolution of the D29 hiPSC-derived retinal organoid shown in Supplementary Fig. 2. Video shows the evolution of the whole organoid over three hours of imaging.

Video 4:

Time-lapse of the D29 hiPSC-derived retinal organoid and of the D28 hiPSC-derived retinal organoid. Both organoids exhibit the same consistent colormap and structures demonstrating that D-FFOCT can reliably images different samples at different times consistently.

Video 5:

Time-lapse video with 1 min temporal resolution of the evolution of a D42 hiPSC-derived retinal organoid. Video shows the evolution of the whole organoid over three hours of imaging, especially the behaviour in a rosette.

Video 6:

Time-lapse video with 5 seconds temporal resolution of the evolution of a D147 hiPSC-derived retinal organoid with zoomed areas. Zoomed areas have a temporal resolution of 1 second and highlight the sensitivity of D-FFOCT to dynamic phenomena. The colors are computed like the images of Fig. 2(f-h).

Chapter 3

Post-processing developments for (D-)FFOCT

Contents

3.1 Article: Motion artifact removal and signal enhancement to achieve in vivo dynamic full field OCT

Dynamic FFOCT has been previously used for ex-vivo cornea and retina imaging [Thouvenin et al., 2017a, Scholler et al., 2019], ex-vivo liver imaging [Apelian et al., 2016], breast cancer biopsies [a la Guillaume et al., 2019]. All of these applications are sharing a common aspect: they have been done ex-vivo in a microscopy setting. The reason behind is that D-FFOCT is tremendously sensitive to axial motions which are detrimental for the image reconstruction, as explain in Section 2.1 in the paper where I propose a model for noise artifacts. Axial motions are not only an issue for in-vivo measurements, but also for microscopy acquisitions due to mechanical vibration and thermal drift. I measured the axial drift[1] by analyzing the fringe drift on our combined FFOCT and fluorescence setup. I computed the fringes drift by analyzing the lateral displacement of the fringes[2] after calibrating that a displacement of $\delta = 44.9 \; pixels$ corresponds to an axial displacement of $\lambda_c = 660 \; nm$. The results for 3.5 minutes are shown Fig. 3.1. Amplitude of axial motion was random (pink noise) with a maximal displacement of around 40 nm.

---

[1]Axial displacement of the sample causes the fringes to move laterally so that it is possible to measure the axial drift by putting a mirror in the sample arm and by analyzing the fringes lateral drift.

[2]Lateral displacement was estimated using [Guizar-Sicairos et al., 2008] after Fourier filtering the direct images around the fringes spatial frequency.
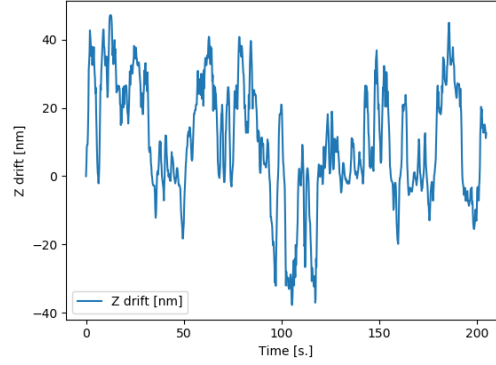
Fig. 3.1: Axial sample drift measured and computed during 3.5 minutes on our combined FFOCT and fluorescence setup. Maximal displacements of 40 nm with a pink spectrum were observed.

The tricky part with removing these artifacts is their random nature preventing traditional Fourier domain filtering approaches. The idea to separate the motility signals from the sample axial motion is that the sample axial motion should be highly correlated spatially and temporally whereas motion of scatterers giving the dynamic signals should be uncorrelated between pixels (or only correlated between neighboring pixel if scatterers happens to travel from one voxel to an adjacent one during the acquisition). With this in mind, I proposed to use the singular value decomposition (SVD) Section 2.2 in order to catch the axial motion on a few singular vectors. Such approach using SVD was already proposed by [Ammari et al., 2017] where they remove the firsts singular vectors, which was not optimal in practice as motion artifacts were also captured by higher ranked singular vectors. Rather than studying the decreasing of the singular value energy, I proposed to detected artifactual singular vectors by analyzing their temporal behavior. Finally this method allowed us to remove most of the artifacts that could manifest in different forms:

- Bright spots on very reflective structures such as collagen fibers Fig. 3.

- Fringes pattern on flat cells acting as a diopter Fig. 4.

- In vivo liver imaging of a mouse where the breathing and heart beat creates axial compression Fig. 6.

In this paper, I also propose a new operator Section 3 to compute the motility metric in order to improve the signal to noise ratio. This operator is based on the cumulative sum which allows to strengthen biased portion in dynamic signals that correspond to driven motion of scatterers. A theoretical analysis on Brownian bridges is proposed to explain the gain in signal to noise ratio when experiments are shot noise limited. Finally I hope that this advances in signal processing will allow to acquire dynamic images in vivo in the retina. As explained in the conclusion, I hope that if we can stabilize the acquisition by doing axial tracking of the retina so that the same retinal layer remains in the coherence plane width[3] we could remove the remaining artifactual fluctuations by using the SVD denoising approach. The development of the axial tracking system is detailed section 4.1 in this thesis.

---

[3]The coherence length is typically 10 μm, so that we would need a tracking accuracy of at least 5 μm.

Motion artifact removal and signal enhancement to achieve in vivo dynamic full field OCT

JULES SCHOLLER[*]

Institut Langevin, ESPCI Paris, CNRS, PSL University, 1 rue Jussieu, 75005 Paris, France
[*]jules.scholler@espci.fr
https://www.jscholler.com

Abstract: We present a filtering procedure based on singular value decomposition to remove artifacts arising from sample motion during dynamic full field OCT acquisitions. The presented method succeeded in removing artifacts created by environmental noise from data acquired in a clinical setting, including in vivo data. Moreover, we report on a new method based on using the cumulative sum to compute dynamic images from raw signals, leading to a higher signal to noise ratio, and thus enabling dynamic imaging deeper in tissues.

1. Introduction

Optical coherence tomography (OCT) is routinely used for 3D imaging of microstructures in tissue and relies on the endogenous backscattering contrast [1, 2]. Full-field optical coherence tomography (FFOCT) is an *en face*, high transverse resolution version of OCT [3, 4]. Using a camera and an incoherent light source, FFOCT acquires *en face* virtual sections of the sample at a given depth and has been used for biology [5] and medicine [6]. Recently, a novel contrast mechanism has been exploited by measuring temporal fluctuations of the backscattered light in a technique called dynamic full field OCT (D-FFOCT) [7]. In ex vivo fresh tissues, these dynamic measurements reveal subcellular structures that are very weak backscatterers and provide contrast based on their intracellular motility [8, 9]. A similar technique is used in regular OCT for retinal angiography called OCTA where speckle variance is analyzed on several B-Scans (typically 8 frames) to produce binary images of the retinal vasculature [10]. Due to the high spatial resolution ($< 1~\mu m$) and the number of frames used in D-FFOCT (typically 512), our method is not only sensitive to capillaries but also to intracellular motility signals and produces a contrast that reveals living cells [11]. The penetration depth of D-FFOCT is typically ten times less than FFOCT due to the small cross-section of the moving scatterers leading to weak signals, limiting its use in thick samples. Up to now, using D-FFOCT for in vivo imaging has remained elusive as this technique is sensitive to nanometric axial displacements of the sample. The same problems arise for OCTA and several approaches have been developed to remove bulk motion of the eye [12, 13]. In this paper we propose two methods to overcome the aforementioned limitations.

First, we introduce a framework based on the singular value decomposition (SVD) to filter out the axial displacement of the sample from the local fluctuations linked to intracellular motility, enabling in vivo use of D-FFOCT. SVD based algorithms have been previously applied to OCT data, e.g. for smart OCT where the SVD is applied to the reflection matrix in order to extend the penetration depth [14]. An SVD filtering method for D-FFOCT has been previously proposed for simulated data [15] but does not work on our experimental data mainly because the image formation model is different. Here we propose to find eigenvectors associated with axial motion and filter them out. Similar SVD based algorithms for spatio-temporal filtering have been used effectively in acoustics for Doppler acquisitions [16, 17]. In each case the goal is to use the SVD to transform the initial data in a new basis that is more suitable for filtering and identifying outliers. As opposed to [16, 17], our approach reconstructs the signals in the initial space before computing the dynamic image rather than constructing the image in the SVD space. The main

advantage of using the SVD rather than Fourier analysis here is that the filter adapts to the data set which exhibits different amounts of artifacts with random patterns.

Secondly, we present a new operator to compute the local dynamics based on the cumulative sum in order to enhance the non-stationary part of the signal, leading to a great increase in the signal to noise ratio (SNR).

Finally, we report on the first D-FFOCT acquisition in vivo to image the mouse liver at 80 μm depth where the two proposed algorithms greatly improved the image quality by removing motion artifacts and increasing the SNR by a factor of 3.

2. Removing artifacts using SVD

In order to construct a D-FFOCT image, a stack of typically 512 direct images (1440 × 1440 pixels) is acquired with a standard FFOCT using our custom software [18]. The FFOCT setup consists of a Linnik interferometer where both arms contain identical microscope objectives. The reference arm contains a silicon mirror mounted on a piezoelectric translation (PZT) used for phase modulation. In a typical FFOCT experiment, at least two images are acquired with different phase modulations and the FFOCT image is constructed by using appropriate phase-shifting algorithms [4, 11]. For D-FFOCT experiments the PZT position is not modulated, fluctuations arise by scatterers motions inside the coherence volume. In this paper we used data acquired from two different setups. The first one is a laboratory setup shown in Fig. 1 and the second one is a LightCT commercial setup manufactured by LLTech SAS. The characteristics of both of these setups are summarized in Table 1. In the first report on D-FFOCT, the level of the dynamic signal at each pixel was computed using a running standard deviation averaged over the whole acquisition [7] so that each pixel is processed independently. Calculating the standard deviation of the signal in time removes highly scattering stationary structures such as collagen or myelin fibers and reveals cells with a much better contrast. Indeed, strongly backscattering structures can dominate the signal even outside the coherence volume thereby masking weakly scattering structures such as cells. In the laboratory, we succeeded in stabilizing the setup by mounting it on a sturdy optical bench, and carried out ex vivo experiments without motion artifacts. For real life applications however, D-FFOCT devices are currently being used by clinicians in hospitals for imaging biopsied tissues [19] and by anatomo-pathologists in busy environments with vibrations arising from vibrational modes of the building, from people walking around the device and from air conditioning. Mechanical vibrations can lead to sample arm motion or oscillations, creating strong signal fluctuations, especially from highly reflective structures such as collagen fibers.

Table 1. **Setup Characteristics.**

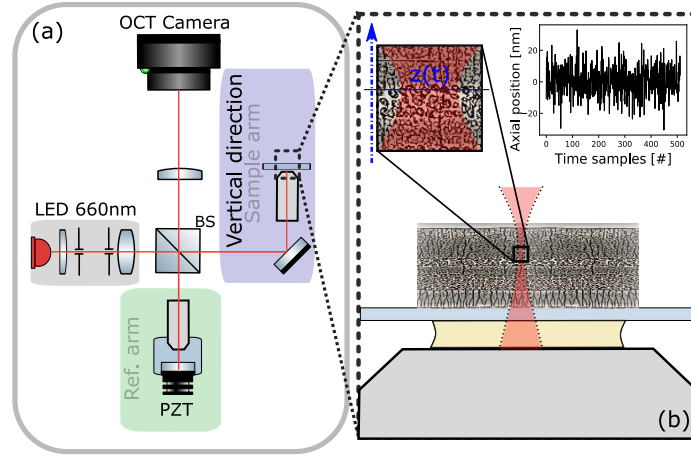| Setup	Lab. setup Fig. 1(a)	LightCT (LLTech SAS)
Transverse resolution [μm]	0.4	1.5
Axial resolution [μm]	1	1
Field of view [$\mu m \times \mu m$]	390 × 390	1260 × 1260
Framerate [Hz]	150	150

Fig. 1. (a) FFOCT setup in inverted configuration *top view*. Microscope objectives are Olympus UPlanSApo 30x 1.05 NA. OCT Camera: ADIMEC Q-2A750-CXP. Light source: Thorlabs M660L3. - PZT: piezoelectric translation - BS: 50/50 beam splitter. (b) Schematic of the sample axial oscillations around the coherence volume due to mechanical vibrations, simulated on a graph in the top right corner. The setup is illustrated with oil immersed objectives where the probed volume depth is 1 μm.

2.1. Motion artifact model

The intensity recorded by the camera is the sum of the backscattered light from both the sample and the reference arm [11]:

$$I(\boldsymbol{r}, t) = \eta \frac{I_0}{4} \left(R(\boldsymbol{r}, t) + R_{inc} + R_{ref} + 2\sqrt{R(\boldsymbol{r}, t)R_{ref}} cos\left(\Delta\phi(\boldsymbol{r}, t)\right) \right) \tag{1}$$

where $I(\boldsymbol{r}, t)$ is the intensity recorded at position $\boldsymbol{r} = (x, y)$ and time t, η is the camera quantum efficiency, I_0 is the power LED output impinging on the interferometer considering a 50/50 beam-splitter, R_{ref} is the reference mirror reflectivity (i.e. the power reflection coefficient), $R(\boldsymbol{r}, t)$ is the sample reflectivity (i.e. the power reflection coefficient) at position $\boldsymbol{r}$ and time t, $\Delta\phi(\boldsymbol{r}, t)$ is the phase difference between the reference and sample back-scattered signals at position $\boldsymbol{r}$ and time t, $I_{incoh} = R_{inc}I_0/4$ is the incoherent light back-scattered by the sample on the camera, mainly due to multiple scattering and reflections out of the coherence volume. The dynamic signal is computed as the average of the running temporal standard deviation and the processed dynamic signal can be written:

$$I_{dyn}(\boldsymbol{r}) = \frac{1}{N} \sum_i SD\left(\frac{\eta I_0}{2} \sqrt{R_s(\boldsymbol{r}, t_{[i,i+\tau]})R_{ref}} cos\left(\Delta\phi_s(\boldsymbol{r}, t_{[i,i+\tau]})\right) \right) \tag{2}$$

where SD is the standard deviation operator, N is the total number of sub-windows, τ is the sub-windows length so that $t_{[i,i+\tau]}$ is the time corresponding to one sub-window, R_s and $\Delta\phi_s$ are respectively the reflectivity and phase of the local scatterers that induce the temporal fluctuations that D-FFOCT aims to measure. In the event of small displacements of the entire sample, on the order of the depth of field or smaller, the processed signals will be the sum of the actual local fluctuations and the modulation created by the bulk sample motion creating a global phase shift. The resulting artifacts are therefore proportional to the sample reflectivity, which is orders of magnitude higher than the reflectivity of the scatterers probed by D-FFOCT (e.g. mitochondria
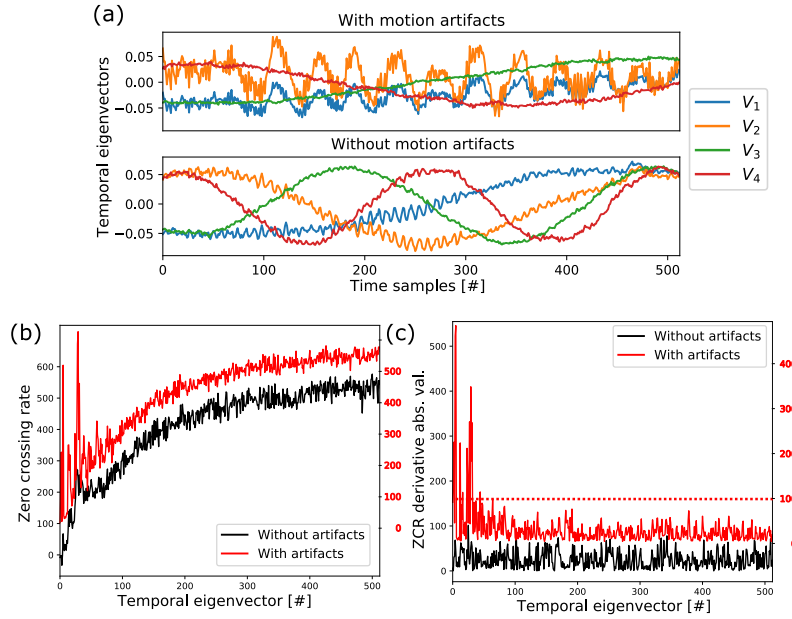
Fig. 2. (a) First few temporal eigenvectors. *Top:* for an acquisition with motion artifacts where V_1 and V_2 were detected as motion artifact and removed. *Bottom:* for an acquisition without visible artifacts. (b) Zero crossing rate computed for each temporal eigenvectors. (c) Absolute value of the derivative of the zero crossing rate computed for each temporal eigenvector. Artifacts were detected by thresholding the curve above 3 standard deviations. The baseline was arbitrarily increased for the red curves in (b) and (c) in order to increase readability.

and vesicles) leading to strong artifacts on the dynamic image, which mask the signal of interest. In the presence of mechanical noise, the measured fluctuation can be written:

$$I_{mes}(\boldsymbol{r}) = I_{dyn}(\boldsymbol{r}) + I_{art}(\boldsymbol{r}) \tag{3}$$

where the artifactual signal can be expressed as:

$$I_{art}(\boldsymbol{r}) = \frac{1}{N} \sum_i SD\left(\frac{\eta I_0}{2}\sqrt{R_s(\boldsymbol{r}, t_{[i,i+\tau]})R_{ref}}\,cos\left(\frac{4\pi}{\lambda}z(t_{[i,i+\tau]})\right)\right) \tag{4}$$

where $z(t_{[i,i+\tau]})$ is the sample axial displacement on the $i-th$ sub-window. Here we neglected the sample deformation for the sake of clarity. Nonetheless it could be taken into account by processing the stack in spatial patches where deformations are negligible. For a highly reflective zone we have $I_{dyn}(\boldsymbol{r}) \ll I_{art}(\boldsymbol{r})$ and the dynamic signal is completely masked by artifacts that look like the corresponding static FFOCT image that could be obtained by randomly sampling the path difference instead of using the standard PZT modulation mentioned before. Indeed, modulating the position of the sample around the coherence volume is equivalent to modulating the piezo position, which explains why artifacts look like the standard FFOCT image.

2.2. Proposed algorithm

In order to remove motion artifacts we want to use the SVD as an adaptive filter that could separate motility signals from motion induced signals. The first step is to unfold the 3D $M(x, y, t)$ cube of data into a 2D matrix $M_u(\boldsymbol{r}, t)$ to perform the decomposition. Higher dimensions of

SVD do exist but are not required here as the horizontal x and vertical y dimension do not differ when considering axial motion artifacts. SVD is the generalization of the eigendecomposition of a positive semidefinite normal matrix, and can be thought of as decomposing a matrix into a weighted, ordered sum of separable matrices which will become handy when reconstructing the SVD-denoised signals:

$$M_u = U\Sigma V^\star = \sum_i \sigma_i \mathbf{U}_i \otimes \mathbf{V}_i \tag{5}$$

where $\otimes$ is the outer product operator, U contains the spatial eigenvectors, V contains the temporal eigenvectors and Σ contains the eigenvalues associated with spatial and temporal eigenvectors. Performing the SVD on an unfolded $M_u(1440 \times 1440, 512)$ dynamic stack takes around 30 seconds on a workstation computer (Intel i7-7820X CPU, 128 Gbyte of DDR4 2666 MHz RAM) and requires 45 GByte of available RAM using LAPACK routine for SVD computation without computing full matrices. Investigating such decomposition for artifact-free data sets we found that spatial eigenvectors related to motion artifacts have particular and easily identifiable associated temporal eigenvectors. Indeed, when looking at the first temporal eigenvectors, we observed sinusoid-like patterns with increasing frequency, see Fig. 2(a). In presence of motion artifacts, temporal eigenvectors appeared with random, high-frequency components that are easy to detect with simple features. Here, the zero crossing rate (the number of times a function crosses $y = 0$) is used to detect temporal eigenvectors involved in motion artifacts. In presence of motion artifacts some of the firsts temporal eigenvectors present a high zero crossing rate, see Fig. 2(b) and 2(c). In order to detect these outliers we computed the absolute value of the derivative of the zero crossing rate (D-ZRC = $|ZRC_{i+1} - ZRC_i|$) and applied a threshold: if the D-ZRC is higher than three times the D-ZRC standard deviation then the corresponding eigenvalue σ_i is set to zero in $\hat{\Sigma}$ and the SVD-denoised stack $\hat{M}_u$ is reconstructed as:

$$\hat{M}_u = \sum_i \hat{\sigma}_i \mathbf{U}_i \otimes \mathbf{V}_i \tag{6}$$

The SVD-denoised stack $\hat{M}_u$ can then be folded back to its original 3D shape $\hat{M}$ and the dynamic computation can be performed. Interestingly, the use of an automatic selection of eigenvectors allows a more reproducible analysis. For example, the SVD can be performed on spatial sub-regions without visible artifacts, something very hard to obtain with manual selection of eigenvectors. This can also improve the filtering procedure in the case of sample spatial deformation or if the computation requires too much RAM.

2.3. Results

We tested the proposed SVD filtering on different acquisitions taken on different setups (the one presented in Fig. 1(a) and the LightCT system manufactured by LLTech SAS). When motion artifacts were present, image quality after denoising was greatly improved in each case. In Fig. 3 we present lung biopsy images taken with the LightCT system in a clinic, where imaged tissues were waste tissues from biopsy procedures that were destined to be destroyed, and we imaged them just before destruction. The imaging was carried out according to the tenets of the Declaration of Helsinki and followed international ethic requirements for human tissues. SVD filtering effectively removes motion artifacts from collagen fibers and reveals cells in Fig. 3(b) and 3(e), see Visualization 1 for complete $1260 \times 1260 \ \mu m$ fields of view. D-FFOCT images were also higher contrast after SVD denoising, allowing easier interpretation for clinical applications, e.g. lung tumor detection in the presented images. We imaged fibroblasts with the setup presented in Fig. 1(a). Cells were very flat leading to fringes pattern created by the specular reflection on their surface. These fringes were highly visible on the processed D-FFOCT image preventing the visualization of subcellular structures, see Fig. 4(a). After SVD filtering it is possible to
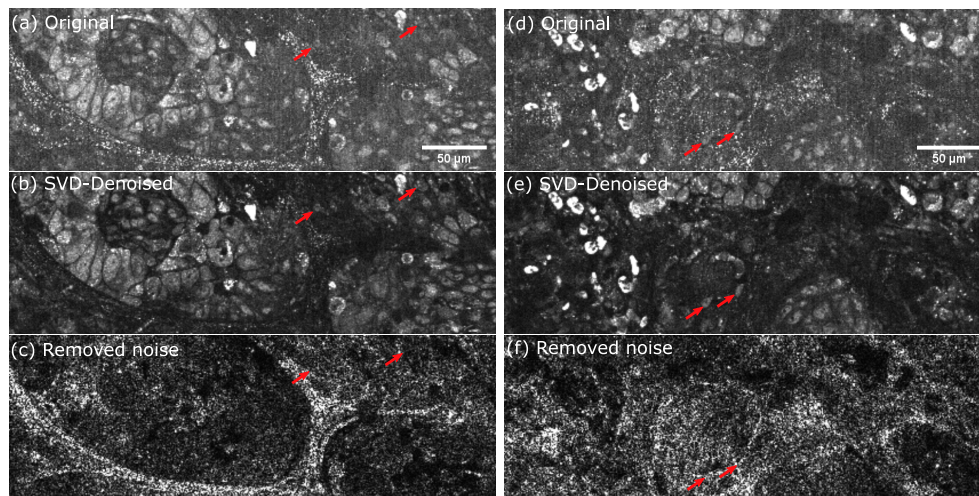
Fig. 3. Lung biopsy for cancer detection taken on the LLTech clinical setup. Artifacts arise mainly from mechanical vibration and air conditioning. (a)(d) Original D-FFOCT images computed on the raw stack. (b)(e) Denoised images computed with SVD filtering. (c)(f) Sum of the spatial eigenvectors absolute value removed by the SVD filtering. Red arrows are highlighting cells that were partially masked by motion artifacts. See Visualization 1 for complete 1260×1260 μm fields of view.

distinguish single subcellular entities and track them, see Fig. 4(b), enabling biological study without the need of a costly optical bench setup.

3. Extending penetration depth using non-stationarities

In addition to motion artifacts, a drawback of D-FFOCT compared to standard static FFOCT is the reduced penetration depth. While FFOCT can acquire images as deep as 1 mm, D-FFOCT is limited to about 100 μm due to the weak signal level produced by the sample fluctuations we wish to measure. In order to enhance the dynamic signal strength and so improve penetration depth, we propose computation of the dynamic image from the cumulative sum of the signal, rather than the raw signal. Indeed, the model for the dynamic image formation is small scatterers moving in the coherence volume during the acquisition leading to phase and amplitude fluctuations in the conjugated camera pixel. While a pure Brownian motion is stationary, hyper-diffusive displacements are not and we therefore propose to use the cumulative sum to enhance these non-stationarities. Intuitively, summing a centered noise will give a noisy trajectory that stays close to zero whereas if there is a small bias it will be summed for every sample and the cumulative sum will therefore have a slope equal to this bias.

3.1. Theoretical considerations

Let us consider an array of random values drawn from a zero centered Gaussian distribution. If the number of samples is large the mean of the array will be close to zero and equivalently the sum of all the samples will also be close to zero. Taking the cumulative sum of such an array gives a so called *Brownian bridge* (the curve starts and ends close to zero and makes a "bridge" between these two points). Theoretically, Brownian bridges are expected to be maximal close to the edges as the probability distribution of the maximum is the third arcsin law which has a typical U-shape [20]. More importantly, the Brownian bridge maximum follows a Rayleigh
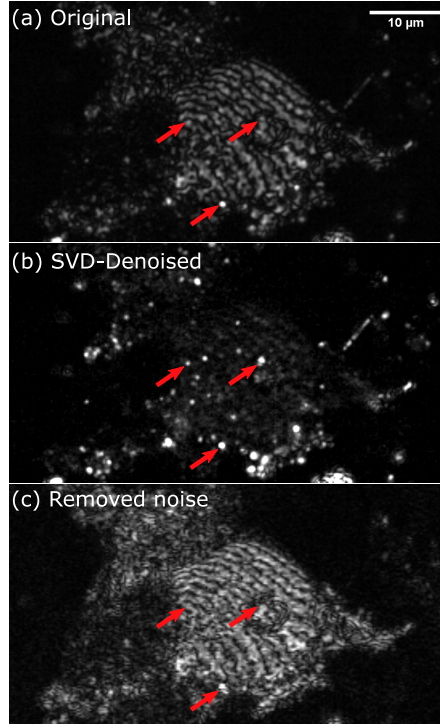
Fig. 4. Fibroblast image taken on the setup presented Fig. 1. Artifacts arise mainly from mechanical vibrations leading to fringes pattern. (a) Original D-FFOCT image computed on the raw stack. (b) SVD-denoised image computed with SVD filtering. Subcellular features appear with a much better contrast enabling segmentation and tracking. (c) Sum of the spatial eigenvectors absolute value removed by the SVD filtering. Red arrows are highlighting subcellular features, only the bottom one was visible on the original image.

distribution. If we consider a Brownian bridge $W_s \forall s \in [0, 1]$:

$$W_M = sup\{W_s : s \in [0, 1]\} \tag{7}$$

$$\mathbb{P}[W_M \leq u] = 1 - e^{-2u^2} \tag{8}$$

where W_M is the supremum of the bridge and $\mathbb{P}[W_M \leq u]$ is the probability of the supremum being less than u. According to the Rayleigh distribution, the Brownian bridge maximum must therefore scale as $\sqrt{t}$ with t scaling as the number of frames. Now, if there is a bias in the distribution, which is the case if a scatterer is moving with constant velocity in the coherence volume, the cumulative sum will scale as $\frac{t}{2}$ due to the slope introduced by the bias. It will also be either always positive or negative and the maximum will be reached around the center of the bridge. The cumulative sum will therefore exhibit a completely different behavior for centered noise than for actual motility signals, leading to a better signal to noise ratio on dynamic images. Note that for Brownian bridges it is often observed that the function changes sign regularly (the probability of sign changes is also well established [20]), which is not the case when there are non-stationarities.

We simulated an experiment by introducing a linear bias of $\sigma/3$ on a centered Gaussian distribution which is not perceptible on the signals presented in Fig. 5(a). Looking at the cumulative sum the bias is much more obvious as the maximum reached by the bridge is three times higher, hence motility signals are detected with a higher sensitivity using the cumulative

sum.

3.2. Results

The dynamic image is computed by taking the average of the maxima of the absolute values of the running cumulative sum:

$$I'_{dyn}(\boldsymbol{r}) = \frac{1}{N} \sum_i max\left(\left| CumSum\left(I(\boldsymbol{r}, t_{[i,i+\tau]}) - \bar{I}(\boldsymbol{r}, t_{[i,i+\tau]}) \right) \right| \right) \tag{9}$$

where *CumSum* is the cumulative sum operator, N is the total number of sub-windows, τ is the sub-windows length so that $t_{[i,i+\tau]}$ is the time corresponding to one sub-window and $\bar{I}(\boldsymbol{r}, t_{[i,i+\tau]})$ is the signal mean on the sub-window. We tested the proposed method with $\tau = 50$ on the photoreceptor layer of an explanted macaque retina at 85 μm depth that presents a horizontal gradient of SNR, see Fig. 5(b) and 5(c). In order to quantify the gain in SNR we segmented 192 single cells using Trainable Weka [21] and computed the SNR for each cell (the SNR was computed as the mean intensity of the pixels inside the cells divided by the mean intensity of the background), see Fig. 5(d). In this case the SNR is doubled with the proposed method and the camera column noise is almost completely removed. We tested the proposed algorithm on several acquisitions on tissues and cell cultures and the average SNR improvement factor was 1.9, allowing imaging deeper into tissues with D-FFOCT.
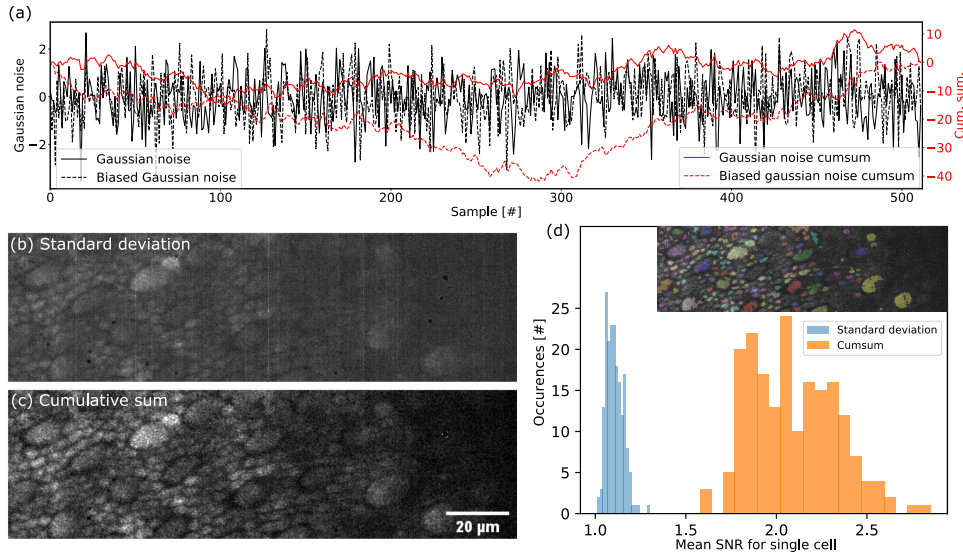
Fig. 5. (a) Simulation of Gaussian noise with and without bias and their cumulative sum. The maximum reached by the cumulative sum is 3 times higher with the bias. (b) Dynamic image of a macaque photoreceptor layer using standard deviation. (c) Dynamic image of a macaque photoreceptor layer using the proposed method based on cumulative sum. (d) Histogram of SNR for 192 single cells segmented in (b) and (c). Segmentation results are shown in the top right corner. The gain in SNR for this data set is 1.96 on average for each cell.

4. Applying both methods for in vivo dynamic imaging

The proposed SVD filtering procedure is of great interest for applying D-FFOCT in vivo for removing sample motion such as eye motion for retinal imaging. In order to limit lateral drifts
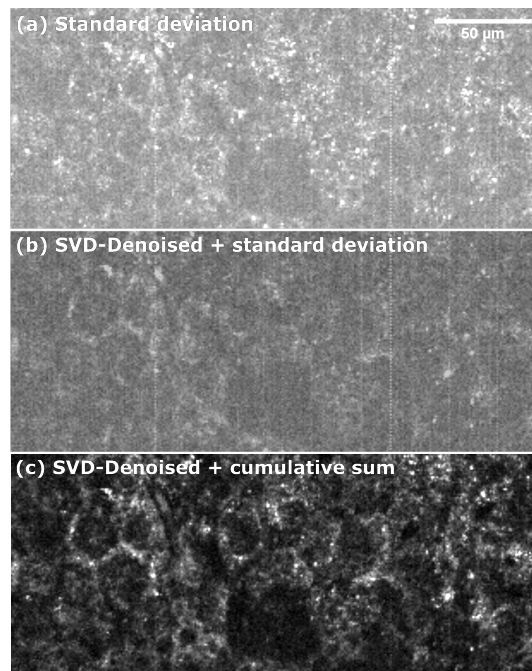
Fig. 6. In vivo mouse liver dynamic image taken on LLTech clinical setup with custom mount. Artifacts mainly arise from the breathing and heartbeat. (a) In vivo D-FFOCT image of a mouse liver computed on the raw stack with the standard deviation. (b) In vivo D-FFOCT image of a mouse liver computed on the SVD-denoised stack with the standard deviation. (c) in vivo D-FFOCT image of a mouse liver computed on the SVD-denoised stack with the cumulative sum. See Visualization 2 for complete $1260 \times 1260 \ \mu m$ fields of view.

and to maintain contact, a custom head was adapted on the sample arm of a LightCT setup combined with a pump to create a weak suction force. We acquired a stack of images on a living mouse liver at 80 μm depth. The animal manipulation protocol was approved by our local animal care committee. The mouse (4 week-old C57BL/6 (Janvier Lab, Le Genest Saint Isle, France)), was anesthetized by isoflurane, and sacrificed after the imaging procedure by CO_2 inhalation. The standard D-FFOCT images were very noisy mainly due to the heartbeat and breathing of the mouse, leading to tissue motion that creates artifacts, see Fig. 6(a). On applying the proposed SVD filtering, we were able to remove motion artifacts Fig. 6(b). Nonetheless signals are still very low due to the deep imaging in a strongly scattering organ and applying the cumulative sum algorithm dramatically increased the SNR by a factor of 3 Fig. 6(c), see Visualization 2 for complete $1260 \times 1260 \ \mu m$ fields of view. In the end, there are remaining artifacts produced by the coherence volume axial drift during the acquisition. Indeed, if the coherence volume shifts more than its axial extension, even if motion artifacts are perfectly removed, the probed dynamics would be averaged over several depths leading to an axial blur. To overcome this issue, the position of the coherence gate inside the sample may be compensated by monitoring the breathing and moving the reference arm with a precision corresponding to the optical sectioning (1 μm for the in vivo acquisition here) in order to compensate for the axial drift.

5. Conclusion

We proposed a filtering algorithm based on the SVD to effectively remove motion artifacts from dynamic images. The proposed method adds ~ 40 seconds for a $(1440, 1440, 512)$ stack which will require GPU processing in order to speed up the process for real time applications. This method was applied on an in vivo data set and is promising as long as axial motion is smaller than the coherence volume depth. Tracking and compensating methods are currently being investigated in order to acquire D-FFOCT stacks in a completely artifact-free manner for cornea [22] and retina [23, 24]. We also proposed a method based on the cumulative sum to enhance non-stationarities in temporal signals which led to an SNR factor increase of 1.9 on average for ex vivo samples and 3 on our in vivo data set. These general techniques could be applied to any other imaging modality with sub-diffraction phase sensitivity.

References

1. D. Huang, E. Swanson, C. Lin, J. Schuman, W. Stinson, W. Chang, M. Hee, T. Flotte, K. Gregory, C. Puliafito, and J. G. Fujimoto, "Optical coherence tomography," Science **254**, 1178–1181 (1991).
2. W. Drexler and J. G. Fujimoto, eds., *Optical coherence tomography: technology and applications* (Springer, 2015), 2nd ed.
3. E. Beaurepaire, A. C. Boccara, M. Lebec, L. Blanchot, and H. Saint-Jalmes, "Full-field optical coherence microscopy," Opt. Lett. **23**, 244–246 (1998).
4. A. Dubois, K. Grieve, G. Moneron, R. Lecaque, L. Vabre, and C. Boccara, "Ultrahigh-resolution full-field optical coherence tomography," Appl. Opt. **43**, 2874–2883 (2004).
5. J. Ben Arous, J. Binding, J.-F. Léger, M. Casado, P. Topilko, S. Gigan, A. C. Boccara, and L. Bourdieu, "Single myelin fiber imaging in living rodents without labeling by deep optical coherence microscopy." Journal of Biomedical Optics **16**, 116012 (2011).
6. M. Jain, N. Shukla, M. Manzoor, S. Nadolny, and S. Mukherjee, "Modified full-field optical coherence tomography: A novel tool for rapid histology of tissues," J. Pathol. Informatics **2**, 28 (2011).
7. C. Apelian, F. Harms, O. Thouvenin, and A. C. Boccara, "Dynamic full field optical coherence tomography: subcellular metabolic contrast revealed in tissues by interferometric signals temporal analysis," Biomed. Opt. Express **7**, 1511–1524 (2016).
8. C.-E. Leroux, F. Bertillot, O. Thouvenin, and A.-C. Boccara, "Intracellular dynamics measurements with full field optical coherence tomography suggest hindering effect of actomyosin contractility on organelle transport," Biomed. Opt. Express **7**, 4501–4513 (2016).
9. O. Thouvenin, C. Boccara, M. Fink, J. Sahel, M. Pâques, and K. Grieve, "Cell motility as contrast agent in retinal explant imaging with full-field optical coherence tomography," Investig. Opthalmology & Vis. Sci. **58**, 4605 (2017).
10. A. H. Kashani, C.-L. Chen, J. K. Gahm, F. Zheng, G. M. Richter, P. J. Rosenfeld, Y. Shi, and R. K. Wang, "Optical coherence tomography angiography: A comprehensive review of current methods and clinical applications," Prog. Retin. Eye Res. **60**, 66 – 100 (2017).
11. J. Scholler, V. Mazlin, O. Thouvenin, K. Groux, P. Xiao, J.-A. Sahel, M. Fink, C. Boccara, and K. Grieve, "Probing dynamic processes in the eye at multiple spatial and temporal scales with multimodal full field oct," Biomed. Opt. Express **10**, 731–746 (2019).
12. Y. Jia, O. Tan, J. Tokayer, B. Potsaid, Y. Wang, J. J. Liu, M. F. Kraus, H. Subhash, J. G. Fujimoto, J. Hornegger, and D. Huang, "Split-spectrum amplitude-decorrelation angiography with optical coherence tomography," Opt. Express **20**, 4710–4725 (2012).
13. T. E. de Carlo, A. Romano, N. K. Waheed, and J. S. Duker, "A review of optical coherence tomography angiography (OCTA)," Int. J. Retin. Vitreous **1**, 5 (2015).

14. A. Badon, D. Li, G. Lerosey, A. C. Boccara, M. Fink, and A. Aubry, "Smart optical coherence tomography for ultra-deep imaging through highly scattering media," Sci. Adv. **2** (2016).
15. H. Ammari, F. Romero, and C. Shi, "A signal separation technique for sub-cellular imaging using dynamic optical coherence tomography," Multiscale Model. & Simul. **15**, 1155–1175 (2017).
16. C. Demené, T. Deffieux, M. Pernot, B. Osmanski, V. Biran, J. Gennisson, L. Sieu, A. Bergel, S. Franqui, J. Correas, I. Cohen, O. Baud, and M. Tanter, "Spatiotemporal clutter filtering of ultrafast ultrasound data highly increases doppler and fultrasound sensitivity," IEEE Transactions on Med. Imaging **34**, 2271–2285 (2015).
17. J. Baranger, B. Arnal, F. Perren, O. Baud, M. Tanter, and C. Demené, "Adaptive spatiotemporal svd clutter filtering for ultrafast doppler imaging using similarity of spatial singular vectors," IEEE Transactions on Med. Imaging **37**, 1574–1586 (2018).
18. J. Scholler, "FFOCT control and acquisition software," (2019). https://doi.org/10.5281/zenodo.3137245.
19. E. B. a la Guillaume, C. Apelian, E. Dalimier, C. Boccara, A. Mansuet-Lupo, G. Chassagnon, and M.-P. Revel, "Lung biopsy assessment with dynamic cell optical imaging," Proc. SPIE 10470, Endosc. Microsc. XIII (2018).
20. P. Lévy, "Sur certains processus stochastiques homogènes," Compos. Math. **7**, 283–339 (1940).
21. I. Arganda-Carreras, V. Kaynig, C. Rueden, K. W. Eliceiri, J. Schindelin, A. Cardona, and H. Sebastian Seung, "Trainable Weka Segmentation: a machine learning tool for microscopy pixel classification," Bioinformatics **33**, 2424–2426 (2017).
22. V. Mazlin, P. Xiao, E. Dalimier, K. Grieve, K. Irsch, J.-A. Sahel, M. Fink, and A. C. Boccara, "In vivo high resolution human corneal imaging using full-field optical coherence tomography," Biomed. Opt. Express **9**, 557–568 (2018).
23. P. Xiao, V. Mazlin, K. Grieve, J.-A. Sahel, M. Fink, and A. C. Boccara, "In vivo high-resolution human retinal imaging with wavefront-correctionless full-field oct," Optica **5**, 409–412 (2018).
24. P. Mecê, P. Xiao, V. Mazlin, J. Scholler, K. Grieve, J.-A. Sahel, M. Fink, and C. Boccara, "Towards lens-based wavefront sensorless adaptive optics full-field oct for in-vivo retinal imaging," Proc.SPIE **10867** (2019).

3.2 Locking plane procedure for time-lapse D-FFOCT imaging

The locking plane procedure is explained in detail in [Scholler et al., 2019] Section 2.3, integrated in section 5.1.1. This method was also used section 2.4 for time-lapse imaging.

3.3 Real-time D-FFOCT imaging using GPU computing

When we image samples in the same plane using the locking plane procedure we can study different cellular mechanisms such as cell migration, cell division, apoptosis which have been shown in section 2.4. Although it can produce very nice movies, there is always some degree of uncertainty regarding the motion of cells. Indeed, when we see something disappearing we cannot tell whether it really vanished or if it went above or below the imaged plane in the tissue bulk. In order to accelerate acquisitions without saving the raw data I used Holovibes[4]. With the help of Michael Atlan, we adapted Holovibes to render D-FFOCT images. However, computation of D-FFOCT images with Holovibes is different than the usual algorithm. In our normal pipeline we use the HSV colorspace to compute dynamic images, see Appendix B. The motility index (computed using the standard deviation or the cumulative sum) is set as the image brightness by putting it in the Value channel. The color and saturation are then computed in the Fourier domain. The color codes for the average frequency of the fluctuations while the saturation codes for the frequency bandwidth. With this construction, we obtain a continuous mapping between fluctuation frequencies and colors. This method is therefore quantitative and it is possible to construct a colorbar, see Fig. 3.2. Holovibes was not natively performing running standard deviation nor running cumulative sum. In order to construct dynamic images with Holovibes I used a simpler construction. First, the intensity trace is Fourier transformed for each pixel. Then, the Fourier spectrum is integrated to generate 3 channels corresponding to red (highest frequencies), green (medium frequencies) and blue (lowest frequencies). Doing that, colored dynamic images are directly computed in the RGB colorspace and there is no continuous visual mapping between frequencies and color anymore. Also, the spectrum integration exhibits a lower SNR than the running standard deviation or the cumulative sum. Colored images generated with Holovibes are therefore less contrasted and not quantitative, see Fig. 3.2.

---

[4]A software for hologram rendering using GPU computation which is developed by Michael Atlan [Atlan, M. et al., 2009]
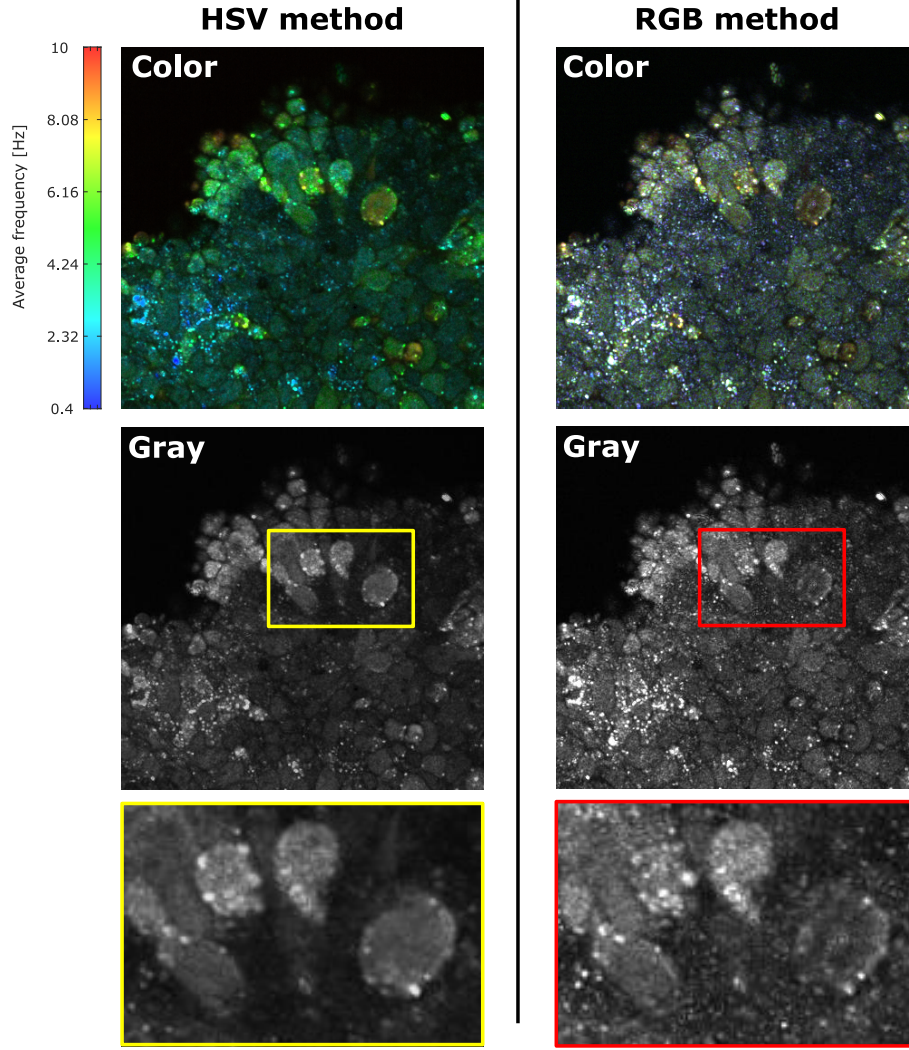
Fig. 3.2: Comparison between HSV and RGB methods. Left: dynamic image of a 26 days old organoids computed using HSV method. Right: same dynamic image computed with the RGB method (compatible with Holovibes, hence enabling faster rendering). Below color images are displayed the V channel where the comparison is easier to make. The HSV method present a higher SNR than the RGB method.

Also, there was no easy way to both control the experimental setup for 3D acquisitions (trigger camera, move motors, etc.) and to control Holovibes. Integrating everything in Holovibes would have required months of development. The idea was to combine Holovibes and our custom Python program. Python would control the trigger and motor parts and Holovibes the computation part with the camera link. The problem was that it requires a synchronisation between Holovibes and Python. As there was no application programming interface (API) to use Holovibes from another program I decided to automate the computer controls using *PyAutoGUI*. The automation algorithm is described below.

Algorithm 1 Quick dynamic 3D FFOCT

Require: Trigger camera with Python at the desired frame-rate
  Initialization: Number of volume N, number of plane per volume n, step size δ
  for $i = 0$ **to** $N - 1$ **do**
    for $j = 0$ **to** $n - 1$ **do**
      Acquire dynamic image I_{i-j}
      if $j \neq n - 1$ **then**
        Move sample by δ
        Wait for motion to end
      end if
    end for
    Move sample by $-n\delta$
    Wait for motion to end
  end for

Each acquisition consists in moving the mouse, clicking on the image name field, incrementing the name and then click on the acquisition button[5]. The duration of the motion depends on the step size and motor configuration (speed and acceleration) and must be carefully chosen in order to optimize the acquisition speed without artifacts. Finally with this method we can acquire a plane in less than 5 seconds and records volumes of 10 planes in less than a minute, allowing to track axially the migration of cells.

3.4 Dust removal using automatic detection and inpainting

Most of the systems I built and used during my PhD were using immersion objectives and therefore immersion mirror in order to maintain a symmetry between both arms. The slightest scratch or dust on the reference mirror surface would induce very bright spots on the FFOCT image because of the reference mirror position modulation. I proposed a method for automatically detecting these bright spots, remove them, and inpaint the FFOCT image (i.e. reconstruct signals at the bright spot locations). Note that although this method might also work for D-FFOCT images it was not necessary because we do not modulate the reference mirror position during the acquisition so we are less sensitive to dust and scratches. This dust denoising algorithm is detailed below:

1. A local thresholding with a Gaussian kernel (the threshold value is computed locally as the weighted average of neighbouring values) is applied on the FFOCT image to detect rapid changes in contrast due to bright spots.

2. The resulting mask is then refined using morphological filters (closings and dilations) to remove outliers.

3. Finally the bright spots are removed and inpainted by propagating the information at their edge using Navier-Stokes equation[6] [Bertalmio et al., 2001]. This inpainting procedure therefore makes the assumption that the image behind the bright spot was smooth and solution of the bi-harmonic equation.

---

[5] These steps are instant and take less than 1 ms to perform.
[6] Other priors could be considered, such as the image sparsity in a typical basis (wavelets or Fourier domain) rather than the smoothness.

An example of this procedure applied on a dirty mirror is shown Fig. 3.3. This method has also been applied successfully on direct image (non-tomographic image as presented above) for tear film imaging section 5.1.2.
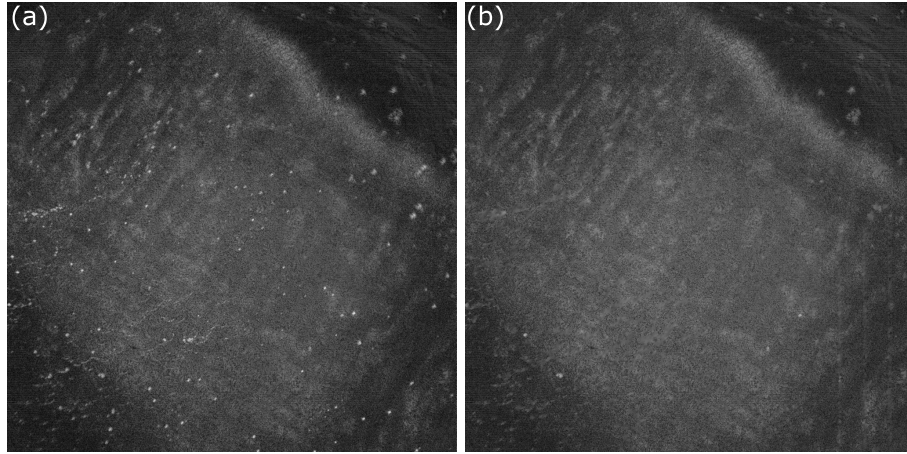
Fig. 3.3: Dust denoising on FFOCT images. (a) Original image. (b) Denoised image.

Chapter 4

Hardware developments: towards in-vivo D-FFOCT

Contents

This chapter features the hardware developments and implementations that I have been doing to improve (D)-FFOCT acquisitions, mainly for in vivo retinal imaging. In the first part, axial tracking of the retina is presented through an article and enabled us to get more consistent FFOCT images of the retina. Then, another article presents a simple and cheap, yet effective way to control and compensate the field curvature created by the optical asymmetry between the eye and the reference arm. This enables us to get images on complete 1 *mm* fields of view. Next, I treat the way aberrations affect conventional and FFOCT images with a theory proposed by Victor Barolle in his thesis [Barolle, 2019] which I experimentally validated with a dedicated adaptive optics FFOCT system that I built. This custom system allowed me to add controlled level of aberrations in order to compare simulations and experiments. Finally, in the last part I use the previous adaptive optics part for our retinal FFOCT setup in order to compensate ocular aberrationd, allowing us to image the photoreceptor layer of subjects with dilated pupils with near diffraction limited resolution and to get, for the first time, FFOCT images of the nerve fiber layer at different depths.

4.1 Article: High-resolution in-vivo human retinal imaging using full-field OCT with optical stabilization of axial motion

The first demonstration of FFOCT's ability to acquire en face images of the human retina in vivo was done in [Xiao et al., 2018]. The consistency of images that contains signals however was very low and experiments were very long and cumbersome for the imaged subjects. Retinal imaging using FFOCT is challenging because axial motions of the eye[1] shifts the coherence plane position with respect to the focal plane which is always on the retina for an emmetropic[2] eye. The first FFOCT retina image was made possible by the combination of FFOCT and a Fourier domain OCT: through the B-Scans generated by the SD-OCT both retinal cross-section and the FFOCT reference mirror were visible, so that a manual match between the reference mirror and the layer of interest had to be done just before acquisition and remains during the acquisition. As a consequence, a considerable amount of images had to be acquired to increase the chances of matching the optical path of both arms for a retinal layer of interest[3].

In order to improve image consistency we implemented an automatic axial tracking of the retina[4]. The first step was to combine FFOCT and SD-OCT on the same computer for synchronisations purposes. Then, I spent a great deal of time and effort on integrating the SD-OCT software development kit (SDK) in my software [Scholler, 2019a] which was natively not supported by Matlab. Then, SD-OCT cross-sectional images could be acquired and analyzed to drive a fast voice-coil translation stage in order to maintain the same optical path difference between the layer of interest and the reference mirror. The experimental setup and the processing steps are presented in Section 2 in the article below. Tracking results can be found in Section 3 where the mean deviation on the coherence plane position was 9.1 μm which represents a 7-fold improvement that allowed us to image more consistently even close to the fovea. The remaining problem was the band shaped signals Fig. 4 that was limiting the field of view for some subjects because of the optical asymmetry between the eye and the reference arm objective, see section 4.2. Finally, with this work we started to envision the possibility of a multimodal system that could provide both cross-sections and high-resolution en face images of the retina[5].

---

[1] Eye axial speed can reach 1 mm/s [Ginner et al., 2017].

[2] Emmetropia of the eye is achieved when the refractive power of the cornea and the axial length of the eye balance out, which focuses rays exactly on the retina, resulting in perfect vision

[3] The only layers that could be imaged was the IS/OS junction and the NFL (only one image) which precluded the study of the entire retina.

[4] This work was done in collaboration with Pedro Mecê.

[5] A startup should be coming up soon with such a device.

High-resolution *in-vivo* human retinal imaging using full-field OCT with optical stabilization of axial motion

PEDRO MECÊ,[*] [iD] JULES SCHOLLER, KASSANDRA GROUX, AND CLAUDE BOCCARA

Institut Langevin, ESPCI Paris, CNRS, PSL University, 1 rue Jussieu, 75005 Paris, France
[*]*pedro.mece@espci.fr*

Abstract: Time-domain full-field OCT (FF-OCT) represents an imaging modality capable of recording high-speed *en-face* sections of a sample at a given depth. One of the biggest challenges to transfer this technique to image *in-vivo* human retina is the presence of continuous involuntary head and eye axial motion during image acquisition. In this paper, we demonstrate a solution to this problem by implementing an optical stabilization in an FF-OCT system. This was made possible by combining an FF-OCT system, an SD-OCT system, and a high-speed voice-coil translation stage. B-scans generated by the SD-OCT were used to measure the retina axial position and to drive the position of the high-speed voice coil translation stage, where the FF-OCT reference arm is mounted. Closed-loop optical stabilization reduced the RMS error by a factor of 7, significantly increasing the FF-OCT image acquisition efficiency. By these means, we demonstrate the capacity of the FF-OCT to resolve cone mosaic as close as 1.5^o from the fovea center with high consistency and without using adaptive optics.

1. Introduction

Optical Coherence Tomography (OCT) has become a gold standard for living human retinal imaging in the clinical environment [1,2]. Owing to its unprecedented axial resolution, OCT enables the diagnosis of retinal disorders at the earliest stages and monitoring of the progression of retinal diseases. While physicians are capable of interpreting tomographic retinal cross-sections from OCT, there is nevertheless a demand for *en-face* views. Although OCT can produce *en-face* retinal images from 3-D stacks, it presents a low lateral resolution compared with Adaptive Optics (AO) ophthalmoscopes [3]. By correcting static and dynamic ocular aberrations [4,5], AO can explore the full aperture of the eye's pupil to achieve micrometer lateral resolution. To be able to combine both high axial resolution from OCT, and the high lateral resolution from AO, a great effort was made to develop AO-OCT systems [6,7]. However, the commercialization and the clinical deployment of AO-OCT are still challenging, mainly because of cost, optical complexity, size and heavy image post-processing linked to the use of AO [6].

Another modality of OCT is the time-domain Full-Field OCT (FF-OCT) [8] (henceforth, we refer to this imaging modality simply as FF-OCT). Contrary to conventional OCT, which scans an illumination spot across a tissue surface and records at each spot the depth structure, FF-OCT uses a spatially incoherent light source, high-speed megapixel camera and time-domain phase modulation to acquire *en-face* sections of the sample at a given depth. One attractive point of this technique for retinal imaging, is the fact that FF-OCT presents a low sensitivity to low-order ocular aberrations (*i.e.* defocus and astigmatism), due to the use of the spatially incoherent light source [9,10]. This interesting feature was highlighted in [11], where cone mosaic at 6° from the foveal center of a healthy subject (without prescription eyeglasses) was resolved without using AO. This first image was made possible by the combination of FF-OCT and a Spectral-Domain OCT (SD-OCT). Through the images generated by the SD-OCT both retinal cross-section and

the FF-OCT reference mirror were visible, and a manual match, just before the acquisition, was possible. Nevertheless, this strategy faces significant challenges in providing consistent and reproducible images, mainly due to involuntary axial head and eye motion, which can achieve a median maximum axial speed in the order of 1mm/s [12]. As a consequence, a considerable amount of images has to be acquired to increase the chances of matching the optical path of both arms for a retinal layer of interest.

Hence, to be able to record efficiently and consistently *en-face* sections of the retina *in-vivo*, an axial optical stabilization strategy is necessary. An optical stabilization of axial motion applied in time-domain FF-OCT for retinal imaging was first proposed by Miller *et al.*, combining the FF-OCT with an auxiliary time-domain 1-D OCT and a voice coil translation stage in the reference arm [13]. However, the time-domain 1-D OCT used for axial motion tracking was too slow to work *in-vivo* (20 A-scans per second). Later, Pircher *et al.* [14] combined a transverse scanning OCT system (which directly extracts *en-face* images) with a high-speed Fourier domain 1-D OCT, used to track the cornea apex signal, and a rapid scanning optical delay line montage for real-time optical stabilization. Although the achieved performance was satisfactory, because of the scanning illumination/detection scheme of the proposed OCT, *en-face* images were acquired with a low frame rate, limited FOV and suffered from motion artifacts and distortion due to fixational eye movements [15]. Therefore, continuous involuntary head and eye motion remains one of the biggest challenges in time-domain FF-OCT when imaging the living human retina.

In this paper, we present an FF-OCT retinal imaging system with optical stabilization of axial motion. This system was made possible by combining the FF-OCT system with an SD-OCT. The idea is to use B-scans generated by the SD-OCT to measure the retinal axial position and to drive a high-speed voice-coil translation stage, where the reference arm of the FF-OCT is mounted, correcting for the eye motion. By these means, we demonstrate the capacity of the FF-OCT to resolve cone mosaics as close as 1.5^o from the fovea center with high consistency and efficiency, without using adaptive optics.

2. Methods

2.1. Experimental setup

Figure 1 presents the schematic drawing of the custom-built FF-OCT system coupled with a SD-OCT system. The FF-OCT comprises a light-emitting diode (LED) with $\lambda = 850$ nm center wavelength and 30 nm bandwidth (M850L3, Thorlabs), used as a spatially incoherent illumination source, giving a theoretical axial resolution of approximately 8 μm in water. The LED is focused by a condenser 20 mm in front of the eye's pupil. A physical diaphragm is positioned in front of the LED, conjugate to the retina and the FF-OCT reference mirror. The illumination beam is split into the reference and the sample arms by a 50:50 cubic beam splitter (BS). For the reference arm, an Olympus 10X/0.25 NA Plan Achromat objective is used with a silicon mirror placed at the focal plane of the objective. The whole reference arm (microscope objective and silicon mirror) is mounted on a fast voice-coil translation stage (X-DMQ12P-DE52, Zaber Technologies Inc.), allowing for adjustment of the coherence gate depth position with a maximum speed of 10 mm/s. For the sample arm, optical windows were introduced to compensate for dispersion effects (not shown in Fig. 1) and the healthy volunteer's eye was aligned along the optical axis. The FF-OCT light beam arrives with an 8 mm diameter in the eye's pupil. The back-scattered photons from both arms are recombined by the same BS and focused onto a high-speed (up to 720 Hz) CMOS camera (Q-2A750-Hm/CXP-6, Adimec) for FF-OCT imaging.

The use of an SD-OCT system coupled with our custom-built FF-OCT is driven by two motivations: firstly, to measure the retinal axial position through SD-OCT cross-sectional images, which is a crucial step to correct for axial motion; secondly, once the axial motion is stabilized, to display in real-time SD-OCT retinal cross-sections of sufficient quality to guide the positioning of the FF-OCT coherence gate at the retinal layer of interest. To address these
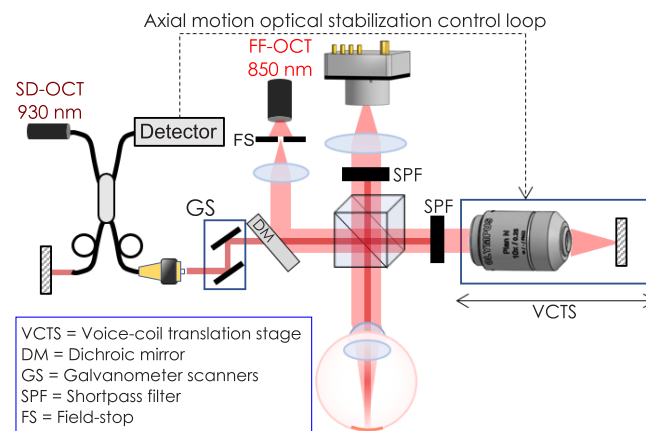
Fig. 1. Schematic drawing of the custom-built FF-OCT system coupled with an SD-OCT for real-time axial motion correction and FF-OCT coherence gate positioning guidance.

motivations, we considered a trade-off between acquisition rate, for fast axial motion tracking, and enough signal-to-noise ratio (SNR), for retinal layer identification, helping the positioning of the FF-OCT coherence gate. The SD-OCT system (Thorlabs Ganymede-II) was coupled through a dichroic mirror positioned between the FF-OCT illumination source and the BS. The SD-OCT galvanometer scanners were 20-cm away and not conjugate to the eye's pupil due to three main factors: mechanical restrictions imposed by the commercial SD-OCT system, to avoid specular reflections in the FF-OCT detector by introducing optical lens in the sample arm [16], and to favor a compact optical design.

The SD-OCT system comprises a broadband superluminescent diode with $\lambda = 930$ nm center wavelength and 60 nm bandwidth, giving a theoretical axial resolution of $4.5 \mu m$ in water. It presents an A-scan rate up to 36 kHz with a sensitivity of about 96 dB and 1024 axial pixels, comprising an imaging depth (axial range) of 2.2 mm in water. As the galvanometer scanners and the eye's pupil are not conjugated, the SD-OCT light beam arrives in the eye's pupil with a 4 mm diameter, slightly scanning the pupil plane. Shortpass filters were introduced to block the SD-OCT signal in the reference and detection arms of the FF-OCT.

2.2. Axial motion correction

Initially, we manually match the optical path of the FF-OCT reference mirror with a fixed model eye in the sample arm to determine the initial position of the voice-coil translation stage. This calibration step is necessary only once. B-scans generated by the SD-OCT are used to measure the retinal axial position by the following means: 1) A-scans composing the B-scan are averaged, obtaining an axial profile with increased SNR (named from here after "averaged A-scan"); 2) the averaged A-scan is cross-correlated with a reference A-scan and the relative retinal axial position is measured, 3) parabolic fitting is used to obtain a subpixel estimation of the axial retinal position with sub-micrometer precision. The reference A-scan is the first averaged A-scan generated after activating the axial motion correction. This reference is kept until the axial motion correction procedure is deactivated. After the measurement, a corresponding voltage is sent to the voice-coil translation stage, which moves the whole reference arm of the FF-OCT to compensate for the axial motion, re-matching the reference arm with the retinal layer of interest. A custom-developed real-time calculator, comprising core libraries written in MATLAB, controls the axial motion stabilization closed-loop with a 50 Hz loop rate. Control strategy is a PI (proportional-integral) controller with 0.5 gain and the main steps of the chronogram are: SD-OCT B-scan acquisition

(7 ms), SD-OCT B-scan processing (2 ms), axial eye motion measurement (1 ms) and voice-coil translation stage reaction and positioning (10 ms).

2.3. Image acquisition

To obtain statistics on axial motion, we acquired 13 SD-OCT image sequences (7 to 28 s of duration) from three healthy subjects, for a total of 4700 analyzed A-scans. Simultaneous FF-OCT and SD-OCT image acquisition was performed on a young healthy subject (aged 25) presenting a refractive error of $1.5D \times 0.5D \times 160^o$ (spherical × cylindrical × axis of cylindrical errors). Research procedures followed the tenets of the Declaration of Helsinki. Informed consent was obtained from the subject after the nature and possible outcomes of the study were explained. This study was authorized by the appropriate ethics review boards (CPP and ANSM (IDRCB number: 2019-A00942-55)). Subjects were seated in front of the system and stabilized with a chin and forehead rest and asked to fixate a target placed at an infinite focal conjugate. During the imaging session, subjects were wearing their prescription glasses to increase the signal level of both SD-OCT and FF-OCT [10]. Image acquisition was realized in a dark room, maximizing the pupil dilation. Four sets of data were recorded simultaneously during imaging sessions: FF-OCT images, SD-OCT B-scans, retinal axial position and the position of the voice-coil translation stage (equivalent to the position of the FF-OCT reference mirror). Phase modulation was performed by the residual axial motion after optical stabilization (*i.e.* the residual tracking error). FF-OCT images were acquired at 300 Hz using custom-built software [17]. The FF-OCT camera worked close to saturation to use the whole full well capacity, decreasing relative importance of shot noise [18]. Concerning the SD-OCT, we empirically chose to scan 1° FOV of the retina with 256 A-scans, providing a good trade-off between acquisition speed and SNR. The latter had to be sufficient to distinguish most of the retinal layers, crucial for guiding the positioning of the FF-OCT coherence gate to the retinal layer of interest. During image acquisition, the total power entering the eye from the FF-OCT illumination source and the SD-OCT scanning source were respectively 1.3 mW (during 0.25s) and 0.25 mW (continuous scanning), which are below the ocular safety limits established by the ISO standards for group 1 devices.

2.4. Image processing

As detailed in [18], the intensity recorded on a camera pixel is the coherent sum of the reference and sample beams, containing coherent and incoherent terms, expressed as follows:

$$I_{\phi=\phi_N} = \eta \frac{I_0}{4}(R_{eye} + R_{ref} + R_{incoh} + 2\sqrt{R_{eye}R_{ref}}cos(\Delta\phi_N)) \tag{1}$$

where $I_{\phi=\phi_N}$ is the intensity recorded at time point N with a ϕ_N phase shift, η is the camera quantum efficiency, I_0 is the LED's power output (we considered a 50/50 beam-splitter), R_{eye} is the eye reflectivity (*i.e.* the power reflection coefficient), R_{ref} is the reference mirror reflectivity (*i.e.* the power reflection coefficient), $I_{incoh} = R_{incoh}\frac{I_0}{4}$ is the incoherent light detected by the camera, mainly induced by multiple scattering and back-scattering from out-of-focus retinal layers, and $\Delta\phi$ is the phase difference between the reference and the sample back-scattered signals.

From the acquired image sequence, each image was normalized by dividing each image by its mean value. Since the phase was randomly modulated by the residual tracking error, and to eliminate the incoherent terms, we adopted a 2-phase demodulation. The 2-phase demodulation consists of subtracting one image $I_{\phi=\phi_N}$ from the next $I_{\phi=\phi_{N+1}}$ and taking the modulus:

$$I_{2-phase} = |I_{\phi_N} - I_{\phi_{N+1}}| = \eta \frac{I_0}{2}\sqrt{R_{eye}R_{ref}}|cos(\Delta\phi_N) - cos(\Delta\phi_{N+1})| \tag{2}$$

Note that for a 2-phase demodulation strategy it is not possible to un-mix amplitude and phase. Next, images with a very low or absent useful signal, mainly due to an insufficient

phase shift between consecutive images (*i.e.* low value for $|cos(\Delta\phi_N) - cos(\Delta\phi_{N+1})|$), were automatically detected using an intensity-based threshold algorithm, and then excluded from the image sequence. Finally, useful images were registered using a custom-built normalized cross-correlation algorithm, where the image presenting the highest signal level was chosen as the reference.

3. Results

3.1. Performance of the axial motion stabilization

Figures 2(A) and (B) present two examples of retinal axial position as a function of time. The black line corresponds to the measured axial position of the retina and the red line corresponds to the position of the FF-OCT reference mirror. Fast oscillations and slower drifts of the retinal axial motion are clearly visible. Time points during blink occurrences (black areas) were automatically excluded from the study after applying an intensity-based algorithm to SD-OCT images. Figures 2(C) and (D) illustrate again the axial motion as a function of time, but now applied to the acquired averaged A-scans, where the red rectangle indicates the coherence gate thickness of the FF-OCT system, *i.e.* depth positions where interference takes place. The continuous motion drastically reduces the chances of acquiring an FF-OCT image of a layer of interest (here the inner/outer segment junction - IS/OS). From the collected data set of retinal axial position temporal evolution (excluding blink occurrences), we computed a peak-to-valley amplitude of $244.9 \pm 49.2\mu m$, a mean deviation from zero position of $62.5 \pm 29.5\mu m$ and a root-mean-square (RMS) error of $61.5 \pm 14.2\mu m$. In this condition, the expected efficiency to acquire FF-OCT images of a layer of interest (absolute error inferior to half of the axial resolution, here $4\mu m$), supposing a perfect initial manual match between both arms of the FF-OCT, is 7.4 ± 1.8 %.

Figures 2(A) and (B) also show the difference (blue line) between measured retinal position and FF-OCT reference mirror position. Slower drifts were filtered out and fast oscillations were reduced. An absolute residual tracking error of $6.7 \pm 3.1\mu m$ remains mainly because of the inherent time delay of the control loop and the inertia of the voice-coil translation stage. However, the residual error is low enough to considerably increase the chances of acquiring FF-OCT of a retinal layer of interest, as illustrated in Figs. 2(E) and (F). The presented axial motion stabilization method reduced peak-to-valley amplitude to $48 \pm 2\mu m$, mean deviation from zero position to $0.31 \pm 0.13\mu m$, and RMS error to $9.1 \pm 0.68\mu m$. In this condition, the expected efficiency was increased by a factor of 8.5 (62.4 ± 4.1 %). Visualization 1 shows a simulation of the expected B-scan temporal evolution with optical stabilization compared to the position of the FF-OCT coherence gate. Table 1 summarizes the achieved performance with the proposed method to optically stabilize the axial motion.

Table 1. Axial motion statistics with and without the use of the method to optically stabilize retinal axial motion. Statistics took into account 13 image sequences of 7 to 28s duration from three subjects, for a total of 4700 analyzed A-scans. PV stands for peak-to-valley amplitude.

	PV (μm)	Mean deviation (μm)	RMS error (μm)	Efficiency (%)
Without stabilization	244 ± 49.2	62.5 ± 29.5	61.5 ± 14.2	7.4 ± 1.8
With stabilization	48 ± 2	0.31 ± 0.13	9.1 ± 0.68	62.4 ± 4.1

To evaluate the temporal performance of the control loop, we computed its rejection transfer function (or sensitivity function) [19], which describes how different axial motion temporal frequencies are attenuated by the optical stabilization control loop. The rejection transfer function is the ratio between temporal power spectral densities (PSD) of the residual tracking error and of the retinal axial position. Figure 3(A) presents an example of the temporal PSD computed for the retinal position (blue line) and residual tracking error (red line). Note that temporal
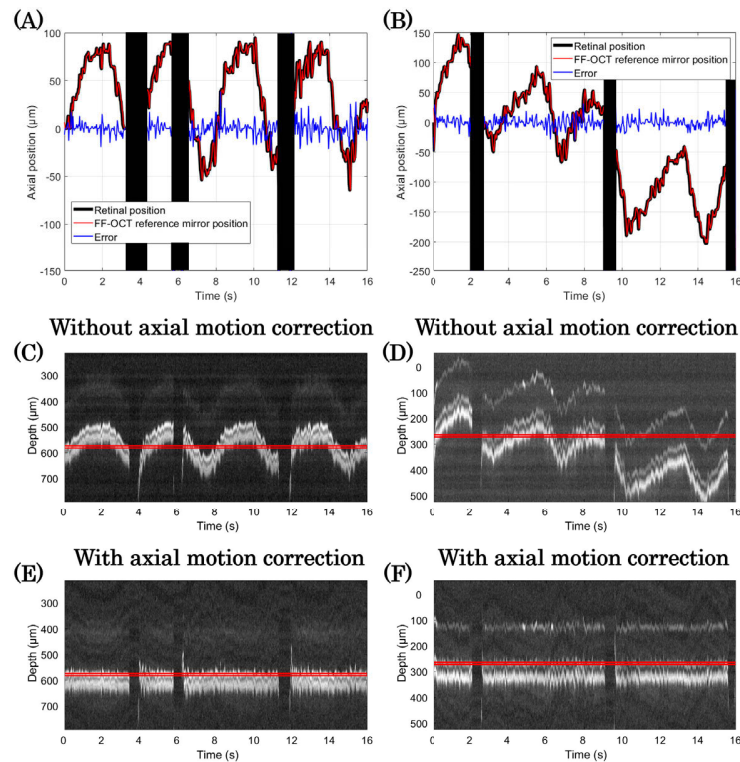
Fig. 2. Performance of the axial eye motion optical stabilization. (A) and (B) are two examples of the axial position temporal evolution. Black line: measured axial position of the retina. Red line: position of the FF-OCT reference mirror. Blue line: Residual tracking error. Black areas represent blink occurrences and were excluded from the study. (C) and (D) averaged A-scan time series without axial motion correction. (E) and (F) presents the same averaged A-scan time series as (C) and (D) but now with expected performance after correcting for axial motion. Red rectangles represent the coherence gate axial position and volume. See Visualization 1 for a simulation of the expected B-scan temporal evolution with optical stabilization compared to the position of the FF-OCT coherence gate. Note that all SD-OCT images are shown in linear scale.

frequencies up to approximately 4 Hz are attenuated. Figure 3(B) shows the rejection transfer function obtained by averaging the temporal PSD for different acquired sequences (black line) and the theoretical temporal PSD (red line), assuming a PI controller with 0.5 gain and two-frame delay [19,20]. The good match between the experimental and theoretical plots demonstrates that no additional delay or jitter was present during the acquisition, meaning that the temporal performance of the loop is as expected. Note that, although a loop rate of 50 Hz is adopted, the loop cut-off frequency, *i.e.* the highest corrected temporal frequency (associated with 0 dB), is approximately 4 Hz [3,19].

3.2.　FF-OCT imaging of living human retina with axial motion correction

Visualization 2 shows an FF-OCT image sequence where the optical stabilization is activated during image acquisition. To begin, the voice-coil translation stage was manually positioned close to the IS/OS junction. A low-signal coming from photoreceptors in the bottom of the frame for a few frames duration is sometimes seen. When optical stabilization is activated, the

Fig. 3. Temporal performance of the axial motion correction control loop. (A) examples of temporal PSD computed for the retinal axial position (blue line) and the residual tracking error (red line). (B) Experimental (black 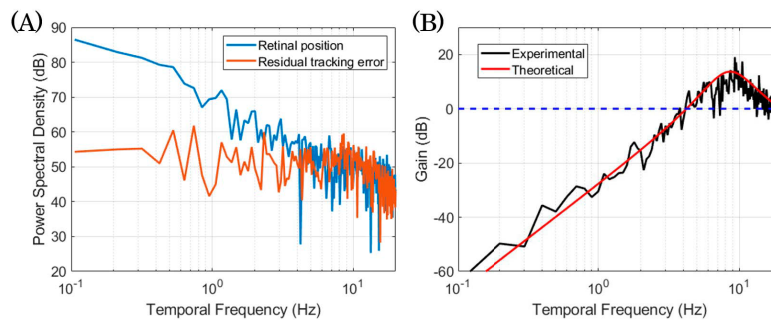line) rejection transfer function obtained by averaging temporal PSD for different acquired sequences, and the theoretical temporal PSD (red line). Note that, although a loop rate of 50 Hz is adopted, the loop cut-off frequency, *i.e.* the highest corrected temporal frequency (associated with 0 dB), is approximately 4 Hz.

photoreceptor mosaic becomes visible and the signal consistency significantly improves. After activating the axial motion correction, one can observe a temporal fluctuation of the intensity signal where the cone mosaic is visible. This intensity fluctuation occurs mainly due to two phenomena: mispositioning of the coherence gate, or an random phase modulation (see Sect.3.3), both due to the residual tracking error. Figure 4(A) shows the averaged image obtained during axial motion correction. The lateral retinal motion was corrected by digital registration. Another interesting retinal feature perceived in the image is the central foveal depression, *i.e.* an elevation of the IS/OS junction compared to the cone outer segment tip (COST) in the center of the foveola (see schematic of Fig. 4(A) at the right upper part). Because of the depression, this region of the retina is perceived as a dark circled area surrounding the foveal center. This phenomenon happens because this region is out of the FF-OCT coherence gate, which is about $8\mu m$ thick. The diameter of the dark circled area is around $180\mu m$ which corresponds to the typical size of the foveal umbo of a healthy subject [21].

By translating the FF-OCT reference arm laterally (*i.e.* not in depth), perpendicularly to the optical axis, one can generate a tilted coherence gate in the sample arm, producing FF-OCT images with band-type useful FOV. In the case of imaging photoreceptor layers, we expect to obtain two bright bands coming from the IS/OS junction and the COST layer. Tilting the coherence gate allows visualization of the impact of the axial motion correction directly in FF-OCT images. Visualization 3 shows an FF-OCT image sequence with a tilted coherence gate without axial motion correction. It is possible to visualize both photoreceptor bands moving continuously. Band motion is mainly due to axial motion. Lateral retinal motion, caused by fixational eye movements [15], only induces a shift of the retinal zone observed in the band FOV. Visualization 4 shows an FF-OCT image sequence with a tilted coherence gate now with axial motion correction, where band motion is strongly attenuated. In this case, due to the axial motion correction, one can register and average consecutive FF-OCT images to achieve a final image with enhanced quality. Figure 4(B) presents the averaged image generated from Visualization 4. Here, both IS/OS and COST photoreceptor mosaics are visible and could be resolved in a single image.

Figure 4 also shows zoomed areas from (A) and (B) and their respective spatial PSD. The estimated eccentricity (distance from the foveal center) of the zoomed areas are respectively 1°, 1.5^o, 3°, 2° and 2°. All zoomed areas, except for the first one, presented a clear and well defined Yellot's ring, the spectral signature of photoreceptor mosaic image [22]. Although it seems that
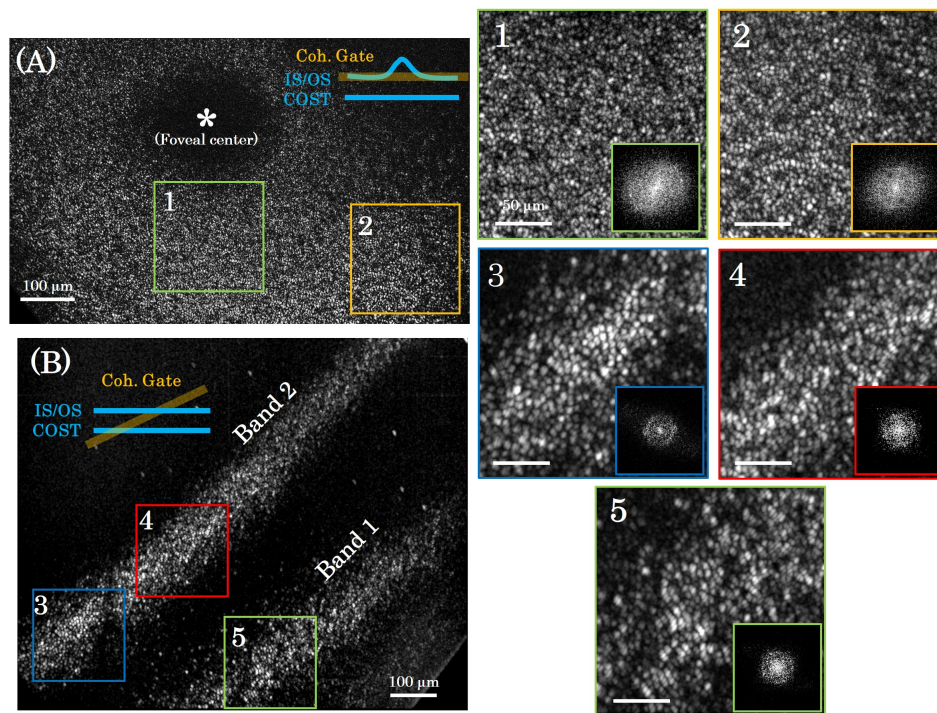
Fig. 4. Images of cone photoreceptor mosaic acquired with the help of the axial motion correction method. (A) Cone mosaic averaged image from Visualization 2, acquired at the IS/OS junction at the fovea center. Eccentricities of zoomed areas 1 and 2 are respectively 1°, 1.5^o. (B) Averaged image from Visualization 4. Both cone mosaic from the IS/OS junction and the COST layer close to the fovea center are visible in a single image. Eccentricities of zoomed areas 3, 4 and 5 are respectively 3°, 2° and 2°. For all zoomed areas the equivalent PSDs were computed.

the subject's pupil diameter was not sufficient to resolve cone mosaic from zoomed area 1, the majority of individual cones are visible. By using modal spacing method proposed by [22], we computed cone densities of 45 000 cones/mm^2, 20 700 cones/mm^2, 29 000 cones/mm^2 and 31 700 cones/mm^2 for zoomed areas 2, 3, 4 and 5 respectively. These values are in accordance with the expected cone density for a healthy subject at the eccentricities observed [23].

3.3. 2-phase demodulation and FF-OCT image averaging

Typically, a 3- or 4-phase modulation/demodulation strategy makes it possible to eliminate incoherent terms and un-mix the amplitude and the phase information [8]. This strategy works fine for static samples, but it fails for *in-vivo* retinal imaging due to the continuous three-dimensional (3D) eye motion, which randomly modulates the phase. Therefore, we adopted a 2-phase modulation/demodulation strategy, where the residual tracking error directly modulates the signal. Although incoherent terms can still be suppressed, it is not possible to separate amplitude and phase, meaning that the FF-OCT signal presents spatial intensity fluctuations. This random fluctuation, along with shot noise, affects the image contrast (see an example for FF-OCT image - N=1 in Fig. 5(A)).
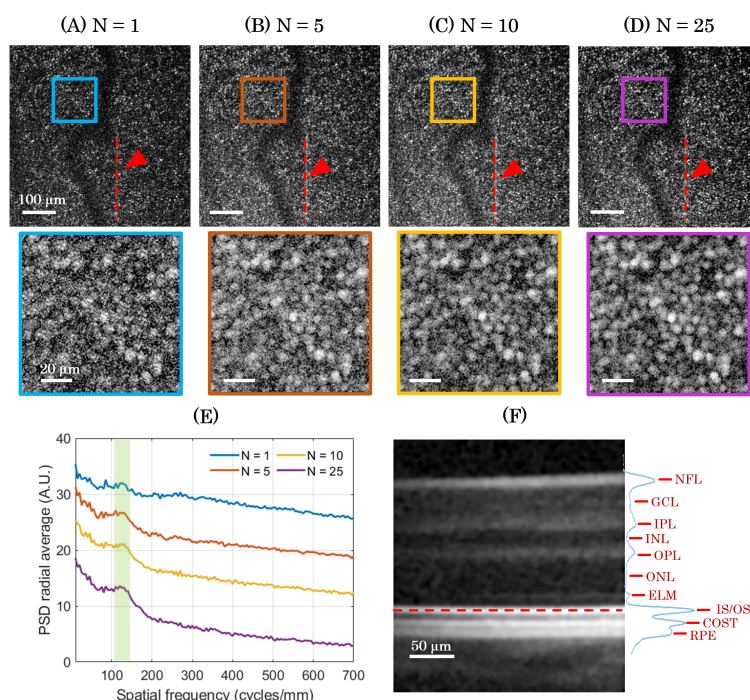
Fig. 5. Averaging registered FF-OCT images improves the clarity of photoreceptors. (A),(B),(C) and (D) show images of photoreceptor mosaic at 4° eccentricity for different amount of averaging (from N = 1, N = 5, N = 10 and N = 25 images). The red dashed line, highlighted by a red arrow, indicates where a simultaneous SD-OCT acquisition took place. The increase of image contrast is more visible in the zoomed areas. (E) Power spectral density radial average from each zoomed area. The green area indicates the photoreceptor mosaic spatial frequency, which is present for all the cases presented. (F) Tomographic retinal cross-section image obtained with the SD-OCT after averaging 10 consecutive B-scans. The red dashed line highlights the location where the FF-OCT images were simultaneously acquired, *i.e.* at the IS/OS junction. All averaged images were extracted from Visualization 5.

Since we adopt a random phase modulation, spatial intensity fluctuations vary from one FF-OCT image to another. Therefore, by averaging consecutive FF-OCT images, both phase and noise average out; the signal becomes proportional only to the amplitude, and its contrast is enhanced. This enhancement is highlighted in Fig. 5 for a different number of averaged images (N), where zoomed areas are also shown. Figure 5(E) introduces the computed PSD for each case. Note that for N=1, although the cone mosaic image does not present a sharp contrast, its PSD already indicates a Yellot's ring (green area highlights the cone mosaic spatial frequency), and cone density can be easily computed. The cone density of the zoomed area, localized at 4° eccentricity, was 18 300 cones/mm^2, which is in accordance with the expected cone density for a healthy subject at the eccentricity observed [23]. Although image averaging helps to visualize and resolve individual photoreceptors, the appearance of the cone mosaic seems different compared to AO-assisted ophthalmoscopes [3]. This might be explained by the fact that the reflection sites of the IS/OS junction and COST layer might not be exactly within the coherence gate [24].

3.4. Simultaneous FF-OCT and SD-OCT imaging of living human retina

Owing to the SD-OCT coupled in our custom-built FF-OCT system, we can access tomographic retinal cross-section images, from the SD-OCT, at the same time as high-resolution *en-face* images from the FF-OCT. Now with the axial motion correction, images from both modalities can be displayed consistently in real-time during the imaging session, helping to position the FF-OCT coherence gate at the retinal layer of interest before image acquisition. Visualization 5 shows one example, where the retinal image sequences from both modalities were recorded simultaneously. We purposely removed the shortpass filter used to block the SD-OCT light source at the FF-OCT camera to help to visualize the SD-OCT acquisition in parallel to the FF-OCT acquisition. The averaged *en-face* image generated by the FF-OCT is shown in Fig. 5(D), where the red dashed line, highlighted by the red arrow, indicates the location where the SD-OCT was acquired simultaneously. The averaged retinal cross-section generated by the SD-OCT is presented in Fig. 5(F). All retinal layers commonly resolved by an SD-OCT were identified and labeled according to [7]. The red dashed line indicates the retinal layer where the FF-OCT image was acquired, *i.e.* the IS/OS junction.

4. Discussion

One of the biggest challenges in applying the FF-OCT technique for living human retinal imaging is the presence of continuous involuntary head and eye axial motion during image acquisition. We showed in Sect. 3.1 that axial motion is mainly composed of slow drifts and fast oscillations. Even though *in-vivo* retinal imaging was possible under this condition [11], long and tedious imaging sessions would be necessary to increase the chances of acquiring enough data (the efficiency would be lower than 7%). Moreover, we saw in Sect. 3.3 that, even if photoreceptors could be visualized and resolved in a single frame (see Fig. 5(A)), image averaging is an important process to eliminate the spatial intensity fluctuation imposed by the random phase modulation of FF-OCT signal.

4.1. Using SD-OCT to guide FF-OCT in-vivo imaging

In this paper, we present a method to overcome this major limitation, based on the combination of an FF-OCT, an SD-OCT and a high-speed voice-coil translation stage. The SD-OCT is used to measure the retinal axial position and to drive the position of the voice-coil translation stage, where the FF-OCT reference arm is mounted. We showed that the proposed method was able to suppress slow drifts and strongly attenuate fast oscillations, increasing the FF-OCT image acquisition efficiency to almost a factor of 10, *i.e* 60% success. This efficiency was highlighted by Visualization 2, Visualization 4 and Visualization 5, where FF-OCT image sequences with axial motion correction were presented.

Another essential role of the SD-OCT is to guide the FF-OCT coherence gate positioning. Indeed, once the axial motion is stabilized, and since the initial position of the FF-OCT coherence gate in the sample arm is known (calibration step described in Sect. 2.2), one can manually position the FF-OCT coherence gate assisted by the SD-OCT retinal cross-sections displayed in real-time. In spite of choices of optical design to favor the FF-OCT system, sometimes to the detriment of the SD-OCT system, and the mechanical restrictions imposed by the SD-OCT commercial system, we showed in Fig. 5 and Visualization 5 that retinal cross-section images, with sufficient contrast to identify all retinal layers, can be generated simultaneously to FF-OCT, a crucial condition to guide FF-OCT image acquisition.

4.2. High cellular resolution in-vivo retinal imaging with FF-OCT

Throughout this paper, we demonstrated the ability of our FF-OCT imaging system to achieve high cellular resolution in the living human retina. There has been increased interest in the

past ten years in associating different retinal imaging modalities to achieve a cellular resolution in all three dimensions, with most groups combining AO-OCT and AO-SLO [25,26]. The main difference of our multimodal imaging system compared to previous works is the potential to achieve cellular resolution in all three dimensions without AO, significantly reducing the system complexity, size and cost. Figure 4 demonstrated the capacity of the FF-OCT to resolve *in-vivo* cone photoreceptors as close as 1.5^o from the foveal center without using any optical aberration compensation other than prescribed eyeglasses. Moreover, the presented FF-OCT has the capacity to generate *en-face* retinal images with an enhanced axial resolution compared to confocal AO-SLO, $8\mu m$ for the former against $40\mu m$ for the latter [13]. Some studies have demonstrated that, for healthy subjects with good eye optics, individual cone photoreceptors could be resolved within SD-OCT or confocal SLO images without optically correcting for ocular aberrations [14,27]. However, most of these studies used illumination/detection scanning techniques, which present an inherent low frame rate, limited FOV and high sensitivity to eye motion, the latter leading to intraframe distortion. All these drawbacks are minimized when using a full-field technique [3,28].

4.3.　Limitations

The presented FF-OCT/SD-OCT imaging system still faces some limitations. Firstly, to favor the FF-OCT system, the capacity of the SD-OCT imaging was diminished by not-conjugating the galvanometer scanners to the eye's pupil, affecting its signal level and increasing its sensitivity to the subject alignment. Secondly, even if FF-OCT presents a low sensitivity to low-order ocular aberrations in terms of resolution, the latter still affects the FF-OCT signal level [10]. Ocular aberrations and the variation of the subject pupil diameter might explain the fact that single-frame images obtained in Visualization 2 (when axial motion correction is activated) present a higher signal than Fig. 5(A). Finally, because ocular aberrations affect the SNR of the current FF-OCT, imaging other retinal layers, such as ganglion cells, possible with AO-OCT systems [29], becomes challenging. As discussed in [10], now that FF-OCT images can be acquired with high consistency, a compact implementation of AO could be used, consisting of a wavefront sensorless approach, and a multi-actuator adaptive lens [30] positioned just in front of the eye, like regular glasses (*i.e.* without strict conjugation). As ocular aberrations are dominated by low-order aberrations [4], we expect to significantly improve the FF-OCT SNR, and therefore hope to be able to image less reflective retinal layers.

4.4.　Towards dynamic FF-OCT in the living human eye

One interesting way to obtain a high image contrast using FF-OCT is by exploring temporal fluctuations of the backscattered light, revealing subcellular structures and transparent tissues [18,31]. So far, this technique, when applied to retinal imaging, has only been shown for *ex-vivo* retinal imaging. To be able to achieve dynamic *in-vivo* retinal imaging an axial motion correction better than the axial resolution of the FF-OCT system is necessary [32]. Our proposed method achieves this performance 60% of the time, and it might be sufficient. Otherwise, a higher performance would only be possible with a faster reaction of the voice-coil translation stage or with an SD-OCT with a higher acquisition rate (here we are limited to 36 000 A-scans per second).

5.　Conclusion

One of the biggest challenges of time-domain FF-OCT when applied for *in-vivo* human retinal imaging is the presence of continuous involuntary head and eye axial motion. We presented a method to optically compensate for axial motion in real-time for time-domain FF-OCT. This was possible by introducing an SD-OCT and a voice-coil translation stage in the system, the former to generate retinal cross-section images, where retinal axial motion could be measured,

and the latter to correct the FF-OCT reference arm position. The closed-loop optical stabilization reduced the RMS error by a factor of 7, significantly increasing the FF-OCT image acquisition efficiency. By these means, we demonstrated the capacity of the FF-OCT to resolve cone mosaic as close as 1.5^o from the fovea center with high consistency and repeatability, without the need for AO. The good precision and efficiency achieved in the FF-OCT system, by virtue of the real-time axial motion optical stabilization, together with its relative simplicity and low-cost compared to the other high-resolution techniques which use conventional AO, may pave the way towards the adoption of FF-OCT as a routine clinical imaging system.

Disclosures

The authors declare no conflicts of interest.

References

1. D. Huang, E. Swanson, C. Lin, J. Schuman, W. Stinson, W. Chang, M. Hee, T. Flotte, K. Gregory, C. Puliafito, and J. G. Fujimoto, "Optical coherence tomography," Science **254**(5035), 1178–1181 (1991).
2. W. Drexler and J. G. Fujimoto eds., *Optical Coherence Tomography: Technology and Applications* (Springer, 2015), 2nd ed.
3. E. Gofas-Salas, P. Mecê, C. Petit, J. Jarosz, L. M. Mugnier, A. M. Bonnefois, K. Grieve, J. Sahel, M. Paques, and S. Meimon, "High loop rate adaptive optics flood illumination ophthalmoscope with structured illumination capability," Appl. Opt. **57**(20), 5635–5642 (2018).
4. J. Jarosz, P. Mecê, J.-M. Conan, C. Petit, M. Paques, and S. Meimon, "High temporal resolution aberrometry in a 50-eye population and implications for adaptive optics error budget," Biomed. Opt. Express **8**(4), 2088–2105 (2017).
5. P. Mecê, E. Gofas-Salas, C. Petit, F. Cassaing, J. Sahel, M. Paques, K. Grieve, and S. Meimon, "Higher adaptive optics loop rate enhances axial resolution in nonconfocal ophthalmoscopes," Opt. Lett. **44**(9), 2208–2211 (2019).
6. R. S. Jonnal, O. P. Kocaoglu, R. J. Zawadzki, Z. Liu, D. T. Miller, and J. S. Werner, "A review of adaptive optics optical coherence tomography: technical advances, scientific applications, and the future," Invest. Ophthalmol. Visual Sci. **57**(9), OCT51–OCT68 (2016).
7. M. Pircher and R. J. Zawadzki, "Review of adaptive optics oct (AO-OCT): principles and applications for retinal imaging," Biomed. Opt. Express **8**(5), 2536–2562 (2017).
8. A. Dubois, K. Grieve, G. Moneron, R. Lecaque, L. Vabre, and C. Boccara, "Ultrahigh-resolution full-field optical coherence tomography," Appl. Opt. **43**(14), 2874–2883 (2004).
9. O. Thouvenin, K. Grieve, P. Xiao, C. Apelian, and A. C. Boccara, "En face coherence microscopy," Biomed. Opt. Express **8**(2), 622–639 (2017).
10. P. Mecê, P. Xiao, V. Mazlin, J. Scholler, K. Grieve, J.-A. Sahel, M. Fink, and C. Boccara, "Towards lens-based wavefront sensorless adaptive optics full-field oct for in-vivo retinal imaging (conference presentation)," in *Optical Coherence Tomography and Coherence Domain Optical Methods in Biomedicine XXIII*, vol. 10867 (International Society for Optics and Photonics, 2019), p. 1086722.
11. P. Xiao, V. Mazlin, K. Grieve, J.-A. Sahel, M. Fink, and A. C. Boccara, "In vivo high-resolution human retinal imaging with wavefront-correctionless full-field oct," Optica **5**(4), 409–412 (2018).
12. L. Ginner, A. Kumar, D. Fechtig, L. M. Wurster, M. Salas, M. Pircher, and R. A. Leitgeb, "Noniterative digital aberration correction for cellular resolution retinal optical coherence tomography in vivo," Optica **4**(8), 924–931 (2017).
13. D. T. Miller, J. Qu, R. S. Jonnal, and K. E. Thorn, "Coherence gating and adaptive optics in the eye," in *Coherence Domain Optical Methods and Optical Coherence Tomography in Biomedicine VII*, vol. 4956 (International Society for Optics and Photonics, 2003), pp. 65–72.
14. M. Pircher, E. Götzinger, H. Sattmann, R. A. Leitgeb, and C. K. Hitzenberger, "In vivo investigation of human cone photoreceptors with slo/oct in combination with 3d motion correction on a cellular level," Opt. Express **18**(13), 13935–13944 (2010).
15. P. Mecê, J. Jarosz, J.-M. Conan, C. Petit, K. Grieve, M. Paques, and S. Meimon, "Fixational eye movement: a negligible source of dynamic aberration," Biomed. Opt. Express **9**(2), 717–727 (2018).

16. E. Auksorius and A. C. Boccara, "Dark-field full-field optical coherence tomography," Opt. Lett. **40**(14), 3272–3275 (2015).

17. J. Scholler, "FFOCT control and acquisition software," (2019). https://doi.org/10.5281/zenodo.3137245.

18. J. Scholler, V. Mazlin, O. Thouvenin, K. Groux, P. Xiao, J.-A. Sahel, M. Fink, C. Boccara, and K. Grieve, "Probing dynamic processes in the eye at multiple spatial and temporal scales with multimodal full field oct," Biomed. Opt. Express **10**(2), 731–746 (2019).

19. F. Roddier, *Adaptive Optics in Astronomy* (Cambridge University Press, 1999).

20. S. Meimon, C. Petit, T. Fusco, and C. Kulcsar, "Tip–tilt disturbance model identification for kalman-based control scheme: application to xao and elt systems," J. Opt. Soc. Am. A **27**(11), A122–A132 (2010).

21. S. Duke-Elder, "The anatomy of the visual system," A System of Ophthalmology **2**, 363–382 (1961).

22. R. F. Cooper, C. S. Langlo, A. Dubra, and J. Carroll, "Automatic detection of modal spacing (yellott's ring) in adaptive optics scanning light ophthalmoscope images," Ophthalmic Physiol. Opt. **33**(4), 540–549 (2013).

23. L. Sawides, A. de Castro, and S. A. Burns, "The organization of the cone photoreceptor mosaic measured in the living human retina," Vision Res. **132**, 34–44 (2017).

24. M. Pircher, B. Baumann, E. Götzinger, H. Sattmann, and C. K. Hitzenberger, "Simultaneous slo/oct imaging of the human retina with axial eye motion correction," Opt. Express **15**(25), 16922–16932 (2007).

25. R. J. Zawadzki, S. M. Jones, S. Pilli, S. Balderas-Mata, D. Y. Kim, S. S. Olivier, and J. S. Werner, "Integrated adaptive optics optical coherence tomography and adaptive optics scanning laser ophthalmoscope system for simultaneous cellular resolution in vivo retinal imaging," Biomed. Opt. Express **2**(6), 1674–1686 (2011).

26. Z. Liu, J. Tam, O. Saeedi, and D. X. Hammer, "Trans-retinal cellular imaging with multimodal adaptive optics," Biomed. Opt. Express **9**(9), 4246–4262 (2018).

27. N. D. Shemonski, F. A. South, Y.-Z. Liu, S. G. Adie, P. S. Carney, and S. A. Boppart, "Computational high-resolution optical imaging of the living human retina," Nat. Photonics **9**(7), 440–443 (2015).

28. P. Bedggood and A. Metha, "De-warping of images and improved eye tracking for the scanning laser ophthalmoscope," PLoS One **12**(4), e0174617 (2017).

29. Z. Liu, K. Kurokawa, F. Zhang, J. J. Lee, and D. T. Miller, "Imaging and quantifying ganglion cells and other transparent neurons in the living human retina," Proc. Natl. Acad. Sci. **114**(48), 12803–12808 (2017).

30. S. Bonora, Y. Jian, P. Zhang, A. Zam, E. N. Pugh, R. J. Zawadzki, and M. V. Sarunic, "Wavefront correction and high-resolution in vivo oct imaging with an objective integrated multi-actuator adaptive lens," Opt. Express **23**(17), 21931–21941 (2015).

31. C. Apelian, F. Harms, O. Thouvenin, and A. C. Boccara, "Dynamic full field optical coherence tomography: subcellular metabolic contrast revealed in tissues by interferometric signals temporal analysis," Biomed. Opt. Express **7**(4), 1511–1524 (2016).

32. J. Scholler, "Motion artifact removal and signal enhancement to achieve in vivo dynamic full field OCT," Opt. Express **27**(14), 19562–19572 (2019).

4.2 Article: Coherence gate shaping for wide field high-resolution in vivo retinal imaging with full-field OCT

As mentioned in the previous section, band shaped signals limiting the FOV were observed for most of the subjects. This issue arises because the FFOCT system arms are not optically symmetric for eye imaging. In microscopy, we are using the same microscope objectives in both arms, thus limiting the asymmetry to the manufacturing tolerances. For eye imaging however, a microscope objective is used in the reference arm and the symmetry is therefore broken even if we use an objective with similar focal length and numerical aperture as the average human eye. In the Letter below, we experimentally demonstrate that when this symmetry is broken the coherence gate is no longer a plane but is rather curved, leading to a mismatch with the retinal curvature, and consequently limiting the useful FOV. To counteract this asymmetry and recover a quasi-symmetry we proposed an optical shaping of the coherence gate enabling single-shot, high-resolution, large FOV images ($1mm \times 1mm$) of the photoreceptor mosaic as close as $0.5°$ from the foveal center. With this improvement we show that we are able to compute important photoreceptor-based bio-markers by using the HSV method presented appendix B and that spatio-temporal monitoring of individual photoreceptors can be achieved [Mecê et al., 2020a].

Coherence gate shaping for wide field high-resolution in vivo retinal imaging with full-field OCT

PEDRO MECÊ,[1,*] **KASSANDRA GROUX,**[1] **JULES SCHOLLER,**[1] **OLIVIER THOUVENIN,**[1] **MATHIAS FINK,**[1] **KATE GRIEVE,**[2,3] **AND CLAUDE BOCCARA**[1]

[1]*Institut Langevin, ESPCI Paris, CNRS, PSL University, 1 rue Jussieu, 75005 Paris, France*
[2]*Institut de la Vision, Sorbonne Université, INSERM, CNRS, F-75012, Paris, France*
[3]*Quinze-Vingts National Eye Hospital, 28 Rue de Charenton, Paris, 75012, France*
*pedro.mece@espci.fr

Abstract: Allying high-resolution with a large field-of-view (FOV) is of great importance in the fields of biology and medicine, but it is particularly challenging when imaging non-flat living samples such as the human retina. Indeed, high-resolution is normally achieved with adaptive optics (AO) and scanning methods, which considerably reduce the useful FOV and increase the system complexity. An alternative technique is time-domain full-field optical coherence tomography (FF-OCT), which has already shown its potential for *in-vivo* high-resolution retinal imaging. Here, we introduce coherence gate shaping for FF-OCT, to optically shape the coherence gate geometry to match the sample curvature, thus achieving a larger FOV than previously possible. Using this instrument, we obtained high-resolution images of living human photoreceptors close to the foveal center without AO and with a $1\,mm \times 1\,mm$ FOV in a single shot. This novel advance enables the extraction of photoreceptor-based biomarkers with ease and spatiotemporal monitoring of individual photoreceptors. We compare our findings with AO-assisted ophthalmoscopes, highlighting the potential of FF-OCT, as a compact system, to become a routine clinical imaging technique.

1. Introduction

Owing to the optical properties of the eye, the retina is the only part of the central nervous system that can be visualized non-invasively *in-vivo* with micrometer resolution, a crucial aspect for studying neuronal activity [1,2]. Due to their capacity to correct for static and dynamic ocular aberrations [3,4], AO ophthalmoscopes have become the primary technique to image individual retinal neurons such as cone and rod photoreceptors in the living human retina [5–8]. Imaging individual retinal neurons *in-vivo* with AO ophthalmoscopes has enabled new insights into retinal function [2] and a better understanding of progression of retinal diseases such as age-related macular degeneration [9]. However, AO systems require quite complex, expensive and cumbersome hardware, limiting their clinical and commercial deployment [10,11]. Moreover, the eye's isoplanatic patch (around 0.6 mm) limits the useful field-of-view (FOV) where high-resolution retinal imaging can be achieved when using AO [12]. Although multi-conjugate AO was demonstrated in order to achieve a larger useful FOV, increasing the eye's isoplanatic patch, this solution adds complexity, as two deformable mirrors are necessary [13]. Thus, achieving cellular resolution in a large portion of the living human retina without using AO is of great interest.

Recent studies have achieved high-resolution retinal imaging without using AO by implementing computational ocular aberration correction [11,14–17]. Although promising, these approaches only presented results in far foveal eccentricities (3° or more), where photoreceptors are most

easily resolved. Moreover, they require heavy post-processing steps hence providing limited feedback during imaging sessions, and, in some cases, expensive hardware was also necessary (*e.g.* a very fast camera and/or swept source laser). The use of a super-resolution optical-reassignment technique was also proposed as a tool to achieve cellular resolution in in-vivo retina without AO [18]. Nevertheless, a scanning illumination/detection is used, presenting an inherently low frame rate, limited FOV (lower than 0.3 *mm* × 0.3 *mm*) and high sensitivity to fixational eye motion [19] leading to intraframe distortion.

An alternative modality to achieve high-cellular resolution without using AO is FF-OCT, which uses a spatially incoherent light source, a high-speed megapixel camera and time-domain phase modulation to acquire *en-face* sections of the sample at a given depth [20]. One attractive point of this technique for retinal imaging is the fact that the optical resolution of FF-OCT has a weak sensitivity to predominant ocular aberrations (*i.e.* defocus and astigmatism) [21–23]. This interesting feature was recently highlighted in [24], where *in-vivo* human cone mosaic at eccentricities close to the fovea was resolved. Although FF-OCT's FOV is theoretically only limited by the spatial sampling of the imaging camera, retinal curvature causes current images to have a limited useful FOV of about 0.4 *mm* × 0.4 *mm* [24,25].

Typically, FF-OCT uses a Linnik interferometer, where identical microscope objectives are placed in both reference and sample arms in a symmetric optical path configuration. When applied to retinal imaging, the FF-OCT symmetry is broken, as the sample arm no longer contains a microscope objective (Fig. 2), but rather contains the anterior segment optics of the human eye. Here, we theoretically and experimentally demonstrate that when the symmetry is broken a curved coherence gate is generated, provoking a mismatch with the retinal curvature, and consequently limiting the useful FOV. The useful FOV can be defined as the FOV over which a structure from a given depth of the sample can be visualized. We present novel advances in FF-OCT allowing for optical shaping of the geometry of the coherence gate, adapting it to the retinal geometry, enabling the generation of single-shot, high-resolution, wide FOV images (1 *mm* × 1 *mm*) of the photoreceptor mosaic as close as 1° from the foveal center. The 1 *mm* × 1 *mm* useful FOV is 6.25 times larger in this new configuration compared to our previous results [24]. Then, we show that useful tools to diagnose retinal disorders at the early stage such as photoreceptor-based biomarkers and spatiotemporal monitoring of individual photoreceptors can be achieved without the need for AO.

2. Methods

2.1. Theory

The optical path length (OPL) when light propagates in a material x of thickness e_x, refractive index n_x for a given angle θ_x can be expressed as:

$$OPL(\lambda) = \sum_{x=1}^{N} n_x(\lambda) \frac{e_x}{cos\theta_x}. \tag{1}$$

Where $n_x(\lambda)$ is given by the Sellmeier equation [26]. The incidence angle in a material x, θ_x, can be expressed as a function of the incidence angle in air θ_1, as follows:

$$\theta_x = sin^{-1}\left(\frac{sin\theta_1}{n_x(\lambda)}\right). \tag{2}$$

Through Eqs. (1) and (2), one can notice the dependency of the OPL on the wavelength (λ) and the incidence angle in air (θ_1):

$$OPL(\lambda, \theta_1) = \sum_{x=1}^{N} n_x(\lambda) \frac{e_x}{cos\left(sin^{-1}\left(\frac{sin\theta_1}{n_x(\lambda)}\right)\right)}. \tag{3}$$

The depth position of the *en-face* image generated by the FF-OCT, *i.e.* the coherence gate, is given by the the optical path difference (OPD) between the reference and sample arms:

$$OPD(\lambda, \theta_1) = OPL_{reference}(\lambda, \theta_1) - OPL_{sample}(\lambda, \theta_1). \tag{4}$$

If the OPL of both arms is symmetric, as is the case when a microscope objective is placed in each arm, the OPD is null for all values of θ_1, *i.e.* in the FOV. On the other hand, an asymmetry between the reference and sample OPLs creates a dependency on the the wavelength (λ) and the incident angle in the air (θ_1). In this case, OPD would only be null for a given incident angle, and it would increase as this angle is increased. This is the origin of the curvature of the coherence gate.

To shape the coherence gate geometry, we propose the use of optical windows. To better understand how optical windows can shape the coherence gate geometry, we can consider a typical FF-OCT set-up composed of identical microscopic objectives positioned in each arm, with an optical window of thickness e_b and refractive index n_b positioned in the sample arm (Fig. 1). For simplicity, we assume that both arms are illuminated with monochromatic light.
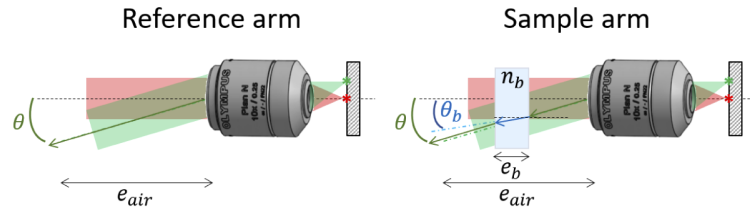
Fig. 1. Schematic of the reference and sample arms introducing notations for the OPD model.

Their respective OPLs will be given as follows (only considering the path between the microscope objective and the beam splitter):

$$OPL_{ref}(\theta) = \frac{e_{air}}{cos(\theta)} \tag{5}$$

$$OPL_{sample}(\theta) = \frac{e_{air} - e_b}{cos(\theta)} + \frac{e_b n_b}{cos(\theta_b(\theta))} \tag{6}$$

where θ_b is given as a function of the incident angle in the air θ according to Eq. (2). In this case, the OPD would be:

$$OPD(\theta) = e_b \left(\frac{n_b}{cos(\theta_b(\theta))} - \frac{1}{cos(\theta)} \right). \tag{7}$$

To image at a depth of interest of the sample, one has to move the reference arm. We can move the reference arm in order to match both OPLs for a given angle, for example at a central point in the FOV, i.e. $\theta = 0$, which gives:

$$OPD(0) = e_b(n_b - 1). \tag{8}$$

Now, the OPD for all the other angles θ will be given by:

$$OPD(\theta) = e_b \left(\frac{n_b}{cos(\theta_b(\theta))} - \frac{1}{cos(\theta)} \right) - e_b(n_b - 1) \tag{9}$$

which can be simplified as follows:

$$OPD(\theta) = e_b \left(n_b \frac{1 - cos(\theta_b(\theta))}{cos(\theta_b(\theta))} - \frac{1 - cos(\theta)}{cos(\theta)} \right). \tag{10}$$

Note that the introduction of an optical window induces a variation of the OPD as a function of the FOV, generating a curved coherence gate.

2.2. Experimental setup

To investigate the impact of the asymmetric Linnik interferometer configuration on coherence gate curvature, three samples were imaged: 1) a standard USAF resolution target; 2) an OEMI-7 model eye (Ocular Instruments, Inc) which takes into account the eye geometry, optical power and dispersion properties (henceforth, named model eye); and 3) *in-vivo* human retina. Figure 2 presents the schematic of the custom-built FF-OCT system coupled through a dichroic mirror with a Thorlabs Ganymede-II SD-OCT system. The FF-OCT comprises a light-emitting diode (LED) with $\lambda = 850$ nm center wavelength and 30 nm bandwidth (M850L3, Thorlabs), used as a spatially incoherent illumination source, giving a theoretical axial resolution of approximately 8 μm in water. The LED is focused by a condenser lens 20 *mm* in front of the eye's pupil. A physical diaphragm is positioned in front of the LED, conjugate to the retina and the FF-OCT reference mirror. The illumination beam is split into reference and sample arms by a 50:50 cubic beam splitter (BS). For the reference arm, an Olympus 10X/0.25 NA Plan Achromat objective is used with a silicon mirror placed at the focal plane of the objective. The whole reference arm (microscope objective and silicon mirror) is mounted on a fast voice-coil translation stage (X-DMQ12P-DE52, Zaber Technologies Inc.), enabling adjustment of the coherence gate position. For the sample arm, two configurations were used. In the case of the USAF target imaging, a microscope objective, identical to the one used in the reference arm, is used leading to a symmetric Linnik configuration (not shown in Fig. 2). In the case of the model eye and *in-vivo* retinal imaging, both were aligned along the optical axis, without the use of a microscope objective, leading to an asymmetric Linnik configuration (shown in Fig. 2). The FF-OCT light beam arrives with an 8 mm diameter in the eye's pupil. The back-scattered photons from both arms are recombined by the same BS and focused onto a high-speed (up to 720 Hz at 1440×1440 pixel) CMOS camera (Q-2A750-Hm/CXP-6, Adimec) for FF-OCT imaging. The FF-OCT system aperture was limited by the eye's pupil. In the case of *in-vivo* retinal imaging, the SD-OCT and the voice-coil translation stage were used to measure and correct for involuntary axial eye movements during the imaging acquisition in a closed-loop fashion [24]. The SD-OCT light beam was filtered out from the FF-OCT reference and detection arms by using a short-pass filter (FESH0850 25mm aperture, Thorlabs).
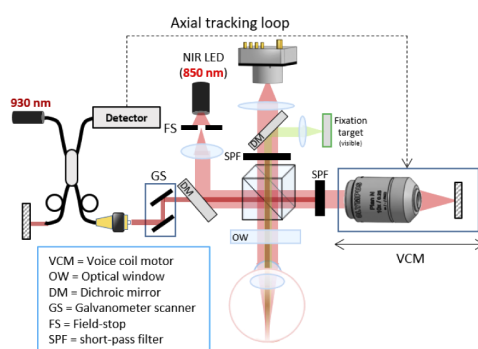
Fig. 2. Schematic drawing of the custom-built FF-OCT system coupled with an SD-OCT for real-time axial motion correction and FF-OCT coherence gate positioning guidance. In the case of the USAF target imaging, a microscope objective, identical to the one used in the reference arm, is used leading to a symmetric Linnik configuration (not shown in the schematic). In the case of the model eye and *in-vivo* retinal imaging, no microscope objective is placed in the sample arm, leading to an asymmetric Linnik configuration (shown in the schematic).

2.3. Image acquisition

In the case of the USAF target and the model eye imaging, a total of 200 images from different depths were acquired at 10 Hz, by moving the voice-coil translation stage of the reference arm at a constant speed of 5 μm/s. This procedure allowed us to acquire *en-face* images from different depths, forming Z-stacks. This procedure was repeated after adding optical windows of N-BK7 of different thicknesses in the reference or sample arms in order to change the geometry of the coherence gate.

In the case of in vivo retinal imaging, the image acquisition was performed on two healthy subjects S1 and S2 aged 25 and 30 respectively. S1 presents a refractive error of $1.5D \times 0.5D \times 160^o$ (spherical $\times$ cylindrical $\times$ axis of cylindrical errors), S2 does not wear prescribed eyeglasses and had had LASIK refractive surgery several years ago. Research procedures followed the tenets of the Declaration of Helsinki. Informed consent was obtained from subjects after the nature and possible outcomes of the study were explained. The study was authorized by the appropriate ethics review boards (CPP and ANSM (IDRCB number: 2019-A00942-55)). Subjects were seated in front of the system and stabilized with a chin and forehead rest and asked to fixate a target placed at an infinite focal conjugate. During the imaging session, the subject S1 was wearing her prescription glasses to increase the signal level of FF-OCT [23]. Image acquisition was realized in a dark room, maximizing the pupil dilation. Phase modulation was performed by the residual axial motion after optical stabilization [24]. Image sequences were composed of 150 frames acquired at 300 Hz using custom-built software. The FF-OCT camera worked close to saturation to use the whole full well capacity, decreasing relative importance of shot noise [27]. During image acquisition, the total power entering the eye from the FF-OCT illumination source and the SD-OCT scanning source were respectively 1.3 mW (for the 0.5 s of image acquisition) and 0.25 mW (continuous scanning), which are below the ocular safety limits established by the ISO standards for group 1 devices.

2.4. Image processing

In the case of the USAF target and the model eye imaging, each Z-stack was digitally converted into axial sections, *i.e.* a cross-sectional view of the sample. This step was possible by taking into account only the pixels of a central row of each image. Next, image segmentation was applied using an intensity-based thresholding algorithm and a least square parabola fitting algorithm, enabling measurement of the degree of curvature of converted cross-sections.

For *in-vivo* retinal imaging, each image was normalized by dividing itself by its mean value. Since the phase was randomly modulated by the residual tracking error, and to eliminate the incoherent terms, we adopted a 2-phase demodulation [24]. The 2-phase demodulation consists of subtracting one image I_N from the next I_{N+1} and taking the absolute value. Next, images with a very low or absent useful signal, mainly due to an insufficient phase shift between consecutive images, were automatically detected using an intensity-based threshold algorithm, and then excluded from the image sequence. Finally, useful images were registered using a custom-built normalized cross-correlation algorithm, where the image presenting the highest signal level was chosen as the reference. Retinal images of subject S1 were also acquired using the rtx-1 adaptive optics flood-illumination ophthalmoscope (AO-FIO - Imagine Eyes, France) and the MAORI confocal adaptive optics scanning-laser ophthalmoscope (AO-SLO - Physical Sciences, Inc, Andover, MA, USA). Retinal fundus images of both subjects were also acquired with Spectralis scanning-laser ophtalmoscope (SLO) (Heidelberg Engineering, Germany). All images were acquired in the same conditions as previously described, *i.e.* in a dark room, maximizing the pupil dilation and with subject S1 wearing her prescribed eyeglasses. To generate a pointwise density map, we divided the cone mosaic image into an overlapping grid of 300 $\times$ 300 pixels (corresponding to 200 $\mu m \times$ 200 μm) regions of interest (ROIs), where each ROI was displaced from the previous by 30 pixels (corresponding to 20μm). These values were chosen empirically

to provide a good trade-off between pointwise accuracy and map smoothness. Then, cone density and spacing were computed for each ROI using a fully automated algorithm based on modal spacing as described in [28]. Bicubic image interpolation was used to increase the size of the cone density map in order to match the cone mosaic image.

3. Results

3.1. Optical shaping of the coherence gate geometry

Figure 3 shows how the coherence gate geometry can be optically shaped by adding optical windows in one of the interferometer arms. When imaging the USAF target (Fig. 3(a)) in a symmetric configuration the cross-section looks completely flat. The addition of an optical window in one of the arms breaks this symmetry, consequently, the flat sample presents an apparent curved cross-section. This apparent curvature happens because of a non-constant optical path difference along the FOV, generating a curved coherence gate.
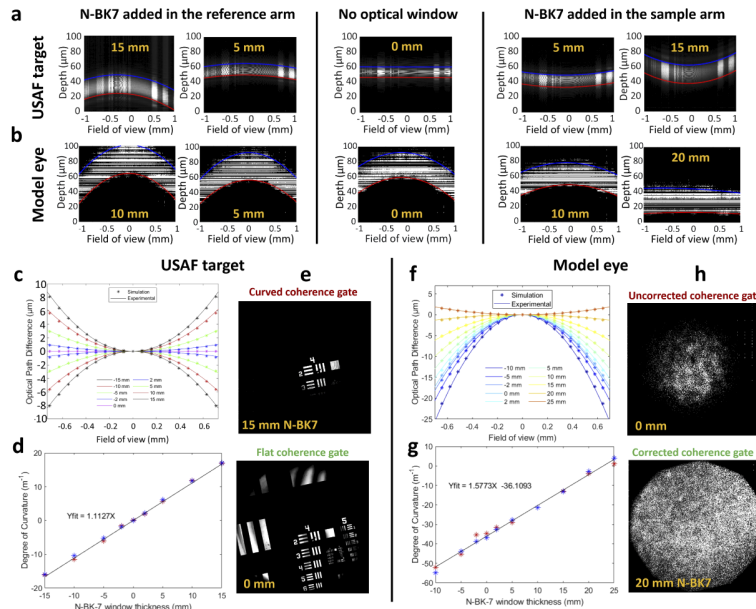
Fig. 3. a-b, Cross-sections after introducing N-BK7 optical windows with various thicknesses (in yellow) in the reference or sample arms when imaging, respectively, the USAF target and the model eye. **c,d,f,g,** Measured and theoretical optical path differences as a function of the FOV for different optical window thicknesses, as well as their respective degree of curvature, for respectively the USAF target and the model eye. When the optical window was introduced in the reference arm, the N-BK7 optical window thickness was represented in negative value. **e,h,** The effect of the coherence gate geometry over the FF-OCT useful FOV.

Figure 3(c) presents the measured and the theoretical (see Sect. 2.1) OPDs as a function of the FOV. Depending on which arm the optical window is introduced in, the coherence gate curvature can present a concave or a convex shape. One can notice that the curvature increases as a function of the thickness of the optical window introduced in one of the arms (Fig. 3(d)). The induced curvature of the coherence gate directly impacts the useful FOV of an FF-OCT system, since it acquires *en-face* curved sections of a flat sample at a given depth (Fig. 3(e)).

The same experiment can be done now using the model eye, which presents similar geometry and dispersion of the eye, in an asymmetric configuration (Fig. 3(b)). In this case, already when no optical window is introduced, the coherence gate presents a significant curvature. Figures 3(f,g) give the measured and theoretical curvature as a function of the FOV and the optical window thickness. The introduction of an 20 mm thick N-BK7 optical window in the sample arm enables compensation for the initial apparent curvature, increasing the useful FOV (Fig. 3(h)). Visualization 1, Visualization 2, Visualization 3, and Visualization 4 show acquired Z-stacks for curved and flat coherence gate when imaging the USAF target and the model eye.

3.2. Living human retinal cone mosaic imaging

Figures 4(a,b) presents *in-vivo* retinal images from the inner/outer segment junction (IS/OS) of subject S1 before and after compensation of the coherence gate curvature respectively. The yellow square in the retinal fundus image (Fig. 4(c)) indicates the location of acquired images, *i.e.* as close as 1° from the foveal center. According to Fig. 3(g), by adding an N-BK7 optical window with 20mm thickness, the coherence gate curvature would be strongly minimized. With this configuration, we obtained a high-resolution foveal cone mosaic imaging with a useful FOV of 1 $mm \times 1$ mm, larger than the previous FOV (0.4 $mm \times 0.4$ mm) [24] by a factor of 6.25, only correcting ocular aberrations with prescribed eyeglasses. Zoomed areas and their respective power spectral densities (PSD) are also presented. All PSDs presented Yellot's ring, the spectral signature of the photoreceptor mosaic image [29].
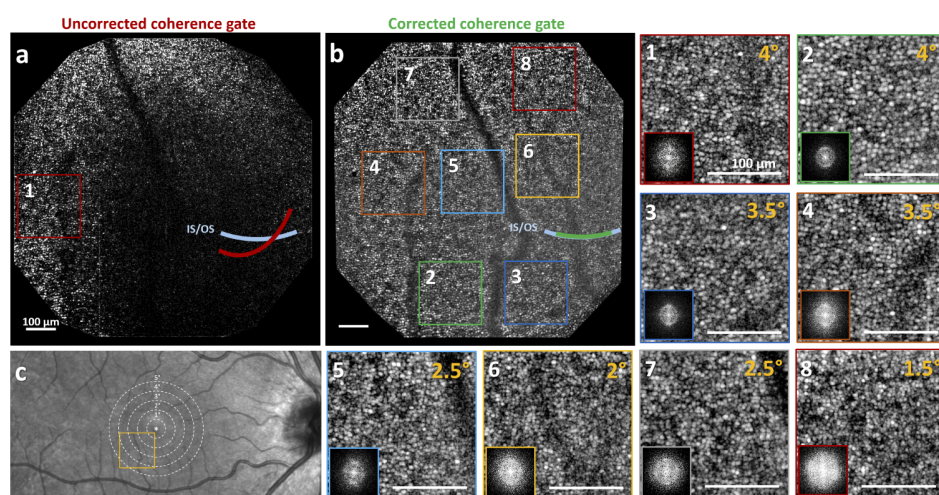
Fig. 4. Foveal cone mosaic images of subject S1 as close as 1° from the foveal center (yellow square of the retinal fundus image). **a,b,** Respectively, acquired images from the IS/OS junction before and after correcting for the coherence gate curvature. Zoomed areas, and their respective eccentricity (in yellow) and PSD are also presented. All PSDs present the Yellot's ring [29]. Scale bar, 100μm.

Figure 5 presents cone mosaic images obtained for subject S2 at 3° eccentricity temporal to the fovea after correcting the coherence gate curvature. Cone photoreceptors can also be resolved in the whole 1 $mm \times 1$ mm FOV. Note that the same 20 mm thick N-BK7 optical window used for S1 is also suitable to correct the coherence gate curvature for S2.
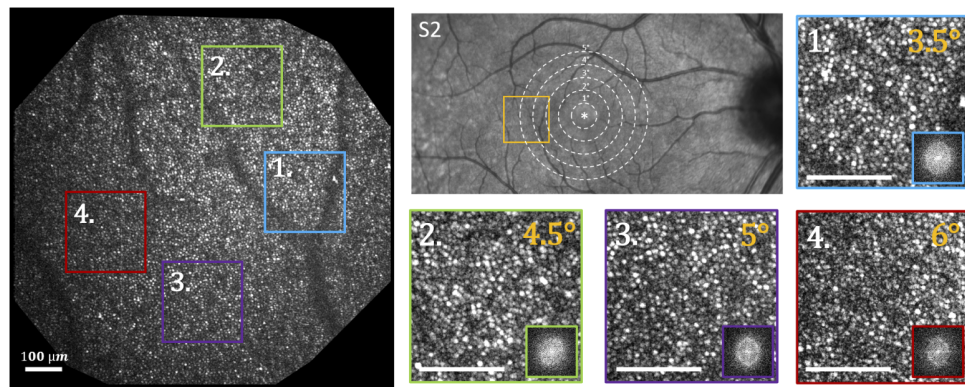
Fig. 5. Foveal cone images of subject S2 after correcting the coherence gate curvature. Zoomed areas, and their respective eccentricity (in yellow) and PSD are also presented. Scale bar, $100\mu m$.

3.3. Photoreceptor-based biomarkers and 4D monitoring of individual photoreceptors

The compensation of the coherence gate curvature enables the visualization of photoreceptors in the whole FOV. Consequently, we can obtain important information on photoreceptor-based biomarkers such as distribution, density, and spacing within a few seconds in a single-shot (no image montaging is necessary) with ease (Fig. 6). All measurements are consistent with histology and AO-assisted cone density measurement [30,31].
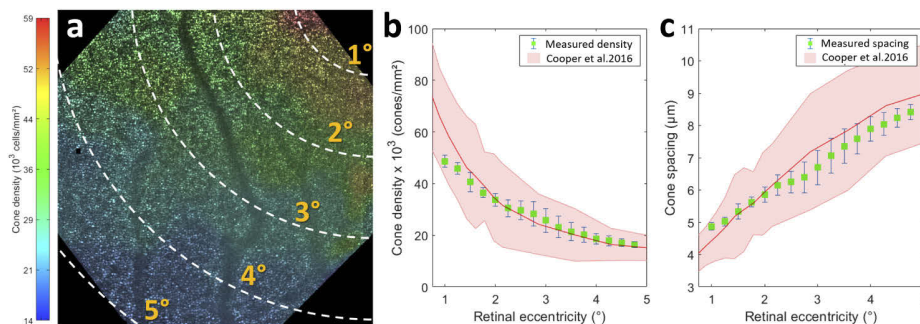
Fig. 6. a, Cone density distribution color coded for the image acquired from subject S1. **b-c,** Respectively, mean (green squares) and standard deviation (blue lines) of the measured cone density and spacing as a function of the retinal eccentricity. The red line is the mean computed density and the shaded region is 95% prediction interval obtained from a dataset of a 20-eye healthy population using an AO scanning-laser ophthalmoscope [31].

Minimizing the effect of the coherence gate curvature also helps to increase the repeatability of the imaging, allowing for spatiotemporal monitoring of individual photoreceptors. Visualization 5 presents four image sequences acquired in the same region with a 10 *min* interval between acquisitions. Note in zoomed areas that individual photoreceptors can be tracked frame-by-frame (3 *ms* interval) and video-by-video (10 *min* interval). Green boxes highlight cones that are visible in all four videos, while yellow boxes highlight those visible for only some of the videos, which might indicate a long-term change of reflectivity [32]. Red hexagons highlight the typical pattern found in cone mosaic close to the fovea [30]. Figure 7(a-d) presents the averaged image obtained from zoomed areas of Visualization 5. Figures 7(e-h) and Visualization 6 and

Visualization 7 show a cone-to-cone comparison of FF-OCT image with images generated by two AO ophthalmoscope modalities for subject S1 at same location. FF-OCT allows visualization of most, if not all, photoreceptors identified in AO-assisted images. Note in Fig. 7(i) that PSDs from all FF-OCT images present a clear and well-defined cone mosaic spatial frequency (vertical pale red bar) at 120 cycles/mm, as is the case for both AO-assisted imaging modalities. On the other hand, when using a scanning laser ophthalmoscope without closing the AO-loop, an erroneous spatial frequency is measured, leading to an error in cone density computation.
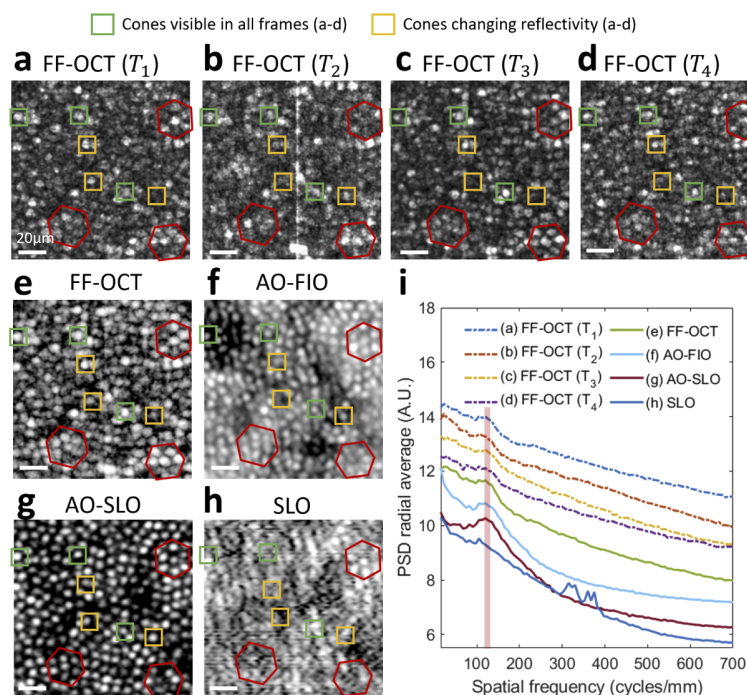
Fig. 7. a-d, Cone mosaic images acquired at the same region (4.5^o eccentricity) for different time points $T_{1,2,3,4}$, with 10 minutes interval between acquisitions, for subject S1, highlighting the capacity of FF-OCT with coherence gate shaping to track individual cones in space and time. Green boxes: cones visible for all four acquisitions. Yellow boxes: cones changing reflectivity. Red hexagons: pattern found in cone mosaic close to the fovea [30]. **e,** Cone mosaic image obtained after averaging images from **a-d**. **f-h,** Cone mosaic image at the same region acquired using AO-ophthalmoscopes. **f,** FIO: Flood-illumination ophthalmoscope. **g,** SLO: confocal scanning-laser ophthalmoscope. **h,** Acquisition made without closing the AO-loop. **i,** PSD radial average for images **a-h**, where the vertical pale red bar outlines the expected cone mosaic spatial frequency. PSDs were vertically displaced for better visualization. Scale bar, 20 μm.

4. Discussion

In this paper, we saw that the Linnik symmetry plays an important role in obtaining a flat coherence gate. Although this symmetry is broken in the case of retinal imaging, inducing an intrinsically curved coherence gate, we showed that the coherence gate geometry can be corrected by introducing a simple optical element such as an optical window into one of the interferometer arms. We used this technique to compensate the intrinsic curved coherence gate in the asymmetric configuration of FF-OCT for retinal imaging, obtaining an useful FOV of

1 *mm* × 1 *mm*, limited only by the size and the spatial sampling of the imaging camera. To the best of our knowledge, this is the first OCT system allying a FOV as large as 1 *mm* × 1 *mm*, high spatial resolution in all three dimensions and high acquisition rate of a given retinal plane (up to 300 Hz), without using any optical or digital aberration compensation other than prescribed eyeglasses, considerably simplifying the hardware and software complexity. The coherence gate curvature was previously reported for scanning-like OCT, mainly linked to the scanning-induced path length variation in non telecentric optical systems [33]. Therefore, the described method to optically shape the coherence gate can also be applied in OCT and Optical Coherence Microscopy imaging techniques to avoid curvature artefacts and to compensate for optical components that are only positioned in one of the arms, inducing an asymmetry.

Another expected effect brought by the asymmetry of the Linnik interferometry is dispersion, affecting the axial resolution of the FF-OCT (*i.e.* axial sectioning capacity). This phenomenon can be noted in cross-sections of Figs. 3(a,b) as an increase of the coherence gate thickness (distance between the blue and red curves). Figure 8 shows the FWHM of the coherence gate thickness (FF-OCT axial resolution) as a function of the optical window thickness in the case of the USAF target imaging (in red) and the model eye imaging (in blue). Note that for the USAF target imaging, a flat coherence gate coincides with the best axial sectioning capability, both happening when no optical window is added (symmetric configuration). In the case of the model eye imaging, not surprisingly, the optimum correction of dispersion does not coincide with the optimum correction of coherence gate curvature, since these two phenomena have different physical origins.
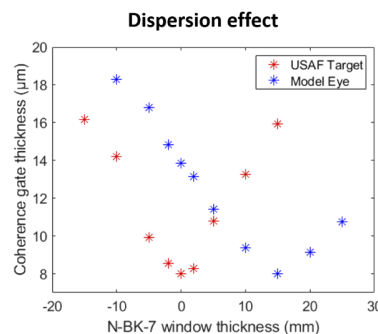
Fig. 8. Experimental data from Fig. 3 showing how dispersion evolves for different thicknesses of optical windows. The FWHM of the coherence gate thickness (FF-OCT axial resolution) as a function of the optical window thickness in the case of the USAF target (red points) and model eye (blue points) imaging respectively.

An optimum compensation of the coherence gate curvature would be possible with a 22 mm N-BK7 optical window (Fig. 3(g)). Figure 8 shows, for the model eye imaging, that an optimum dispersion compensation would be possible with a 15 mm of N-BK7 optical window. In this study, in order to compromise and minimize the effects of both curvature of the coherence gate and dispersion for *in-vivo* retinal imaging, we used a N-BK7 optical window with 20 mm thickness. According to Fig. 3(g) and Fig. 8, a good trade-off could be found in this case: the axial resolution would be around 9μm, instead of 8μm, and the degree of curvature would be lower than 5, meaning an edge-center difference of 1μm.

We presented results in two different subjects presenting different refractive errors at two different retinal eccentricities. In both cases, a 20-mm thick N-BK7 optical window was suitable to achieve a 1 *mm* × 1 *mm* FOV. Indeed, since the axial resolution is around 9μm, a mismatch between the coherence gate geometry and the retina curvature inferior to the optical sectioning (given by the FF-OCT axial resolution) would not be seen (Fig. 9(a-c)). Figure 9(d) shows

theoretical degree of curvature values, validated by our previous model (Sect. 2.1 and Fig. 3(c,f)), for different eye lengths. One can see that a 20-mm thick N-BK7 optical window would be suitable (edge-center distance inferior to $1\,\mu$m) to achieve a $1\,mm \times 1\,mm$ FOV for eye lengths varying from 20 mm to 28 mm, which covers the majority of cases in the population [34]. It is therefore not necessary to swap optical window for each subject: the 20mm thick window covers the whole range of eye lengths that one would typically see in the clinic.

Fig. 9. (a-c) Schematic showing different degrees of curvature for the coherence gate and their consequence on the FOV of the FF-OCT image. Although the coherence gate curvature does not perfectly match the retinal curvature in the case of (c), a full FOV is still generated, as the coherence gate has a given thickness defined by the axial resolution. (d) Expected theoretical value of degree of curvature (computed using Eq. (1)) as a function of the thickness of the N-BK7 introduced to compensate for coherence gate curvature for different eye lengths. Green shaded area 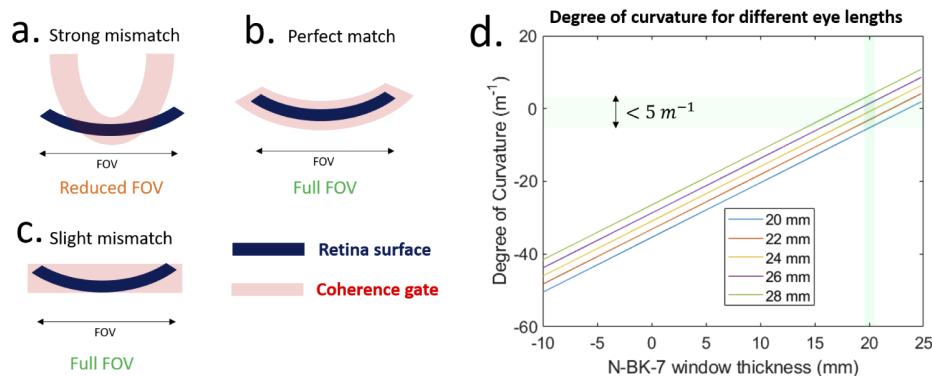highlights that a N-BK7 of 20 mm thickness covers the majority of eye lengths in the population (from 20 mm to 28 mm) [34].

In this study, we only considered N-BK7 optical windows to minimize effects of both coherence gate curvature and dispersion. Another solution to optically shape the geometry of the coherence gate is the introduction of a deformable reference mirror in the reference arm. This solution would decouple the correction of the coherence gate curvature and dispersion, since a suitable optical window in the sample arm could compensate for dispersion effect and the deformable reference arm would correct the residual curvature of the coherence gate, without affecting dispersion, improving signal level, axial resolution and possibly achieving even larger FOV. Moreover, this solution might extend the coherence gate shaping to samples with an irregular surface, more complex than a curvature, such as deformed retina due to degeneration, detachment, etc. In the case of imaging a deformed retina, a deformable reference would enable imaging an irregular retinal layer over a large FOV in a single shot instead of acquiring *en-face* images for different coherent plane positions. Nevertheless, the main drawback of this solution is the considerable increase of the system complexity and cost, making clinical transfer challenging. A solution considering only a 20 mm thick N-BK7 optical window, as presented in this paper, seems suitable to minimize both curvature of the coherence gate and dispersion for a large population.

The direct visualization of individual photoreceptors together with photoreceptor-based biomarkers, such as distribution, density and spacing, could be useful tools to diagnose retinal disorders at the early stages, in order to monitor retinal disease progression as well as the effect of potential therapeutic interventions [32]. The presented FF-OCT system with coherence gate shaping enables 4D monitoring of individual photoreceptors and photoreceptor-based biomarkers with good accuracy and repeatability in a wide FOV, without image distortion (due to eye motion) and long, fastidious acquisition sessions to cover the retinal area of interest, as is the case with

lab-built scanning systems with limited FOV such as AO-SLO and AO-OCT. While AO-FIO can achieve 1 *mm* × 1 *mm* FOV at a high-frame rate [8], high-resolution brought by ocular aberration correction using AO is limited by the eye's field aberrations, commonly known as the isoplanatic patch [12], affecting the accuracy of the resultant photoreceptor-based biomarkers. This issue can be tackle by limiting the system aperture (around 5 mm in the eye's pupil plane), provoking a decrease of resolution and signal-to-noise ratio (SNR), as rtx-1 (Imagine Eyes, France) and [8]; or by using multi-conjugated AO, with an increased system complexity as a second deformable mirror is necessary [13]. The present FF-OCT with coherence gate shaping can resolve photoreceptor and extract photoreceptor-based biomarkers in the whole FOV without AO, considerably decreasing the system complexity and footprint, which may help clinical deployment. Additionally, FF-OCT has the capacity to generate en-face retinal images with an enhanced axial resolution (9 *μm*) compared to confocal AO-SLO (around 40 *μm* [35]) and AO-FIO (no inherent optical sectioning). This advantage can be observed in Fig. 7, especially in comparison with AO-FIO, where a structured background can be observed in the latter, probably coming from the choroid positioned beneath the photoreceptor layer, which is completely filtered out by the FF-OCT thanks to its high axial resolution. Although FF-OCT axial resolution may be slightly poorer than AO-OCT [10], it has advantages of larger FOV, higher-frame rate and lower complexity and size, and is still able to resolve the photoreceptor interfaces such as IS/OS junction and cone outer segment tips. Moreover, the high temporal resolution of FF-OCT may play an important role to characterize the temporal behavior of retinal capillaries from different plexus [36,37] and the temporal dynamics of subcellular structures [27]. Finally, although FF-OCT is only weakly sensitive to low-order ocular aberrations in terms of resolution, aberrations still reduce the FF-OCT signal level [38]. Ocular aberrations may explain why the SNR of FF-OCT images varies across the FOV (Figs. 4 and 5) and why the AO-SLO image has higher contrast than the FF-OCT image (Fig. 7). Although the presented imaging technique presents lower SNR compared to AO-SLO, photoreceptors can still be visualized in single unaveraged frames, as it was demonstrated in Visualization 5, and photoreceptor-based biomarkers can still be extracted with accuracy (Fig. 6).

5. Conclusion

In conclusion, we have developed coherence gate shaping for FF-OCT to adapt coherence gate geometry to the curvature of the sample being imaged, making large FOV imaging possible while keeping high-resolution in samples under constant motion, such as the living human eye. We applied this method to achieve, in a single shot, and without the use of AO, 1 *mm* × 1 *mm* FOV image of the living human cone mosaic as close as 1° from the foveal center. We showed that a large FOV allied with a high resolution in all three dimensions, brings a significant benefit for retinal imaging: the large FOV facilitates the localization of the region of interest, allows a global interpretation of the retinal condition over this area, such as cone density distribution, and drastically reduces the image session duration; the high resolution allows tracking of individual cones and computation of cellular information, such as cell density and spacing, that could be used as biomarkers to diagnose retinal disorders at early stages. FF-OCT with improved performance thanks to coherence gate shaping may pave the way towards its adoption as a routine clinical imaging system, helping to understand retinal structure and disease.

Acknowledgments

Disclosures

P. Mecê: PSL University (P), C. Boccara: PSL University (P), others: none.

References

1. A. London, I. Benhar, and M. Schwartz, "The retina as a window to the brain - from eye research to cns disorders," Nat. Rev. Neurol. **9**(1), 44–53 (2013).
2. J. J. Hunter, W. H. Merigan, and J. B. Schallek, "Imaging retinal activity in the living eye," Annu. Rev. Vis. Sci. **5**(1), 15–45 (2019).
3. J. Jarosz, P. Mecê, J.-M. Conan, C. Petit, M. Paques, and S. Meimon, "High temporal resolution aberrometry in a 50-eye population and implications for adaptive optics error budget," Biomed. Opt. Express **8**(4), 2088–2105 (2017).
4. P. Mecê, E. Gofas-Salas, C. Petit, F. Cassaing, J. Sahel, M. Paques, K. Grieve, and S. Meimon, "Higher adaptive optics loop rate enhances axial resolution in nonconfocal ophthalmoscopes," Opt. Lett. **44**(9), 2208–2211 (2019).
5. J. Liang, D. R. Williams, and D. T. Miller, "Supernormal vision and high-resolution retinal imaging through adaptive optics," J. Opt. Soc. Am. A **14**(11), 2884–2892 (1997).
6. A. Roorda, F. Romero-Borja, W. J. Donnelly III, H. Queener, T. J. Hebert, and M. C. Campbell, "Adaptive optics scanning laser ophthalmoscopy," Opt. Express **10**(9), 405–412 (2002).
7. M. Zacharria, B. Lamory, and N. Chateau, "Biomedical imaging: New view of the eye," Nat. Photonics **5**(1), 24–26 (2011).
8. E. Gofas-Salas, P. Mecê, C. Petit, J. Jarosz, L. M. Mugnier, A. M. Bonnefois, K. Grieve, J. Sahel, M. Paques, and S. Meimon, "High loop rate adaptive optics flood illumination ophthalmoscope with structured illumination capability," Appl. Opt. **57**(20), 5635–5642 (2018).
9. M. Paques, S. Meimon, F. Rossant, D. Rosenbaum, S. Mrejen, F. Sennlaub, and K. Grieve, "Adaptive optics ophthalmoscopy: Application to age-related macular degeneration and vascular diseases," Prog. Retinal Eye Res. **66**, 1–16 (2018).
10. R. S. Jonnal, O. P. Kocaoglu, R. J. Zawadzki, Z. Liu, D. T. Miller, and J. S. Werner, "A review of adaptive optics optical coherence tomography: technical advances, scientific applications, and the future," Invest. Ophthalmol. Visual Sci. **57**(9), OCT51–OCT68 (2016).
11. N. D. Shemonski, F. A. South, Y.-Z. Liu, S. G. Adie, P. S. Carney, and S. A. Boppart, "Computational high-resolution optical imaging of the living human retina," Nat. Photonics **9**(7), 440–443 (2015).
12. P. Bedggood, M. Daaboul, R. A. Ashman, G. G. Smith, and A. Metha, "Characteristics of the human isoplanatic patch and implications for adaptive optics retinal imaging," J. Biomed. Opt. **13**(2), 024008 (2008).
13. M. Laslandes, M. Salas, C. K. Hitzenberger, and M. Pircher, "Increasing the field of view of adaptive optics scanning laser ophthalmoscopy," Biomed. Opt. Express **8**(11), 4811–4826 (2017).
14. D. Hillmann, H. Spahr, C. Hain, H. Sudkamp, G. Franke, C. Pfäffle, C. Winter, and G. Hüttmann, "Aberration-free volumetric high-speed imaging of in vivo retina," Sci. Rep. **6**(1), 35209 (2016).
15. D. Borycki, E. Auksorius, P. Węgrzyn, and M. Wojtkowski, "Computational aberration correction in spatiotemporal optical coherence (stoc) imaging," Opt. Lett. **45**(6), 1293–1296 (2020).
16. L. Ginner, A. Kumar, D. Fechtig, L. M. Wurster, M. Salas, M. Pircher, and R. A. Leitgeb, "Noniterative digital aberration correction for cellular resolution retinal optical coherence tomography in vivo," Optica **4**(8), 924–931 (2017).
17. H. Sudkamp, D. Hillmann, P. Koch, M. vom Endt, H. Spahr, M. Münst, C. Pfäffle, R. Birngruber, and G. Hüttmann, "Simple approach for aberration-corrected oct imaging of the human retina," Opt. Lett. **43**(17), 4224–4227 (2018).
18. T. B. DuBose, F. LaRocca, S. Farsiu, and J. A. Izatt, "Super-resolution retinal imaging using optically reassigned scanning laser ophthalmoscopy," Nat. Photonics **13**(4), 257–262 (2019).
19. P. Mecê, J. Jarosz, J.-M. Conan, C. Petit, K. Grieve, M. Paques, and S. Meimon, "Fixational eye movement: a negligible source of dynamic aberration," Biomed. Opt. Express **9**(2), 717–727 (2018).
20. A. Dubois, K. Grieve, G. Moneron, R. Lecaque, L. Vabre, and C. Boccara, "Ultrahigh-resolution full-field optical coherence tomography," Appl. Opt. **43**(14), 2874–2883 (2004).
21. O. Thouvenin, K. Grieve, P. Xiao, C. Apelian, and A. C. Boccara, "En face coherence microscopy," Biomed. Opt. Express **8**(2), 622–639 (2017).
22. P. Xiao, M. Fink, and A. C. Boccara, "Full-field spatially incoherent illumination interferometry: a spatial resolution almost insensitive to aberrations," Opt. Lett. **41**(17), 3920–3923 (2016).
23. P. Mecê, P. Xiao, V. Mazlin, J. Scholler, K. Grieve, J.-A. Sahel, M. Fink, and C. Boccara, "Towards lens-based wavefront sensorless adaptive optics full-field oct for in-vivo retinal imaging (conference presentation)," in *Optical Coherence Tomography and Coherence Domain Optical Methods in Biomedicine XXIII*, vol. 10867 (International Society for Optics and Photonics, 2019), p. 1086722.

24. P. Mecê, J. Scholler, K. Groux, and C. Boccara, "High-resolution in-vivo human retinal imaging using full-field oct with optical stabilization of axial motion," Biomed. Opt. Express **11**(1), 492–504 (2020).

25. P. Xiao, V. Mazlin, K. Grieve, J.-A. Sahel, M. Fink, and A. C. Boccara, "In vivo high-resolution human retinal imaging with wavefront-correctionless full-field oct," Optica **5**(4), 409–412 (2018).

26. W. Sellmeier, "Zur erkarung der abnormen farbenfolge im spectrum einiger. substanzen," Ann. Phys. **219**(6), 272–282 (1871).

27. J. Scholler, V. Mazlin, O. Thouvenin, K. Groux, P. Xiao, J.-A. Sahel, M. Fink, C. Boccara, and K. Grieve, "Probing dynamic processes in the eye at multiple spatial and temporal scales with multimodal full field oct," Biomed. Opt. Express **10**(2), 731–746 (2019).

28. R. F. Cooper, G. K. Aguirre, and J. I. Morgan, "Fully automated estimation of spacing and density for retinal mosaics," Trans. Vis. Sci. Tech. **8**(5), 26 (2019).

29. J. I. Yellott Jr, "Spectral analysis of spatial sampling by photoreceptors: topological disorder prevents aliasing," Vision Res. **22**(9), 1205–1210 (1982).

30. C. A. Curcio, K. R. Sloan, R. E. Kalina, and A. E. Hendrickson, "Human photoreceptor topography," J. Comp. Neurol. **292**(4), 497–523 (1990).

31. R. F. Cooper, M. A. Wilk, S. Tarima, and J. Carroll, "Evaluating descriptive metrics of the human cone mosaic," Invest. Ophthalmol. Visual Sci. **57**(7), 2992–3001 (2016).

32. K. M. Litts, R. F. Cooper, J. L. Duncan, and J. Carroll, "Photoreceptor-based biomarkers in aoslo retinal imaging," Invest. Ophthalmol. Visual Sci. **58**(6), BIO255 (2017).

33. A. Podoleanu, M. Seeger, G. Dobre, D. Webb, D. Jackson, and F. Fitzke, "Transversal and longitudinal images from the retina of the living eye using low coherence reflectometry," J. Biomed. Opt. **3**(1), 12 (1998).

34. H. Kolb, "Gross anatomy of the eye," in *Webvision: The Organization of the Retina and Visual System [Internet]*, (University of Utah Health Sciences Center, 2007).

35. D. T. Miller, J. Qu, R. S. Jonnal, and K. E. Thorn, "Coherence gating and adaptive optics in the eye," in *Coherence Domain Optical Methods and Optical Coherence Tomography in Biomedicine VII*, vol. 4956 (International Society for Optics and Photonics, 2003), pp. 65–72.

36. E. Gofas-Salas, P. Mecê, L. Mugnier, A. M. Bonnefois, C. Petit, K. Grieve, J. Sahel, M. Paques, and S. Meimon, "Near infrared adaptive optics flood illumination retinal angiography," Biomed. Opt. Express **10**(6), 2730–2743 (2019).

37. C. Lavia, P. Mecê, M. Nassisi, S. Bonnin, J. Marie-Louise, A. Couturier, A. Erginay, R. Tadayoni, and A. Gaudric, "Retinal capillary plexus pattern and density from fovea to periphery measured in healthy eyes with swept-source optical coherence tomography angiography," Sci. Rep. **10**(1), 1474 (2020).

38. J. Scholler, K. Groux, K. Grieve, C. Boccara, and P. Mecê, "Adaptive-glasses wavefront sensorless full-field oct for high-resolution retinal imaging over a wide field-of-view," arXiv preprint arXiv:2007.04986 (2020).

4.3 Aberrations: signal and contrast loss

In the first chapter I mentioned that low spatial frequency distortions of the wavefront are called aberrations. For a well designed system, these aberrations are induced by the sample (and not by the system itself) by low spatial frequency variations of the refractive index. Without aberrations, the transverse resolution of an optical system due to diffraction is[6] $\delta_{x,y} = \frac{\lambda_c}{2NA}$ where NA is the numerical aperture of the optical system and λ_c is the central wavelength of the detected light. When the wavefront is distorted by aberrations, the resolution is degraded. The way aberrations affect the optical transfer function[7] depends on how images are formed on the detector. Consider a fluorescence microscope where the detection is incoherent, aberrations for the in-going illumination does not create any distortion as long as the illumination remains homogeneous in the sample plane in order to excite the fluorophores. The collected fluorescence however will be affected by aberrations in the way out before being collected on the detector. For a coherent system such as OCT, the transport of the coherence for the illumination beams also matters and aberrations will affect images differently. In this section I will derive and explain the well known influence of aberrations on a conventional system, then I will present the influence of aberrations for a (D-)FFOCT system, which was derived by Victor Barolle in his thesis [Barolle, 2019] and finally I will present how we experimentally validated Barolle's theory. Aberrations that are treated in this section are supposed to act the same for each wavelength in the illumination. In practice, aberrations can be wavelength dependent because of dispersion; this chromatic dependence of geometrical aberration could be neglected here because of the narrow spectral bandwidth.

4.3.1 Aberrations theory in conventional optical systems

Before deriving the effect of aberrations on a conventional imaging system we must understand how images forms in such systems. Due to the diffraction, geometric light propagation is not satisfactory close to the focal plane and light propagation must be treated with care to understand how an optical system behave. Under the hypothesis of linearity, spatial invariance and without absorption in the optical system the light propagation of a complex light field E_i in the imaged plane will give a complex field E_o at the output of the optical system which is the superposition of each punctual fields propagated from the imaged plane to the detector plane:

$$E_o(x', y') = \int_{-\infty}^{\infty} \int_{-\infty}^{\infty} h(x' - x, y' - y) E_i(x, y) dx dy \tag{4.1}$$

where $h(x' - x, y' - y)$ is the point spread function[8] in amplitude, (x, y) are coordinates of the imaged plane, (x', y') are coordinates of the detector plane. The coordinates $(x', y') = (Mx, My)$ where M is the magnification of the imaging system. The above expression is the 2D convolution of the input light field U_i with the point spread function and can be written using the convolution operator:

$$E_o = h * E_i \tag{4.2}$$

---

[6]Depending on the nature of the measurement (confocality, filtering, etc.) some pre-factor can arise but for far field measurements the transverse resolution is always proportional to $\frac{\lambda_c}{2NA}$

[7]For coherent systems the term amplitude transfer function is usually used.

[8]In digital signal processing the point spread function is referred as impulse response.

where $*$ is the 2D convolution. The amplitude response of a point source object at position (x, y) is given by the exit pupil Fraunhofer diffraction [Goodman, 2005]:

$$h(x' - x, y' - y) = -\frac{A}{\lambda z_i} \int_{-\infty}^{\infty} \int_{-\infty}^{\infty} t(u, v) \, e^{-\frac{i2\pi}{\lambda z_i}((x'-x)u+(y'-y)v)} du dv \tag{4.3}$$

where A is the light field amplitude, z_i is the distance from the exit pupil to the image plane, (u, v) are coordinates of the exit pupil, (x, y) are coordinates of the imaged plane, t is the pupil function and is constant across the aperture and zero outside. Finally we obtain that for a diffraction-limited system we can regard the image as being a convolution of the image predicted by geometrical optics with an impulse response that is the Fraunhofer diffraction pattern of the exit pupil. Introducing reduced coordinates $u' = \frac{-u}{\lambda z_i}$ and $v' = \frac{-v}{\lambda z_i}$, we have $du = -\lambda z_i u'$ and Eq. 4.3 boils down to a Fourier transform of the scaled exit pupil:

$$h(x, y) \propto \int_{-\infty}^{\infty} \int_{-\infty}^{\infty} t\left(-\lambda z_i u', -\lambda z_i v'\right) e^{i2\pi(xu'+yv')} du' dv' \tag{4.4}$$

$$\propto \mathcal{F}^{-1}\left\{t(-\lambda z_i u', -\lambda z_i v')\right\} \tag{4.5}$$

$$\propto \mathcal{F}^{-1}\left\{t(u'', v'')\right\} \tag{4.6}$$

$$\tag{4.7}$$

For incoherent systems, the propagation is linear in intensity, therefore the point spread function in intensity $\mathcal{H}(x, y)$ is given by:

$$\mathcal{H}(x, y) = |h(x, y)|^2 \tag{4.8}$$

$$= h(x, y)h^*(x, y) \tag{4.9}$$

$$\propto \mathcal{F}^{-1}\left\{t(u'', v'')\right\} \mathcal{F}^{-1}\left\{t^*(u'', v'')\right\} \tag{4.10}$$

$$\tag{4.11}$$

where * denotes the complex conjugate. The optical transfer function can be computed by taking the Fourier transform of the above expression:

$$\hat{\mathcal{H}}(\nu_x, \nu_y) \propto \mathcal{F}\left\{\mathcal{F}^{-1}\left\{t(u'', v'')\right\} \mathcal{F}^{-1}\left\{t^*(u'', v'')\right\}\right\} \tag{4.12}$$

and then by using the Fourier convolution theorem we can write:

$$\hat{\mathcal{H}}(\nu_x, \nu_y) \propto \mathcal{F}\left\{\mathcal{F}^{-1}\left\{t(u'', v'')\right\}\right\} * \mathcal{F}\left\{\mathcal{F}^{-1}\left\{t^*(u'', v'')\right\}\right\} \tag{4.13}$$

$$\propto t(u'', v'') * t^*(-u'', -v'') \tag{4.14}$$

$$\propto t(u'', v'') \otimes t(u'', v'') \tag{4.15}$$

where $\otimes$ denotes the correlation operator. The optical transfer function $\hat{\mathcal{H}}(\nu_u, \nu_v)$ is therefore proportional to the scaled auto-correlation of the pupil function $t(u'', v'')$. For a circular pupil this equation yields the Fourier transform of the Airy function[9]. This formalism is very convenient because optical systems can be described by transfer functions and it is therefore easy to simulate optical performances. I simulated the PSF without aberration for a conventional microscope with similar objectives as our FFOCT setup, see Fig. 4.1.

---

[9]The Airy function is the PSF of an optical system with circular pupil.

The lateral resolution is given by the PSF width $\delta_{x,y} = \frac{\lambda_c}{2NA}$[10] and the axial resolution is given by the depth of focus $\delta_z = \frac{n\lambda_c}{NA^2}$. Without aberrations the wavefront is not distorted during the propagation in Eq. 4.3 and the pupil function is flat. With aberrations however, the pupil function $t(u,v)$ adds local phase distortions and can therefore be represented by a complex function with unit amplitude $t(u,v) = e^{i\phi(u,v)}$, where $\phi(u,v)$ are the phase distortions in the pupil plane. The previous formalism remains valid and it is possible to compute the optical transfer function by taking the auto-correlation of $t(u'',v'')$. Because of energy conservation, the optical transfer function must be equal to 1[11] at the origin and the cutoff frequency is $\nu_{max} = \frac{2NA}{\lambda_c}$. Finally, the intensity measured by the camera in a conventional microscope under homogeneous illumination can be written:

$$I_{conv}(x,y) \propto \int\int_S |h(x-x',y-y')|^2 |\rho(x',y')|^2 dx'dy' \tag{4.16}$$

$$\propto \mathcal{H}(x,y) * |\rho(x,y)|^2 \tag{4.17}$$

where $\rho(x,y)$ is the object reflectivity in amplitude and S is the imaged sample domain[12]. The above equation is the well known result that the imaged object through the optical system is the convolution between the intensity PSF and the object power reflectivity coefficient. By injecting Eq. 4.15 in Eq. 4.17 we can see that it is possible to simulate the effect of aberrations on the image of a given object:

$$\mathcal{F}\{I_{conv}(x,y)\} = \hat{\mathcal{H}}(\nu_x,\nu_y)\mathcal{F}\left\{|\rho(x,y)|^2\right\} \tag{4.18}$$

The auto-correlation of the pupil function acts as a linear filter on the object spatial frequencies. Aberrations affect the size of the optical transfer function $\hat{\mathcal{H}}(\nu_x,\nu_y)$ support hence damping part of the object spatial frequencies.

---

[10]For the sake of clarity, I neglected the pre-factor that can arise depending on the resolution criterion. Rayleigh criterion relies on the separability of two Airy disks when the maximum of one Airy disk corresponds to the first zero of the seconds yields $\delta_{x,y} = 1.22\frac{\lambda_c}{2NA}$.

[11]This is a consequence of Wiener–Khinchin theorem.

[12]I considered a flat sample here but the 3D nature can be explicitly taken into account by integrating over z.
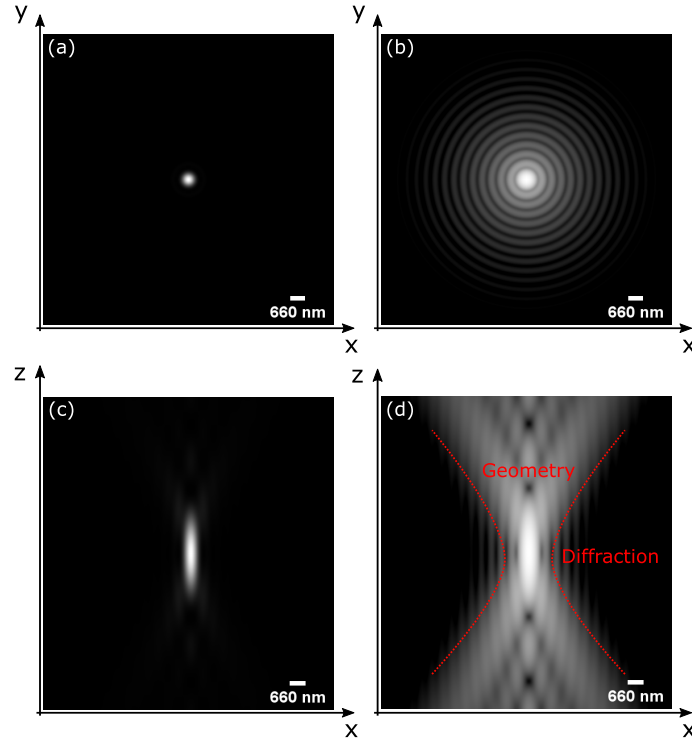
Fig. 4.1: 3D point spread function. (a) Lateral point spread function simulated for $NA = 0.8$ and $\lambda_c = 660\ nm$ in linear scale and **(b)** logarithmic scale. **(c)** Axial point spread function simulated with the same parameters in linear scale and **(d)** logarithmic scale. The 3D PSF was simulated using Richards and Wolf model [Richards et al., 1959].

For circular pupils it is convenient to decompose aberrations on a basis of orthogonal polynomials described by polar coordinates. Zernike polynomials are traditionally used to decompose aberrations where the firsts polynomials are typically the type of aberrations that are found in optical systems. Zernike polynomials are either odd or even depending on their spatial symmetry. Even Zernike polynomials are defined as:

$$Z_n^m = R_n^m(\rho)cos(m\Phi) \tag{4.19}$$

while odd Zernike polynomials are defined as:

$$Z_n^{-m} = R_n^{-m}(\rho)sin(m\Phi) \tag{4.20}$$

where m and n are non-negative integers with $n \geq m$, Φ is the azimuthal angle, $\rho \in [0, 1]$ is the radial distance, and R_n^m are the radial polynomials defined below:

$$R_n^m(\rho) = \sum_{k=0}^{\frac{n-m}{2}} \frac{(-1)^k(n-k)!}{k!\left(\frac{n+m}{2} - k\right)!\left(\frac{n-m}{2} - k\right)!}\rho^{n-2k} \tag{4.21}$$

The firsts fifth orders polynomials are depicted Fig. 4.2.
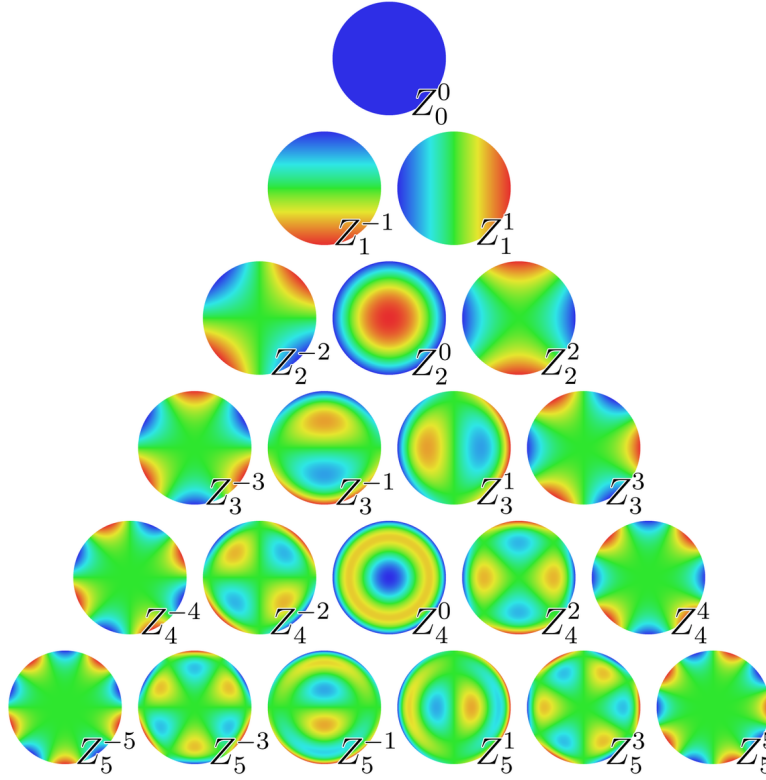
Fig. 4.2: Zernike polynomials classified by order from top to bottom.

I simulated the most common aberrations Fig. 4.3 and Fig. 4.4 for an optical system with similar objectives as the one used in our FFOCT setup (0.8 NA 40x). Without aberrations the PSF is diffraction limited and the modulation transfer function[13] (MTF) shape is given by the auto-correlation of a disk. With defocus, which corresponds to a parabolic phase error[14], the MTF support decreases uniformly and the PSF remains isotropic. This interesting property comes from the radial symmetry of the pupil function which is preserved by the Fourier transform, hence it is also valid for the spherical aberration[15]. Coma is typically observed when lenses are not correctly centered and is an odd function, leading to an asymmetry in the PSF and OTF. Finally I want to point out that for a conventional system, the auto-correlation of the pupil function leads to several properties that are not found in FFOCT:

1. The auto-correlation is always an even function. The Fourier transform of an even function is real, meaning that the PSF is real for a conventional system. Therefore, the resolution can be measured by the width of the PSF or by the cutoff frequency of the OTF. This is only because the convolution with a real function can be performed in the spatial domain, we will see in the next section that the PSF is no longer real for FFOCT and that reasoning with PSF is therefore not advised and can lead to confusions.

2. The auto-correlation is maximum at the origin and from energy conservation in

---

[13]The MTF is the amplitude of the OTF.

[14]Defocus can be approximated by translating the sample axially for small displacements.

[15]Spherical aberration is the type of aberration that is generated by a planar index mismatch (microscope coverslip) in samples. Typically, microscope objectives are corrected to counteract this aberration for a given coverslip thickness.

conventional system we have $\hat{\mathcal{H}}(\nu_x = 0, \nu_y = 0) = 1$. For FFOCT however, part of the light can lose coherence and be rejected, so that the system can't be considered energy conserving anymore ($\hat{\mathcal{H}}(\nu_x = 0, \nu_y = 0) < 1$).
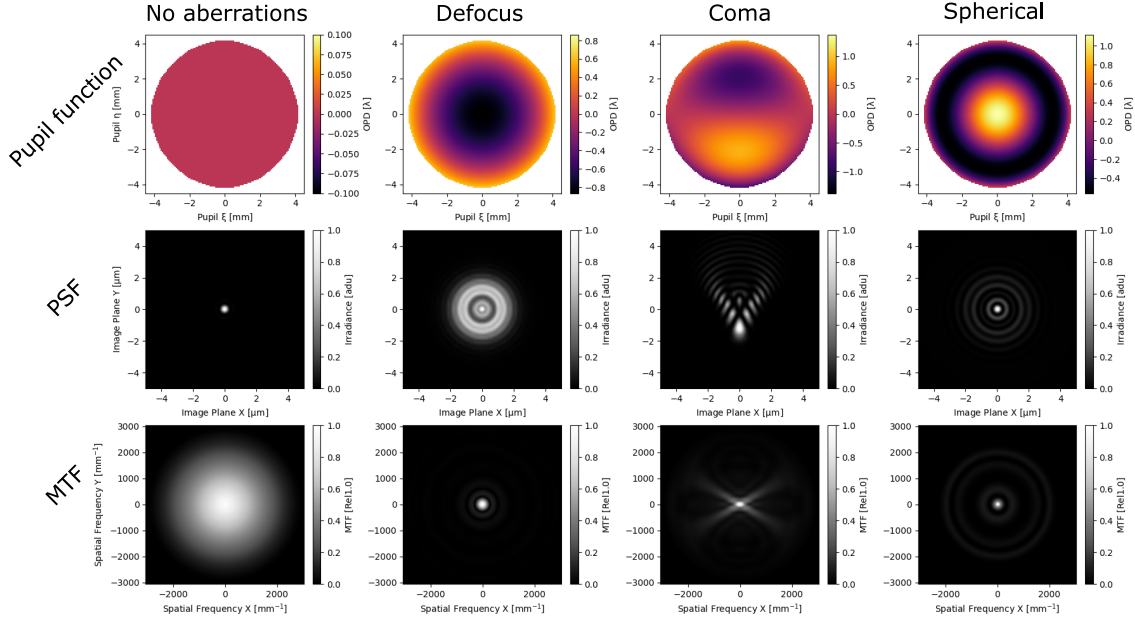
Fig. 4.3: Aberrations simulation in a conventional imaging system. Pupil functions without aberration and for 3 common aberrations (defocus, coma and spherical aberration) are depicted on the first row. On the second row the corresponding intensity PSF and on the third row the corresponding MTF. Panels have been generated using the open source python library Prysm [Dube, 2019].
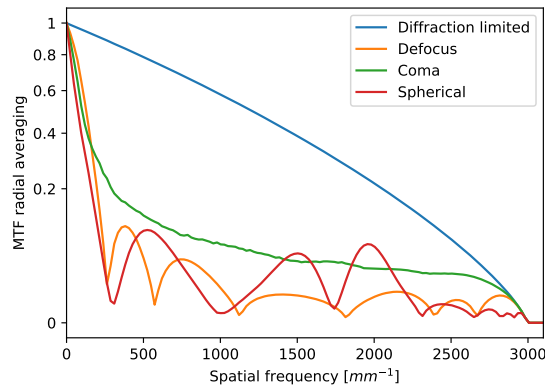
Fig. 4.4: MTF radial averaging simulation in a conventional imaging system. These curves represent the radial averaging of the 2D MTF depicted Fig. 4.3 on the bottom row. I scaled them with the square root in order to increase visual differences between the curves.

4.3.2 Aberrations theory in FFOCT

Spatially incoherent FFOCT was found to behave differently with aberrations. A primary experiment [Xiao et al., 2016] showed that applying defocus on FFOCT does not drastically

reduce the support of the MTF, therefore the resolution was robust against this aberration, see Fig. 4.5 where I reproduced this experiment on an USAF resolution target. The signal to noise ratio (SNR) for FFOCT however dramatically decreases even if the resolution does not suffer much. In order to provide a satisfactory explanation[16] two groups worked on developing a physical model for aberrations in FFOCT. The first group proposed a model in [Tricoli and Carminati, 2019] which focused on modeling FFOCT in scattering media and the second a model [Barolle, 2019] which is consistent with the first with particular emphasis on aberrations.
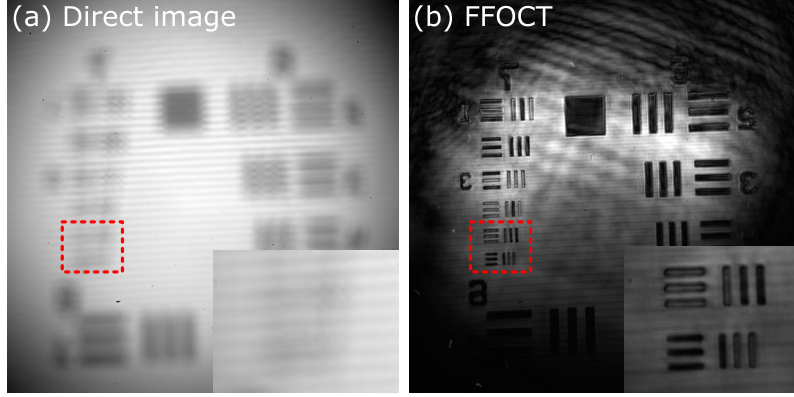
Fig. 4.5: Conventional vs FFOCT and defocus. (a) Conventional image observed on the camera with a strong defocus. **(b)** Corresponding FFOCT amplitude image acquired with a 4 phases demodulation.

The following is dedicated to derive aberrations manifestation in FFOCT and is greatly inspired from [Barolle, 2019]. Multiple scattering is neglected (this should remain valid at shallow depth due to time gating). The model is derived in the paraxial approximation where the light field is considered as a scalar function. The incident light field E_0 in the source plane[17] is a complex random variable whose phase is randomly distributed in $[0, 2\pi[$. Moreover, we will assume that the source is completely spatially incoherent:

$$\langle E_0(\mathbf{r}) E_0^*(\mathbf{r'}) \rangle = I_0 \delta(\mathbf{r} - \mathbf{r'}) \tag{4.22}$$

where $\mathbf{r}$ and $\mathbf{r'}$ are the position vectors[18] of two points in the source plane, I_0 is the mean intensity of the source, which is supposed to be spatially homogeneous, and the symbol $\langle . \rangle$ accounts for an ensemble average over different realizations of the field E_0. We will then assume that the light field is monochromatic[19]. The propagation between the source plane Σ_{source} and the sample plane Σ_{sample} is described by the impulse response $h(\mathbf{r'}, \mathbf{r''})$ between a point in the source plane at coordinate $\mathbf{r''}$ and a point in the sample plane at coordinate $\mathbf{r'}$. Because of spatial invariance[20], the impulse response satisfies $h(\mathbf{r'}, \mathbf{r''}) = h(\mathbf{r'} + \mathbf{r''})$ where h is the PSF in amplitude of the optical system. Magnification has been set to 1

---

[16]The explanations in [Xiao et al., 2016] and in [Ilina et al., 2020] do not take into account the effect of aberrations in the illumination but only in the detection.

[17]In practice it is not the source plane because we use a Köhler illumination but the plane where the field diaphragm is located. The spatial incoherence is still valid in this configuration.

[18]I replaced the coordinates by a position vector to alleviate notations.

[19]Monochromaticity is defined here as $\Delta\lambda/\lambda \ll 1$.

[20]In practice spatial invariance is not always achieved. Aberrations can vary in the field of view and lead to an isoplanetic patch where aberrations are the same. When the isoplanetic patch is very small, it is therefore not optimal to reason in the pupil plane [Mertz et al., 2015].

for the sake of clarity. The incident light field in the sample plane can be written:

$$E_i(\mathbf{r'}) = \int_{\Sigma_{Source}} h(\mathbf{r'} + \mathbf{r''})E_0(\mathbf{r''})d\mathbf{r''} \tag{4.23}$$

where the integral is over the whole source plane Σ_{source}. Let us consider an object whose reflectivity is given by the complex function $\rho(\mathbf{r'})$. The reflected field in the sample plane can be written:

$$E_r(\mathbf{r'}) = \rho(\mathbf{r'})E_i(\mathbf{r'}) = R(\mathbf{r'})\int_{\Sigma_{source}} h(\mathbf{r'} + \mathbf{r''})E_0(\mathbf{r''})d\mathbf{r''} \tag{4.24}$$

The propagation between the focal and camera planes is described by the same impulse response as the propagation from the source plane to the focal plane. The light field propagated in the sample arm, reflected by the object and propagated back to the camera can be written:

$$E_{sample}(\mathbf{r}) = \int_{\Sigma_{sample}} h(\mathbf{r} + \mathbf{r'})E_r(\mathbf{r'})d\mathbf{r'} \tag{4.25}$$

where the integral is over the sample plane Σ_{sample}. By re-injecting Eq. 4.24 into Eq. 4.25, it yields:

$$E_{sample}(\mathbf{r}) = \int_{\Sigma_{source}} \int_{\Sigma_{sample}} h(\mathbf{r} + \mathbf{r'})\rho(\mathbf{r'})h(\mathbf{r'} + \mathbf{r''})E_0(\mathbf{r''})d\mathbf{r'}d\mathbf{r''} \tag{4.26}$$

The light field transmitted by the sample arm $E_{sample}(\mathbf{r})$ is given by the double convolution of the object reflectivity ρ with the sample arm impulse response h on the way in and out of the microscope objective. Then, the FFOCT image is obtained from the interference between the sample and the reference field $\langle E_{sample}(\mathbf{r})E_{ref}^*(\mathbf{r})\rangle$ where $E_{ref}(\mathbf{r})$ is the light field transmitted by the reference arm and measured on the camera:

$$E_{ref}(\mathbf{r}) = \int h_{ref}(\mathbf{r} - \mathbf{r''})E_0(\mathbf{r''})d\mathbf{r''} \tag{4.27}$$

The *en face* image is then obtained by combining Eqs. 4.22, 4.26 and 4.27:

$$\langle E_{sample}(\mathbf{r})E_{ref}^*(\mathbf{r})\rangle = I_0 \iint h(\mathbf{r} + \mathbf{r'})\rho(\mathbf{r'})h(\mathbf{r'} + \mathbf{r''})h_{ref}^*(\mathbf{r} - \mathbf{r''})d\mathbf{r'}d\mathbf{r''} \tag{4.28}$$

Integrations over $\mathbf{r''}$ and $\mathbf{r'}$ are convolutions and Eq. 4.28 can be recast using the convolution operator:

$$\langle E_{sample}(\mathbf{r})E_{ref}^*(\mathbf{r})\rangle = I_0 \left(h \times [h \otimes h_{ref}]\right) * \rho_-(\mathbf{r}) \tag{4.29}$$

where $\rho_-(\mathbf{r}) = \rho(\text{-}\mathbf{r})$ is the spatially reversed amplitude due to the reflection. Taking the Fourier transform and using the convolution theorem, Eq. 4.29 becomes:

$$\mathcal{F}^{-1}\left(\langle E_{sample}(\mathbf{r})E_{ref}^*(\mathbf{r})\rangle\right) = I_0 \left(\hat{h} * \left(\hat{h} \times \hat{h}_{ref}\right)\right) \times \hat{\mathcal{R}} \tag{4.30}$$

Without aberrations in the reference arm we have $\hat{h}_{ref} = 1$ on the whole pupil so that $\hat{h} \times \hat{h}_{ref} = A$ and Eq. 4.30 becomes:

$$\mathcal{F}^{-1}\left(\langle E_{sample}(\mathbf{r})E_{ref}^*(\mathbf{r})\rangle\right) = I_0 \left(\hat{h} * \hat{h}\right) \times \hat{\mathcal{R}} \tag{4.31}$$

where $\hat{\mathcal{R}}$ is the Fourier transform of the object reflectivity. Taking the Fourier transform of the above expression and going back to the spatial domain, the FFOCT image finally writes:

$$\langle E_{sample}(\mathbf{r})E_{ref}^*(\mathbf{r})\rangle = I_0\left(h^2 * \rho_-(\mathbf{r})\right) \tag{4.32}$$

Aberrations in FFOCT also affect the object image like a frequency filter. As opposed to conventional systems, the transfer function $\hat{h} * \hat{h}$ is not always even, hence the PSF h is not real anymore. For even aberrations, the support of the auto-convolution is wider than the auto-correlation so that FFOCT is less sensitive to even aberrations than conventional imaging. I simulated the effect of defocus Fig. 4.6 and one can see that the FFOCT image is less affected in terms of resolution than the conventional image, which is what we experimentally observed Fig. 4.5. On the contrary, when $\hat{h}$ is odd, then $\hat{h}$ satisfies $\hat{h}(-\mathbf{u}) = \hat{h}^*(\mathbf{u})$ and the auto-convolution is equal to the auto-correlation: $\hat{h} * \hat{h}(\mathbf{u}) = \hat{h} \otimes \hat{h}(\mathbf{u})$. For binary objects like a resolution target, the reflectivity in amplitude or in intensity are equal. Therefore, when $\hat{h}$ is an odd function, FFOCT and conventional images should suffer the same way from aberrations. I simulated the effect of coma Fig. 4.7 where the OTF is the same for both systems. Finally FFOCT behaves the same as a confocal microscope linear in amplitude rather than intensity [Sheppard and Wilson, 1981]:

$$I_{confocal} = I_0\left|h^2 * \rho_-(\mathbf{r})\right|^2 \tag{4.33}$$

The confocal gating being created by the time gating combined with the spatial incoherence of the illumination for FFOCT rather than the confocal pinhole in the case of confocal microscopy[21].

---

[21]At this step the advantage of FFOCT is that it does not require scanning because the gating is multiplexed on all camera pixels. Also, FFOCT can access the complex nature of the field and therefore retrieve phase information.
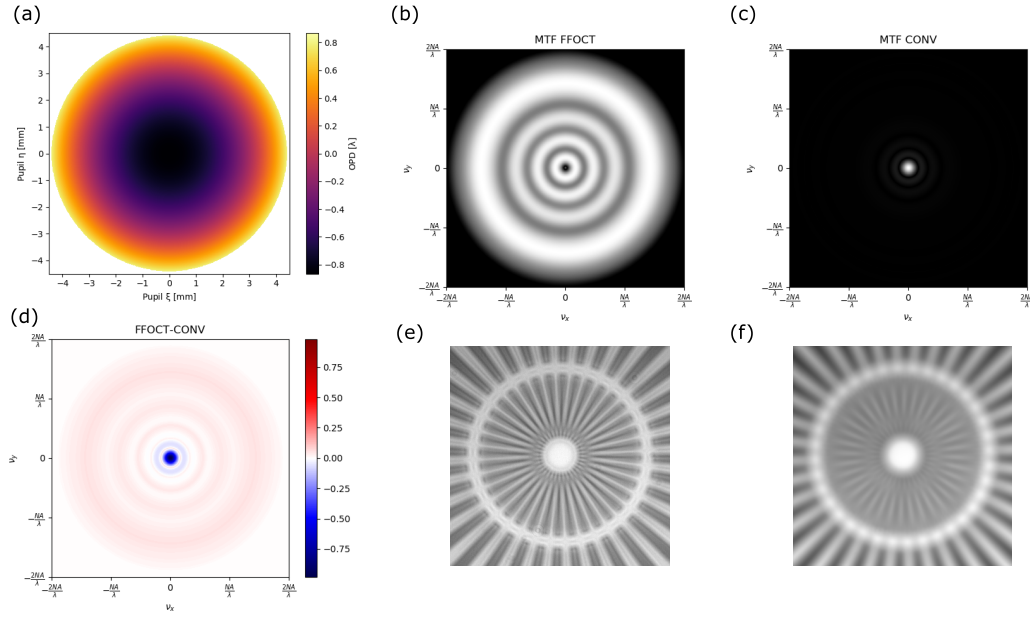
Fig. 4.6: Defocus simulation: FFOCT and conventional comparison. **(a)** Pupil function with $0.5Z_2^0$. **(b)** MTF for FFOCT which maintains a large support. **(c)** MTF for conventional imaging which has a shrinked support due to the defocus. **(d)** Difference $MTF_{FFOCT} - MTF_{Conv}$. **(e)** Simulation on a Siemens star target of FFOCT image with the given aberration. **(e)** Simulation on a Siemens star target of conventional image with the given aberration.
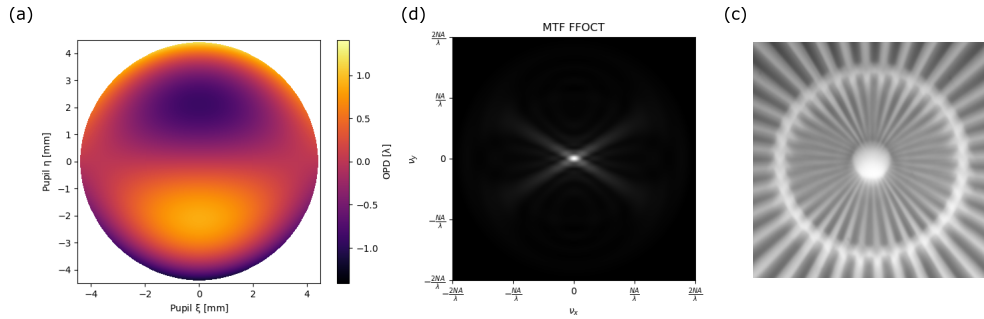
Fig. 4.7: Coma simulation: FFOCT and conventional comparison. **(a)** Pupil function with $0.5Z_3^{-1}$. **(b)** MTF for FFOCT and conventional imaging are the same and exhibits a shrinked support. **(c)** Simulation on a Siemens star target of FFOCT and conventional image with the given aberration. Coma being an odd aberrations, aberrated image of a binary object is the same for both technique.

In order to quantify the resolution gain in FFOCT, I defocused a resolution target from -20 μm to 20 μm with 1 μm steps[22], see Fig. 4.8(a-c). By re-slicing the 3D stacks on a circle Fig. 4.8(d) it is possible to see the effect of defocus on conventional imaging: the contrast decreases with an opening angle corresponding to the NA Fig. 4.8(e) whereas the boundary remains sharp for FFOCT. A few oscillation artifacts can be observed with the same angle whose origin is explained later. I computed the 2D Fourier transform of

---

[22]I compensated the defocus on the reference arm by adjusting the optical path length in order to match the target.

each image[23] and performed a radial averaging. Doing that I obtain an approximation of the MTF, see Fig. 4.8(f,g). From these curves it is clear that FFOCT exhibits a MTF which does not change much when adding defocus. Nonetheless the signals are lower and the phase does not remain unaffected: contrast inversion can be seen for a given spatial frequency, which corresponds to the dark ring in the MTF Fig. 4.6(b).
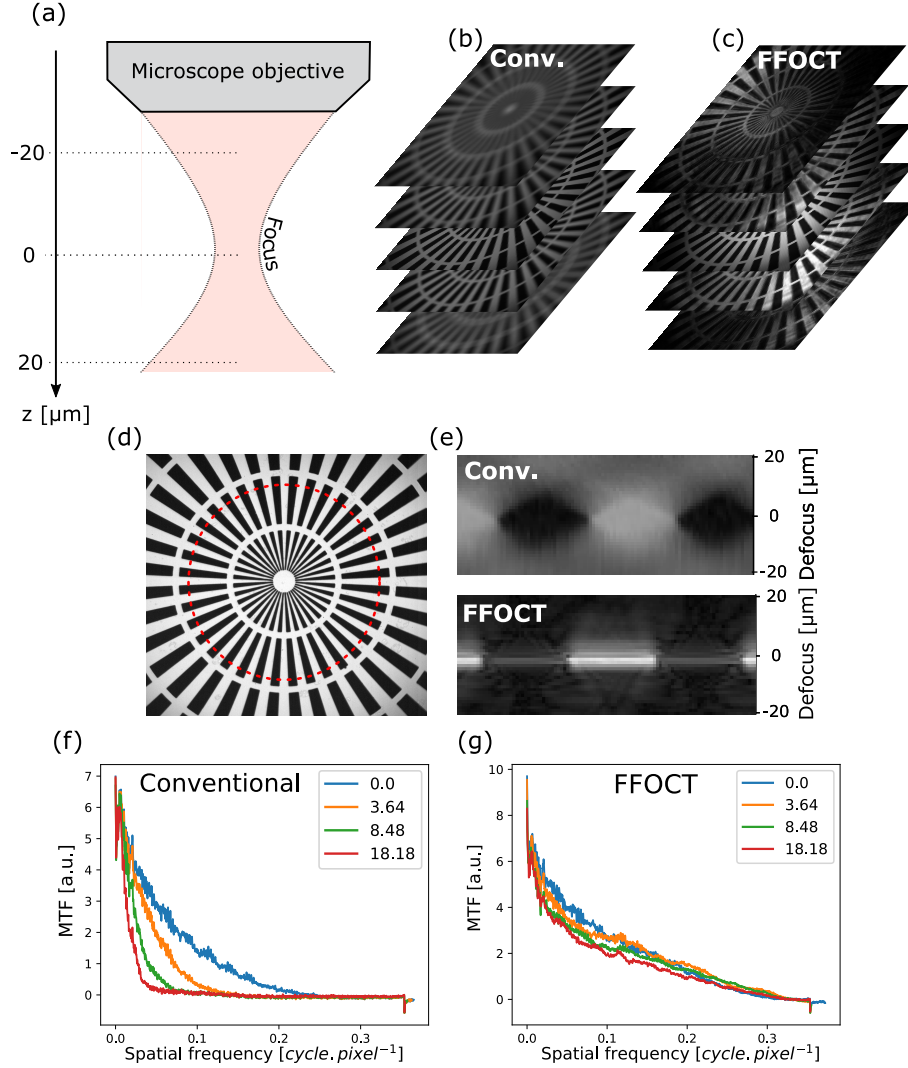
Fig. 4.8: Defocus experiment (a) A Siemens star target was imaged from -20 μm to 20 μm around the focal plane with 1 μm steps in **(b)** conventional images and **(c)** FFOCT. A radial reslice for constant spatial frequency **(d)** allow to see the difference in behavior for conventional systems compared to FFOCT **(e)**. The MTF is approximated using a radial averaging of the Fourier transform magnitude for conventional images **(f)** and FFOCT **(g)**. Each curve correspond to different amount of defocus adimensionned in NA/λ_c μm.

In order to quantify phase artifacts I computed the phase difference for each spatial frequency between a defocused image and the focused one Fig 4.9 with the following equation:

$$\phi(\nu) = arg\left(\hat{R_{foc}}\hat{R_{def}^{*}}\right) \tag{4.34}$$

---

[23]I used the period plus smooth decomposition [Moisan, 2011] to avoid the cross artifact when taking the Fourier transform. Replicating the image in order to introduce symmetry can also work but images gets bigger and the computation heavier.

where $\hat{R_{foc}}$ is the 2D Fourier transform of the focused image and $\hat{P_{def}}$ is the 2D Fourier transform of the defocused image. By computing the radial averaging on the positive frequencies, phases inversion are more visible. One can see that with defocus, the phase difference for conventional imaging is random for high frequencies. Indeed, these frequencies cannot reach the camera, they are filtered out by the MTF, so the phase difference is just noise.
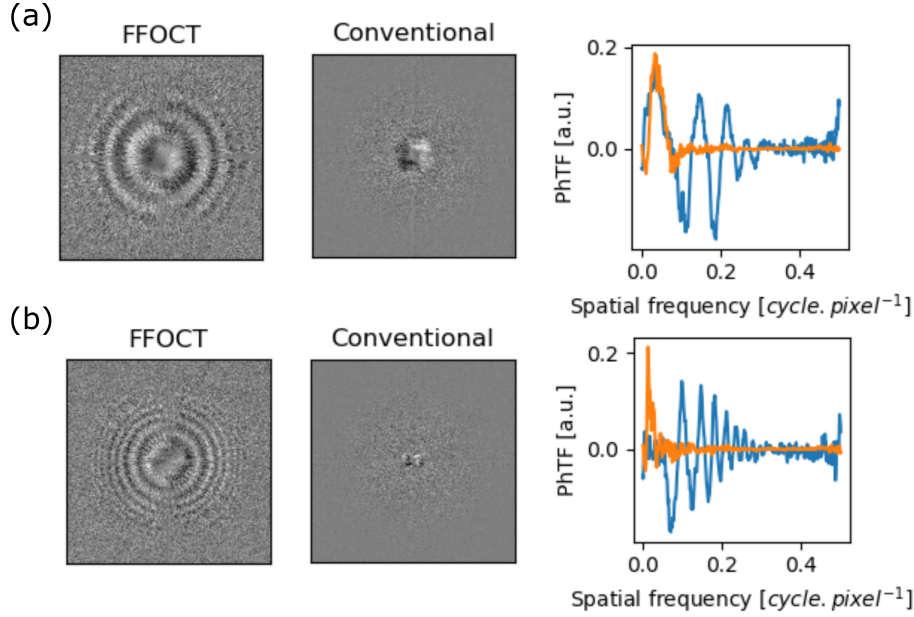
Fig. 4.9: Phase inversion in FFOCT and conventional images for **(a)** a moderate and **(b)** a strong defocus. Contrast inversions are seen for FFOCT even for higher spatial frequencies, meaning that these frequencies can propagate through the optical system but their phases can be modified, leading to artifacts on FFOCT images.

4.3.3 Experimental validation of the theory in FFOCT

In the aim of further validating the aforementioned simulations and results, I built a system that combines a standard FFOCT setup with an adaptive optics (AO) closed loop[24]. To do so, I used a Shack-Hartmann wavefront sensor (SH-WFS) and an adaptive lens (AL) both from Dynamic Optics that recently shown great performances for retinal imaging [Bonora et al., 2015, Verstraete et al., 2017]. The setup is depicted on Fig. 4.10, the FFOCT part shown in blue consists of a Linnik interferometer (with Olympus UCPLFLN20X objectives) with an LED source (*M850L3*, Thorlabs), the sample arm is mounted on a translation stage (T-LSR150B, Zaber Technologies) and the reference mirror is mounted on a piezoelectric translation stage (STr-25, Piezomechanik) for phase-shifting. The beam from a He:Ne laser (633 nm) is expanded and collimated using a 4x microscope objective and a $f_1 = 100mm$ lens and used as a plane wave reference for the AO part. This beam is combined with FFOCT illumination using a dichroic mirror (*FM02R*, Thorlabs) before the 45:55 beam splitter (*BP145B2*, Thorlabs) and blocked from entering the reference arm using a high pass filter as I wish to image the aberrated PSF in the sample arm only. The AL is set a few centimeters back from the pupil plane of the sample arm

---

[24]At first I tried with SLM (Meadowlarks). Unfortunately these SLM are limited in the maximal phase-shift that they can induce (around 0.5 λ) which is not sufficient to distinguish the advantage of FFOCT over traditional imaging techniques.

objective. The field curvature is compensated by a 2 *mm* thick NBK7 glass plate in the reference arm [Mecê et al., 2020a]. In the sample arm, the beam is split by the same dichroic mirror as in the illumination arm. The AL plane is relayed using a $4f$ telescope with a diaphragm (to filter out parasite reflections) onto the SH-WFS lenslet array. The remaining LED infrared photons are filtered out using a laser line filter centered at 633nm. In this configuration, I do not block the laser photons from impinging the FFOCT camera so I can image the sample arm PSF. This setup allows to jointly acquire the FFOCT image and the associated pupil function (after numerically propagating the measured wavefront in the AL plane [Mertz, 2019]). Note that the SH-WFS arm could be put at the exit of the interferometer to perform AO correction but the measured wavefront would correspond to the round trip[25] and could therefore not be used in this study to extract the pupil function $\hat{h}$.
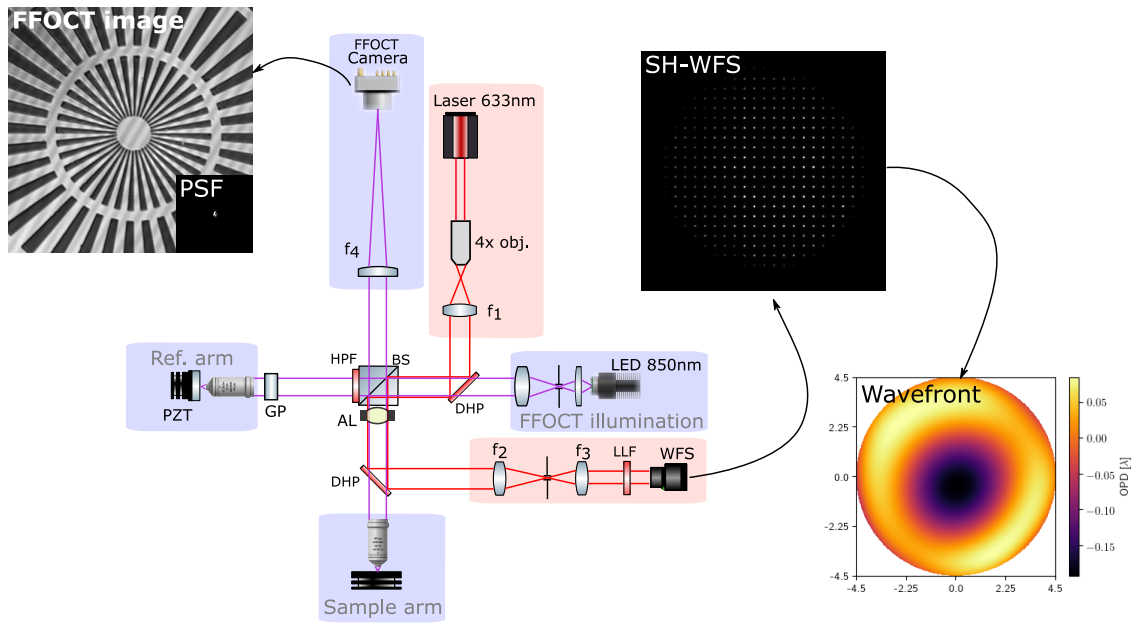
Fig. 4.10: Experimental setup: combining FFOCT with adaptive optics. Blue parts correspond to FFOCT arms and red parts correspond to AO arms. WFS: wavefront sensor - AL: adaptive lens - GP: 2 mm glass plate used for field curvature compensation - DHP: dichroic high pass mirror - HPF: high pass filter - BS: beam splitter - LLF: laser line filter - $f_1 = 150mm$ - $f_2 = 150mm$ - $f_3 = 60mm$ - $f_4 = 350mm$. An example of FFOCT image acquired after correcting aberrations is shown next to the camera with an inset of the conventional PSF. The associated image measured on the Shack-Hartmann wavefront sensor is shown on the right, together with the reconstructed wavefront with an RMS error below 0.04 λ.

The AL was calibrated following the procedure described Appendix C. The wavefront was controlled in closed loop after the acquisition of the influence functions of each single actuator. The first step for operating the system is to correct for the AL initial aberrations. Correcting these aberrations leads to a wavefront distortion of 0.04 λ RMS and required 55% RMS[26] of the lens dynamic thus leaving room for introducing deterministic wavefront errors. I imaged a Siemens star target, which is the recommended practice for coherent microscopy [Horstmeyer et al., 2016] in order to gather the maximum number

---

[25]Consequently, the wavefront seen by the WFS is not a true representation of the AL shape. This is akin to the double pass effect whereby odd aberrations cancel out between the two paths and even aberrations are doubled in amplitude.

[26]Note that this value can greatly vary depending on the lens. The second lens I ordered was 22% RMS.

of spatial frequency on the same image. Aberrations were computed on the 15 firsts[27] (ANSI/OSA index) Zernike polynomials on 363 centroids (corresponding to 20 centroids on the pupil diameter). The pupil function $\hat{h}$ was then constructed without the piston (non-measureable with a SH-WFS) and simulations were conducted on a reference Siemens star target image without aberrations. Direct images were taken by blocking the reference arm in order to remove unwanted light and fringes. FFOCT images were taken with a linear 4 phase buckets scheme in order to extract the amplitude term [Creath, 1988]. Using this setup, it is therefore possible to jointly acquire conventional images, FFOCT images and associated pupil functions $\hat{h}$ (after numerically propagating the AL wavefront in the pupil plane). For the first experiment I introduced a simple defocus in order to compare with the manual defocusing and validate that the AL and numerical pupil propagation were working correctly. Results are shown Fig. 4.11 for a wavefront error of 0.62 λ RMS. The reconstructed wavefront measured by the Shack-Hartmann wavefront sensor is depicted on the left. Next to the wavefront, the simulated MTF for conventional (Eq. 4.18) and FFOCT (Eq. 4.31) are shown, where one can see that FFOCT MTF exhibits a much larger support, suggesting that the resolution is better with such aberrations in FFOCT than in conventional imaging. Next to the MTF are shown simulated and experimental data for conventional imaging (with simulated and experimental PSF in inset) and for FFOCT. Simulations and experimental data match perfectly, and this could already be observed for a manual defocusing applied by translating the target axially. I reproduced the same experiment for astigmatism (Fig. 4.12) and coma (Fig. 4.13), which also contains defocus due to the AL being set a few centimeters back the pupil plane. The experimental results again closely match the simulations, validating Barolle's theory [Barolle, 2019].
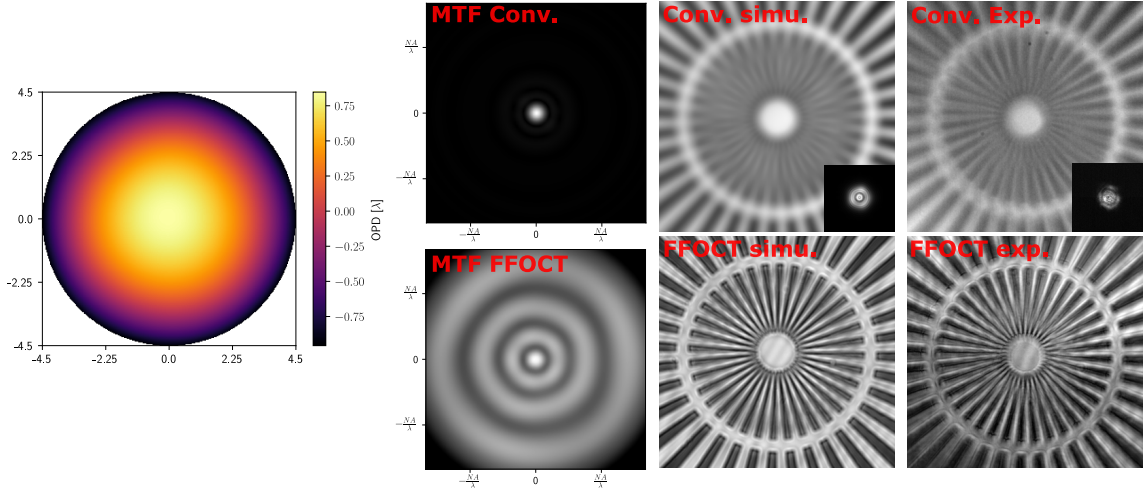
Fig. 4.11: Results for defocus. Left: wavefront applied with the AL. MTF for conventional imaging and FFOCT are simulated according to the proposed model. Simulated and experimental data on a Siemens star target are shown for conventional images (with simulated and experimental PSF in inset) and FFOCT.

---

[27]AL can correct only up to 15 Zernike modes [Bonora et al., 2015].
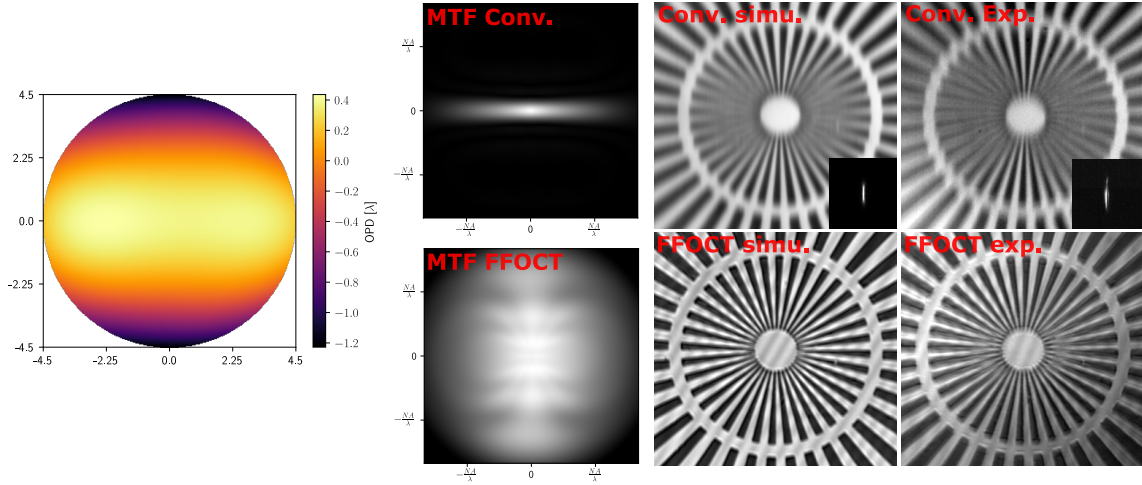
Fig. 4.12: Results for defocus + astigmatism. Left: wavefront applied with the AL. MTF for conventional imaging and FFOCT are simulated according to the proposed model. Simulated and experimental data on a Siemens star target are shown for conventional images (with simulated and experimental PSF in inset) and FFOCT.
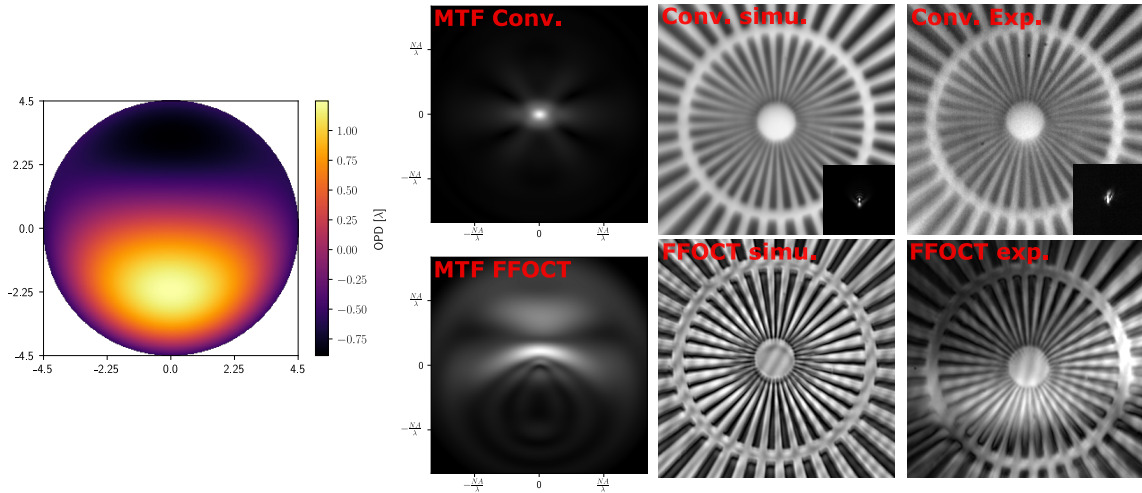
Fig. 4.13: Results for defocus + coma. Left: wavefront applied with the AL. MTF for conventional imaging and FFOCT are simulated according to the proposed model. Simulated and experimental data on a Siemens star target are shown for conventional images (with simulated and experimental PSF in inset) and FFOCT.

Discussion

These results were very hard to obtain because the alignment of the system is critical. If the AL or the WFS is off centered, even by a few hundreds micrometers, then the simulated MTF dramatically changes (parity is lost by translation). Also, the target needs to be perfectly orthogonal to the optical axis otherwise a varying amount of defocus will be present in the field of view. This alignment is especially difficult to obtain for the high numerical aperture used here ($NA = 0.8$) hence the small depth of focus. The field curvature also needs to be precisely corrected for the simulations to match the experimental data. If the field curvature is not perfectly corrected, then the SNR is not homogeneous on FFOCT images (visible in Fig. 4.13) and it seems that we can observe a smaller isoplanetic

patch on FFOCT images in this case. Correcting the wavefront however is much easier than introducing controlled amount of aberrations, especially for higher order aberrations. Indeed, when the AL corrects the wavefront, it doesn't matter if it is centered as long as the wavefront is compensated (with or without using a wavefront sensor). The drawback would be that the reconstructed aberrations would be biased and that the system could not be used to perform precise aberrometry but it could nonetheless correct for aberrations (even for higher order ones on dilated pupils), see next section where I used the AO part to correct for ocular aberrations and obtained near diffraction limited images of the retina.

In addition to the previous experiments I also studied the evolution of the PSF for various amount of defocus. The point spread function for FFOCT in amplitude is:

$$\mathcal{F}^{-1}(\hat{h} * \hat{h}) = h^2 \tag{4.35}$$

while the point spread function for conventional imaging is:

$$\mathcal{F}^{-1}(\hat{h} \otimes \hat{h}) = |h|^2 \tag{4.36}$$

Notice that the amplitude of the PSF in FFOCT should be the same as the conventional PSF: $|h^2| = |h|^2$. In order to compare both PSF, I imaged a 3D phantom sample containing 0.05% (w/v) TiO_2 nanobeads with 2% (w/v) agarose. At this concentration the nanobeads were isolated in 3D which makes it possible to measure individual PSF. In order to measure FFOCT PSF, I started by aligning the coherence plane with the focal plane where I could measure the PSF on a single nanobead in focus. I then shifted the coherence plane by translating the sample arm (by doing so, I avoid the backlash effect from the motor and perform very precise shifts) and measured the PSF with various amount of defocus expressed in micrometer in the air, see Fig. 4.14. For each experimental FFOCT PSF I simulated the theoretical PSF given by Eq. 4.32. I made the same measurement for conventional images by blocking the reference arm and by applying the previous amount of defocus on a single bead. According to the presented model, the width of the PSF modulus should be the same for conventional and FFOCT. One can see Fig. 4.14(b) that the width is higher than expected for conventional images, especially close to the focus position. This is due to the agarose sample being weakly scattering. This also explains that the shape of the simulated FFOCT PSF are also different from the experimental ones which exhibits a speckle pattern (small scatterers composed of air bubbles are present in the coherence volume leading to random patterns). However the width of the amplitude of the experimental PSF for FFOCT is consistent with the model.
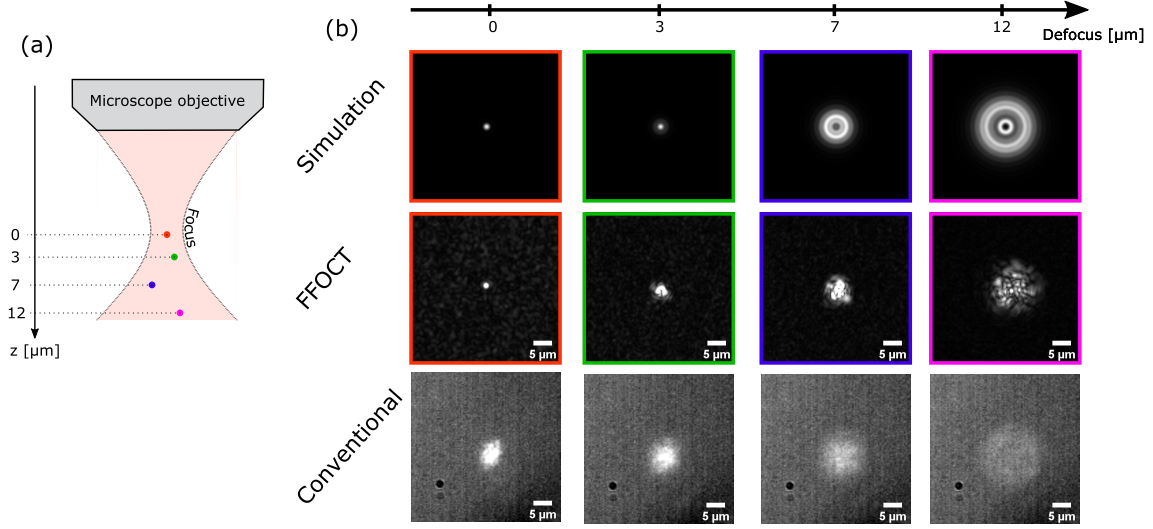
Fig. 4.14: PSF experiment. **(a)** Scheme of the FFOCT experiment measuring PSF for various amount of defocus. The focal plane is kept the same but the coherence plane is shifted by translating the sample arm. PSF are measured with different amount of defocus on different nanobeads. **(b)** PSF for different amount of defocus. The first row is the theoretical PSF according to Eq. 4.32. The second row is the experimental FFOCT PSF. The third row is the conventional PSF for the same amount of defocus, acquired by blocking the reference arm.

These results seems to contradict the ones found in [Xiao et al., 2016] where the authors conclude that PSF width in FFOCT is robust against defocus (and other aberrations) whereas I found that the magnitude of the PSF width is behaving the same for FFOCT and for a conventional system: it will be broadened by the presence of aberrations. Their model neglects the propagation from the source to the object and therefore fail at completely describing the image formation process on the detector. Regarding the experimental part, several flaws in their experiment could explain that they measured the same PSF width for various amount of defocus:

- Their PSF images are interpolated with an unknown kernel which could modify the PSF width (spline kernels can introduce oscillations that are not present in the original image) and original PSF are not shown.[28] The PSF width measurements are not performed in 2D but along a cross section. It is not stated if the cross-section is the same for each defocus position but the PSF asymmetry could potentially lead to wrong conclusions.

- It seems that the authors did not measure the magnitude of the PSF because one can clearly see the negative side-lobes on the PSF, see Fig. 4.15(A). These side-lobes should be positive and included in the PSF width computation using an envelop. Also, the photons backscattered by the bead can interfere with the photons backscattered by the coverslip and give non-interpretable results. The fact that the FFOCT PSF is complex is also adding ambiguities in this experiment.

- The signal to noise ratio of the background (coverslip) is not following the signal to noise ratio of the bead with respect to the applied defocus, see Fig. 4.15(B,C). Their claimed correct focus position was probably wrong, or the reference arm was

---

[28]The optimal interpolation (in the L2 norm) when signals are correctly sampled is Shannon interpolation (interpolation by sinc) by zero padding the image Fourier transform [Pianykh, 2011].

not correctly compensated during the experiment because the signal to noise ratio of the background should follow the signal to noise ratio of the bead. In either case, combined with the unknown interpolation, it seems that the PSF width could not be reliably determined in this experiment.
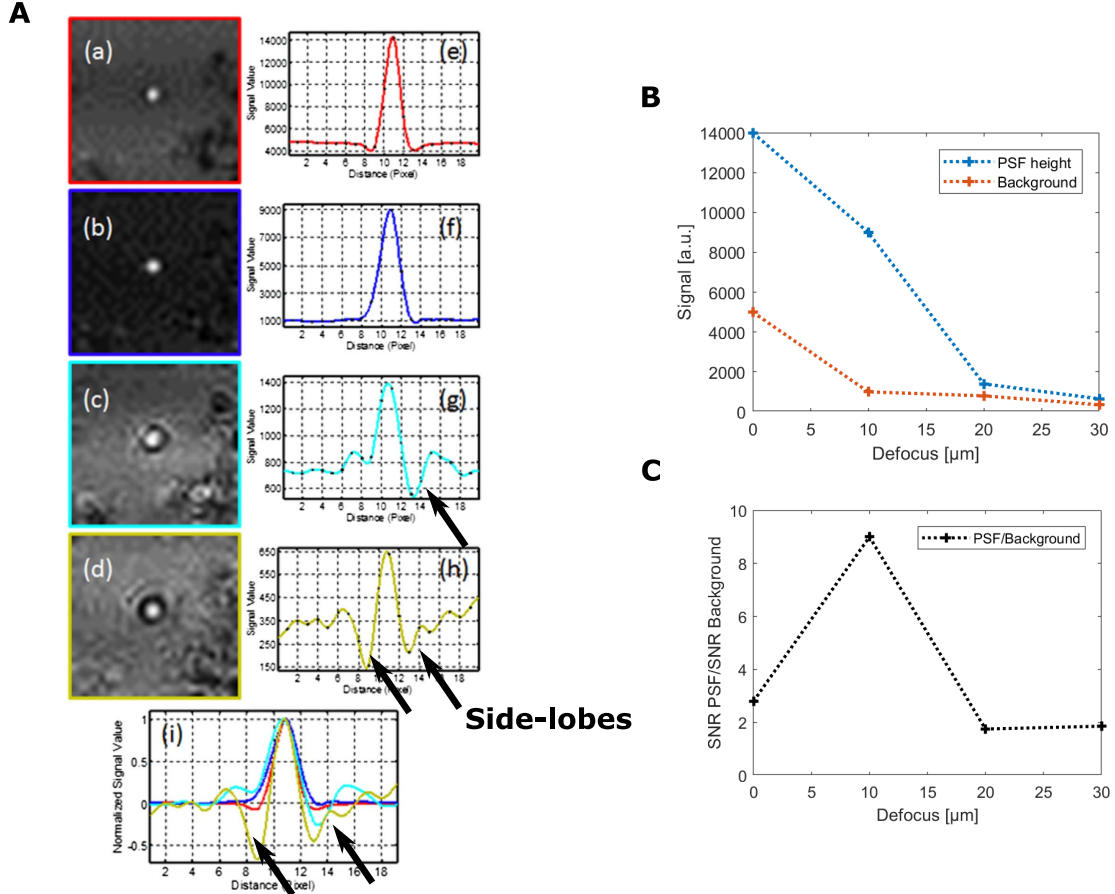
Fig. 4. FFOCT experiment results of gold nanoparticles by adding different levels of defocusing. (a)–(d) FFOCT images and (e)–(h) the corresponding intensity profile of a targeted nanoparticle are shown for (a) and (e) well-focused and defocused situations for (b) and (f) 10 μm, (c) and (g) 20 μm, and (d) and (h) 30 μm. Normalized PSF profiles are shown in (i), indicating that no obvious broadening is observed after inducing different level of defocus.

Fig. 4.15: Previous experiment suggesting that PSF width is robust against defocus in FFOCT. (A) Figure taken from [Xiao et al., 2016]. **(B)** PSF maximum and background level computed from (A). **(C)** Ratio of the PSF maximum and background level. This should remain constant and the pic for 10 μm suggests that something was wrong for the acquisition at this defocus position.

In this section I demonstrated the theory proposed by Victor Barolle [Barolle, 2019], which mitigates the previous claims that FFOCT is almost insensitive to aberrations [Xiao et al., 2016]. FFOCT is in fact to some extent less sensitive to aberrations than a conventional system but several artefacts such as contrast inversion and ringing can prevent to obtain clear images e.g. for retinal imaging with ocular aberrations. A mechanism to counteract these aberrations is therefore needed to perform near diffraction limited imaging of the retina in order to improve both the resoltution and the signal to noise ratio. Such approach is discussed in the following section.

4.4 Development of wavefront sensorless AO-FFOCT using an adaptive lens

In this section, I investigate various optimisation strategies in order to correct for wavefront distortion in FFOCT. Adaptive optics approaches were first demonstrated for conventional microscopy using a wavefront sensor in a closed loop fashion [Neil et al., 2000]. This technique was then applied for confocal microscopy [Booth et al., 2002] and OCT [Hermann et al., 2004][29]. In order to correct the wavefront I used the same adaptive lens as previously used to validate the model of how aberrations affects FFOCT. The wavefront correction is performed without measuring the wavefront but by measuring a quality criterion on the images, called a merit function. This merit function is sequentially optimized to correct for aberrations. Wavefront sensorless approaches were first developed for conventional microscopy [Débarre et al., 2007], two-photon microscopy [Débarre et al., 2009], OCT [Jian et al., 2014] and super-resolution microscopy [Booth et al., 2015]. Wavefront sensorless approaches present the advantage of being simpler and cheaper to implement, making them good candidates for clinical applications. The AL is quasi-conjugated in the pupil plane of the FFOCT sample arm for imaging a USAF target or in front of the eye for retinal imaging. I did not use a strict conjugation, even for microscopy testing because in the end the retinal setup for in vivo imaging would not have a strict conjugation. This is done to avoid relaying the AL in the pupil plane, which would need to be compensated in the reference arm, leading to a bigger and more complicated system. Our approach mimics prescription glasses where the correction is done ahead of the pupil plane without strict conjugation. This should work for correcting low spatial frequency modes such the ones corrected by the AL [Bonora et al., 2015].

4.4.1 Strategies for optimizing the wavefront

The general strategy to perform an optimization is to choose a basis and then explore the states space in this basis. In our case valid basis can be the set of actuators or the set of AL singular modes determined in the calibration step, see Appendix C. This basis will be explored and at each step an evaluation of the performance will be done using a merit function, typically corresponding to a criteria on the FFOCT image quality. There are several approaches that are used to perform such optimizations which can be classified in two classes depending on whether it computes the gradient of the merit function with respect to the basis coordinates. In our case, computing the gradient is both time consuming and cumbersome. Indeed, the AL is suffering from strong hysteresis, which means that evaluating the gradient shifts the current position and the optimization becomes very complicated. Our goal is to find an optimization scheme that is both fast (meaning minimal number of function evaluations) and reliable (meaning it finds an acceptable minimum). Several approaches are compared in the following sections.

Coordinate descent in actuator space

The first naive algorithm we can think of is optimizing each actuators individually one after each other. By sweeping each actuator across their admissible voltage range and keeping the best position before repeating the procedure to the next actuator we can reach an optimum. In order to find a good optimum, this procedure needs to be repeated several times. Such optimization strategies are commonly called coordinate descent algorithms.

---

[29]Historical developments of AO for microscopy can be found in [Booth, 2007]

An example of an optimization is shown Fig. 4.16 for a two steps optimization (each actuator is optimized sequentially twice). The signal to noise ratio is improved by 3 orders of magnitude. The number of iterations was quite high with around 600 function calls. In the following, this experiment will represent our gold standard in term of performance because this algorithm was able to converge even when starting with minimal signals, i.e. very far from the optimum. Note that at the end of the optimization procedure the merit function is decreasing even if the optimal voltages are kept. This could be due to the actuator hysteresis which prevent us to come back exactly to the optimally determined position. Also, by deforming the AL shape, its thickness can vary, hence the coherence plane can shift from the focal plane leading to FFOCT signal damping. This phenomenon makes it hard to find the optimal correction without any feedback on the reference arm position.

Fig. 4.16: Coordinate descent in actuator space results. Left: Optimization of the lens shape. Each actuator is optimized sequentially with 2 passes. - Right: Merit function (mean of 4 phases FFOCT image) evolution for each optimization step, corresponding to the left panel. Same colors represent same actuators.

Coordinate descent in AL singular space

Replacing the set of actuators by the set of singular modes (which look like Zernike polynomials, see Fig. C.4) we can follow the same procedure as the coordinate search but in the singular basis. The set of constraints must be adapted in order to stay in the allowed range of voltage for each actuator. This approach leads to poor performances well below the coordinate descent in actuator space. I think the reason behind is the actuator hysteresis which prevent to come back to the optimal position for each modes. Because the derivative of the merit function is greater for each step (see Fig. 4.17, especially for the blue modes), the hysteresis is more detrimental when using modes.
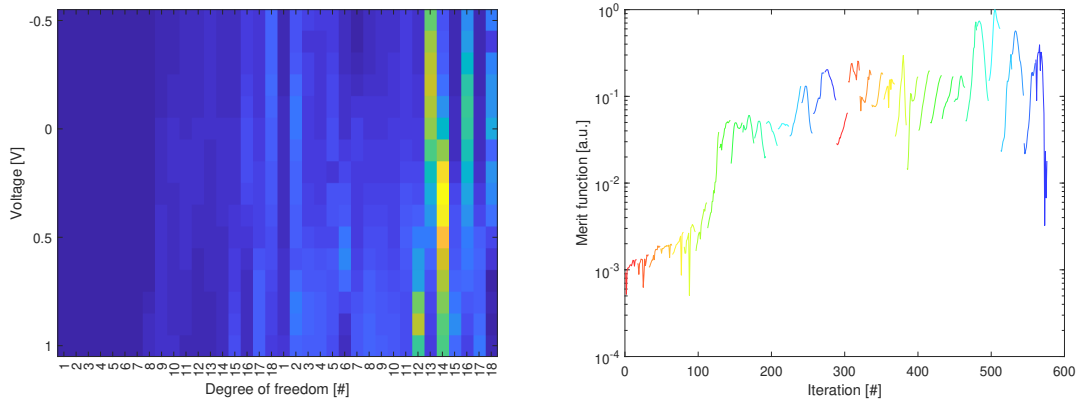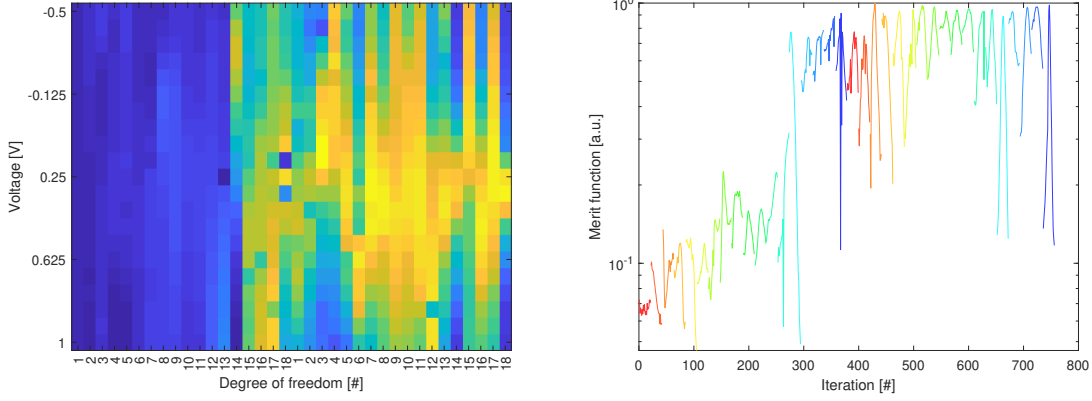
Fig. 4.17: Coordinate descent in AL singular space results. Left: Optimization of the lens shape. Each AL modes is optimized sequentially with 2 passes. - Right: Merit function (mean of 4 phases FFOCT image) evolution for each optimization step, corresponding to the left panel. Same colors represent same modes.

DONE algorithm

Instead of coordinate search, one can use more advanced strategies to reach the optimum. The Data-based Online Nonlinear Extremum seeker (DONE) models the unknown merit function and attempts to find an optimum of the underlying function [Verstraete et al., 2015, Verstraete et al., 2017, Bliek et al., 2018]. The DONE algorithm was developed for noisy functions such as experimental measurements and does not require derivatives. One of the advantages of DONE over similar algorithms, such as Bayesian optimization, is that the computational cost per iteration is independent of the number of function evaluations. The DONE algorithm is used to iteratively find a minimum of a merit function f (representing the FFOCT image quality) on a compact set $X \subseteq [V_{min}, V_{max}]^d$ (representing each actuator voltage, where d is the number of actuators) by updating a Random Fourier Expansion (RFE) $g(x) = \sum_{k=1}^{D} c_k cos(\omega_k^T x + b_k)$ at each new measurement (the computational limiting factor being the number of functions D that serves as surogate for the unknown function, the complexity scaling as $O(D^2)$), and using this RFE as a surrogate of the merit function f for optimization. It is assumed that the function f is unknown and only measurements perturbed by noise can be obtained: $y_n = f(x_n) + \eta_n$. The algorithm consists of four steps that are repeated for each new measurement:

1. At the start of iteration n, a new measurement $y_n = f(x_n) + \eta_n$ is taken at the point x_n. f representing a metric of the FFOCT image quality given the voltage x_n applied to the AL actuators.

2. Update the RFE model $g(x) = \sum_{k=1}^{D} c_k cos(\omega_k^T x + b_k)$ based on the new measurement from Step 1. Only the weights c_k are updated. The parameters ω_k and b_k stay fixed throughout the whole optimisation. ω_k are drawn from a zero-mean Gaussian probability distribution with variance σ_ω^2, whereas b_k are drawn from a uniform probability distribution in $[0, 2\pi[$.

3. After updating the RFE, an iterative optimization algorithm is used to find a (possibly local) minimum $\bar{x}_n$ of the RFE. All derivatives of the RFE can easily be calculated while not requiring extra measurements of f as in the finite difference method

which is faster than taking a new measurement. The initial guess for the optimization is the projection of the current measurement point plus a random perturbation $x_{init} = P_X(x_n + \zeta_n)$ where P_X is the projection onto the actuator voltage space X. The random perturbation prevents the optimization algorithm from starting exactly in the point where the model was trained. Increasing its value will increase the exploration capabilities of the DONE algorithm but might slow down convergence. ζ_n is chosen to be white Gaussian noise.

4. The minimum found in the previous step is used to update the RFE again. A perturbation is added to the current minimum to avoid the algorithm getting trapped unnecessarily in insignificant local minima or saddle points $x_{n+1} = P_X(\bar{x}_n + \xi_n)$. The random perturbations can be seen as an exploration strategy and are again chosen to be white Gaussian noise. Increasing their variance increases the exploration capabilities of the DONE algorithm but might slow down convergence. In practice, I use the same distribution for ξ and ζ. Finally, the algorithm increases n and returns to Step 1.

The performance of DONE depends on the following hyperparameters:

- Number of basis functions D. The influence of D is simple: increasing D will lead to a better RFE fit at the cost of more computation time. Hence, D should be set high enough in order to get a good approximation, but not too high to avoid unnecessarily long computation times (especially since the complexity is $O(D^2)$). D does not need to be very precise and overfitting should not be a concern for this parameter, since there is regularization.

- Regularization parameter λ used in the least square fit for finding the RFE coefficients c_k. It is used to prevent underfitting or overfitting of the RFE under noisy conditions or when dealing with few measurements.

- The probability density function of frequencies ω for the RFE model.

- The variance σ_ζ^2 of ζ and σ_ξ^2 of ξ. These parameters influences the exploration of both the RFE surrogate in Step 3 and of the original function in Step 4.

The DONE algorithm showed similar performances (same improvement in signal to noise ratio) as the coordinate search in actuator space. The convergence however was much faster with around 80 steps compared to 600 with our golden standard experiment. As long as the DONE parameters have been fine tuned by tries and errors, the convergence was satisfactory for microscopy and retinal imaging, as shown in the next section where using the DONE algorithm allowed us to optimize the wavefront for ocular aberrations in less than 1 second (8 seconds for coordinate descent). It is easier for subjects to keep still during 1 second than 8 seconds and therefore improved the quality and probability of convergence.
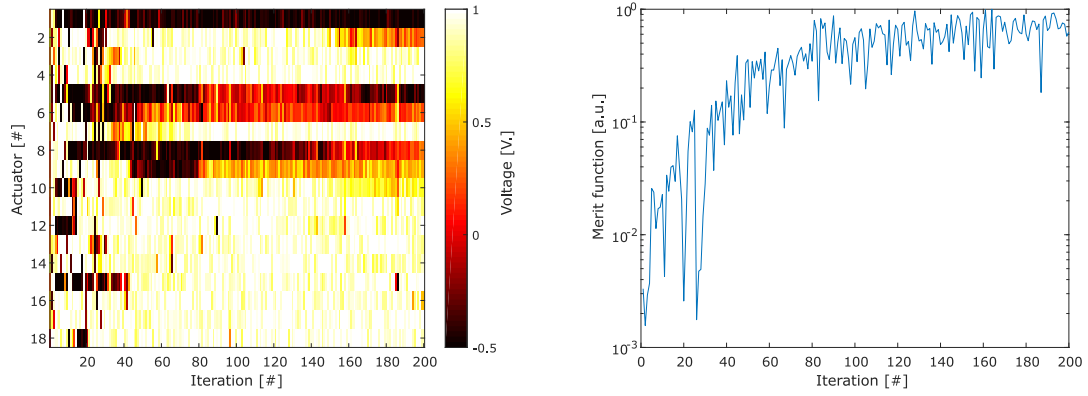
Fig. 4.18: DONE optimisation results. Left: actuators voltages during the optimisation process. - Right: Merit function (mean of 4 phases FFOCT image) evolution for each optimization step, corresponding to the left panel.

Other approaches

I also tested several optimization algorithms including interior-point [Mehrotra, 1992], sequential quadratic programming [Bonnans et al., 2006] (which is basically Newton's method with constraints) and active-set methods but the noisy nature of the measurements were leading to poor results with slow convergence.

4.4.2 Practical application for retinal imaging

Aberrations of the human eye

Ocular aberrations can be divided into static[30] and dynamic aberrations[31]. Static aberrations are routinely corrected using glasses and contact lens prescribed to correct mainly defocus and astigmatism[32] but rarely for higher order aberrations which need to be corrected for diffraction limited imaging of the retina, especially when the pupil is dilated[33]. The distribution of such static and dynamic aberrations are shown Fig 4.19 for a population of 50 healthy patients with a temporal resolution of 236 Hz [Jarosz et al., 2017]. Dynamic aberrations are mainly caused by tear film dynamics and micro-fluctuation of accommodation rather than fixational eye movement [Mecê et al., 2018]. Most of ocular aberrations are composed of low order aberrations, defocus and astigmatisms accounting for more than 92% of the total wavefront variance [Porter et al., 2001].

---

[30]Corresponding to the temporal average of ocular aberrations.

[31]Corresponding to the time variation of ocular aberrations.

[32]However prescribed correction have a precision of $\pm 0.125D$ [Thibos et al., 2002] which is not sufficient for diffraction limited imaging.

[33]Dilated pupils allow for a higher NA, hence a better theoretical resolution. It is known however that aberrations strength increase with the pupil size [Maguen et al., 2004] so that adaptive optics approaches are mandatory to resolve cellular features on the retina.
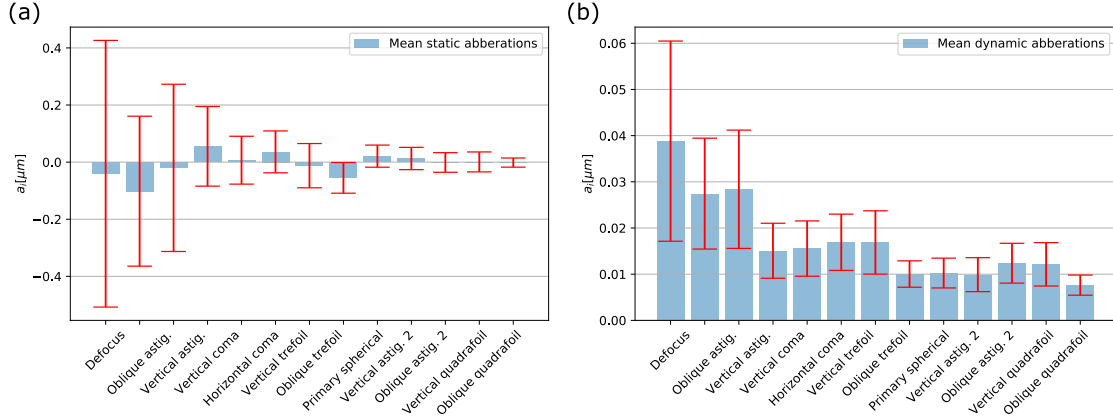
Fig. 4.19: Eye aberrations distribution on 50 healthy patients. (a) Mean static aberrations for each Zernike mode with error-bars computed as the standard deviation of each mode on the 50 patients. **(b)** Mean dynamic aberrations for each Zernike mode with error-bars computed as the standard deviation of each mode on the 50 patients. Data obtained from authors of [Jarosz et al., 2017].

Using the models presented in section 4.3 we can simulate retinal images that would be acquired using a conventional system (flood illumination opthtalmoscope) or an FFOCT system given the static and dynamic aberrations from one of the 50 patients. Simulation for static aberrations are shown Fig. 4.20 for conventional and FFOCT imaging. I plotted a radial averaging of the MTFs Fig. 4.20(d) in order to compare the different curves. At this step one can point out the following properties:

1. The diffraction limited MTF is above both curves: aberrations are only detrimental to an optical system.

2. The energy contained in both conventional and FFOCT MTF are equal[34] and because the MTF for FFOCT is less than 1 at the origin, higher frequencies have a better gain with respect to lower frequencies hence the resolution is usually better with FFOCT at the price of a signal loss.

3. The resolution defined as the frequency radius where 50% of the MTF energy is contained can be higher for FFOCT with aberrations because the MTF slope is lower. This does not mean that FFOCT probes more information but rather than the ratio of information from higher spatial frequencies over lower frequencies is higher, hence FFOCT provides better images as long as the SNR is sufficient.

---

[34]Indeed we have $|h^2| = |h^2|$ and then by applying Perseval equality we obtain $\int |\hat{h} * \hat{h}|^2 = \int |\hat{h} \otimes \hat{h}|^2$.
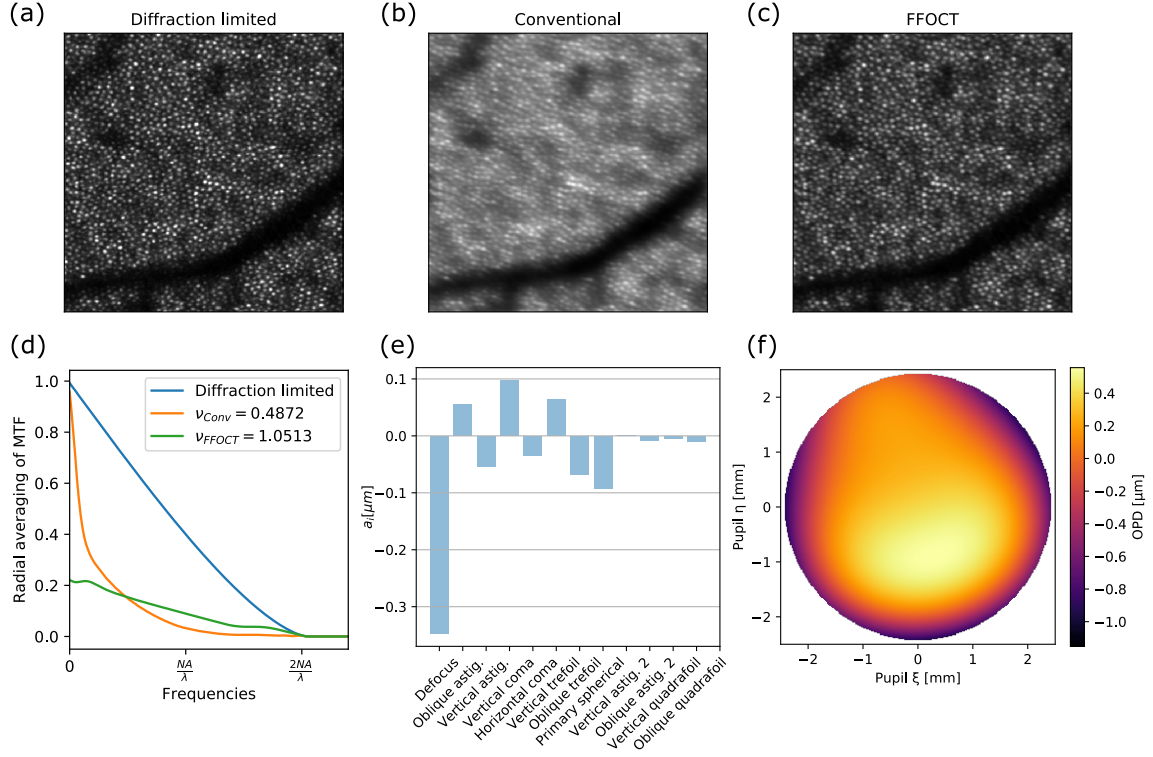
Fig. 4.20: Static ocular aberration simulation. **(a)** Diffraction limited image (acquired with an AO-SLO) which is used as reference image for the simulation. **(b)** Aberrated image simulated for a conventional imaging system. **(c)** Aberrated FFOCT image simulated with the presented model. **(d)** MTF radial averaging. ν is defined as the frequency radius where 50% of the MTF energy is contained normalized by the diffraction limited radius ($\nu = 1$ without aberration). In this case FFOCT performs twice better in terms of cutoff frequency. **(e)** Bar plots of Zernike polynomials coefficients and **(f)** associated wavefront.

These interesting properties are making FFOCT quite robust against ocular dynamic aberrations so that a slow adaptive correction is sufficient to maintain a diffraction limited resolution with sufficient signals. I simulated the dynamic aberrations[35] after correcting the 15 firsts Zernike polynomials below Maréchal criterion Fig. 4.21. After a few hundred milliseconds, photoreceptors are blurred on the conventional image while they are still distinguished with FFOCT after 3 seconds.

---

[35]Aberrations where measured at 236 Hz for 808 data points [Jarosz et al., 2017].
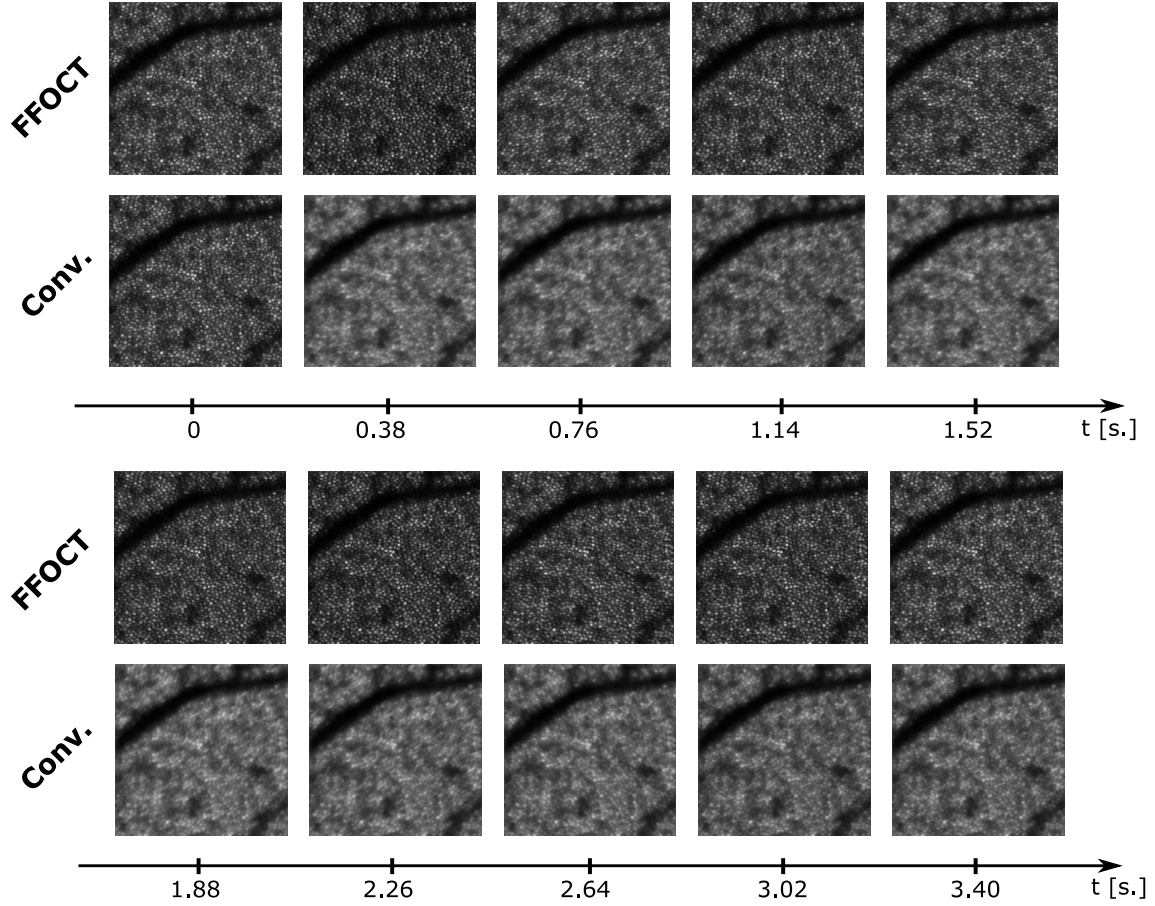
Fig. 4.21: Dynamic ocular aberration simulation. Top row are the simulated FFOCT images after initial correction of the 15 firsts Zernike modes. Bottom row are the corresponding simulation for conventional imaging.

Experimental setup and algorithms

Methods and experimental setup are presented in section 4.1 and [Mecê et al., 2020b]. Briefly, in the case of in vivo human retinal imaging, the subject is seated in front of the system depicted Fig. 4.22 and stabilized with a chin and forehead rest and asked to fixate a target placed at an infinite focal conjugate. Image acquisition is realized in a dark room in order to maximize natural pupil dilation. Phase modulation was performed by the residual axial motion after optical stabilization so that we don't need to modulate the PZT position. Image sequences were composed of 150 images acquired at 300 Hz. Images without signals are automatically removed from the acquired stack before registration and averaging. The FFOCT camera worked close to saturation to use the whole full well capacity, decreasing relative importance of shot noise. During image acquisition, the total power entering the eye from the FFOCT illumination source and the SD-OCT scanning source were respectively 1.3 mW (for 0.5 s) and 0.25 mW (continuous scanning), which are below the ocular safety limits established by the ISO standards for group 1 devices. Fig. 4.22 presents the schematic of the custom-built FFOCT system coupled through a dichroic mirror with a Thorlabs Ganymede-II SD-OCT system. The FFOCT comprises a LED with $\lambda_c = 850$ nm center wavelength and 30 nm bandwidth (M850L3, Thorlabs), used as a spatially incoherent illumination source, giving a theoretical axial resolution of approximately 8 μm in water. The LED is focused by a condenser $f = 20$ mm in front

of the eye's pupil. A physical diaphragm is positioned in front of the LED, conjugated to the retina and the FFOCT reference mirror. The illumination beam is split into the reference and the sample arms by a 50:50 cubic beam splitter (BS). For the reference arm, an Olympus 10X/0.25 NA Plan Achromat objective is used with a silicon mirror placed at the focal plane of the objective. The whole reference arm (microscope objective and silicon mirror) is mounted on a fast voice-coil translation stage (X-DMQ12P-DE52, Zaber Technologies Inc.), allowing for adjustment of the coherence gate position. The FFOCT light beam arrives with an 8 mm diameter in the eye's pupil. The back-scattered photons from both arms are recombined by the same BS and focused onto a high-speed (up to 720 Hz at full-frame) CMOS camera (Q-2A750-Hm/CXP-6, Adimec) for FFOCT imaging. In the case of in vivo retinal imaging, the SD-OCT and the voice-coil translation stage were used to measure and correct for involuntary axial eye movements during the imaging acquisition in a closed-loop fashion.
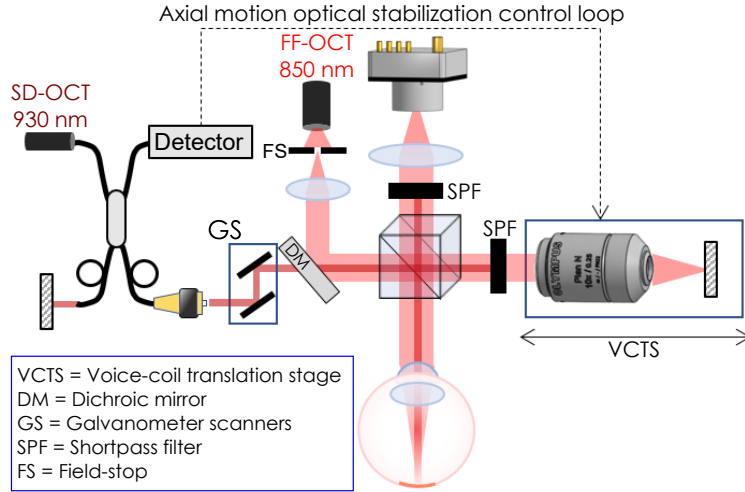
Fig. 4.22: Schematic drawing of the custom-built FFOCT system coupled with an SD-OCT for real-time axial tracking and FFOCT coherence gate positioning guidance.

In order to perform the correction for retinal imaging, consistent images must be acquired. The issue is that in order to get consistent images, the adaptive correction is needed to increase the signal to noise ratio. FFOCT images can therefore not be used to perform the correction because the signal to noise ratio is too low to reliably initialize the correction. Also, FFOCT images contains several megapixels and are therefore slower to process, which would reduce the speed of the adaptive correction. To overcome this issue, the idea is to use the axial tracking device, an SD-OCT, as a surrogate of the FFOCT. Indeed, SD-OCT can be consistently acquired and the optimisation can be performed for a given layer, increasing the chances of getting more signals in the imaged layer. One of the tricky part is to design a metric to be optimized on the SD-OCT signals that will also jointly optimize the FFOCT signals. Wavelength of both modalities are 50 *nm* apart, which only represents 5.9% of the central wavelength. The difference in wavelength should therefore have little to no effects on the correction performance. Then, because the image formation is different for both imaging modalities [Tricoli and Carminati, 2019, Barolle, 2019], the merit function must be wisely chosen to satisfy both imaging condition. First, we tested two naive approaches. We considered the total energy in the SD-OCT B-Scan (which was primarily averaged over the lateral dimension, so that we obtained a spatially averaged

A-Scan) and the maximum of the SD-OCT signals (which often corresponds to the IS/OS junction). The results we obtained with these were acceptable (good convergence and gain) for the USAF target and the model eye, but for in-vivo the convergence was more random, often leading to an increase of the the SD-OCT signals, but losing on the resolution, which indicates that we found a local minimum with good SNR but aberrations remained. These aberrations were probably more detrimental on the FFOCT which led to difficulties in acquiring images. In order to overcome this issue I designed a hybrid metric $\mathcal{L}$ with a penalization on the peak width, see Fig. 4.23(c):

$$\mathcal{L} = max(\text{SD-OCT}) \times \left(1 + \frac{\alpha}{width(\text{SD-OCT})} \right) \tag{4.37}$$

where α is a regularization parameter that was set close to 1. This hybrid metric $\mathcal{L}$ can be applied for any layer of interest to automatically adjust the lens shape to focus the beam on said layer.
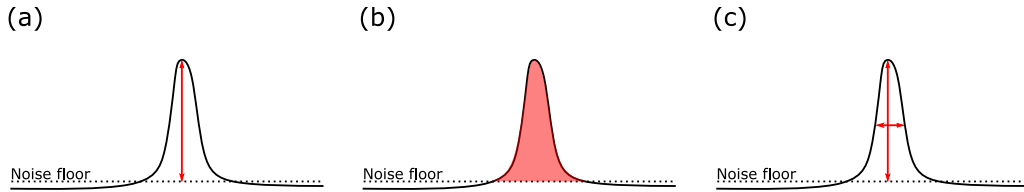
Fig. 4.23: Different metrics used for optimizing FFOCT signals and correcting aberrations. (a) Peak height. (b) Total energy. (c) Hybrid metric combining peak height and peak width

I compared the aberration correction performance using the FFOCT and the SD-OCT as a surrogate for the sensorless optimisation, see Fig. 4.24. To do so, I induced a strong aberration and then corrected it with coordinate descent in actuator space using either the hybrid metric function on the SD-OCT signals shown Fig. 4.23(c) or the average amplitude in the FFOCT amplitude image. Both optimisation methods performed similarly (approximately the same number of steps and same gain on FFOCT amplitude image), however it was around 1000 times faster using the SD-OCT signals as it is faster to acquire and process.
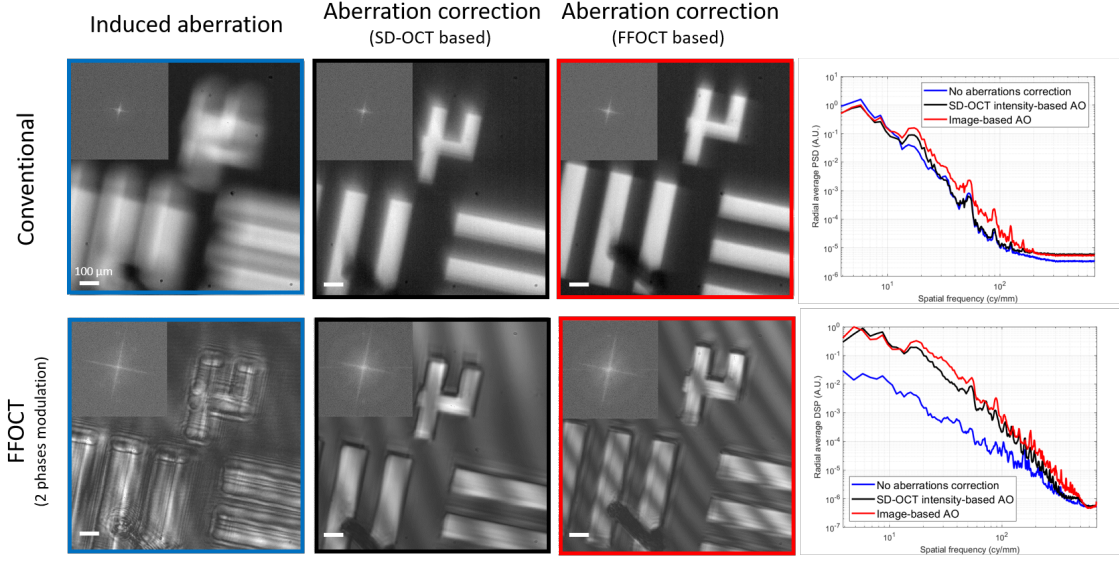
Fig. 4.24: Comparison of wavefront optimisation using FFOCT or SD-OCT signals. The top row shows the conventional images before and after optimisation using B-Scans from the SD-OCT or en face amplitude images from FFOCT. The bottom row shows the corresponding amplitude FFOCT images. Both optimisation approaches show similar quality improvement on FFOCT amplitude images, as highlighted by the PSD insets for each image and the PSD radial averaging on the right.

4.4.3   Results: better SNR and images of nerve fiber layer

I started by imaging a 30 years old subject with a dilated pupil (7.5 mm) who had LASIK surgery, resulting in important amount of high order aberrations, especially at full pupil size. Without correcting the wavefront and even-though this subject had a good sight with regular sized pupil, there are almost no signals on the FFOCT image Fig. 4.25(a) with the AL resting in its flattened state. One can only guess the vessel in the middle of the frame. After optimizing the wavefront[36] we observed a 10-fold improvement in signal strength[37] Fig. 4.25(b). Even without strict pupil conjugation, the adaptive correction was valid for the whole FOV, see Fig. 4.25(c) where one can see the cone mosaic on the 1×1 mm^2 FOV. This is, to the best of my knowledge, the largest FOV of the retina acquired on a single frame with cellular resolution. Other adaptive optics techniques are currently limited by the eye isoplanetic patch to around 0.5×0.5 mm^2 FOV [Bedggood et al., 2008, Han et al., 2018]. The adaptive correction is usually done using a guiding star on the retina and the resolution will degrade in the field of view farther from the guiding star. In order to overcome this limitation, multi-conjugate AO was proposed [Thaung et al., 2009, Laslandes et al., 2017] using several guiding stars and two optical adaptive elements. At the expense of an increased complexity, these systems can obtain near diffraction limited images of the retina on 1.5×1.5 mm^2. Another possibility is to reduce the pupil size in order to lower aberrations effects. By limiting the pupil size to 5 mm the commercial device RTX1 (flood illumination camera) achieve near diffraction limited resolution on 1×1 mm FOV. Finally, computational aberrations correction can be performed sequentially for different spatial patch on the FOV and achieve near diffraction limited imaging on arbitrary sized

---

[36]It took 0.8 s using DONE algorithm on the hybrid metric $\mathcal{L}$

[37]I can't compute the signal to noise ratio improvement as it would require dividing by 0 in this case.

FOV [Sudkamp et al., 2018].

We imaged a second subject (25 years old) with (1.5D x 0.5D x 160°) prescribed correction with dilated pupil (7 mm). In order to compare the AL approach with regular prescription glasses we imaged this subject without any correction, with her prescription glasses and with the AL approach. For each acquisition we plotted the radial averaging of the spatial frequency PSD where the spatial frequency linked to the photoreceptor mosaic is clearly visible after optimization Fig. 4.25(d). Without correction no signals could be acquired and with her regular glasses, signals were very low. This experiment suggests that the AL approach can effectively correct for higher orders modes not corrected by prescription glasses, hence improving image SNR and acquisition consistency. We obtained consistent images of the photoreceptor layer on this subject from 0° temporal to 8° temporal, allowing us to explore a large area of the retina with diffraction limited resolution in only 3 acquisitions to cover approximately 3 mm^2, see Fig. 4.25(e-g).
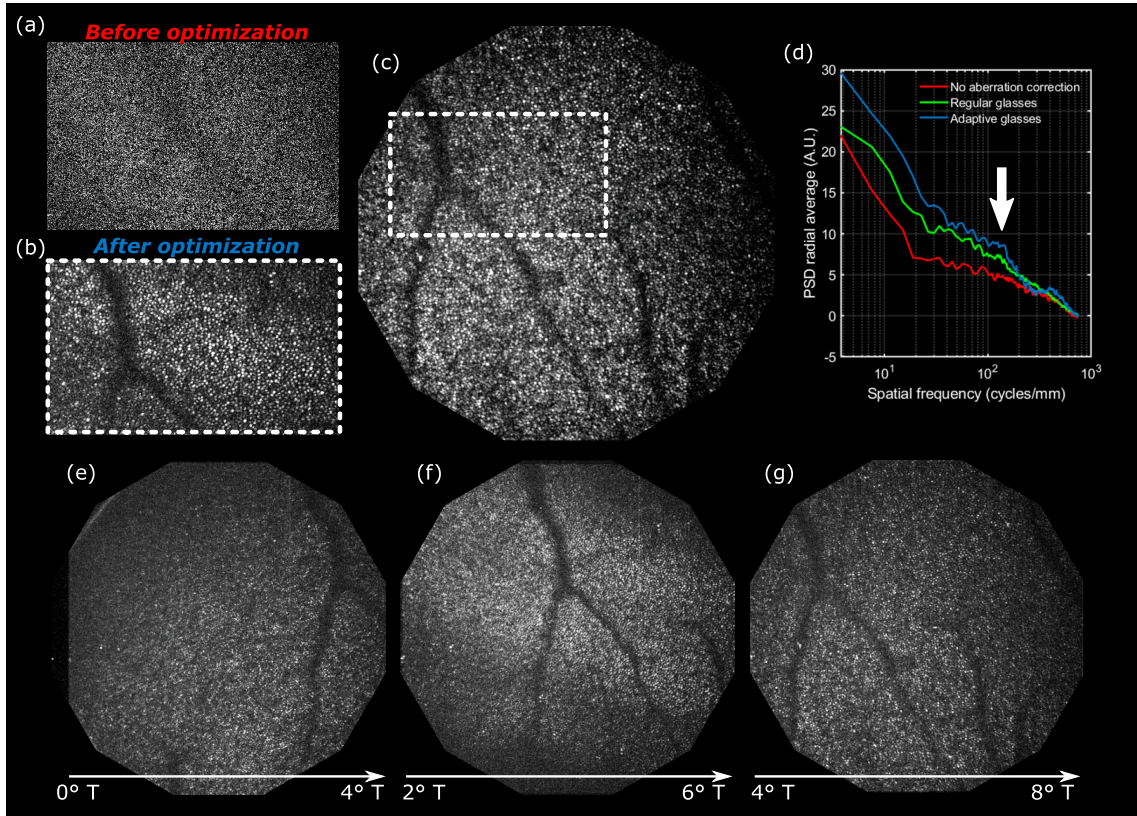
Fig. 4.25: AO-FFOCT acquisition of the photoreceptors. **(a)** FFOCT image with the AL resting flat and **(b)** after optimization. The correction is valid for a large FOV of $1 \times 1~mm^2$ **(c)**. A second subject with (1.5D x 0.5D x 160°) prescribed correction was imaged without correction, with her prescription glasses and with the AL approach and the radial averaging of the PSD was computed **(d)** and show the superior results using the AL. The white arrow indicates the spatial frequency linked with the photoreceptor mosaic. Finally we imaged this subject from 0°temporal to 8°temporal **(e-g)** in only 3 acquisitions.

Owing to the AL capability to optimize the signal for any given layer visible on the SD-OCT, we could obtain FFOCT images for the first time on the nerve fiber layer (NFL) at multiple depths in vivo. The SD-OCT B-Scan acquired with the lens resting in its flat state

is shown Fig. 4.26(a). After optimizing on the NFL layer, signals from this layer became much stronger on the SD-OCT B-Scan Fig. 4.26(b) and we could acquire FFOCT images for 3 different depths Fig. 4.26(d-f). In these images one can see a capillary plunging from the top of the NFL to the bottom. This capillary is nowhere visible on the SD-OCT B-Scan because of its small thickness. The blood flow in the capillary was visible but automatic computation of the blood flow velocity failed because signals were too low in each frame to perform such analysis. Optimizing the AL for the photoreceptor layer Fig. 4.26(c) we could acquire the photoreceptor mosaic Fig. 4.26(g) during the same acquisition session paving the way for 3D high resolution imaging with FFOCT.
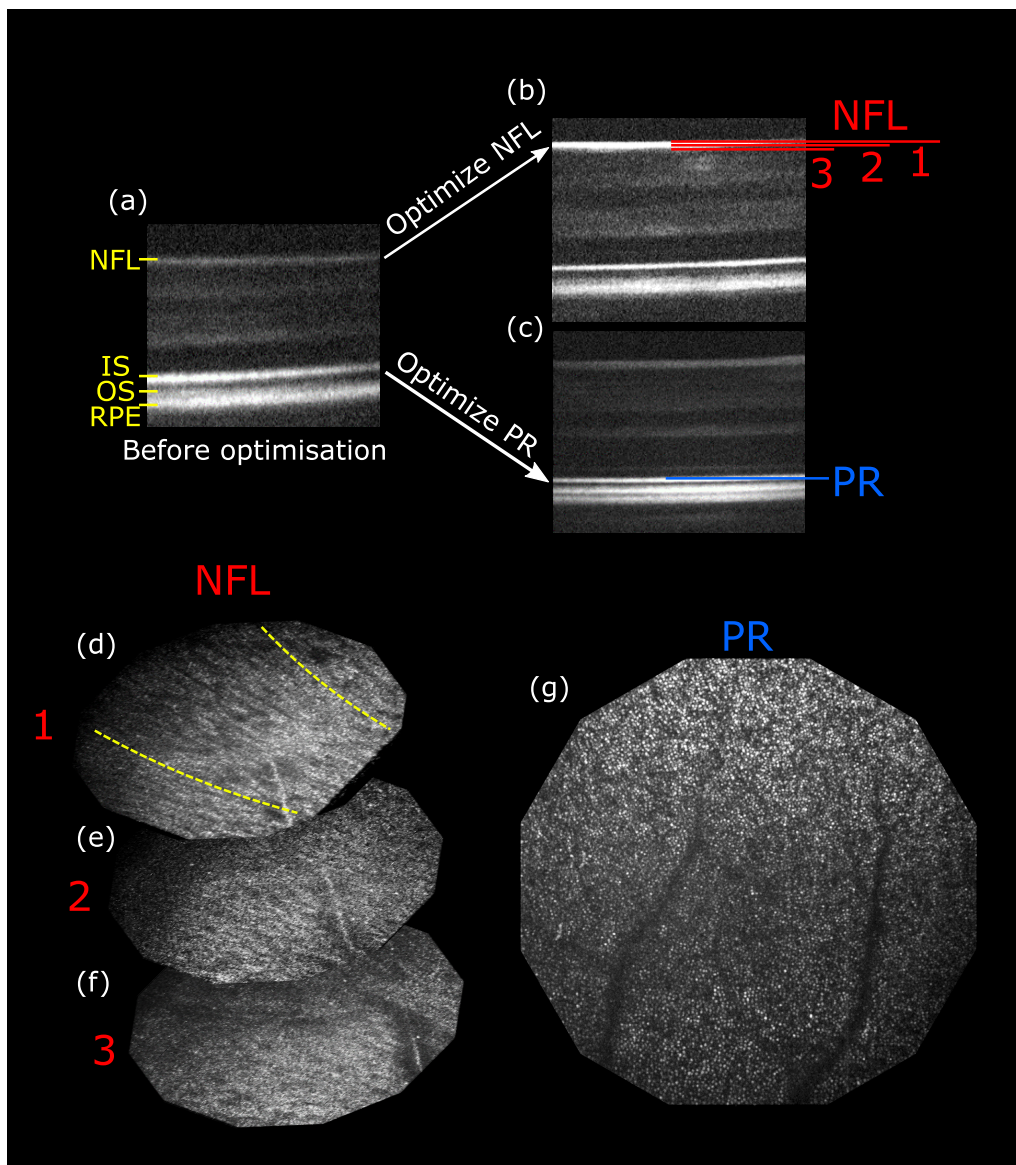
Fig. 4.26: AO-FFOCT acquisition of the NFL. (a) SD-OCT B-Scan before optimization and after optimization on the NFL **(b)** and photoreceptor layer **(c)**. **(d-f)** FFOCT images of the NFL were acquired at 3 different depths. Fibers orientations on the top layer are highlighted with yellow dashed lines. **(g)** FFOCT image of the photoreceptor layer was acquired during the same imaging session.

Chapter 5

From signals to diagnostics

Contents

5.1 Motion tracking using FFOCT

Part of the work presented in this thesis was aiming at measuring fluctuations and construct images based on fluctuations properties. For some applications it was even of great interest to measure the fluctuation of fluctuations. Such applications can be the study of wound healing or the imaging of blood flow. In each case, these applications felt into motion tracking where the aim is essentially to locate and follow a particle or cell between several images. Quantitative measurements such as velocity maps can then be constructed by analyzing many particles.

5.1.1 Article: Probing dynamic processes in the eye at multiple spatial and temporal scales with multimodal full field OCT

In this paper, motion tracking was first applied to measure corneal wound healing ex vivo on a macaque retina on D-FFOCT images. In Section 3.2, I scraped the cornea with metallic tweezers and imaged the wound during nearly two hours and observed the healing with epithelial cell migrating towards the center of the wound to close it. In order to measure the migration velocities, I computed the optical flow[1] [Horn and Schunck, 1981] which is an ill-posed problem because it has more unknowns than equations[2]. In order to be able to compute the optical flow I used the Horn-Shunck method which is explained in detail in Section 2.5. Finally, migration velocities matching with existing

---

[1] The optical flow computation results in a dense association of a pixel between two images so that each pixel in an image is associated with another pixel in a second image, giving the displacement for each pixel.

[2] This is known as the aperture problem.

studies were found. In this article we also measured blood flow velocity in the conjunctiva on a FFOCT movie acquired by my fellow colleague Viacheslav Mazlin on his experimental setup dedicated to in vivo human corneal imaging. We were able to measure red blood cell velocity by constructing a Kymograph plot which was cumbersome and not automatable. Later I found a way to make it automatically and generated angiography images, see section 5.1.2.

Probing dynamic processes in the eye at multiple spatial and temporal scales with multimodal full field OCT

JULES SCHOLLER,[1] VIACHESLAV MAZLIN,[1] OLIVIER THOUVENIN,[1] KASSANDRA GROUX,[1,2] PENG XIAO,[3] JOSÉ-ALAIN SAHEL,[4,5,6] MATHIAS FINK,[1] CLAUDE BOCCARA,[1,2] AND KATE GRIEVE[4,5,*]

[1]*Institut Langevin, ESPCI Paris, CNRS, PSL University, 1 rue Jussieu, 75005 Paris, France*
[2]*LLTech SAS, 29 Rue du Faubourg Saint Jacques, Paris, 75014, France*
[3]*Zhongshan Ophthalmic center, Sun Yat-sen University, Guangzhou, China*
[4]*Vision Institute/CIC 1423, UPMC-Sorbonne Universities, UMR_S 968/INSERM, U968/CNRS, UMR_7210, 17 Rue Moreau, Paris, 75012, France*
[5]*Quinze-Vingts National Eye Hospital, 28 Rue de Charenton, Paris, 75012, France*
[6]*Department of Ophthalmology, University of Pittsburgh School of Medicine, Pittsburgh, PA 15213, USA*
[*]*kategrieve@gmail.com*

Abstract: We describe recent technological progress in multimodal en face full-field optical coherence tomography that has allowed detection of slow and fast dynamic processes in the eye. We show that by combining static, dynamic and fluorescence contrasts we can achieve label-free high-resolution imaging of the retina and anterior eye with temporal resolution from milliseconds to several hours, allowing us to probe biological activity at subcellular scales inside 3D bulk tissue. Our setups combine high lateral resolution over a large field of view with acquisition at several hundreds of frames per second which make it a promising tool for clinical applications and biomedical studies. Its contactless and non-destructive nature is shown to be effective for both following in vitro sample evolution over long periods of time and for imaging of the human eye in vivo.

1. Introduction

Optical coherence tomography (OCT) is used in the biomedical field to image microstructures in tissue using mostly the endogenous backscattering contrast [1, 2]. Full-field optical coherence tomography (FFOCT) is an *en face*, high transverse resolution version of OCT [3, 4]. Using incoherent light sources, two-dimensional detectors and a time-domain phase stepping scheme, FFOCT acquires en face oriented virtual sections of the sample at a given depth and has been used for biology [5], and medicine [6]. Recently, new multimodal techniques, based either on OCT or FFOCT, have enabled the study not only of the static 3D morphology of a sample but also of the dynamics of its scatterers [7, 8] by measuring phase-sensitive temporal fluctuations of the backscattered light. In ex-vivo fresh unfixed tissues, these dynamic techniques reveal subcellular structures that are very weak backscatterers and provide additional contrast based on their intracellular motility [9, 10]. FFOCT multimodal techniques can also detect collective subcellular motion of scatterers resulting from either static deformations or propagating elastic waves for mapping elastic properties or flow of cells in capillaries [11, 12]. Complementary contrast from dynamic and static properties coupled in a multimodal setup with high resolution FFOCT thus enables noninvasive visualization of biological tissue, microstructural, morphological and dynamic properties at the cellular level without the use of exogenous markers. Nevertheless, in order to achieve identification of specific molecular structures, OCT images often need to be compared with fluorescence images or stained histology slides to understand and identify the

observed microstructures. Indeed, fluorescence microscopy reveals molecular contrast using dyes or genetically encoded proteins that can be attached to a specific structure of interest and/or monitor changes of the biochemical properties of the tissue. Structured illumination microscopy (SIM) [13–15], a full-field version of confocal microscopy, can perform micrometer scale optical sections in a tissue and has been coupled to static and dynamic FFOCT (D-FFOCT) [16, 17] to allow simultaneous coincident multimodal fluorescence and FFOCT acquisitions.

OCT and FFOCT are often used in tissue to overcome the difficulties linked to scattering induced by small scale refractive index discontinuities, but large-scale discontinuities are also present and induce aberrations that could affect the resolution [18]. Recently, we have demonstrated that low order geometrical aberrations do not affect the point spread function (PSF) but mostly reduce the signal to noise ratio (SNR) when using interferometry with a spatially incoherent source [18, 19]. This allows us to achieve resolution of cone photoreceptors in vivo in the human retina without adaptive optics [19].

In vivo imaging, and detection of in vitro subcellular dynamics, would not have been possible using FFOCT without recent technological advances in detector technology that we will evaluate for static and dynamic FFOCT cases. Although we have developed different multimodal FFOCT-based biomedical imaging applications in oncology [20], embryology, cardiology and ophthalmology [21–23], we will restrict the field of the present paper to new results obtained in ophthalmology. We will discuss the technical issues of sample immobilization for in vitro and ex vivo imaging, along with processing methods that were applied for the first time in FFOCT leading to the first dynamic 3D reconstruction with sub-micron resolution of a macaque retinal explant. An axial sub-micron plane locking procedure is presented to image the same sample plane over several hours in a time-lapse fashion, and applied to image slow wound healing on a macaque cornea. Quantitative methods derived from computer vision were adapted to produce a cell migration map with micrometer resolution. We also introduce a combined posterior/anterior eye imaging setup which in addition to traditional FFOCT imaging offers the possibility to measure the blood flow in the anterior eye that compares favorably to existing techniques [24–26]. Finally, an approach that combines fluorescence labeling for live cells with static and dynamic FFOCT is presented.

2. Methods

Although the principle of OCT is mature and well established, it is still an active area of research where improvements mainly rely on hardware performance. In the case of FFOCT, the camera performance is critical to achieve sufficient single shot sensitivity for imaging 3D biological samples with low reflectivity such as cornea and retina in depth. Recently, a new sensor with an improved full well capacity (FWC) combined with faster electronics allowed faster acquisition with better SNR. The gain in speed is of critical importance when it comes to imaging moving samples, whereas the improvement in SNR is particularly important to image weakly reflective samples in-depth. With the recent development of D-FFOCT, the need for a high FWC camera is even greater as the dynamic fluctuations probed are weaker than the static signals, due to the small size of the moving scatterers. Also the setup stability needs to be studied to ensure that the measured dynamics are in the sample and are not caused by artifactual mechanical vibrations.

2.1. Signal to noise ratio in FFOCT

Two FFOCT modalities were used throughout this work - static images were acquired using a two phase scheme and dynamic images are processed using a stack of direct images - and in both cases the camera is used close to saturation in order to use the whole FWC. For a two phase acquisition, two frames are recorded with a π-shift phase difference. The intensity recorded on a camera pixel is the coherent sum of the reference and sample beams (which contains coherent

and incoherent terms) and can be written:

$$I_{\Phi=0} = \eta \frac{I_0}{4}(R + R_{incoh} + \alpha + 2\sqrt{R\alpha}cos(\Delta\phi)) \tag{1}$$

$$I_{\Phi=\pi} = \eta \frac{I_0}{4}(R + R_{incoh} + \alpha - 2\sqrt{R\alpha}cos(\Delta\phi)) \tag{2}$$

where $I_{\Phi=0}$ is the intensity recorded without phase shift, $I_{\Phi=\pi}$ is the intensity recorded for a π phase shift, η is the camera quantum efficiency, I_0 is the power LED output (we considered a 50/50 beam-splitter), α is the reference mirror reflectivity (i.e. the power reflection coefficient), R is the sample reflectivity (i.e. the power reflection coefficient), $\Delta\phi$ is the phase difference between the reference and sample back-scattered signals, $I_{incoh} = R_{incoh}I_0/4$ is the incoherent light back-scattered by the sample on the camera, mainly due to multiple scattering and specular reflection on the sample surface. The static image is formed by subtracting $I_{\Phi=\pi}$ from $I_{\Phi=0}$ and taking the modulus:

$$I_{2-phase} = \eta I_0 \sqrt{R\alpha}|cos(\Delta\phi)| \tag{3}$$

For a 2-phase scheme it is not possible to un-mix amplitude and phase. To get rid of the cosine term we consider that the phase is uniformly distributed (both in time and space) in biological samples and we can average $I_{2-phase}$ with respect to the phase distribution:

$$< I_{FFOCT} > = \eta I_0 \sqrt{R\alpha} \frac{1}{2\pi} \int_0^{2\pi} |cos(\Delta\phi)|d\Delta\phi = \frac{2\eta I_0 \sqrt{R\alpha}}{\pi} \tag{4}$$

Returning to the recorded intensity I_Φ, the terms related to sample arm reflectivity are negligible compared to the incoherent and reference terms so the intensity corresponding to pixel saturation I_{sat} can be written:

$$I_{sat} \approx \frac{\eta I_0}{4}(\alpha + R_{incoh}) \tag{5}$$

Combining Eq. 4 and Eq. 5 we obtain:

$$< I_{FFOCT} >= \frac{8I_{sat}\sqrt{R\alpha}}{\pi(\alpha + R_{incoh})} \tag{6}$$

If we consider an ideal case when the experiment is shot noise limited, the noise is proportional to $\sqrt{I_{sat}}$, which gives the following signal to noise ratio:

$$SNR_{2-phase} \sim \frac{8\sqrt{R\alpha I_{sat}}}{\pi(\alpha + R_{incoh})} \propto \sqrt{I_{sat}} \tag{7}$$

The SNR is proportional to $\sqrt{I_{sat}}$ and is therefore proportional to the maximal number of photoelectrons that a pixel can generate before saturation, which is the definition of the FWC. Thus the SNR is proportional to the FWC for a 2-phase FFOCT image. D-FFOCT images are computed by taking the temporal standard deviation of the signal, see Section 2.4. We consider that both the local reflectivity and phase can fluctuate. The noise term remains the same, as we also work close to saturation during dynamic acquisitions. The measured intensity can then be written:

$$I_{dynamic} = SD\left(\frac{\eta I_0}{2}\sqrt{R(t)}\alpha cos(\Delta\phi(t))\right) \tag{8}$$

$$= \frac{2I_{sat}}{\alpha + R_{incoh}}SD\left(\sqrt{R(t)}\alpha cos(\Delta\phi(t))\right) \tag{9}$$

Where SD is the standard deviation operator. The dynamic SNR can therefore be written:

$$SNR_{dynamic} \sim \frac{2\sqrt{I_{sat}}}{\alpha + R_{incoh}} SD\left(\sqrt{R(t)\alpha} cos(\Delta\phi(t))\right) \propto \sqrt{I_{sat}} \qquad (10)$$

Eq. 10 shows that the camera FWC also limits the SNR in D-FFOCT experiments. One can argue that averaging several FFOCT images could be a workaround for 2-phase images. Considering the case of a weakly reflective sample (e.g. cornea and retina) and a moving sample (e.g. the eye) then one needs to have sufficient signal to perform registration before averaging, therefore SNR on single frames is of great importance and thus all experiments are conducted with the camera working close to saturation.

2.2. Improving signal to noise ratio and speed

The most widely used camera for FFOCT (MV-D1024E-160-CL-12, PhotonFocus, Switzerland) has a 2×10^5 electrons FWC with a maximum framerate of 150 $frame.s^{-1}$ at 1024×1024 pixels. With $\alpha = 0.08$ (as we typically use 4% to 18% reflectivity mirrors) it leads to a 70 dB sensitivity for a 2-phase image reconstruction with 75 processed $images.s^{-1}$. Averaging 100 images with this camera takes just over 1 second and leads to a 90 dB sensitivity. A major recent change in our setups has been the introduction of a new camera, specifically designed for FFOCT requirements (Quartz 2A750, ADIMEC, Netherlands) that has a maximum framerate of 720 $frame.s^{-1}$ at 1440×1440 pixels and a 2×10^6 FWC. With the new camera characteristics, it is possible to achieve 83 dB sensitivity for a 2-phase image reconstruction. Acquiring and averaging 100 images takes under 0.2 second and leads to 103 dB sensitivity. This result brings the SNR of FFOCT and the speed per voxel in *en-face* views up to the typical range of conventional OCT systems, but with a better transverse resolution given by the NA of the objective. Aside from SNR improvement, the second major advantage of this new camera is its acquisition speed. Speed is an important issue for detection of in vitro subcellular dynamics, and crucial to in vivo eye examination. Indeed, in contrast to scanning OCT setups, FFOCT requires the acquisition of a full megapixel image in a single shot, and the signal can be lost if a lateral displacement occurs between two successive images. This typically imposes a minimum acquisition speed higher than 200 $frames.s^{-1}$ as eye motions are mainly below 100 Hz [27, 28], a condition that is easily met by the new camera which offers 720 $frames.s^{-1}$.

2.3. Improving sample stability

Previously described in vitro imaging setups [10, 16] were mounted vertically with the sample placed under the objective and imaged from above, see Fig. 1(a). This setup consists of a Linnik interferometer with an excitation source (M405L3, Thorlabs) for fluorescence imaging and an FFOCT source (M660L3, Thorlabs). Illumination paths are combined and separated using dichroic filters. Both sample and reference arms are mounted on translation stages (X-NA08A25, Zaber Technologies). In addition, the reference mirror is mounted on a piezoelectric translation stage (STr-25, Piezomechanik) for phase-shifting. In this configuration, in order to image fresh ex-vivo samples in immersion, we had to fix them in place using a 3D printed mounting system with transparent membrane covering and gently restraining the sample in order to prevent any movement during imaging. To facilitate imaging of cell cultures that are directly adhered to the base of a dish, and to use gravity to assist immobilization for other tissue samples, we have built a new system in an inverted configuration where the sample is directly placed on a coverslip and imaged from beneath with high-numerical-aperture oil-immersed objectives, see Fig. 1(b). This setup is mounted with the same parts as the previous one, except that it does not feature fluorescence measurement capabilities and is mounted horizontally, with the sample arm mounted vertically. The main advantage is that the sample is held motionless by gravity and is naturally as flattened as possible (thus providing a flat imaging plane) against the coverslip

surface without applying compression. Despite these efforts to immobilize the sample, axial drift on the micrometer scale over long periods of time can occur in either configuration. In order to compensate for the axial drift we introduced an automated plane locking procedure based on static FFOCT image correlation around the current position, see Fig. 1(d). FFOCT images are acquired over an axial extent of 10 μm, taking 0.5 μm steps with the sample translation stage, and are then cross-correlated with the target image. The sample is then axially translated to the position corresponding to the maximum of the cross-correlation, which was typically between 0.5-0.8. After each plane correction procedure, a new FFOCT image is taken as target for the next correction in order to account for evolution in the sample position. This procedure was performed every 10 minutes. We observed that for long acquisitions of several hours, the time between autofocus procedures could be increased as we reached a quasi-equilibrium state. Using this procedure we are able to image the same plane in biological samples over a day. The in vivo imaging was performed according to procedures already described in [23] which essentially acquire images in a plane chosen by visual inspection of the live image, and did not include active plane locking.
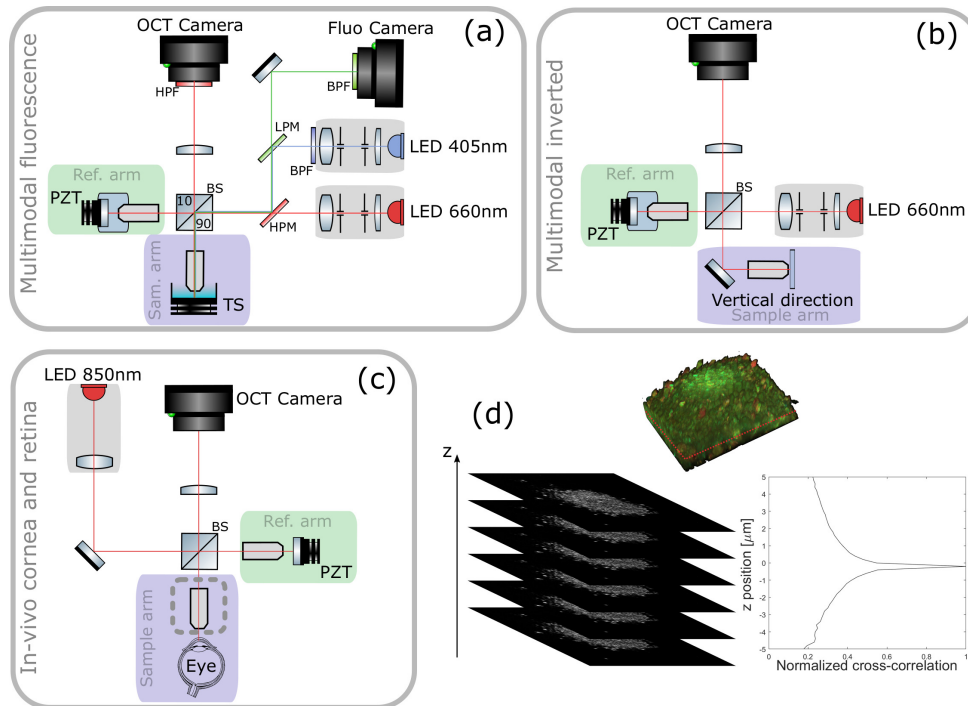
Fig. 1. PZT: piezoelectric translation - TS: translation stage - LPM: low pass dichroic filter - HPM: high pass dichroic filter - (a) Multimodal static and dynamic FFOCT combined with fluorescence *side view*. The camera used for FFOCT in all setups is an ADIMEC Quartz 2A750. The camera used for fluorescence is a PCO Edge 5.5. Microscope objectives are Nikon NIR APO 40x 0.8 NA. (b) Multimodal static and dynamic FFOCT inverted system *top view*. Microscope objectives are Olympus UPlanSApo 30x 1.05 NA. (c) In vivo FFOCT setup for anterior eye imaging (with Olympus 10x 0.3 NA objectives in place) and retinal imaging *top view* (with sample objective removed, at the location indicated by the dashed line box), which is capable of imaging both anterior and posterior eye, in both static mode to image morphology or time-lapse mode to image blood flow. (d) Locking plane procedure. FFOCT images are acquired over an axial extension of 10 μm with 0.5 μm steps and are then cross-correlated with the target image. The sample is then axially translated to the position corresponding to the maximum of the cross-correlation. This example is illustrated with retinal cells.

Table 1. Setup characteristics.

Setup	Transverse resolution [μm]	Axial resolution [μm]	Field of view [$\mu m \times \mu m$]
Fig. 1(a)	0.5	1.7	320×320
Fig. 1(b)	0.4	1	390×390
Fig. 1(c)	1.7	7.7	1260×1260

2.4. Image computation

FFOCT images presented here are constructed using the 2-phase stepping algorithm. FFOCT images, as well as OCT images, exhibit speckle that is due to the random positions of the back scatterers. In this situation a 2-phase stepping algorithm is enough to recover the FFOCT signal, and moreover 2-phase acquisitions are faster. The method to compute the D-FFOCT images (Fig. 2) is explained in [10] for both grayscale and colored dynamic images. Briefly, grayscale images are constructed from a (N_x, N_y, N_t) tensor, where (N_x, N_y) is the camera sensor dimension and N_t is the number of frames recorded, by using a standard deviation sliding window on the time dimension and then averaged to obtain an image. Colored images are computed in the Fourier domain. The temporal variation of each pixel is Fourier transformed and then integrated between $[0, 0.5]$ Hz to form the blue channel, between $[0.5, 5]$ Hz to for the green channel and integrated over $5Hz$ for the red channel. The arbitrary selection of which frequencies to assign to which color bands aims to subjectively optimize the visualization in RGB, meaning that color scales are non quantitative. Note that the maximal detectable frequency of the phase fluctuations depends on the acquisition speed and is typically 50 Hz for biological samples (corresponding to the Shannon sampling theorem for an acquisition framerate of 100 $frames.s^{-1}$).

2.5. Computing and displaying temporal variations in time-lapse sequences

Due to its non-invasive nature, FFOCT can be used to acquire time-lapse sequences at a fixed plane and position over long periods to assess slow dynamics on in-vitro samples, or over short periods in-vivo to assess fast dynamics such as blood flow. This data can be displayed in movie format to visualize movement (Visualization 1, Visualization 2), or can be processed to quantify the movement speed and directionality of target features (Figs 3, 4). There are two main methods to extract quantitative information on motion in image sequences. The first method is solving the optical flow equations. Optical flow is the pattern of apparent motion of objects, surfaces, and edges in a visual scene. The second type of method is to use block-matching algorithms where the underlying supposition behind motion estimation is that the patterns corresponding to objects and background in a frame of video sequence move within the frame to form corresponding objects on the subsequent frame. The former technique is a differential method where a partial differential equation is solved with typical constraints whereas the latter looks to maximize the correlation between blocks of given size between each frame. We tested block-matching methods with phase correlation and normal correlation, as well as differential methods with different regularizers. The one that gave the best result for our corneal wound healing data-set was the Horn–Schunck method [29] which solves the optical flow equations by optimizing a functional with a regularization term expressing the expected smoothness of the flow field. This algorithm is particularly suitable to extract motion on diffeomorphisms which are differentiable maps (i.e. smooth, without crossing displacement fields). Block-matching methods, in addition to being slow for high-resolution images, were failing due to the apparent homogeneity of the intracellular signals requiring blocks of great size, decreasing the accuracy and leading to very long computations. On the contrary, Horn-Shunck regularization considers the image as a whole and provides a regularizing term that controls the expected velocity map smoothness. The optical flow problem consists of solving the following equation:

$$I_x u + I_y v + I_t = 0 \tag{11}$$

where I_x, I_y and I_t are the spatiotemporal image brightness derivatives, and u and v are the horizontal and vertical optical flow, respectively. This is an equation in two unknowns that cannot be solved as such. This is known as the aperture problem. To find the optical flow another set of

equations is needed and Horn-Shunck regularization introduces the following functional:

$$\mathcal{L} = \iint \left(I_x u + I_y v + I_t\right)^2 dx dy + \alpha \iint \left\{ \left(\frac{\partial u}{\partial x}\right)^2 + \left(\frac{\partial u}{\partial y}\right)^2 + \left(\frac{\partial v}{\partial x}\right)^2 + \left(\frac{\partial v}{\partial y}\right)^2 \right\} dx dy \quad (12)$$

where $\frac{\partial v}{\partial x}$ and $\frac{\partial v}{\partial y}$ are the spatial derivatives of the optical velocity v, and the regularizer α scales the global smoothness term. The idea is to minimize the optical flow problem by penalizing flow distortions, where the amount of penalization is controlled by the constant α. This constant gives weight to the right integral term which corresponds to the optical flow Laplacian summed over the whole image, thus containing information on the total flow unsmoothness. The functional is then easily optimized because of its convex nature:

$$[u, v]^T = argmin_{u,v} (\mathcal{L}) \quad (13)$$

For the wound healing migration problem we optimized α by looking at the L_2 error between the velocities computed by the algorithm and 200 manually tracked voxels, see Fig. 3(c). The optimal α was found to be 100.

2.6. Blood flow measurement with FFOCT

For our in vivo blood flow dataset, automated methods based on optical flow failed to extract a velocity map due to the speckle pattern of the images inside vessels. Motion no longer corresponded to a diffeomorphism field, especially locally, leading to a complete divergence of the previous algorithm even with smaller α. Nonetheless we succeeded in extracting a velocity profile inside a vessel using a kymograph plot, i.e. plotting the vessel curvilinear abscissa against time. On such a plot, each event (i.e. a passing particle, such as a blood cell) produces a line, and the slope of this line corresponds to the speed. Using a custom segmentation algorithm, we automatically fit these lines and extracted the speed for each event at a given vessel cross-position. We averaged the speed over the 4 to 18 detected events at each position, and calculated the standard error at each position to evaluate the error in the average speed calculation. Ultimately, the profile can be smoothed and fit to a Poiseuille flow, typically observed in capillaries [30] to extract the maximal velocity v_{max} defined by:

$$v(r) = v_{max} \left(1 - \frac{r^2}{R_{cap}^2}\right) \quad (14)$$

where r is the axial distance to the center of the capillary and R_{cap} is the capillary radius. This fit allows averaging over more than 400 tracked events and reduces the error on the maximal blood flow velocity from $\pm 50\ \mu m.s^{-1}$ in a single position down to $\pm 15\ \mu m.s^{-1}$.

2.7. Samples and subjects

All animal manipulation was approved by the Quinze Vingts National Ophthalmology Hospital and regional review board (CPP Ile-de-France V), and was performed in accordance with the ARVO Statement for the Use of Animals in Ophthalmic and Vision Research. Macaque and porcine ocular globes were obtained from a partner research facility and transported to the Vision Institute in CO_2-free neurobasal medium (Thermo Fisher Scientific, Waltham, MA, USA) inside a device that maintained oxygenation, for transport to the laboratory for dissection. We imaged a 2 mm^2 piece of peripheral macaque retina, prepared as described in [10]. Briefly, an incision was made in the sclera to remove the anterior segment. The retina was gently removed from the choroid, with separation occurring at the RPE, and flattened into petals by making

four incisions (nasal, temporal, superior, inferior). Pieces approximately 3 mm from the fovea toward the median raphe were selected for imaging. We also imaged a porcine retinal pigment epithelium cell culture, prepared as described in [31]. Briefly, porcine eyes were cleaned from muscle, and incubated during 4 minutes in Pursept-AXpress (Merz Hygiene GmbH, Frankfurt, Germany) for disinfection. The anterior portion was cut along the limbus to remove the cornea, lens and retina. A solution containing 0.25% trypsin-EDTA (Life Technologies, Carlsbad, CA, USA) was introduced for 1 hour at $37°C$ in the eyecup. RPE cells were then gently detached from the Bruch's membrane and resuspended in Dulbecco's Modified Eagle medium (DMEM, Life Technologies) supplemented with 20% Fetal Bovine Serum (FBS, Life Technologies) and 10 $mg.ml^{-1}$ gentamycin (Life Technologies). Cells were allowed to grow in an incubator with a controlled atmosphere at 5% CO_2 and $37°C$. Samples were placed in transwells, and immersed in CO_2-free neurobasal and HEPES (Thermo Fisher Scientific, Waltham, MA, USA) medium for imaging. Fluorescent labeling in RPE cultures used a polyanionic green fluorescent (excitation/emission 495 nm/ 515 nm) calcein dye (LIVE/DEAD® Viability/Cytotoxicity Kit, Thermo Fischer Scientific, France) which is well retained within live cells. For in vitro setups, typical power incident on the sample surface is approximately 0.1mW, though this varies from sample to sample as the power level is adapted to work close to saturation of the camera for each experiment.

Using the new combined anterior/posterior setup (Fig. 1(c)) similar to those described in [19,23], in vivo imaging was performed on a healthy volunteer who expressed his informed consent, and the experimental procedures adhered to the tenets of the Declaration of Helsinki. For in vivo imaging, thorough calculations of light safety according to the appropriate standards are available in [23]. Weighted retinal irradiance of our setup is 49 $mW.cm^{-2}$, corresponding to 7% of the maximum permissible exposure (MPE), and corneal irradiance is 2.6 $W.cm^{-2}$, corresponding to 65% of the MPE, which is further reduced by operating the light source in pulsed mode.

3. Results

3.1. Subcellular contrast enhancement and dynamics detection in retinal explants and cell cultures

FFOCT and D-FFOCT are useful to reveal contrast inside transparent tissue such as retina. We imaged a fresh retinal explant from macaque with the inverted setup shown Fig.1(b). We acquired 100 μm deep FFOCT and D-FFOCT stacks with 1 μm step leading to stacks of 101 en-face images. Fig. 2 shows a 3D volume, en face slices and a reconstructed cross sectional view from this acquisition. Fig. 2(a-e) show the contrast enhancement in D-FFOCT on cellular features in layers such as the inner and outer nuclear and photoreceptor layers. Fig. 2(g) demonstrates the complementarity of static and dynamic FFOCT modes, for example to understand the disposition of nerve fibers and inner plexiform structures (visible in static mode) in relation to ganglion cells (visible in dynamic mode). In comparison to the stack acquisition performed in past setups [10], the improved immobilisation of the sample in the new inverted multimodal setup facilitated automated acquisition of 3D stacks with reliable micrometer steps so that volumetric and cross-sectional representations (Fig. 2(a, b)) may be constructed to improve understanding of retinal cellular organization. The automated plane locking procedure to correct for axial drift means that we are able to repeatedly acquire 3D stacks beginning at the exact same plane, making 3D time-lapse imaging possible and ensuring perfect coincidence of multimodal FFOCT/D-FFOCT stacks. In addition to volumetric imaging through bulk tissue, D-FFOCT can also be used to image 2D cell cultures to monitor culture behavior over time. An en face image of a 2D retinal pigment epithelium cell (RPE) culture (Fig. 2(f)) shows high contrast on cell nuclei and cytoplasm and enables identification of multinucleated cells or cytoplasmic variations from cell to cell. As a result of the improvements in sample stability and time-lapse acquisition offered

by the inverted setup, time-lapse imaging over periods of hours, in conjunction with the fast dynamic signal which creates the D-FFOCT contrast in a single acquisition, can now be reliably performed. This allows us to identify dynamic behavior at various time scales in these in vitro conditions over time. We can therefore follow in vitro cellular decline in situ in explanted tissues, or in vitro cellular development in a growing culture. These capabilities allow understanding of retinal organization and monitoring of cell viability in disease modeling applications or quality control of cultured tissue for graft.
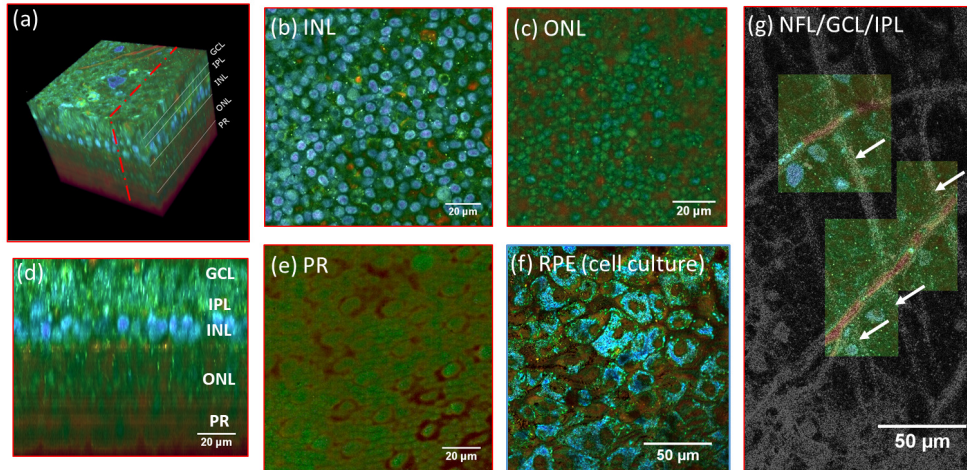
Fig. 2. (a) 3D reconstruction of a D-FFOCT image stack in explanted macaque retina over a 120 by 120 μm field of view. Note that FFOCT signal is damped with increasing penetration depth, so that upper retinal layers are more clearly visible than lower ones. (b, c, e) En-face images of the (b) inner nuclear layer, (c) outer nuclear layer and (e) photoreceptor layer presenting a similar appearance to two-photon fluorescence imaging [32] and (d) reconstructed cross-section at the location represented by the red dotted line in (a). The cross-section in (d) was linearly interpolated to obtain a unitary pixel size ratio. (f) D-FFOCT image of a porcine retinal pigment epithelium cell culture [31]. (g) Overlay of colored D-FFOCT and FFOCT at the interface between the layers of the nerve fibers (white arrows point to nerve bundles that are very bright in static and invisible in dynamic mode), ganglion cells (blue and green cells, visible in dynamic mode) and inner plexiform (fibrous network, bottom left, visible in static mode). Samples were maintained in vitro in culture medium at room temperature during imaging.

3.2. Slow dynamics: corneal wound healing imaging

To demonstrate the potential benefits of time-lapse D-FFOCT we imaged a corneal wound. A macaque cornea was maintained in graft storage conditions, i.e. at room temperature in graft transport medium (CorneaJet, Eurobio, France), during imaging. Epithelium was scraped in a small region of the corneal surface using tweezers, creating a wound in the epithelial layer. The acquired time-lapse sequence in the epithelial layer showed that in addition to revealing epithelial cells and their arrangement, we were also able to detect the slow corneal healing with the migration of cells to fill the wound. We acquired 112 dynamic images in a time-lapse fashion on a wounded macaque cornea with the method and setup introduced in [7], but with the inverse configuration, as described in Section 2.3 above. The acquisition duration was 112 minutes, corresponding to 1 minute between each dynamic image (see Visualization 1). We optimized the grayscale range of the dynamic image by applying a non-local mean filter to remove

the noise while preserving the edges and then averaged 8 images leading to a stack composed of 14 grayscale images. We computed 13 optical flow maps (between each of the 14 frames) and summed them to compute the motion map, see Fig. 3(b). The velocities measured range between $10 - 25 \ \mu m.h^{-1}$ from near the wound center to periphery respectively. In the literature, epithelial cell migration speed in vivo in wound healing is around $50 \ \mu m.h^{-1}$ and lower when the wound is starting to close [33]. Our figures are therefore of a similar order of magnitude, although lower, possibly as we were imaging ex-vivo samples at $25°C$ instead of in vivo cornea at $37°C$ and imaged close to an almost closed wound. Indeed, our measured migration rates are closer to those reported for similar in vitro reepithelialization cell migration studies in rabbit ($10 - 16 \ \mu m.h^{-1}$ [34]). Our algorithm was validated by comparing with manual tracking of 200 voxels in cells on successive images. Using the previous errors computation presented in Section 2.5 with $\alpha = 100$ we obtained an accuracy of $2.9 \pm 0.6 \ \mu m.h^{-1}$.
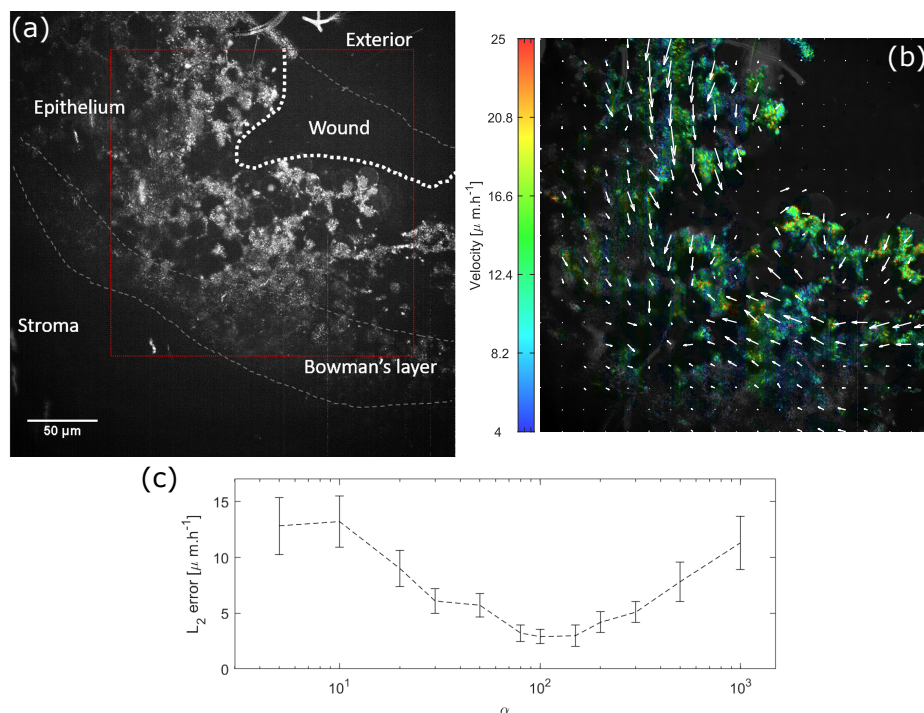
Fig. 3. (a) Dynamic grayscale image of a wounded macaque cornea - the red box shows where the computation is done, see Visualization 1 (b) Same dynamic image superimposed with colors coding for the cell migration velocity averaged over the 112 minute acquisition. Each arrow represents the mean motion in a pixel - (c) Velocity errors for different Horn-Shunk smoothness terms α. The curve represents the mean error we found by comparing the optical flow computation with 200 manually tracked voxels. Error-bars represent the error standard deviation. The optimal α was found to be 100.

3.3. Fast dynamics: blood flow in vivo anterior eye

The fast acquisition speed allows FFOCT to obtain images in vivo and estimate velocities of physiological processes. Fig. 4 and Visualization 2 depict FFOCT images of conjunctival blood flow in the in vivo human eye. Images were obtained using a fast acquisition at 275 $frames.s^{-1}$ [23] followed by template-matching with an ImageJ plugin to remove lateral

misalignment [35, 36]. Flow was quantified using the method described in Section 2.6. The measured flow profile was fitted to a Poiseuille flow profile with good accuracy ($R^2 > 0.95$) and showed a maximal velocity of $600 \pm 15 \mu m.s^{-1}$ (Fig. 4(c)), where both speed and diameter are in agreement with previous experimental findings in the literature, which used slit-lamp microscopy, coupled with a CCD camera [24, 37]. The accuracy of our technique seems to outperform the accuracy we can estimate from other existing techniques to measure blood flow in the eye by about one order of magnitude [24–26].
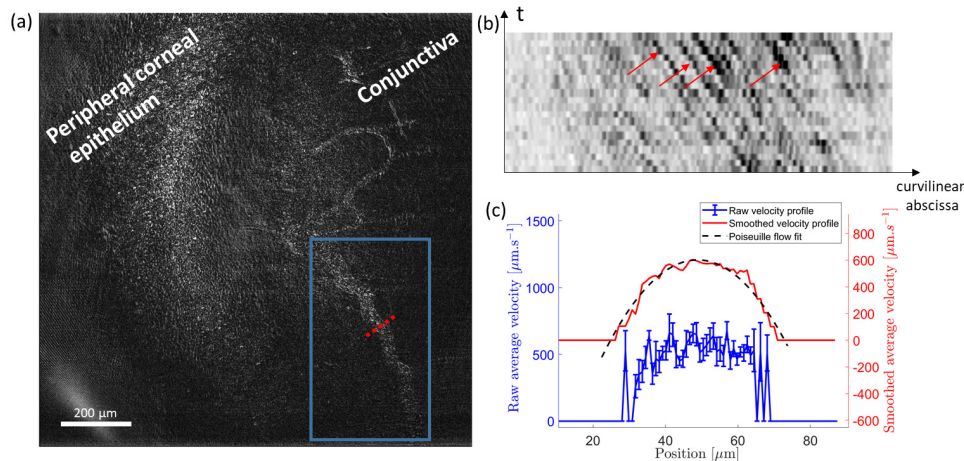
Fig. 4. (a) Single FFOCT-frame of conjunctival blood flow near the limbal region of the in vivo anterior human eye. See Visualization 2 for a movie of blood flow in the drawn box. (b) Kymograph plot (space-time domain) inside the blood vessel at $x = 10$ μm. Grayscale is inverted so that the black particles indicated by the red arrows are red blood cells flowing into the vessel. The slope corresponds to the particle speed. (c) Raw velocity profile inside the blood vessel (blue) computed along the dotted line in (a) with the method explained in Section 2.6. The standard error is calculated at each position and ranges around 50 $\mu m.s^{-1}$ at the center of the profile and 200 $\mu m.s^{-1}$ on the sides. The smoothed profile (red) with the fit to a Poiseuille flow profile (black dashed line) are superimposed and voluntarily shifted up for increased visibility.

3.4. Towards label free non invasive specific imaging

Multimodal setups that combine fluorescence microscopy and OCT have been developed [38, 39] in order to combine the targeted contrast of fluorescent dyes and antibodies with the structural contrast of OCT. Recently, a multimodal setup (Fig. 1(a)) was proposed to combine static and dynamic FFOCT with fluorescence microscopy [40]. This setup can be used to confirm the FFOCT identity of specific cell types or behaviours via comparison with the fluorescent signal. Simultaneous coincident imaging on a single multimodal setup is vital in order to correctly identify the cells at the pixel to pixel scale and so remove any uncertainty that can occur when imaging one sample on multiple microscopes. To illustrate this validation approach, we labelled living retinal pigment epithelium (RPE) cells in a sparse culture, using calcein dye. The polyanionic dye calcein is well retained within live cells, producing an intense uniform green fluorescence in live cells. We jointly acquired FFOCT, D-FFOCT and fluorescence images of the labeled cells, in order to compare the different modalities within the same plane at precisely the same time. Static FFOCT provided the baseline information about cell presence. The refractive index mismatch between the culture medium and the cells induces light backscattering from cells

measured by FFOCT. Dynamic FFOCT highlights areas where there is motion of back-scatterers (e.g. mitochondria), indicating that the cell metabolism was somewhat active. Fluorescence images showed which cells were alive when we carried out the labelling procedure. The results are shown in Fig. 5 by merging each channel by pairs: (a) merges static FFOCT and dynamic FFOCT, highlighting the active cells over all the cells; (b) merges the static and fluorescently labeled live cells, validating successful labeling as only a subset of cells are fluorescent; (c) merges dynamic FFOCT and fluorescently labeled live cells allowing the comparison between live, dead and dying cell dynamics. As shown in Fig. 5(a-c), we thereby observed 3 different configurations: i) Active cells exhibiting fluorescence indicating that these cells were alive (green in b, c); ii) Inactive cells without fluorescence indicating that these cells were dead (red arrows in Fig. 5(b,c)); iii) Highly active cells without fluorescence suggesting that the cell was dying (white arrows on Fig. 5(a-c)).
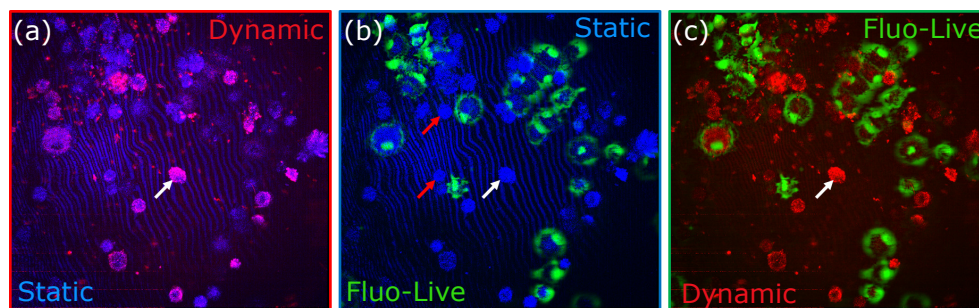
Fig. 5. Multimodal binary merging. Static FFOCT is represented in blue, dynamic FFOCT in red and living labeled cells in green, imaged with the fluorescence setup presented Fig. 1(a). White arrows show active cells without fluorescence suggesting that apoptosis was occuring. Red arrows show inactive cells without fluorescence indicating that these cells were dead.

4. Discussion

Through these examples of multimodal static and dynamic FFOCT images, we have demonstrated the imaging of multiple spatial scales of morphology and temporal scales of dynamic processes in the eye with multimodal FFOCT. However in order for the technique to be adopted by the microscopy and medical communities as true label-free microscopy, validation is required in relation to existing techniques. In addition, further technical improvements could be made with regards to improving efficiency of data management to enable real-time dynamic imaging and improve real-time in vivo image display.

4.1. Towards label free dynamic FFOCT

Using the validation approach of fluorescent labeling in tandem with static and dynamic FFOCT to identify the dynamic signature for specific cell behaviors or types should allow us to achieve reliable true label-free imaging in 3D tissue samples with FFOCT alone. The proof of concept presented in Section 3.4 was a first step toward label free imaging as we only used the dynamic image which is the result of a strong dimension reduction. Indeed, in order to construct an image, we map the dynamic signal over one or three dimensions depending on the desired output (i.e. grayscale or color image). The next step is to consider the full signal in order to train machine learning algorithms to find the optimal signal representation that could distinguish cells based on different criteria, e.g. live, dead and undergoing apoptosis. We hope that by studying the dynamic distribution inside cells it will be possible to extract more information such as cell cycle, cell type, etc. making D-FFOCT a powerful tool for cell biology.

4.2. Towards real time dynamic FFOCT

Currently each dynamic image is computed in approximately 10 seconds on a GPU (NVidia Titan Xp). Most of this time is dedicated to memory management. In the original D-FFOCT configuration [7], images were computed using the CPU so the frame grabber was configured to save data directly on the computer Random Access Memory (RAM). The difficulty for real-time applications is the data transfer bottleneck. Indeed, a GPU can process data only as fast as the data can be transferred to it. In traditional system memory models, each device has access only to its own memory so that a frame grabber acquires to its own set of system buffers. Meanwhile, the GPU has a completely separate set of system buffers, so any transfer between the two must be performed by the CPU, which take times if the amount of data is important. Our current framework waits for the image to be completely copied to the RAM and then transfers it to the GPU which limits the maximal system speed. The average load of the GPU during the overall procedure is less than 5%. In the near future we plan to take advantage of the latest advance in GPU computing and establish a direct link between the frame grabber and the GPU memory. Taking the Titan Xp as reference and being limited only by the computation, we expect to be able to achieve real-time dynamic images. We hope that real-time dynamic movies could highlight new biological behavior at the cellular and subcellular level. In addition, the faster processing will improve our real-time in vivo image display.

5. Conclusion

We have demonstrated detection of slow and fast dynamic processes in the eye thanks to recent technological progress in multimodal full-field optical coherence tomography. Combined static, dynamic and fluorescence contrasts are moving towards the goal of achieving label-free high-resolution imaging of anterior eye and retina with temporal resolution from milliseconds to several hours. Its contactless and non-destructive nature makes FFOCT a useful technique both for following in vitro sample evolution over long periods of time and for imaging of the human eye in vivo.

Disclosures

CB: LLTech SAS (I), K. Groux: LLTech SAS (E), others: none.

References

1. D. Huang, E. Swanson, C. Lin, J. Schuman, W. Stinson, W. Chang, M. Hee, T. Flotte, K. Gregory, C. Puliafito *et al.*, "Optical coherence tomography," Science **254**, 1178–1181 (1991).
2. W. Drexler and J. G. Fujimoto, eds., *Optical Coherence Tomography: Technology and Applications* (Springer, 2015), 2nd ed.
3. E. Beaurepaire, A. C. Boccara, M. Lebec, L. Blanchot, and H. Saint-Jalmes, "Full-field optical coherence microscopy," Opt. Lett. **23**, 244–246 (1998).
4. A. Dubois, K. Grieve, G. Moneron, R. Lecaque, L. Vabre, and C. Boccara, "Ultrahigh-resolution full-field optical coherence tomography," Appl. Opt. **43**, 2874–2883 (2004).
5. J. Ben Arous, J. Binding, J.-F. Léger, M. Casado, P. Topilko, S. Gigan, A. C. Boccara, and L. Bourdieu, "Single myelin fiber imaging in living rodents without labeling by deep optical coherence microscopy," Journal of Biomedical Optics **16**, 116012 (2011).

6. M. Jain, N. Shukla, M. Manzoor, S. Nadolny, and S. Mukherjee, "Modified full-field optical coherence tomography: A novel tool for rapid histology of tissues," J. Pathol. Informatics **2**, 28 (2011).

7. C. Apelian, F. Harms, O. Thouvenin, and A. C. Boccara, "Dynamic full field optical coherence tomography: subcellular metabolic contrast revealed in tissues by interferometric signals temporal analysis," Biomed. Opt. Express **7**, 1511–1524 (2016).

8. J. Lee, W. Wu, J. Y. Jiang, B. Zhu, and D. A. Boas, "Dynamic light scattering optical coherence tomography," Opt. Express **20**, 22262–22277 (2012).

9. C.-E. Leroux, F. Bertillot, O. Thouvenin, and A.-C. Boccara, "Intracellular dynamics measurements with full field optical coherence tomography suggest hindering effect of actomyosin contractility on organelle transport," Biomed. Opt. Express **7**, 4501–4513 (2016).

10. O. Thouvenin, C. Boccara, M. Fink, J. Sahel, M. Pâques, and K. Grieve, "Cell motility as contrast agent in retinal explant imaging with full-field optical coherence tomography," Investig. Opthalmology & Vis. Sci. **58**, 4605 (2017).

11. A. Nahas, M. Tanter, T.-M. Nguyen, J.-M. Chassot, M. Fink, and A. C. Boccara, "From supersonic shear wave imaging to full-field optical coherence shear wave elastography," J. Biomed. Opt. **18**, 18 (2013).

12. J. Binding, J. B. Arous, J.-F. Léger, S. Gigan, C. Boccara, and L. Bourdieu, "Brain refractive index measured in vivo with high-na defocus-corrected full-field oct and consequences for two-photon microscopy," Opt. Express **19**, 4833–4847 (2011).

13. M. A. A. Neil, R. Juškaitis, and T. Wilson, "Method of obtaining optical sectioning by using structured light in a conventional microscope," Opt. Lett. **22**, 1905–1907 (1997).

14. J. Mertz, *Introduction to Optical Microscopy*, vol. 138 (W. H. Freeman, 2009).

15. M. G. L. Gustafsson, "Nonlinear structured-illumination microscopy: Wide-field fluorescence imaging with theoretically unlimited resolution," Proc. Natl. Acad. Sci. **102**, 13081–13086 (2005).

16. E. Auksorius, Y. Bromberg, R. Motiejūnaitė, A. Pieretti, L. Liu, E. Coron, J. Aranda, A. M. Goldstein, B. E. Bouma, A. Kazlauskas, and G. J. Tearney, "Dual-modality fluorescence and full-field optical coherence microscopy for biomedical imaging applications," Biomed. Opt. Express **3**, 661–666 (2012).

17. O. Thouvenin, M. Fink, and A. C. Boccara, "Dynamic multimodal full-field optical coherence tomography and fluorescence structured illumination microscopy," J. Biomed. Opt. **22**, 226004 (2017).

18. P. Xiao, M. Fink, and A. C. Boccara, "Full-field spatially incoherent illumination interferometry: a spatial resolution almost insensitive to aberrations," Opt. Lett. **41**, 3920–3923 (2016).

19. P. Xiao, V. Mazlin, K. Grieve, J.-A. Sahel, M. Fink, and A. C. Boccara, "In vivo high-resolution human retinal imaging with wavefront-correctionless full-field oct," Optica **5**, 409–412 (2018).

20. K. Grieve, L. Palazzo, E. Dalimier, P. Vielh, and M. Fabre, "A feasibility study of full-field optical coherence tomography for rapid evaluation of EUS-guided microbiopsy specimens," Gastrointest. Endosc. **81**, 342–350 (2015).

21. K. Grieve, M. Paques, A. Dubois, J. Sahel, C. Boccara, and J.-F. Le Gargasson, "Ocular tissue imaging using ultrahigh-resolution, full-field optical coherence tomography," Investig. Ophthalmol. & Vis. Sci. **45**, 4126 (2004).

22. K. Grieve, O. Thouvenin, A. Sengupta, V. M. Borderie, and M. Paques, "Appearance of the retina with full-field optical coherence tomography," Investig. Ophthalmol. & Vis. Sci. **57**, OCT96 (2016).

23. V. Mazlin, P. Xiao, E. Dalimier, K. Grieve, K. Irsch, J.-A. Sahel, M. Fink, and A. C. Boccara, "In vivo high resolution human corneal imaging using full-field optical coherence tomography," Biomed. Opt. Express **9**, 557–568 (2018).

24. M. Shahidi, J. Wanek, B. Gaynes, and T. Wu, "Quantitative assessment of conjunctival microvascular circulation of the human eye," Microvasc. research **79**, 109–113 (2010).

25. A. Wartak, R. Haindl, W. Trasischker, B. Baumann, M. Pircher, and C. K. Hitzenberger, "Active-passive path-length encoded (apple) doppler oct," Biomed. optics express **7**, 5233–5251 (2016).

26. C. J. Pedersen, D. Huang, M. A. Shure, and A. M. Rollins, "Measurement of absolute flow velocity vector using dual-angle, delay-encoded doppler optical coherence tomography," Opt. letters **32**, 506–508 (2007).

27. C. K. Sheehy, Q. Yang, D. W. Arathorn, P. Tiruveedhula, J. F. de Boer, and A. Roorda, "High-speed, image-based eye tracking with a scanning laser ophthalmoscope," Biomed. Opt. Express **3**, 2611–2622 (2012).

28. K. V. Vienola, B. Braaf, C. K. Sheehy, Q. Yang, P. Tiruveedhula, D. W. Arathorn, J. F. de Boer, and A. Roorda, "Real-time eye motion compensation for oct imaging with tracking slo," Biomed. Opt. Express **3**, 2950–2963 (2012).

29. B. K. Horn and B. G. Schunck, "Determining optical flow," Artif. Intell. **17**, 185–203 (1981).

30. B. R. Munson, D. F. Young, T. H. Okiishi, and W. W. Huebsch, *Fundamentals of Fluid Mechanics*, vol. 69 (John Wiley & Sons, Inc, 2006).

31. E. Arnault, C. Barrau, C. Nanteau, P. Gondouin, K. Bigot, F. Viénot, E. Gutman, V. Fontaine, T. Villette, D. Cohen-Tannoudji, J.-A. Sahel, and S. Picaud, "Phototoxic action spectrum on a retinal pigment epithelium model of age-related macular degeneration exposed to sunlight normalized conditions," PLOS ONE **8**, 1–12 (2013).

32. R. Sharma, D. R. Williams, G. Palczewska, K. Palczewski, and J. J. Hunter, "Two-photon autofluorescence imaging reveals cellular structures throughout the retina of the living primate eye," Investig. Ophthalmol. & Vis. Sci. **57**, 632 (2016).

33. B. D. Ashby, Q. Garrett, and M. Dp, "Corneal Injuries and Wound Healing – Review of Processes and Therapies," Austin J. Clin. Ophthalmol. p. 25 (2014).

34. M. Gonzalez-Andrades, L. Alonso-Pastor, J. Mauris, A. Cruzat, C. H. Dohlman, and P. Argüeso, "Establishment of a novel in vitro model of stratified epithelial wound healing with barrier function," Sci. Reports **6** (2016).

35. J. Schindelin, C. T. Rueden, M. C. Hiner, and K. W. Eliceiri, "The imagej ecosystem: An open platform for biomedical

image analysis," Mol. Reproduction Dev. **82**, 518–529 (2015).

36. Q. Tseng, E. Duchemin-Pelletier, A. Deshiere, M. Balland, H. Guillou, O. Filhol, and M. Théry, "Spatial organization of the extracellular matrix regulates cell–cell junction positioning," Proc. Natl. Acad. Sci. **109**, 1506–1511 (2012).

37. L. Wang, J. Yuan, H. Jiang, W. Yan, H. R. Cintrón-Colón, V. L. Perez, D. C. DeBuc, W. J. Feuer, and J. Wang, "Vessel sampling and blood flow velocity distribution with vessel diameter for characterizing the human bulbar conjunctival microvasculature," Eye & contact lens **42**, 135 (2016).

38. F. Harms, E. Dalimier, P. Vermeulen, A. Fragola, and A. C. Boccara, "Multimodal full-field optical coherence tomography on biological tissue: toward all optical digital pathology," Proc.SPIE **8216**, 821609 (2012).

39. H. Makhlouf, K. Perronet, G. Dupuis, S. Lévêque-Fort, and A. Dubois, "Simultaneous optically sectioned fluorescence and optical coherence microscopy with full-field illumination," Opt. Lett. **37**, 1613–1615 (2012).

40. O. Thouvenin, C. Apelian, A. Nahas, M. Fink, and C. Boccara, "Full-field optical coherence tomography as a diagnosis tool: Recent progress with multimodal imaging," Appl. Sci. **7**, 236 (2017).

5.1.2 Article: Real-time, non-contact, cellular imaging and angiography of human cornea and limbus with common-path Full-field/SD-OCT
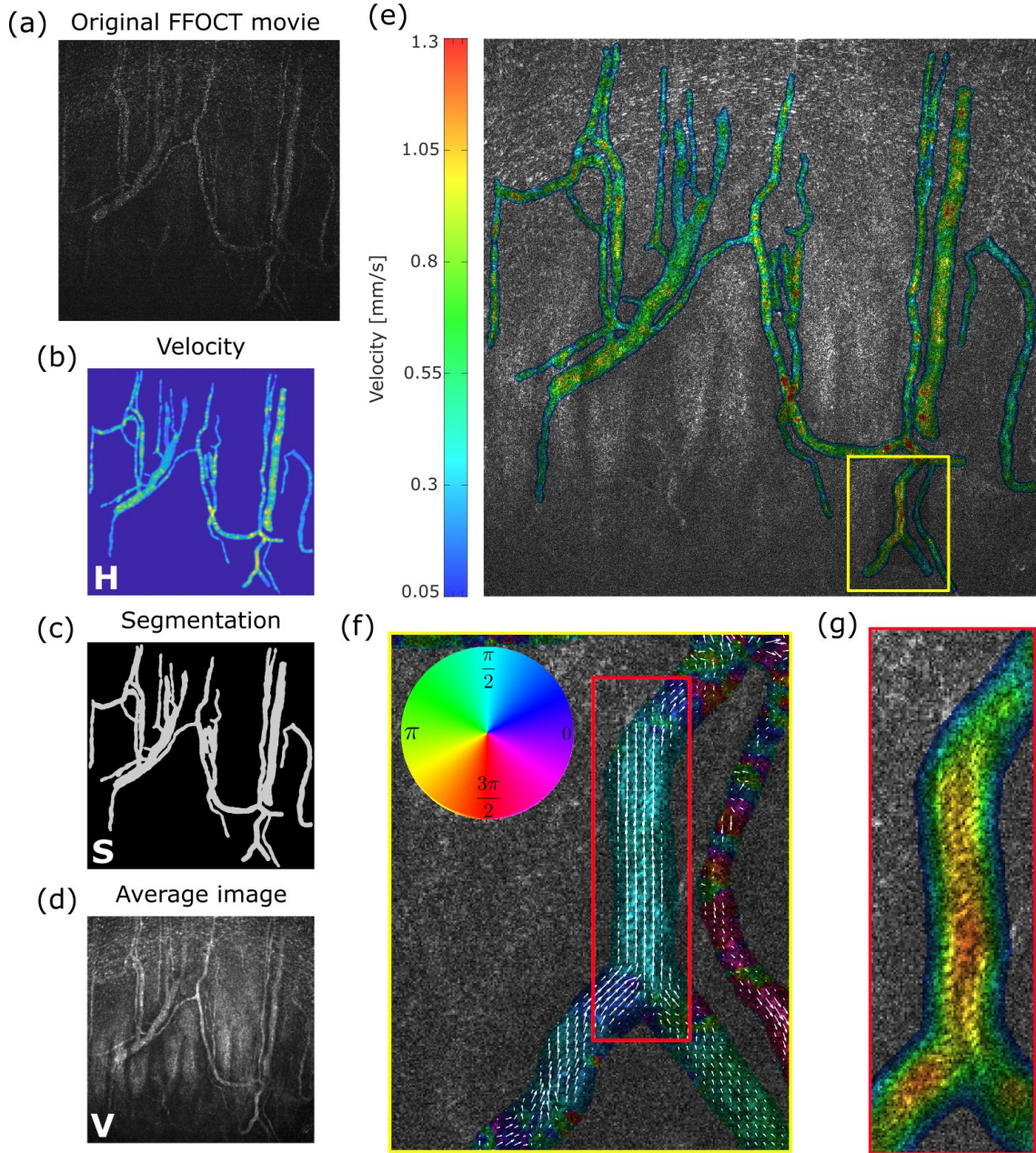
Fig. 5.1: Angiography of conjunctiva blood flow. The original FFOCT movie **(a)** is processed to extract the flow velocity **(b)** in each pixel, the segmented capillaries **(c)** and the average FFOCT image **(d)**. These images are combined to compute angiography velocity maps **(e)** and angiography direction maps **(f)** where interesting areas highlighting Poisseuille flow is zoomed in **(g)**.

I only contributed on a small part of this study which was aiming at acquiring FFOCT corneal images on humans in vivo. I worked on automatically generating angiography images of the blood flow in the cornea that were previously computed using a cumbersome

approach with Kymograph plots [Scholler et al., 2019]. Computing the optical flow using Horn-Shunck method was not giving satisfactory results[3]. I solved this by using block matching algorithms [Yaakob et al., 2013] where a similarity function is used to compare a block of pixel in a first image with the neighboring blocks in a second image. The most probable displacement being the one that maximizes the similarity function. In this case the similarity function I used was the cross-correlation computed on blocks of size 16×16 pixels. In order to remove outliers, I filtered low cross-correlation values and applied a Gaussian filter to smooth the angiography map[4] shown Fig. 5.1(b). Finally, I created a mask depicted Fig. 5.1(c) by segmenting the capillaries with an adaptive thresholding on the temporally averaged FFOCT image. In order to compute the final angiography map, I used the HSV method explained appendix B by putting the velocity in H[5], the segmentation result in S and the average FFOCT image in V. The same can also be done for the direction of the flow, see Fig. 5.1(f). Poiseuille flow with quadratic velocity distribution across the capillary width can be observed in the zoom Fig. 5.1(g) with a maximum velocity of around $1.2 \ mm.s^{-1}$ which was in adequation with the literature [Munson et al., 2006].

I also applied the dust denoising algorithm explained section 3.4 to remove dark spots that were present on Fig. 7 (article below) on the tear film direct images caused by dust on the camera sensor[6].

---

[3]The reason why it was not giving satisfactory results is because Horn-Shunck method prior is that the underlying displacement field is smooth and is a diffeomorphism (it is an invertible function that maps one differentiable manifold to another such that both the function and its inverse are smooth) where there is no crossing in the displacement field. In vessels, red blood cell are giving speckle pattern so that the optical flow was not a diffeomorphism anymore.

[4]Flows in capillaries typically follows Poiseuille flow [Munson et al., 2006] and are therefore C-infinity functions.

[5]Velocities were inverted and rescaled between 0 and 0.66 so that slow flow corresponds to blue while fast flow corresponds to red.

[6]Tutorial and videos of dust denoising available at `https://www.jscholler.com/2019-02-28-remove-dots/`.

Real-time non-contact cellular imaging and angiography of human cornea and limbus with common-path full-field/SD OCT

Viacheslav Mazlin [1✉], Peng Xiao [1,2✉], Jules Scholler [1], Kristina Irsch[3,4], Kate Grieve[3,4], Mathias Fink [1] & A. Claude Boccara[1✉]

In today's clinics, a cell-resolution view of the cornea can be achieved only with a confocal microscope (IVCM) in contact with the eye. Here, we present a common-path full-field/ spectral-domain OCT microscope (FF/SD OCT), which enables cell-detail imaging of the entire ocular surface in humans (central and peripheral cornea, limbus, sclera, tear film) without contact and in real-time. Real-time performance is achieved through rapid axial eye tracking and simultaneous defocusing correction. Images contain cells and nerves, which can be quantified over a millimetric field-of-view, beyond the capability of IVCM and conventional OCT. In the limbus, palisades of Vogt, vessels, and blood flow can be resolved with high contrast without contrast agent injection. The fast imaging speed of 275 frames/s (0.6 billion pixels/s) allows direct monitoring of blood flow dynamics, enabling creation of high-resolution velocity maps. Tear flow velocity and evaporation time can be measured without fluorescein administration.

[1] Institut Langevin, ESPCI Paris, PSL University, CNRS, 1 Rue Jussieu, 75005 Paris, France. [2] State Key Laboratory of Ophthalmology, Zhongshan Ophthalmic Center, Sun Yat-sen University, 510060 Guangzhou, China. [3] Vision Institute/CIC 1423, Sorbonne University, UMR_S 968/INSERM, U968/CNRS, UMR_7210, 17 Rue Moreau, 75012 Paris, France. [4] Quinze-Vingts National Eye Hospital, 28 Rue de Charenton, 75012 Paris, France. ✉email: mazlin.slava@gmail.com; xiaopengaddis@hotmail.com; claude.boccara@espci.fr

The cornea is the front part of the eye acting as a clear window into the world. In order to maintain optical clarity, it has a complex and highly-specialized micromorphology of fibers, cells and nerves. The tear film protecting the cornea on top and limbus with blood flow supply at the periphery also play essential roles in maintaining corneal health. A small malfunction in any part of this sophisticated system may lead to a broad range of potentially blinding (4th leading cause of blindness worldwide[1]) corneal disorders: degenerative (keratoconus), inherited or infectious (bacterial, viral, and fungal keratitis). Taking into account that the largest corneal blindness burden falls on developing countries[2], cost-effective disease prevention through early diagnosis and treatment, and through public health programs is preferable over costly surgical interventions[3]. However, early and precise diagnosis is frequently complicated as various pathologies, requiring different therapies, may show the same symptoms on a macroscopic level[4]. Clinical OCT[5–7] with microscopic axial resolution proved to be useful for differentiating between many anterior eye conditions. Nevertheless, a number of pathologies were left unaddressed by clinical OCT, because of an unmet need for high lateral resolution in the en face view. The first screening method to identify specific disease biomarkers with isotropic micrometer-level resolution was in vivo confocal microscopy (IVCM)[8]. Today IVCM is used in clinical practice as an important quantitative tool[9]. Nevertheless, its use is frequently avoided, primarily because of the requirement for direct physical contact with the patient's eye preceded by ocular anesthesia. This results in discomfort for the patient, increased risk of corneal damage and risk of infection. Moreover, IVCM provides a limited field of view (FOV), well below 0.5 mm × 0.5 mm, which results in a long examination time as the clinician searches for the region of interest. Despite its drawbacks, IVCM, has remained the only cell-resolution corneal screening tool available in clinics, with no alternatives up to now.

Recently, we developed in vivo full-field optical coherence tomography (FFOCT) and demonstrated its capability to capture images of the central human cornea, resolving features such as nerves, cells, and nuclei without touching the eye[10]. This technology, originating from the lower speed ex vivo FFOCT[11–14], uses a 2D camera to acquire high-resolution en face images (i) directly without beam scanning artifacts, (ii) rapidly (at a camera frame rate), (iii) with flexible FOV. These qualities distinguish FFOCT from another high-resolution modality—UHR-OCT, which also achieved impressive cell-detail imaging in the cornea and limbus using a conventional scanning approach[15,16]. The combination of benefits, provided by FFOCT (non-contact operation, cell-resolution, and en face optical sectioning without beam scanning artifacts) was achieved thanks to our full-field interferometry approach. Nevertheless, the first in vivo FFOCT design captured an image only when the optical path lengths of the two interferometer arms were perfectly matched, which occurred only when the cornea happened to land in the perfect position. Indeed, given that the in vivo cornea is constantly moving, even during steady fixation, such matching only occurs at rare random moments, prohibiting consistent real-time imaging and visualization of the whole breadth and depth of the cornea, necessary for clinical use of FFOCT.

Here we demonstrate a combined common-path FFOCT/SDOCT microscope (FF/SD OCT), which tracks the axial position of the eye and matches the optical arm lengths of FFOCT in real time to allow consistent imaging of the entire ocular surface (central, peripheral and limbal cornea, limbus, sclera, tear film). We demonstrate that real-time, millimeter-field movies of central and peripheral in vivo corneas consistently reveal cells and nerves, which can be quantified according to the existing medical protocols used for IVCM. This makes FF/SD OCT ready for clinical research and translation into clinical practice as a non-contact OCT-based alternative to IVCM with higher resolution than conventional OCT, and capable of detecting changes in the entire ocular surface. Moreover, we show that our setup also provides the possibility of monitoring tear film evolution, opening a door to quantitative and non-contact assessment of dry eye conditions. Beyond the cornea, the instrument visualizes the scleral and limbal regions, important to stem cell storage and regeneration. FF/SD OCT can also directly view blood flow with high contrast and without fluorescein injection at a high frame rate of 275 frames per second (fps), which, paired with its high-resolution capabilities, allows individual blood cells to be followed. Furthermore, we demonstrate a method to reveal high-resolution blood flow velocity and orientation maps, which may lead the way to new localized diagnostic methodologies of scleral inflammation and approaches to monitor therapeutic effects locally.

Results

Tracking eye position with common-path FF/SD OCT. The central idea in a common-path FF/SD OCT interferometer is to detect the axial position of the cornea in real-time with SDOCT and use this information to optically match the arms of the FFOCT interferometer by moving the reference arm, leading to consistent FFOCT imaging of a moving in vivo cornea (Fig. 1 and Supplementary Movies 1, 2). SDOCT, coupled to the microscope objectives, displays the locations of the corneal surface and other reflecting surfaces in the XZ plane with high axial resolution (<3.9 μm) by acquiring 2D cross-sectional 1.25 mm × 2.7 mm images of backscattered light intensity. 2D SDOCT images are formed through rapid 100 kHz A-line scanning with a galvanometer mirror. Combined SDOCT and FFOCT share the same optical paths in the arms of the FFOCT interferometer, which is apparent in the SDOCT image by appearance of a common-path FF/SD OCT peak in addition to the conventional peaks from the cornea and reference mirror of FFOCT (Fig. 2a–d). As the common-path and reference mirror peaks never overlap, we can simultaneously detect them and calculate actual position of the cornea, imaging depth inside the cornea, optimal reference position, actual reference position and error for validating and improving the feedback loop (Fig. 2e and Supplementary Movie 3). Every 8.2 ± 0.5 ms (mean ± standard deviation (s.d.)) information about the current corneal position is sent to the FFOCT system, where it is used to correct optical mismatch between the interferometer arms.

Real-time optical path length matching of interferometer arms. The FFOCT interferometer, equipped with a near-infrared (NIR) 850 nm incoherent light-emitting diode (LED) source and moderate numerical aperture (0.3 NA) 10× air microscope objectives (MO), acquires 2D en face 1.25 mm × 1.25 mm images of XY corneal sections with 1.7 μm lateral and 7.7 μm axial resolutions (see Methods section) by a time-domain two-phase shifting scheme[12] (Fig. 1 and Supplementary Movies 1, 2). Each FFOCT image, composed of 1440 × 1440 pixels, is captured by a 2D CMOS camera in 3.5 ms at 275 FFOCT frames/s (or 0.6 billion pixels/s), which is 130 times faster (in terms of pixel rate) than the state-of-the-art corneal confocal scanning IVCM systems, imaging at 30 fps over 384 × 384 pixels FOV (or 3.6 million pixels/s)[17].

When the FFOCT interferometer is focused on the surface of the cornea, the sample and reference arms are optically matched (or more precisely, the focus spot of light on the cornea matches with the coherence plane, which is located at the position that matches (in terms of optical path length) with the reference mirror). However, as the cornea shifts axially, interferometer
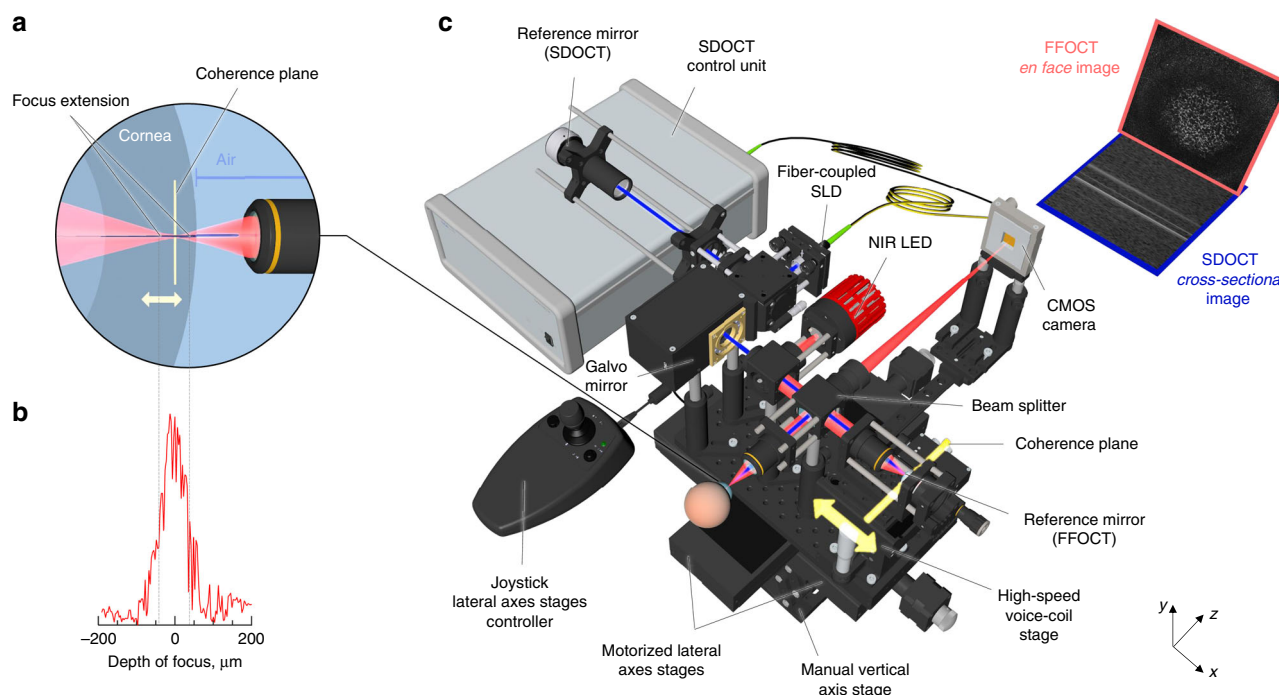
Fig. 1 Common-path FF/SD OCT with axial eye tracking and real-time defocus adjustment. a Side-view of the FFOCT sample arm with the cornea. Location of the focus changes with changing corneal position, due to refraction at the air-cornea boundary (Supplementary Movie 1). The location of the coherence plane (depicted in yellow), corresponding to the position of the FFOCT reference arm, also shifts, but in the opposite direction, leading to an optical mismatch between the two and loss of FFOCT signal. **b** Measured depth of focus. **c** The microscope consists of two interferometers: FFOCT, which acquires en face images using a 850 nm light-emitting diode illumination (depicted in red), and SDOCT, capturing cross-sectional images with a 930 nm superluminescent diode light (depicted in blue). SDOCT data is used to calculate the current corneal position and the optical mismatch correction required, which is fed into the fast voice coil stage in the FFOCT reference arm. The stage shifts rapidly to place the coherence plane within the changing position of the depth of focus. As a result, the FFOCT interferometer arms match, and en face images are acquired consistently and in real-time (Supplementary Movies 1, 2). All unlabeled scale bars are 400 µm. The source data underlying the plot in **b** are provided as a Source Data file.

arms become mismatched due to two factors: (i) the spread of the focal point into the sample due to Snell's law, originating from the large illumination angle and difference between the refractive indexes of cornea (1.376) and air (1.0), (ii) the shift of the coherence plane in the opposite direction towards the objectives, also caused by the refractive index difference (Fig. 3). The optical mismatch can be measured from the axial location of the cornea, provided in real-time by SDOCT. The mismatch is used to calculate, how far the reference arm of the interferometer should be extended (Fig. 2), in accordance with the defocus correction procedure[18], in order to match the coherence plane with a new focal position. This extension should be precise enough to land within the objective's depth of focus (measured ~ ±35 µm at FWHM) (Fig. 1b) and rapid enough to follow in vivo movements of the cornea, which is achieved using a voice coil motor (accuracy = 2.2 µm, velocity = 1 mm/s, acceleration ~25 mm/s^2) operating at a 50 Hz update rate. The entire combined FF/SD OCT system is mounted on a manual vertical and two motorized horizontal stages, controllable by the operator using a joystick.

Imaging of ex vivo cornea, mimicking in vivo eye movements. We tested and optimized real-time feedback of the common-path FF/SD OCT instrument by imaging ex vivo cornea (Fig. 4a), mounted on a moving stage. At first, the stage was programmed to produce a slow steady movement (20 µm/s) to compare system performance with enabled and disabled defocus correction. With defocus correction, as the SDOCT detects the cornea coming closer to the objective, and the image plane going deeper into the sample, the voice coil stage extends the reference arm to put it in

the optimal position for the current corneal location (Supplementary Movie 4). As a result, the FFOCT interferometer arms were well matched (Fig. 4f) with 3.7 ± 0.8 µm (mean ± s.d.) error well within the depth of focus, and FFOCT consistently displayed corneal images from various depths (Fig. 4g). Only occasionally the signal vanished due to phase changes induced by unwanted mechanical vibrations, caused by external factors (e.g., an underground metro passing nearby). Conversely, without defocus correction, the reference arm position remains fixed and FFOCT images are visible only at a single corneal position within the objective's depth of focus, which corresponds to matched optical path lengths of the interferometer arms (Fig. 4d, e and Supplementary Movie 4).

Next, we programmed the stage to move similarly to the physiological movements of the eye. This was achieved by first measuring the axial movements of the normal human cornea in vivo (Fig. 4b) and extracting the underlying frequencies and amplitudes (Fig. 4c). Two typical movements were visible: (i) heartbeat at 1.1 Hz with higher harmonics at 2.2, 3.3 Hz, etc., and (ii) slow breathing at 0.34 Hz, both in agreement with the literature[19]. We used the frequencies with the two highest amplitudes (0.34 Hz with 33 µm amplitude and 1.1 Hz with 13 µm amplitude) as our input for the motorized stage with the sample (Supplementary Movie 5). In the two cases, applying defocus correction led to positioning errors of only 1.5 ± 2.2 µm (mean ± s.d.) (Fig. 4h) and 5.3 ± 4.0 µm (mean ± s.d.) (Fig. 4i), i.e., within the depth of focus. Higher frequencies were not important, as the corresponding amplitudes were smaller than the axial resolution as well as the depth of focus of the FFOCT device.
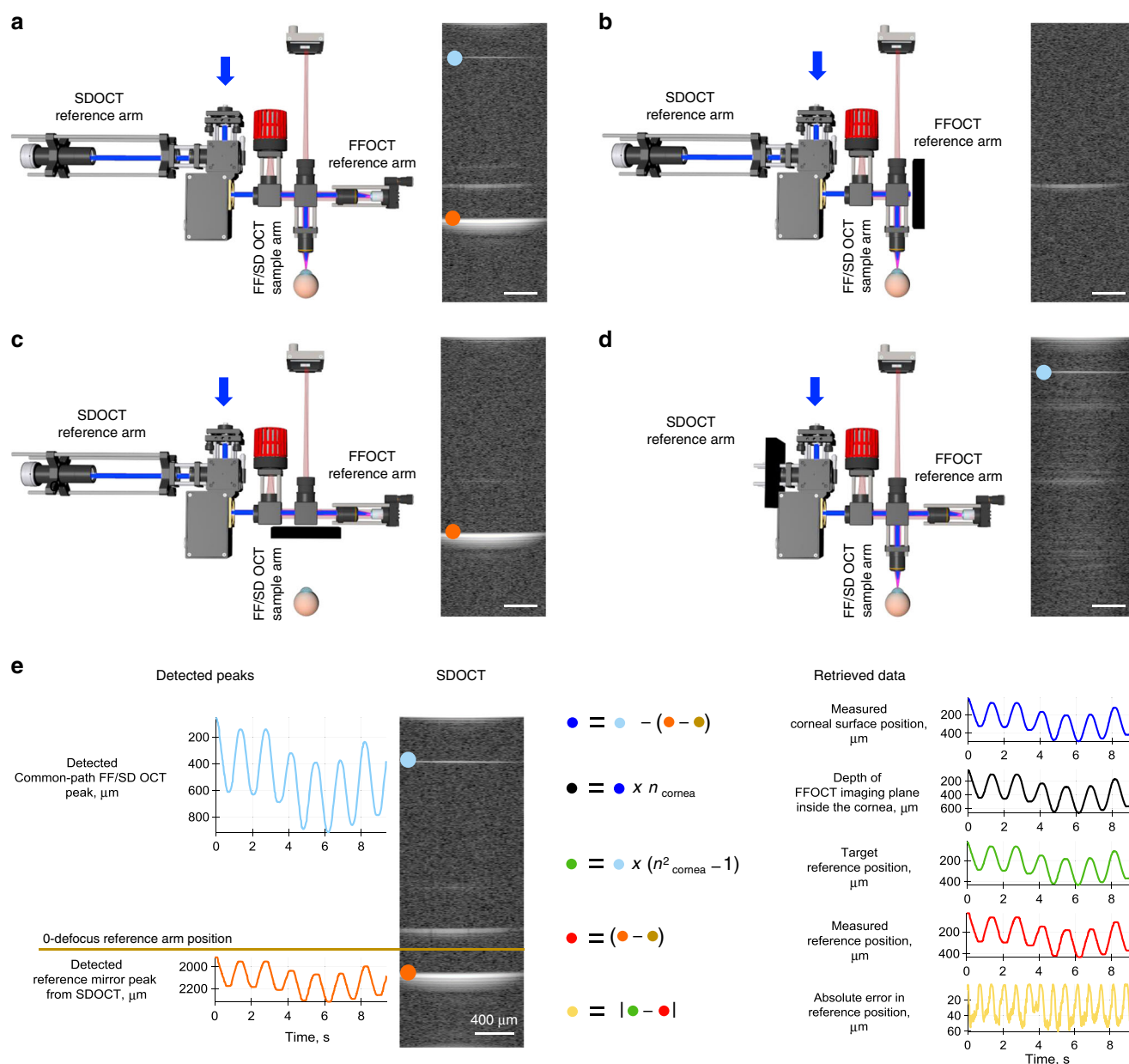
Fig. 2 Real-time detection of back-scattering intensity in SDOCT and calculation of corneal and reference mirror locations. a Left, common-path FF/SD OCT interferometer with light passing through all optical arms. **a** Right, SDOCT image with three planes of backscattered/reflected light. **b** Left, the same device with blocked FFOCT reference arm. Right, SDOCT image with a single reflected peak, corresponding to the surface of the cornea. **c** Left, device with blocked sample arm. Right, SDOCT image with reflection from the FFOCT reference mirror (orange dot). **d** Left, device with blocked SDOCT reference arm. Right, SDOCT image shows on top a single sharp reflection, originating from the FFOCT interference and captured by SDOCT (common-path peak, light-blue dot). Its narrowness reflects the perfect dispersion matching in identical arms of the FFOCT interferometer. **e** Left, SDOCT image with common-path and reference mirror peaks being detected in real-time (Supplementary Movie 3). Both of these maxima move down when the reference arm is extended for defocus correction. This facilitates their detection, as we can separate only the common-path peak for the upper area of the SDOCT image and the reference arm peak for the lower part without their overlapping. Right, using current locations of the two maxima and initial location of the reference mirror, one can calculate the corneal surface position in real-time, along with the depth of the FFOCT imaging plane in the cornea, the optimal reference position for the current corneal location, the actual reference position and the error between the two, used for validating and improving the optical arms matching loop. All scale bars are 400 μm. The source data underlying plots in **e** are provided as a Source Data file.

Imaging of in vivo human cornea and sclera. We used common-path FF/SD OCT to view in vivo human cornea in real-time. The study was carried out on three healthy subjects (1 female and 2 males, aged 36, 24, and 26 years respectively), which was confirmed by routine eye examination in the hospital preceding the experiment. Subjects expressed informed consent and the experimental procedures adhered to the tenets of the Declaration of Helsinki. Approval for the study was obtained, in conformity with French regulations, from CPP (Comité de Protection de Personnes) Sud-Est III de Bron and ANSM (Agence Nationale de Sécurité du Médicament et des Produits de Santé) study number 2019-A00942-55. During the experiment, subjects were asked to rest their chin and temples on a standard headrest, while looking at a fixation target. Examination was non-contact and without prior introduction of cycloplegic or mydriatic agents, nor topical anesthetics. While the system was heavily

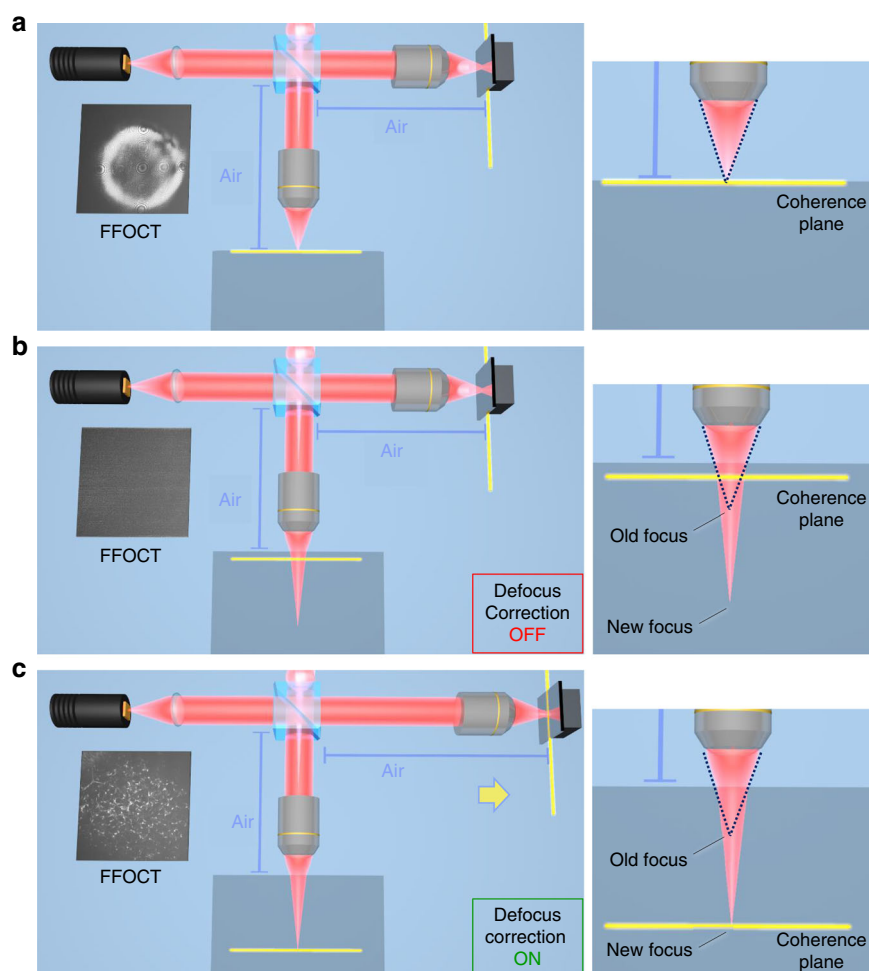**Fig. 3 Principle of defocus correction for matching the optical arms of FFOCT interferometer. a** The FFOCT interferometer is focused on the surface of the sample (blue square). The focus spot matches with the coherence plane. An FFOCT image from the surface is captured and defocus correction is not needed. **b** FFOCT interferometer is focused inside the sample. Due to Snell's law the focus is extended. At the same time the coherence plane is shifted in the opposite direction due to the higher refractive index inside the sample than in the air. The focus spot and the coherence plane are mismatched and an FFOCT image cannot be captured without defocus correction. **c** The FFOCT interferometer is focused inside the sample and the focus is extended. The defocus correction procedure is performed: the reference arm is extended to put the coherence plane in the new location of the focus and the FFOCT image from inside of the sample is captured.

optimized for both fast acquisition rate and simultaneous display at 275 FFOCT images/s, we artificially lowered both acquisition and display rates of real-time imaging to 10 fps (with each frame captured in 3.5 ms) in order to be compliant with ocular safety standards. The pulsed light irradiance was below the maximum permissible exposure (MPE) levels of up-to-date ISO 15004-2:2007 (52% of MPE for cornea and 0.5% of MPE for retina) and ANSI Z80.36-2016 (3.7% of MPE for cornea and 0.5% of MPE for retina) (for more details see Methods section). Illumination was comfortable for viewing, due to the low sensitivity of the retina to NIR and IR light. The operator of the instrument could simultaneously view FFOCT movies of en face images, OCT movies with cross-sectional images of the main corneal reflex, which serves as an indicator of the current imaging depth, and plots illustrating the performance of the defocus correction. The instrument was able to acquire movies (Supplementary Movies 6, 7, 8, 9) from central, peripheral, and limbal zones of the in vivo cornea (Figs. 5, 6), simultaneously correcting defocus with $9.4 \pm 6.2\,\mu m$, $11.3 \pm 7.2\,\mu m$, and $7.2 \pm 6.6\,\mu m$ (mean ± s.d.) errors (Figs. 5e, 6b, c), respectively.

Non-averaged single FFOCT frames, extracted from the movies, had high signal from all corneal layers. Over the central

cornea we observed tear film. It appears with a fringe pattern, as FFOCT is an interferometric technique, meaning that interference fringes are visible on flat surfaces such as tear film (Fig. 5f). Just beneath the tear film, we could see superficial epithelial cells 40–50 μm in diameter with dark 8–13 μm nuclei, in agreement with the literature[20] (Fig. 5b, g). These cells were revealed by filtering the image in the Fourier domain (see Methods section). We could also see structures from other epithelial layers (wing, basal), however were unable to reliably resolve individual cells, due to low contrast between them. Beneath the epithelium, we saw the sub-basal nerve plexus (SNP) with 2–4 μm thick nerves in a vertical orientation (Fig. 5h), which is characteristic of the central corneal area, located superior to the whorl-like nerve pattern[21]. Due to the curvature of the cornea and small thickness of the SNP, only part of the layer was visible. Nevertheless, the area of the visible nerve section was 0.317 mm², three times larger compared to what is possible with the state-of-the-art IVCM. As a result, a large-scale view of SNP can potentially be obtained with a smaller number of "stitched" images[22], leading to significantly faster screening and processing times. We also show that clinically valuable[23] measurement of nerve density can be performed with FFOCT. Nerves were
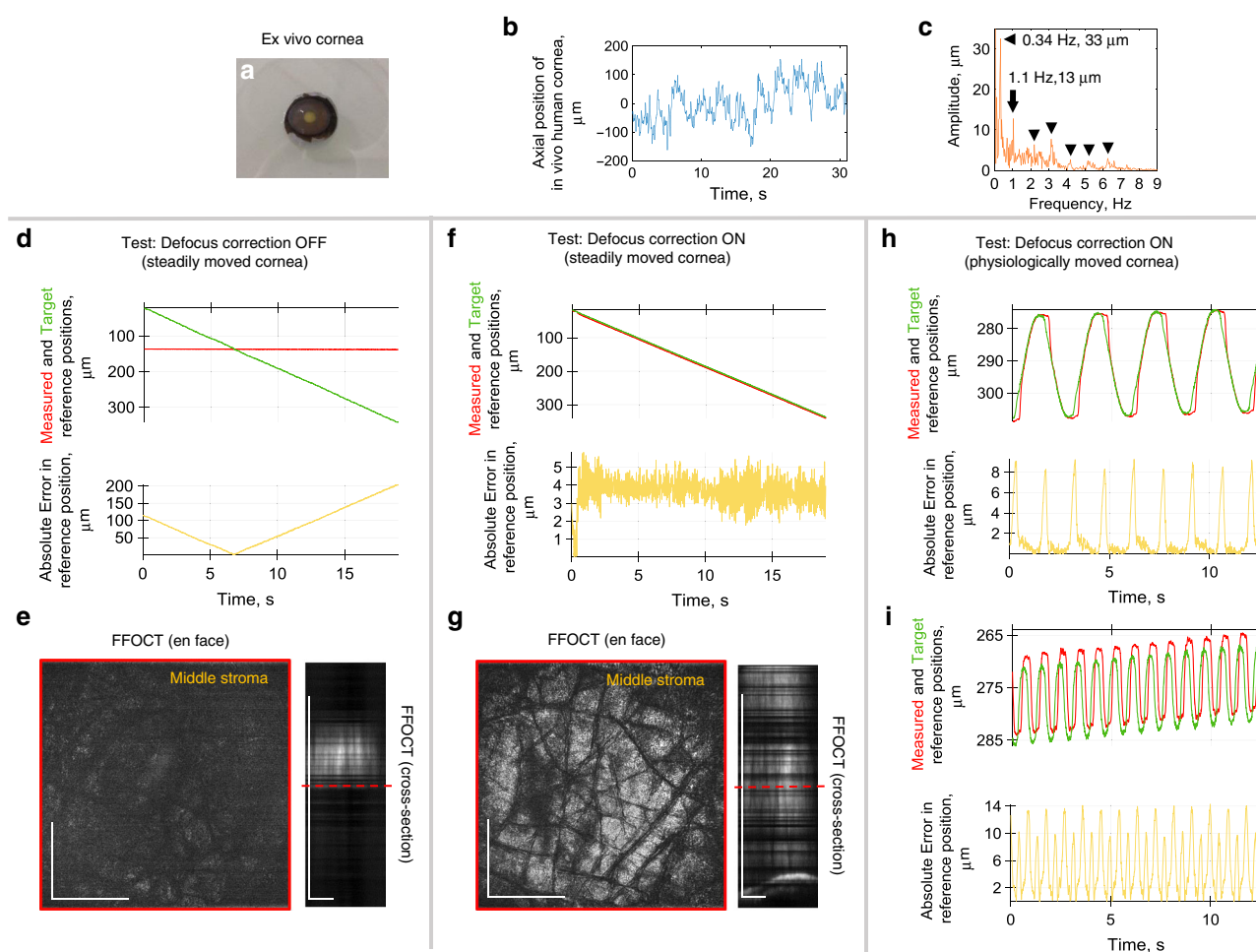
Fig. 4 Validating the real-time defocusing correction on an ex vivo cornea, driven by the motorized stage. a Photo of the corneal sample (without motor mount). Sample had visible stromal striae, indicative of tissue stress[49]. **b** Axial position of the in vivo human cornea over time, measured with SDOCT. **c** Extracted amplitudes and frequencies of the in vivo human corneal axial movements. **d** Steadily moved ex vivo cornea with deactivated defocus correction. Plots with measured reference mirror position (red), required reference location for ideal defocus correction (green) and error between the two (yellow). **e** Corresponding en face FFOCT and (reconstructed) cross-sectional FFOCT images. Red line shows location of en face FFOCT image. Without defocus correction, the reference arm position was fixed and FFOCT images were visible only at a single corneal position within the objective's depth of focus, where the optical path lengths of the interferometer arms match. **f** Steadily moved ex vivo cornea with active defocus correction. Small positioning error of $3.7 \pm 0.8\,\mu m$ (mean $\pm$ s.d.) was estimated from 2104 positions acquired over 19 s. **g** FFOCT images are consistently acquired from various depths, while only occasionally the signal vanishes due to the additional phase introduced to the tomographic signal by unwanted mechanical vibrations, caused by external factors (e.g., an underground metro passing nearby) (Supplementary Movie 4). **h** Test of defocusing correction with ex vivo cornea mimicking the physiological ocular displacement at 0.34 Hz and 33 μm amplitude. Positioning error of $1.5 \pm 2.2\,\mu m$ (mean $\pm$ s.d.), estimated from 1157 positions acquired over 12.4 s. **i** Test of defocusing correction with ex vivo cornea, moved at physiological 1.1 Hz and with 13 μm amplitude (Supplementary Movie 5). Positioning error is $5.3 \pm 4.0\,\mu m$ (mean $\pm$ s.d.), estimated from 1502 positions acquired over 12.5 s. The source data underlying plots in **b**–**d**, **f**, **h**, **i** are provided as a Source Data file. Experiments were reproduced several times using the same ex vivo cornea. All scale bars are 400 μm.

segmented using NeuronJ[24] and their density measured 15 mm/mm^2 (Fig. 5c), within the healthy margins[25]. Underneath the SNP, we enter the anterior part of the stroma with numerous bright oval-shaped nuclei of keratocyte cells, measured about 15 μm in diameter (Fig. 5i). From the anterior to posterior stroma the density of keratocytes gradually decreases down to the deep stromal layer, adjacent to Descemet's membrane, where the keratocyte density shows a slight increase, in agreement with the literature[26]. Moreover, with the increasing depth, the nuclei show a more elongated shape[27] (Fig. 5k, l). In addition to keratocyte nuclei, we can resolve keratocyte cell bodies and branching 10 μm thick stromal nerves (Fig. 5j, k). Descemet's membrane was also visible as a dark band separating stromal keratocytes from the endothelial cells (Fig. 5l). Central endothelium viewed in a single FFOCT image was hindered by a strong specular reflection and interference fringe artifacts; nevertheless, after lateral image

registration and averaging (see Methods section) we could resolve the hexagonal mosaic of 20 μm diameter cells and sometimes a 5 μm nucleus (Fig. 5d, m). While the reflectivity of the endothelium-aqueous interface is expected to be 100 times less than the air-tear film interface (based on the refractive index difference), FFOCT images show only 10 times difference in brightness, because FFOCT acquires the images of amplitude (due to the 2-phase amplitude retrieval process) and not intensity like the conventional OCT. It should be noted that in the figures these interfaces appear with similar brightness due to an adjustment of brightness and contrast. We were able to perform clinically significant[28] cell counting and measured the normal endothelial cell density of 3096 cells/mm^2 (Fig. 5d), in agreement with the literature[29], and confirmed on the same subject using a clinical specular microscope, which counted 3100 cells/mm^2. All of the above images were acquired without any physical contact
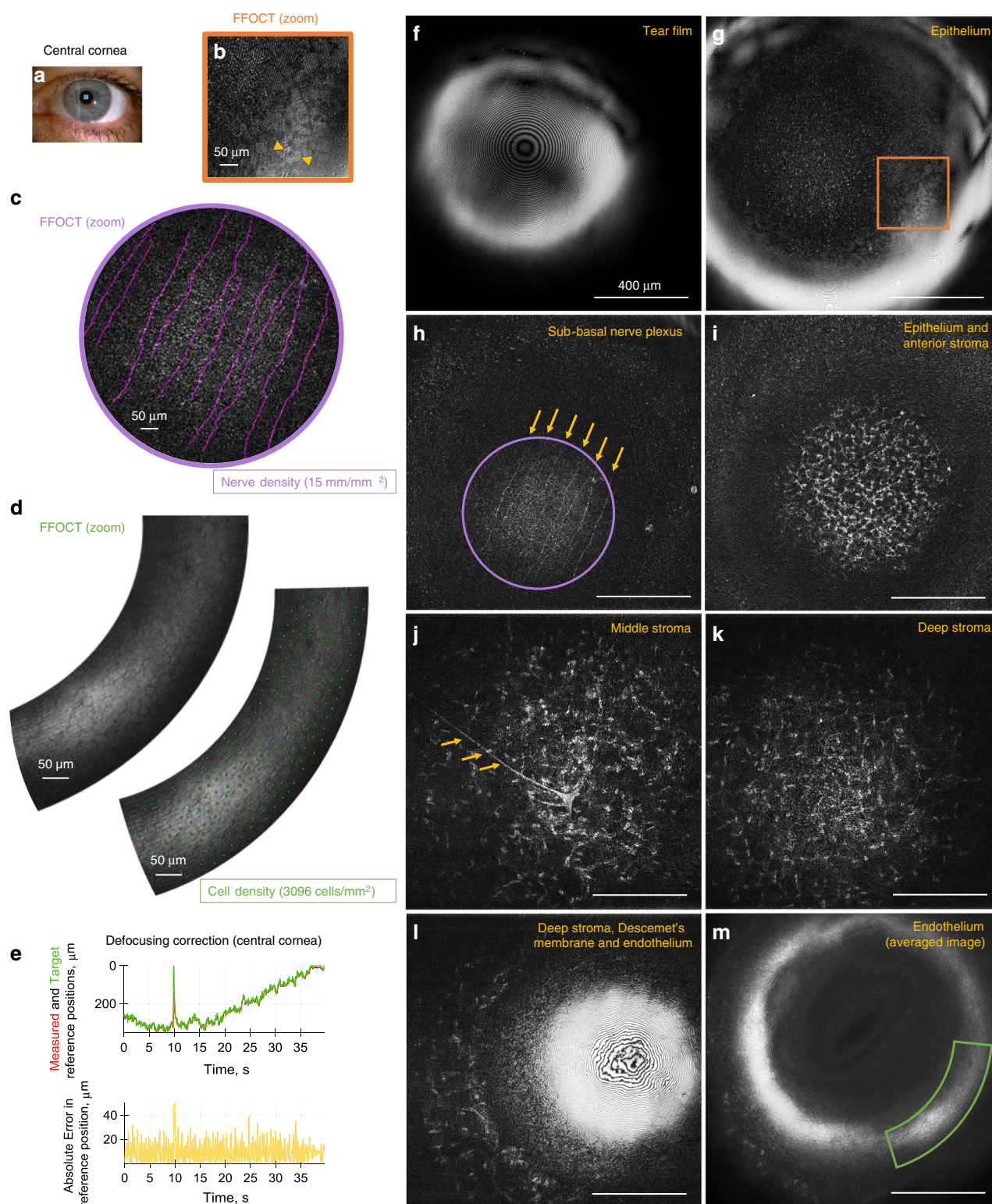
Fig. 5 Common-path FF/SD OCT imaging of central human cornea in vivo. a Slit-lamp macro photo obtained from one of the subjects. Blue square depicts the FFOCT field of view. **b** Zoomed and bandpass filtered (see Methods section) FFOCT image of superficial epithelial cells with dark nuclei. **c** Zoomed FFOCT image of sub-basal nerves. NeuronJ[24] was used for nerve tracing and quantification. **d** Zoomed FFOCT image of endothelial cell mosaic. ImageJ[47] point tool was used for cell counting. **e** Performance of real-time defocus correction, when imaging in vivo human corneal center. Measured reference mirror position (red), required reference location for ideal defocus correction (green) and error between the two (yellow). The peak at 10 s corresponds to a blink. Positioning error was 9.4 ± 6.2 μm (mean ± s.d.), estimated from 1488 positions acquired over 38.6 s. **f–m** Single frame FFOCT images through the entire thickness of the central cornea extracted from the real-time movies (Supplementary Movies 6, 7). Surface epithelial cells, sub-basal, and stromal nerves (yellow arrows), keratocyte cells and their nuclei, and endothelial cells were visible. The source data underlying plots in **e** are provided as a Source Data file. All unlabeled scale bars 400 μm. Experiments were reproduced several times in each of the three healthy subjects.
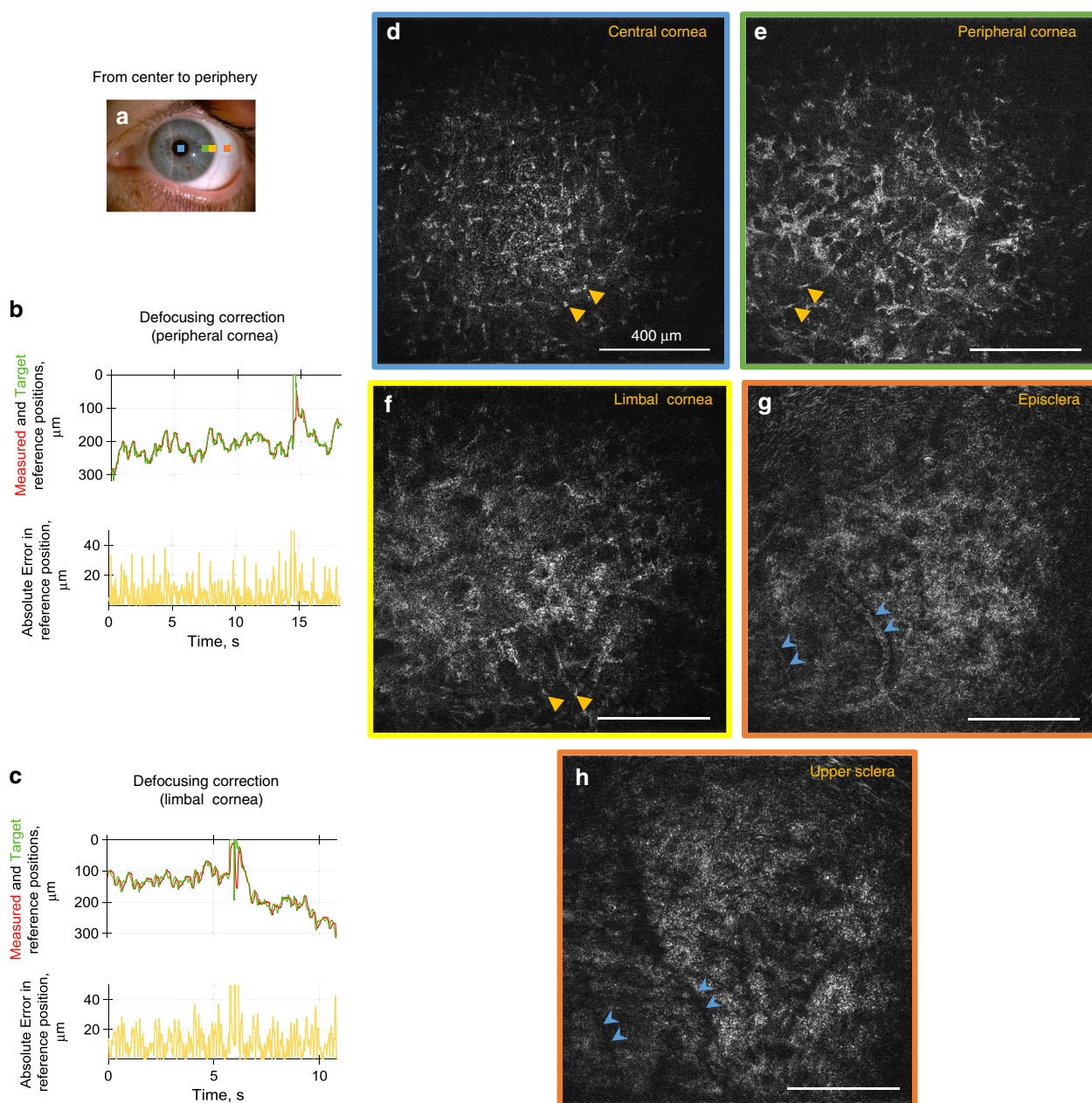
Fig. 6 Common-path FF/SD OCT imaging of peripheral human cornea, episclera and upper sclera in vivo. a Slit-lamp macro photo obtained from one of the subjects. Squares depict the peripheral locations, where FFOCT images were acquired. **b**, **c** Performance of real-time defocus correction, when imaging the corneal periphery. Measured reference mirror position (red), required reference location for ideal defocus correction (green) and error between the two (yellow). Peaks at 6 and 14 s correspond to blinks. Positioning errors were 11.3 ± 7.2 μm and 7.2 ± 6.6 μm (mean ± s.d.) estimated from 1022 and 1222 positions acquired over 18.2 and 10.8 s, respectively. **d–h** Single frame FFOCT images from central cornea to periphery, extracted from real-time movies (Supplementary Movies 8, 9). Resolving individual keratocyte nuclei (yellow arrows) was increasingly more difficult, when imaging further from the center, due to stronger light scattering from the stromal fibrils and consequent glare over the entire image. Blue arrows show vessels of episclera, which produced shadows in the upper sclera. The source data underlying plots in **b** and **c** are provided as a Source Data file. All unlabeled scale bars 400 μm. Experiments were reproduced several times in each of the three healthy subjects.

with the eye, with a distance of about 2 cm between the cornea and the microscope objective. We also benefited from the insensitivity of FFOCT to aberrations[30]. More precisely, the spatially incoherent light source in full-field illumination ensures that the non-aberrated light from the reference arm can effectively interfere only with a non-aberrated portion of light from the sample, while interference with the aberrated part is heavily suppressed[31]. As a result, FFOCT keeps the diffraction-limited 1.7 μm resolution through the entire cornea, despite the presence of spherical aberrations, which are expected to reduce

the resolution of conventional OCT and IVCM systems by three times to 5.1 μm (at the paraxial focus 550 μm deep inside the cornea). Nonetheless, it should be noted that both spectrally-dependent scattering and absorption in biological tissue, that is also spatially-dependent, do affect the FFOCT axial resolution.

We also looked at the appearance of stroma in the central and peripheral cornea, and sclera. The dark background of the central corneal stroma (Fig. 6d), becomes bright at the periphery (Fig. 6e, f), which is explained by the increased light scattering from the stromal fibrils, irregular in diameter and arrangement, known
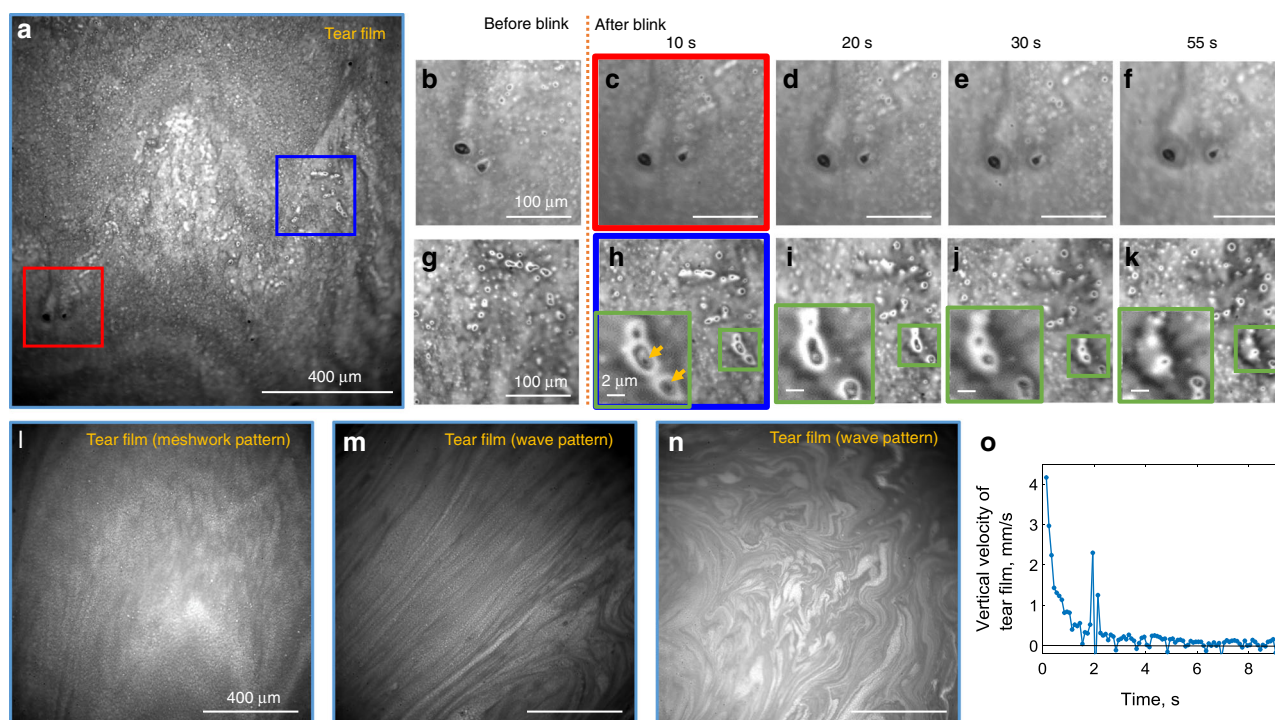
Fig. 7 Imaging human tear film in vivo with conventional microscope configuration of FF/SD OCT. a, **l–n** Single frame direct reflection images from the tear film. Interference patterns form the tear lipid layer can be used to evaluate its thickness. **b–f**, **g–k** Zoomed images from the real-time blink movie (Supplementary Movie 10). Isolated particulate matter, thought to be cellular debris or accumulations of newly secreted lipid from the Meibomian glands, were found in all subjects. Particles were static, changing locations only from blink to blink together with the movement of the tear film. Green zoomed images show liquid drops surrounding small particles. Liquid was evaporating over time. **o** Vertical velocity of the tear film, measured by manually tracking movements of particles in the movie. Tear film stabilized after 9 s following the blink. Peak at 2 s corresponds to saccadic eye motion. The source data underlying the plot in **o** are provided as a Source Data file. All unlabeled scale bars 400 μm. Experiments were reproduced several times in each of the three healthy subjects.

from electron microscopy studies[32]. The aforementioned scattering bright glare of the background makes it more difficult to resolve keratocyte cell nuclei at the periphery, comparing to those in the central cornea, easily visible against the dark background, in agreement with previous confocal microscopy data[33]. Blood vessels (Fig. 6g) were perforating the conjunctiva and episclera and produced shadows (Fig. 6h) in the upper sections of the sclera.

It should be noted that ocular movements not only shift the position of the eye leading to the problem of defocus, but they also intervene in the FFOCT image retrieval scheme, affecting image quality. The rapid axial motion of the eye can introduce additional phase modulation, which, when added to the π piezo modulation, reduces the FFOCT signal. This effect is seen in FFOCT movies as occasional wash out of the tomographic signal (Supplementary Movies 6–9). The rapid saccadic lateral motion of the eye as well as the rapid flow of tears after a blink can also introduce the artifacts to the FFOCT images. More precisely, the two-phase retrieval scheme is unable to completely remove the light originating from outside of the coherence volume, because the scene in the two images is shifted. As the largest proportion of out-of-coherence-volume light comes from the air-tear film interface, the artifacts manifest the defocused view of the ocular surface. The artifacts occasionally appear in the FFOCT movies (Supplementary Movies 6–9) and are more seldom present when imaging the deeper corneal layers (deep stroma, endothelium), as the surface gets further from the focus of the optical system.

Imaging of in vivo human tear film. We were able to demonstrate tear film evolution by blocking the reference arm, thus

converting our FF/SD OCT setup into a conventional microscope. In order to increase contrast, an image of stray light from the beam splitter, acquired without the sample, was subtracted from the tear film image. Before each examination, subjects were asked to keep their eyes closed for 2 min to replenish the tear film. Right after the eye opened, a wave pattern was typically observed (Fig. 7m, n), originating from the interference within the tear film lipid layer[34]. In the normal condition (opened eyes, free to blink) we often saw meshwork (Fig. 7a, l) patterns. We acquired movies of tear flow after a blink (Supplementary Movie 10) and after a half-blink, when the eye was not completely closed, but the tear film shifted (Supplementary Movie 11). With a blink, the upper lid rapidly moved upward and the layer of tears followed with a slight delay. At 150 ms after the blink, the flow velocity was 4.2 mm/s and rapidly decreased to 0.8 mm/s after 1 s, completely stabilizing to zero in 9 s, in agreement with literature[35,36] (Fig. 7o). Isolated particulate matter, about 1–40 μm in size, was found in all the subjects in lipid and aqueous layers (Fig. 7a, b, g), thought to be cellular debris or accumulations of newly secreted lipid from the Meibomian glands[35]. Particles were static (Fig. 7c–f, h–k), changing locations only from blink to blink together with the movement of the tear film (Fig. 7b, c, g, h). We also noticed that small particles were frequently surrounded by liquid drops, which evaporated over time (Fig. 7h–k).

Imaging of in vivo human limbus. In the inferior limbal region, 30 μm wide radial palisades of Vogt (POV) were visible (Fig. 8f). The distance between the palisades measured 30–200 μm. Marginal corneal vascular arcades (MCA) with thin 3–7 μm vessels
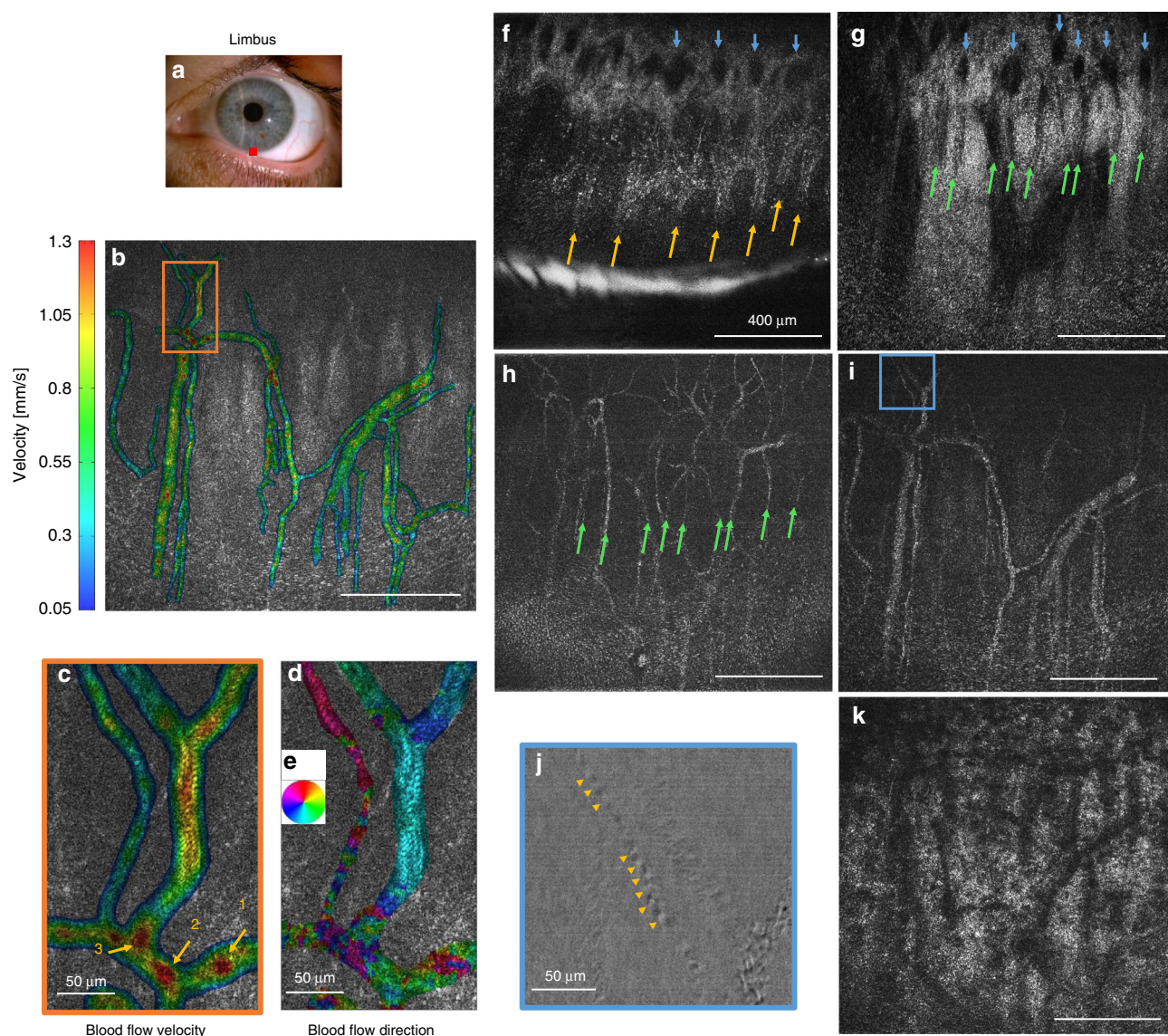
Fig. 8 Common-path FF/SD OCT imaging and angiography of in vivo human limbus. a Slit-lamp macro photo obtained from one of the subjects. Red square depicts location, where FFOCT images were acquired. **b, c** Blood flow velocity map, retrieved from the rapidly acquired movie at 275 images/s (Supplementary Movie 12), together with a zoomed image. The lowest speeds were measured close to vessel walls and highest speeds in the middle of the vessels, in junction points (point 2 and point 1 (with merging vessel coming to point 1 visible only in the movie)) and also, as artifacts, if vessels overlaid each other (point 3). **d** Blood flow orientation map retrieved from the movie. Each color corresponds to a certain direction of blood flow, according to the colormap **e. f–k** Single frame FFOCT images of consecutive depths in limbus. Yellow arrows—palisades, green arrows—thin vessels hosted within palisades, blue arrows—perpendicular vessel network thought to be connected with horizontal vessels. Underneath, thicker vessels and scattering stroma-sclera medium with vessel shadows were seen. **j** Zoomed view on thin vessel in **i**. Image is obtained by subtracting the two camera shots. Contrast is reduced (see Methods), but is more intuitive for resolving and following individual blood cells (yellow arrows) (Supplementary Movie 12). Unlabeled scale bars are 400 μm. Experiments were reproduced several times in each of the three healthy subjects.

(Fig. 8g, h) appeared to protrude from inside of the palisades, in agreement with the literature[16,37,38]. These vessels, parallel to the ocular surface, appeared to be connected with a perpendicular oriented vessel network, visible as dark round shadows (Fig. 8f, g). Closer to the cornea, MCA vessels curled into the loops, while continuing to spread in the radial direction. Beneath, we could see thicker 40 μm branching vessels (Fig. 8i). By looking at the difference between two camera images (see Methods section), it was possible to resolve individual 7 μm blood cells (Fig. 8j and Supplementary Movie 12), which were difficult to see with a tomographic FFOCT image. Moreover, using rapid 275 frame/s acquisition, we could visualize and track the flow of these cells,

which had a speed of about 1 mm/s (Supplementary Movie 12). Furthermore, in order to capture the full-field information about the blood flow, important for addressing inflammatory conditions in the anterior eye, we measured the local cross-correlation for each 16 pixel × 16 pixel sub-image and retrieved blood flow velocity and blood flow direction maps with micrometer-level resolution (Fig. 8b–e). Average velocity was measured to be 0.446 ± 0.270 mm/s, with the lowest speeds close to vessel walls and highest speeds in the middle of the vessels, at junctions and also in locations where vessels were overlaying each other (Fig. 8c). Blood flow was mostly radial, going back and forth from the cornea (Fig. 8d, e).

Discussion

Confocal microscopy, the state-of-the-art tool for cellular-resolution imaging of the cornea, requires contact with the eye, preceded by ocular anesthesia. Conventional OCT provides high axial resolution of corneal layers, but does not resolve cells, while UHR-OCT resolves cells, however the en face images suffer from eye movement artifacts during X–Y beam scanning. Our common-path FF/SD OCT reveals the same micrometer corneal features (cell, nerves, and nuclei), but in a completely non-contact way, with a 2 cm distance from the eye, does not require use of any medication and is immune to beam scanning artifacts. These features improve patient comfort, remove risk of corneal damage and risk of infection, and open up the possibility for high-resolution imaging in a risk-sensitive population (e.g., young children, candidates for corneal transplant surgery with fragile corneas). Compared to our previous preliminary work[10], in this article we have integrated SDOCT into FFOCT, which allowed tracking of the eye position and matching the arms of the FFOCT interferometer in real-time. This has enabled consistent real-time acquisition of corneal images and movies with high signal and allowed exploration of the entire ocular surface (central, peripheral, and limbal cornea, as well as limbus, episclera and sclera). This opens a path for FFOCT implementation in clinical research and translation into clinical practice. Our device provides images with three times larger field of view than IVCM (nine times larger in area), which makes it easier to locate the clinical area of interest and follow the same location over time. Furthermore, a larger viewing area is useful for quantitative measurements of sub-basal nerve and endothelial cell densities, which were demonstrated with common-path FF/SD OCT following methodologies, used in confocal studies. Both are clinically valuable parameters: nerve density correlates with keratoconus, dry eye, several types of keratitis and diabetes[39], while endothelial cell density correlates with dystrophies, uveitis and acute ischemic stroke[40]. As FFOCT lateral resolution is immune to aberrations[31], the device is expected to resolve nerves and cells in pathological distorted corneas as well (e.g., in the case of keratoconus). Axial resolution could be improved (for resolving finer corneal layers) in future iterations of the device through increasing the spectral bandwidth of the source, for example by implementing emerging broadband NIR LEDs of sufficient power or by combining several existing NIR LEDs with close spectral characteristics.

The instrument also opens a door to quantitative diagnosis of dry eye condition by providing information about tear film velocity and stabilization time following a blink, the evaporation time of the liquid micro-droplets on the surface of the eye, and potentially the thickness of the tear film by grading lipid interference patterns in a similar way to the Guillon Keeler tear film grading system[41]. Common-path FF/SD OCT can resolve finer high-resolution sections of the limbus and is able to distinguish layers of palisades of Vogt and underlying vessels, compared to UHR-OCT[16] and IVCM[42]. Furthermore, our instrument is not limited to diagnosis of "static" corneal disorders, but can potentially monitor inflammatory and scarring conditions affecting the fast (millisecond) dynamics of the blood flow in the eye. Previously, general information about the blood flow velocity and vessel dimensions from anterior segment fluorescein angiography (ASFA) and indocyanine green dye angiography (IGDA) proved to be useful for distinguishing between the various forms of scleral inflammation, in particular between severe episcleritis and diffuse anterior scleritis or between peripheral corneal opacification and corneal thinning[43]. With FF/SD OCT, we can have access to the same information and view the blood flow with high contrast, but without fluorescein injection and with the examination taking a fraction of a second. Furthermore, the ability of the instrument to capture high-resolution maps of blood flow velocities and orientations can potentially be useful for opening up new localized diagnostic methodologies and ways to monitor effects of therapies locally. This could bring insights about the anatomy and physiology of the vascular system in the anterior eye and in particular the limbal vessels and MCA supplying the cornea. Moreover, we suggest that the intravascular mapping of blood flow with our device may be a promising platform for testing in vivo microfluidic theories[44]. Last, but not least, common-path FF/SD OCT can also be used for non-contact examination of various in vivo human, animal and ex vivo tissues.

Methods

FFOCT device. The FFOCT device is based on an interference microscope in a Linnik configuration with identical microscope objectives in the two arms of the interferometer. Objectives (LMPLN10XIR, Olympus, Japan) have a numerical aperture (NA) of 0.3, 10× magnification and give high lateral resolution of 1.7 μm (with a filled 10.8 mm entrance aperture). The lateral resolution (identical in cornea and in free space) was estimated according to the Rayleigh criterion and experimentally confirmed with a resolution target and by measuring the diameters (FWHM) of 80 nm gold nanoparticles imaged on a glass plate, located at the focal plane of the FFOCT objective. The working distance of the objectives was 18 mm, sufficient to avoid the risk of accidental physical contact with the eye. Illumination is provided by an NIR 850 nm light-emitting diode (LED) source (M850LP1, Thorlabs, USA). The axial resolution of 7.7 μm in the cornea was estimated from the experimentally measured spectral bandwidth of the LED (30 nm) with a spectrometer (CCS175/M, Thorlabs, USA) and by using the average corneal refractive index of 1.376, often quoted in the literature[45]. Light from the LED is collected by an aspheric condenser lens (ACL12708U-B, Thorlabs, USA) and is focused on the back focal plane of the objective. Before entering the objective, light from the source is equally separated by the 50:50 beam splitter cube (BS) (BS014, Thorlabs, USA) into the sample and reference arms of the interferometer. The arms are slightly tilted from a perpendicular orientation in order to avoid specular reflection from the BS side. The objective in the reference arm focuses light onto an absorptive neutral density (ND) glass filter (NENIR550B, Thorlabs, USA), which plays the role of a single mirrored surface with 4% reflectivity. Use of an ND filter with OD 5.0 instead of a glass plate enables elimination of ghost reflections from the back surface of the filter. A low reflectivity value is chosen to achieve high detection sensitivity, which is maximized when the total reflectivity (from all the layers participating or not to the FFOCT signal) of the sample and reflectivity of the reference mirror match, as indicated by FFOCT signal to noise calculations[12]. Total reflectivity from all corneal layers, estimated from the Fresnel relations, is around 2%. By using a reference mirror with a reflectivity of 4%, we can expect sensitivity close to the ideal condition[12]. Light in the sample arm, backscattered from the different planes in the cornea, and light in the reference arm, back-scattered from a single mirror plane, are collected by the objectives, and recombined on the BS. This results in interference, but only for the light coming from the corneal plane, and light coming from the reference mirror plane, which match in terms of optical path length. The temporal coherence length of the light source determines the thickness of the interference fringe axial extension and therefore the optical sectioning precision, which is 7.7 μm. Interfering light and non-interfering light, arising from other planes of the cornea, are focused onto a sensor by a magnifying tube lens (AC254-250-B, Thorlabs, USA), leading to 14× overall system magnification. The sensor is a high-full well capacity (2Me⁻) 1440 × 1440 pixel CMOS camera (Q-2A750-CXP, Adimec, Netherlands), which captures each 2D image in 1.75 ms. In order to reach the expected axial sectioning in the system, light which has interfered must be extracted from the background. To do so, we use a two-phase shifting scheme, where we rapidly modulate the position of the reference mirror using a piezo mirror-shifter (STr-25/150/6, Piezomechanik GmbH, Germany), synchronized with the camera, to capture two consecutive images, which have a π phase shift, and subtract them. The absolute value of the resulting image contains only interfering light from a 7.7 μm thick section in the cornea. We can capture images in two modes: (i) fast acquisition mode for visualizing blood flow, where a sequence of 40 images is captured at 550 fps, and (ii) slow mode for real-time imaging, where images are displayed live on screen at 10 fps. The real-time mode has artificially lowered acquisition and display rate to 10 fps in order to be compliant with the European ISO 15004-2:2007 ocular safety standard (see below). 10 fast pulsed LED exposures/s (3.5 ms each exposure) with pauses in between each exposure allow us to increase the output of the LED to saturate the high full-well capacity camera, while still being below the maximum permissible light levels. It should be noted that the most recent US ocular safety standard ANSI Z80.36-2016 imposes a much less strict limitation for exposure of the anterior eye, which in the future potentially enables the prolonged use of our device at full speed frame rate at 275 fps without LED pulsation.

A complete evaluation of corneal and retinal safety, involving scenarios of real-time imaging (used to visualize static corneal structures) and single prolonged LED exposure (used to visualize blood flow dynamics), was performed. The results are summarized below.

For real-time imaging we took into consideration the durations of pulsed light exposures (3.5 ms for LED and 1.37 ms for SLD (beam scanning)), durations of pauses without the light (100 ms for LED and 0.41 ms for SLD) and irradiances per pulse (2 W/cm^2 for LED and 35 mW/cm^2 for SLD). These values were used to calculate the corneal and retinal exposures. The calculated time-dependent graphs show that during real-time acquisition we reach up to 52% of MPE for the cornea and only 0.5% of MPE for the retina (according to ISO 15004-2:2007) and 3.7% of MPE for the cornea and 0.5% of MPE for the retina (ANSI Z80.36-2016).

For single prolonged LED exposure we took into consideration the durations of pulsed light exposures (70 ms for LED and 1.37 ms for SLD (beam scanning)), durations of pauses without the light (30 s for LED and 0.41 ms for SLD) and irradiances per pulse (2 W/cm^2 for LED and 35 mW/cm^2 for SLD). The calculated time-dependent graphs show that during real-time acquisition we reach up to 18% of MPE for the cornea and only 1% of MPE for the retina (according to ISO 15004-2:2007) and 1.3% of MPE for the cornea and 1% of MPE for the retina (ANSI Z80.36-2016). The major contributor to the exposure is the LED.

SDOCT device. The SDOCT device is based on a commercial general-purpose spectral-domain OCT (GAN510, Thorlabs, USA). It consists of an interferometer with a galvanometric mirror system (OCTP-900(/M), Thorlabs, USA), which rapidly scans a collimated light beam laterally at 100 kHz to form a 2D cross-sectional image. In order to increase the frame-rate, the lateral extension of the image was limited to 64 pixels. The 2D image is averaged over the lateral dimension and the resulting 1D data is processed with Labview Peak detector VI (National Instruments, USA) to locate the maxima. As these are single non-overlapping peaks, their positions can be detected with a precision better than 3.9 μm in the cornea, as determined by the Rayleigh criterion and spectral bandwidth of infrared (IR) 930 nm superluminescent diode (SLD). Because the SDOCT and FFOCT interferometers share the same optical arms, we detect not only the conventional SDOCT peaks corresponding to the reflection from the cornea and from the FFOCT reference mirror, but also the third common-path peak corresponding to the interference inside the FFOCT interferometer (i.e., between FFOCT sample and FFOCT reference arms). The latter maximum has the advantages that (i) it does not suffer from dispersion, due to the perfect dispersion symmetry between the arms of the FFOCT interferometer; (ii) it is moving in the same direction on the 2D image as the reference arm, extended for defocus correction. As a result, since the common-path and reference mirror peaks never overlap, we can simultaneously detect them and calculate positions of the cornea, the imaging depth inside the cornea, the optimal reference position for the defocus correction[18], the actual reference position and the error for validating and improving the feedback loop. By reducing the light entering into the reference arm of SDOCT, we suppress the conventional peak from the cornea to further facilitate acquisition of common-path and conventional reference arm peaks. Maxima were detected over a 1.25 mm lateral range, matching the FFOCT field of view and over a 2.7 mm axial range, determined by the SDOCT spectrometer. Information about the locations of the peaks was refreshed every 8.2 ± 0.5 ms (mean ± standard deviation (s.d.)).

Integrated FFOCT-SDOCT instrument. SDOCT is optically integrated through the dichroic mirror (Edmund Optics, USA) into the illumination arm of FFOCT. In order to block the SDOCT light from reaching the FFOCT camera, two filters with opposite spectral characteristics (low and high pass at 900 nm cutoff) (FELH0900 and FESH0900, Thorlabs, USA) are positioned at the entrance and exit of the FFOCT device. Glass windows (WG11050-B, Thorlabs, USA) are inserted into the reference arm of SDOCT to dispersion match with the FFOCT sample and reference arms. The combined instrument is positioned on two high-load lateral translation stages (NRT150/M, Thorlabs, USA), controlled by a driver (BSC202, Thorlabs, USA) with a joystick (MJC001, Thorlabs, USA). Beneath, a laboratory jack (L490/M, Thorlabs, USA) is used to position the whole device vertically. The reference arm of the FFOCT device is mounted on a voice-coil translation stage (X-DMQ12P-DE52, Zaber, Canada), driven with 2.2 μm accuracy, 1 mm/s velocity and 25 mm/s^2 acceleration for rapid defocus adjustment. Information about the currently required defocus correction shift is communicated to the stage from the SDOCT system through the same personal computer (PC) to avoid time delays. The weak link in the communication is the limited read frequency of the stage encoder, which can accept 50 new positions/s—about two times slower compared to the rate of positions provided by SDOCT. SDOCT image acquisition is controlled by a separate PC, which is synchronized with the FFOCT PC using the 11 ± 3 ms (mean ± s.d.) precision NI-PSP protocol via the local network of the Langevin Institute. Generation of 3D images should be possible in the future generations of the device with FFOCT and SDOCT being driven by a single PC.

Software. Custom programs written in Labview 2014 and Thorlabs SpectralRadar SDK were used for FFOCT and SDOCT image acquisition and display, peak detection and motor control. MATLAB R2017a was used for plots and calculation of angiography maps. We utilized ImageJ 1.51p for image display and measurements of cell and nerve densities. ZEMAX Optics Studio was used to simulate the light propagation inside the cornea and measure aberrations.

Artifact suppression and contrast enhancement. In order to remove surface interference fringes and reveal superficial epithelial cells (Fig. 5b), we transformed the image into the Fourier domain and masked the bright spots, corresponding to fringes. Inverting this Fourier image with suppressed artifacts revealed the cells. The same artifacts were also visible at the outer endothelial layer. We were able to suppress them by registering and averaging multiple (23) tomographic FFOCT images with ImageJ[46] without Fourier domain conversion (although averaging and Fourier domain processing can be used together to improve the final image). It is worth noting that filtering the interference fringes was more difficult in cases, when the endothelium was captured exactly in line with the corneal apex, because the fringes had varying spatial frequency and spacing. The endothelium on the apex had the smallest fringe frequency, because its orientation was perpendicular to the optical axis, i.e.,—the same orientation as the reference mirror. The endothelium elsewhere than at the apex was tilted due to the corneal curvature, which increased the interference fringe frequency.

The image and movie (Fig. 8j and Supplementary Movie 12) of individual blood cells was obtained not with a FFOCT image retrieval scheme, but by subtracting two consecutive images from the camera without taking the absolute value. The reason for this is the following: when we retrieve the FFOCT image via the two-phase method, the two consecutive images from the camera are subtracted and then the absolute of the image is taken to reveal the pixels, previously hidden due to their negative value after subtraction. Unfortunately, in the case of FFOCT imaging of a moving particle, we get a "doubling artifact", i.e. we see the moving particle as the two objects separated by a small gap. This complicates particle tracking. To get a better view of moving particles, we performed image subtraction without taking the absolute value. In this case each particle is seen as a single object, which simplifies its tracking. However, half of the signal (i.e., corresponding to the negative pixels) is lost.

Quantitative image analysis. Semi-automated nerve segmentation and density analysis (Fig. 5c) was performed with ImageJ[47] using the NeuronJ plugin[24]. Manual endothelial cell counting (Fig. 5d) was done with the Multi-point Tool in ImageJ. A Manual Tracking ImageJ plugin enabled manual blood cell tracking and the subsequent particle velocity analysis (Supplementary Movie 12).

Mapping blood flow velocity and orientation. Previously, we demonstrated the possibility of local blood flow measurements from the conjunctival surface using manually drawn kymograph plots (i.e., plotting the vessel curvilinear abscissa against time)[48]. However, each plot provided only a single local velocity value, so that obtaining a full-field velocity map would require considerable manual effort. Here we used a method based on a block-matching algorithm to track single features inside vessels, which allows rapid semi-automatic mapping of blood flow velocities and orientations in full-field. We cross-correlated 16×16 pixels windows and retrieved the cross-correlation maximum for each pixel in the vicinity corresponding to a maximal speed of 2 mm/s. Low cross-correlation peaks were discarded in order to remove artifacts and outliers. A velocity array is then created based on eight frames, so that the velocity computed for each pixel is the average of the seven velocities computed by the block-matching algorithm. Then the velocities and orientations are mapped on the hue channel, the FFOCT image is mapped on the value channel and the saturation is arbitrarily set to 0.8 for each pixel in order to construct the velocity and orientation map of the blood flow (Fig. 8b–e).

Ex vivo cornea. Ex vivo macaque corneas were obtained from a partner research institution as recuperated waste tissue from an unrelated experiment. Corneas were dissected from the ocular globes within two hours post-mortem and fixed in 2% paraformaldehyde prior to transfer to the imaging lab. Some edematous swelling occurred, causing enhanced visibility of stromal striae[49], indicative of tissue stress.

In vivo imaging. Informed consent was obtained from all subjects and the experimental procedures adhered to the tenets of the Declaration of Helsinki. Examination was non-contact and no medication was introduced into the eye. Light illumination, visible as a dim red circular background, was comfortable for viewing, due to the low sensitivity of the retina to NIR and IR light. For real-time imaging, light exposures measured 52% of maximum permissible exposure (MPE) for cornea and only 0.5% of MPE for the retina (according to ISO 15004-2:2007) and 3.7% of MPE for the cornea and 0.5% of MPE for the retina (ANSI Z80.36-2016). For single exposure imaging (angiography), light exposures measured 18% of maximum permissible exposure (MPE) for cornea and only 1% of MPE for retina (according to ISO 15004-2:2007) and 1.3% of MPE for the cornea and 1% of MPE for the retina (ANSI Z80.36-2016). These values reflect that the light beam is focused on the cornea and widely spread on the retina. Up-to-date ISO and ANSI standards specify different MPE levels for corneal imaging at 850 nm wavelength, leading to different safety margins. The subject's head was comfortably positioned with temple supports and a chin rest. While one eye was imaged, the second eye was fixating on a target. When imaging non-central parts of the cornea, the subject's head was tilted by the examiner to position the eye's surface plane perpendicular to the direction of the incoming light beam.

Other instruments. Macro images were obtained with a slit-lamp biomicroscope (Topcon, France Medical S.A.S.) using 10× magnification and the lowest illumination. For comparison with FFOCT images, the endothelium was photographed using a clinical specular microscope (SP-3000P, Topcon, Japan) with 0.25 × 0.5 mm field of view.

Reporting summary. Further information on research design is available in the Nature Research Reporting Summary linked to this article.

Data availability

The data that support the findings of this study are available from the first author and the corresponding author upon request. The source data underlying plots in Figs. 1b, 2e, 4b–d, f, h, i, 5e, 6b, c, and 7o are provided as a Source Data file.

Code availability

Code that supports the findings of this study is available upon reasonable request from the first author but third party restrictions may apply (e.g., Thorlabs SDK).

References

1. Pascolini, D. & Mariotti, S. P. Global estimates of visual impairment: 2010. *Br. J. Ophthalmol.* **96**, 614–618 (2012).
2. Whitcher, J. P. & Upadhyay, M. P. Corneal blindness: a global perspective. *Bull. World Health Organ.* **79**, 214–221 (2001).
3. WHO. *Universal Eye Health: A Global Action Plan 2014–2019*. (WHO, 2013).
4. Mascarenhas, J. et al. Acanthamoeba, fungal, and bacterial keratitis: a comparison of risk factors and clinical features. *Am. J. Ophthalmol.* **157**, 56–62 (2014).
5. Huang, D. et al. Optical coherence tomography. *Science* **254**, 1178–1181 (1991).
6. Drexler, W. & Fujimoto, J. G. *Optical Coherence Tomography: Technology and Applications*. (Springer International Publishing, 2015).
7. Steinert, R. F. & Huang, D. *Anterior Segment Optical Coherence Tomography*. (Slack Incorporated, 2008).
8. Cavanagh, H. D. et al. Clinical and diagnostic use of in vivo confocal microscopy in patients with corneal disease. *Ophthalmology* **100**, 1444–1454 (1993).
9. Guthoff, R. F., Zhivov, A. & Stachs, O. In vivo confocal microscopy, an inner vision of the cornea - a major review. *Clin. Exp. Ophthalmol.* **37**, 100–117 (2009).
10. Mazlin, V. et al. In vivo high resolution human corneal imaging using full-field optical coherence tomography. *Biomed. Opt. Express* **9**, 557 (2018).
11. Beaurepaire, E., Boccara, A. C., Lebec, M., Blanchot, L. & Saint-Jalmes, H. Full-field optical coherence microscopy. *Opt. Lett.* **23**, 244 (1998).
12. Dubois, A. *Handbook of Full-Field Optical Coherence Microscopy: Technology and Applications*. (Pan Stanford publishing, 2016).
13. Grieve, K. et al. In vivo anterior segment imaging in the rat eye with high speed white light full-field optical coherence tomography. *Opt. Express* **13**, 6286 (2005).
14. Grieve, K. et al. Ocular tissue imaging using ultrahigh-resolution, full-field optical coherence tomography. *Investig.Opthalmol. Vis. Sci.* **45**, 4126 (2004).
15. Tan, B. et al. 250 kHz, 1,5 μm resolution SD-OCT for in-vivo cellular imaging of the human cornea. *Biomed. Opt. Express* **9**, 6569 (2018).
16. Bizheva, K. et al. In-vivo imaging of the palisades of Vogt and the limbal crypts with sub-micrometer axial resolution optical coherence tomography. *Biomed. Opt. Express* **8**, 4141 (2017).
17. Petroll, W. M., Weaver, M., Vaidya, S., McCulley, J. P. & Cavanagh, H. D. Quantitative 3-dimensional corneal imaging in vivo Using a modified HRT-RCM confocal microscope. *Cornea* **32**, e36–e43 (2013).
18. Labiau, S., David, G., Gigan, S. & Boccara, A. C. Defocus test and defocus correction in full-field optical coherence tomography. *Opt. Lett.* **34**, 1576 (2009).
19. de Kinkelder, R. et al. Heartbeat-induced axial motion artifacts in optical coherence tomography measurements of the retina. *Investig. Opthalmol. Vis. Sci.* **52**, 3908 (2011).
20. Guthoff, R. F., Baudouin, C. & Stave, J. *Atlas of Confocal Laser Scanning In-vivo Microscopy in Ophthalmology*. (Springer, Berlin Heidelberg, 2006).
21. Patel, D. V. & McGhee, C. N. J. Mapping of the normal human corneal sub-basal nerve plexus by in vivo laser scanning confocal microscopy. *Investig. Opthalmol. Vis. Sci.* **46**, 4485 (2005).
22. Allgeier, S. et al. 3D confocal laser-scanning microscopy for large-area imaging of the corneal subbasal nerve plexus. *Sci. Rep.* **8**, 1–10 (2018).
23. Shaheen, B. S., Bakir, M. & Jain, S. Corneal nerves in health and disease. *Surv. Ophthalmol.* **59**, 263–285 (2014).
24. Meijering, E. et al. Design and validation of a tool for neurite tracing and analysis in fluorescence microscopy images. *Cytometry* **58A**, 167–176 (2004).
25. Copeland, R. A. & Afshari, N. *Copeland and Afshari's Principles and Practice of Cornea*. (JP Medical Ltd, 2013).
26. Berlau, J., Becker, H.-H., Stave, J., Oriwol, C. & Guthoff, R. F. Depth and age-dependent distribution of keratocytes in healthy human corneas: a study using scanning-slit confocal microscopy in vivo. *J. Cataract Refract. Surg.* **28**, 611–616 (2002).
27. Dartt, D. A. et al. *Ocular Periphery and Disorders*. (Academic Press, 2011).
28. Tuft, S. J. & Coster, D. J. The corneal endothelium. *Eye* **4**, 389–424 (1990).
29. McCarey, B. E., Edelhauser, H. F. & Lynn, M. J. Review of corneal endothelial specular microscopy for FDA clinical trials of refractive procedures, surgical devices, and new intraocular drugs and solutions. *Cornea* **27**, 1–16 (2008).
30. Xiao, P. et al. In vivo high-resolution human retinal imaging with wavefront-correctionless full-field OCT. *Optica* **5**, 409 (2018).
31. Xiao, P., Fink, M. & Boccara, A. C. Full-field spatially incoherent illumination interferometry: a spatial resolution almost insensitive to aberrations. *Opt. Lett.* **41**, 3920 (2016).
32. Komai, Y. & Ushiki, T. The three-dimensional organization of collagen fibrils in the human cornea and sclera. *Invest. Ophthalmol. Vis. Sci.* **32**, 2244–2258 (1991).
33. Zheng, T., Le, Q., Hong, J. & Xu, J. Comparison of human corneal cell density by age and corneal location: an in vivo confocal microscopy study. *BMC Ophthalmol.* **16**, 109 (2016).
34. Aranha dos Santos, V. et al. Super-resolved thickness maps of thin film phantoms and in vivo visualization of tear film lipid layer using OCT. *Biomed. Opt. Express* **7**, 2650 (2016).
35. Owens, H. & Phillips, J. Spreading of the tears after a blink: velocity and stabilization time in healthy eyes. PubMed—NCBI. *Cornea* **20**, 484–487 (2001).
36. Németh, J. et al. High-speed videotopographic measurement of tear film build-up tme. *Invest. Ophthalmol. Vis. Sci.* **43**, 1783–1790 (2002).
37. Vogt, A. & von der Heydt, R. Atlas of the slitlamp-microscopy of the living eye. (Springer, Berlin Heidelberg, 1921).
38. Grieve, K. et al. Three-dimensional structure of the mammalian limbal stem cell niche. *Exp. Eye Res.* **140**, 75–84 (2015).
39. Cruzat, A., Pavan-Langston, D. & Hamrah, P. In vivo confocal microscopy of corneal nerves: analysis and clinical correlation. *Semin. Ophthalmol.* **25**, 171–177 (2010).
40. Khan, A. et al. Corneal confocal microscopy detects a reduction in corneal endothelial cells and nerve fibres in patients with acute ischemic stroke. *Sci. Rep.* **8**, 1–8 (2018).
41. Guillon, J.-P. Non-invasive tearscope plus routine for contact lens fitting. *Contact Lens Anterior Eye* **21**, S31–S40 (1998).
42. Patel, D. V., Sherwin, T. & McGhee, C. N. J. Laser scanning in vivo confocal microscopy of the normal human corneoscleral limbus. *Investig. Opthalmol. Vis. Sci.* **47**, 2823 (2006).
43. Aydin, P., Akova, Y. A. & Kadayifçilar, S. Anterior segment indocyanine green angiography in scleral inflammation. *Eye* **14**, 211–215 (2000).
44. Sebastian, B. & Dittrich, P. S. Microfluidics to mimic blood flow in health and disease. *Annu. Rev. Fluid Mech.* **50**, 483–504 (2018).
45. Patel, S. & Tutchenko, L. The refractive index of the human cornea: a review. *Contact Lens Anterior Eye* **42**, 575–580 (2019).
46. Tseng, Q. et al. Spatial organization of the extracellular matrix regulates cell-cell junction positioning. *Proc. Natl Acad. Sci.* **109**, 1506–1511 (2012).
47. Schneider, C. A., Rasband, W. S. & Eliceiri, K. W. NIH Image to ImageJ: 25 years of image analysis. *Nat. Methods* **9**, 671–675 (2012).
48. Scholler, J. et al. Probing dynamic processes in the eye at multiple spatial and temporal scales with multimodal full field OCT. *Biomed. Opt. Express* **10**, 731 (2019).
49. Grieve, K. et al. Stromal striae: a new insight into corneal physiology and mechanics. *Sci. Rep.* **7**, 1–11 (2017).

Author contributions

V.M., M.F., and A.C.B. conceptualized the general idea. V.M., P.X., and A.C.B conceived and developed the optical design. V.M., J.S., and A.C.B. conceived the software and

Competing interests

The authors declare no competing interests.

Additional information

Supplementary information is available for this paper at https://doi.org/10.1038/s41467-020-15792-x.

Correspondence and requests for materials should be addressed to V.M., P.X. or A.C.B.

Peer review information *Nature Communications* thanks Kostadinka Bizheva and the other, anonymous, reviewer(s) for their contribution to the peer review of this work. Peer reviewer reports are available.

Reprints and permission information is available at http://www.nature.com/reprints

Publisher's note Springer Nature remains neutral with regard to jurisdictional claims in published maps and institutional affiliations.

5.2 Combining fluorescence and FFOCT

The understanding of dynamic signals is investigated through parallel measurement with labeled cells and organoids using fluorescent dies. The problem that quickly arises is the scattering that prevent us to image deep inside organoid with fluorescence. Typically, biologists use confocal microscopes to reject the out of focus light and image samples in 3D up to several millimeters deep. They can also use clearing procedures to increase the scattering mean free path and image even deeper [Richardson and Lichtman, 2015]. The problem with confocal microscopy is that it is a scanning technique and it is therefore not straightforward to combine it with (D-)FFOCT. One possibility is to use HiLo microscopy [Lim et al., 2008, Mertz, 2011] to obtain optical sectioning and reconstruct 3D structures. More details on fluorescent imaging methods are presented in section 2.4 in the article supplementary material, especially in Table 1 where each technique is compared to (D-)FFOCT.

5.2.1 Adding optical sectioning to wide-field fluorescence with HiLo

The setup is the same as the one used for combined FFOCT and structured illumination microscopy (SIM) proposed in [Thouvenin et al., 2017b]. SIM was originally aiming at obtaining super resolved images rather than optical sectioning [Sheppard, 1988, Chasles et al., 2007]. A modified version of SIM called HiLo and requiring only two images was then proposed in [Lim et al., 2008] using a coherent source to generate speckle in the in focus plane. The advantage of HiLo over SIM was that it required a fewer number of images to reconstruct the fluorescence image with background rejection, hence allowing to image in vivo with a fast camera. Later, the same team proposed the same HiLo approach using a grid pattern rather than a speckle pattern in [Bozinovic et al., 2008] which was compatible with our LED illumination and which could be implemented with minimal modifications on a FFOCT setup. In order to combine HiLo with (D-)FFOCT, a grid is conjugated in the sample plane using a microscope objective and a 200 $lp.mm^{-1}$ ronchi ruling grid. The magnification is chosen adequately to obtain a period of around 40 pixels on the camera which is a good trade-off between optimal reconstruction (which requires the highest possible frequency) and signal-to-noise ratio (because higher frequencies are more attenuated in scattering media). The experimental setup is depicted on Fig. 5.2.

In order to reconstruct the HiLo image, the technique requires two different acquisitions. First, a uniform illumination is used to image the sample. To achieve this and rather than using a motor to place and remove the grid, I decided to use a piezoelectric translation[7]. By applying a sinusoidal voltage with several periods[8] per exposure time, I was able to successfully acquire uniform images. This image contains both in-focus and out-of-focus contributions. However out-of-focus contributions are blurred due to the optical transfer function, hence containing only low frequency contents. To remove the out-of-focus contributions, a high-pass filter is applied on the image in order to extract the high frequency content that was present in the in-focus plane. The second image is acquired with the structured illumination[9] by projecting the grid on the sample in-focus plane. Doing that, the contrast of the imaged modulation is attenuated by the optical transfer function two times for out-of-focus planes: when projected and when measured. The

---

[7]Current amplification was necessary in order to reach satisfactory speed and displacements.

[8]Typically the piezo frequency was 500 times faster than the exposure time.

[9]HiLo can also work with speckle pattern instead of a grid. It was originally proposed with a laser source and a rotating scattering disk to obtain uniform images.

structured illumination image is demodulated by locally measuring the contrast. The evaluation of this contrast being coarse, it is only possible to extract a low resolution image of the in-focus object which corresponds to low frequency components. Finally, both high frequency and low frequency images are combined in an optimal manner such that we can recover the object.
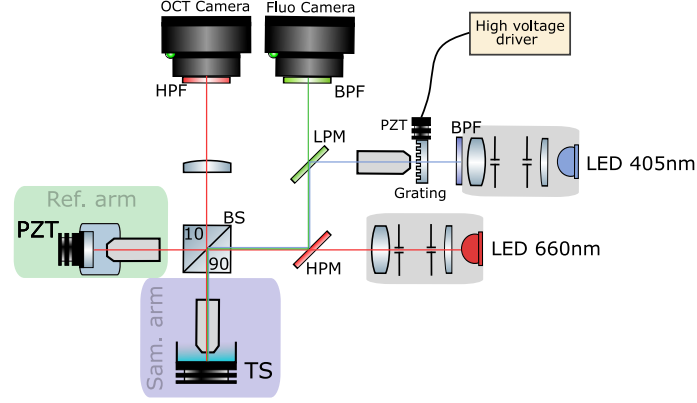
Fig. 5.2: HiLo combined with FFOCT setup. The ronchi rulling is 200 $lp.mm^{-1}$ and the microscope objective used to preject the grid is a Olympus Plan N 10x 0.25NA.

I tested the method on cell culture, see Fig. 5.3(a-c). For these samples, HiLo was able to reject the out of focus light, the only drawback was a 30% signal loss. Aberrations can affect HiLo performances. Indeed, even if the PSF is diffraction limited in the imaged plane, its 3D profile can exhibits a particular shape with high frequencies in the (x, y) plane. I observed ring pattern, see Fig. 5.3(d), that dramatically decreases the performance of HiLo because high spatial frequencies where present in the out of focus plane. Finally, HiLo suffers from two important drawbacks. For point like sources, the PSF can have a halo shape due to aberrations and give ring on the reconstructed images. The second problem is that I couldn't image deep inside tissues and organoids because I couldn't project the grid inside samples, even if it was a low spatial frequency pattern, preventing me to reconstruct images and thus obtain optical sectioning, which was the point of using HiLo in the first place. Jerome Mertz, the inventor of the technique, confirmed that it only works for weakly scattering medium at shallow depth and that this technique suffers from the same low penetration in biological medium as structured illumination. As a consequence, it is hard to obtain sharp fluorescence images simply because it is hard to compete with OCT in terms of optical sectioning[10]. These simultaneous measurements are therefore limited to shallow depth or 2D cell cultures.

---

[10]OCT can image up to 9 scattering mean free path [Badon et al., 2017], which is tremendously high compared to incoherent techniques.
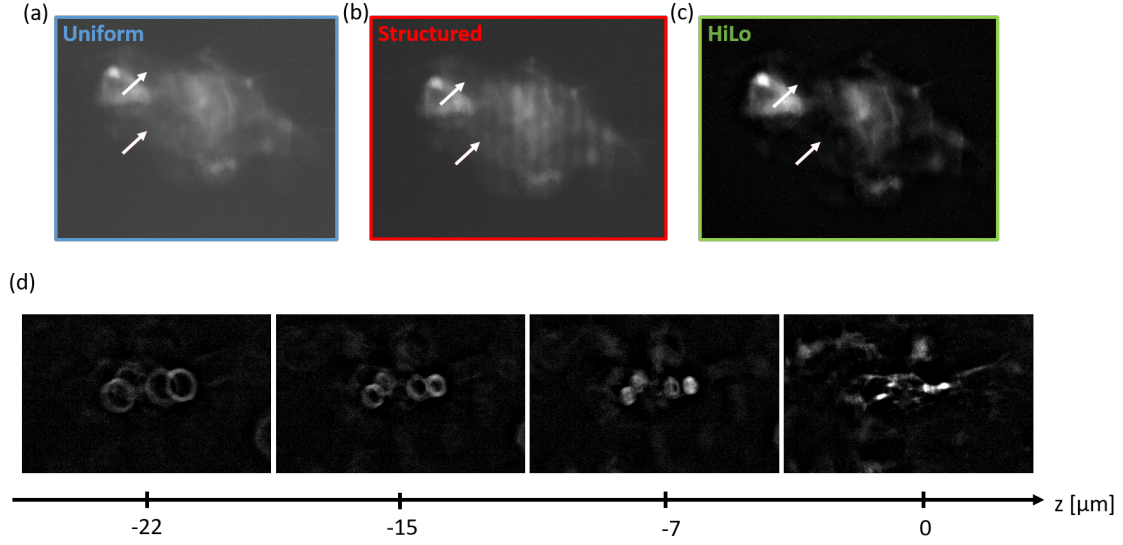
Fig. 5.3: HiLo results. (a) Uniform image. **(b)** Structured image. **(c)** HiLo reconstructed image. White arrows indicate out of focus light that is effectively filtered out by HiLo. **(d)** Aberrations can lead to dramatic decreases in performance for HiLo. Here, the defocused PSF exhibits a ring shape which led to high frequencies that are not filtered by the algorithm.

5.2.2 Sub-pixel registration of (D-)FFOCT and fluorescence images

When performing multimodal imaging with (D-)FFOCT and fluorescence, a registration step is necessary in order to overlay both modalities. Indeed, obtaining optical alignment of both camera is nearly impossible as it requires micrometer precision with cameras that can weight more than 1kg and which are connected with multiples cables to the computer and cooled (for the fluorescence camera). The first method I tried in order to register images was based on [Matungka et al., 2009] which takes advantage of the polar transform that transforms rotation and scaling into shifting so that by iterating between the initial domain and the log polar domain one can find the (x, y) shifts and the rotations and scaling for registering two images. Unfortunately most of the time the transformation between both cameras was not a rigid transformation but rather a projective transformation, see Fig. 5.4. Indeed, if both cameras are not perfectly aligned, i.e their sensor are not perfectly co-planar then a rigid transformation is theoretically not able to register both images. A projective transformation P transforms u_1 in u_2 with the equation:

$$u_1 = Pu_2$$

where:

$$P = \begin{pmatrix} p_{11} & p_{12} & p_{13} \\ p_{21} & p_{22} & p_{23} \\ p_{31} & p_{32} & p_{33} \end{pmatrix}$$

In order to find the projective transformation to perform the registration I used the following approach:

1. Compute characteristic points on each image using SURF algorithm [Oyallon and Rabin, 2015].

2. Robustly match points in each image using RANSAC algorithm for projective transformations [Fischler and Bolles, 1987].

After finding the projective transformation, both images are finally registered for translation with a sub-pixel accuracy using a simple phase cross-correlation with a bicubic interpolation in Fourier domain. The bicubic interpolation allows to locate the maximum of the phase cross-correlation with a sub-pixel accuracy. The final registration is shown Fig. 5.4 on a Siemens star target.
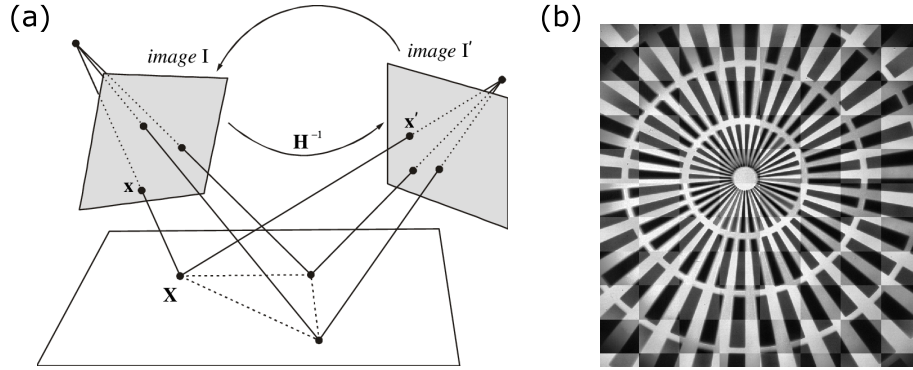
Fig. 5.4: (D-)FFOCT and Fluorescence registration. (a) Projective transform scheme. Imaging a plane on two different planes lead to projective transform between both planes. **(b)** Registration results on a Siemens star target. The checker pattern allows to see both images.

Conclusion and perspectives

In this thesis I investigated the hardware and software axes to achieve high-resolution dynamic and static FFOCT acquisitions while keeping a low complexity experimental setup with a high level of robustness. For microscopy, I applied D-FFOCT for the imaging of retinal organoids and demonstrated that this technique can bring interesting biological insights owing to its metabolic contrast. I found a new method based on singular value decomposition to remove unwanted artifacts coming from the sample axial motion during acquisitions. I also proposed a new operator to compute dynamic images based on the cumulative sum to enhance non-stationnarities, which lead to an improvement on the signal to noise ratio. This allowed us to image deeper with D-FFOCT inside samples. For retinal imaging, I implemented a real-time tracking of the retina which operates at 50 Hz and with a root mean square error of 9.1 μm which allowed us to obtain images of the retina reliably. Then, I studied the field curvature due to the optical asymmetry in the Linnik interferometer for retinal imaging and proposed a method to find the optimal compensation to correct for the field curvature which also reduces dispersion effects. This allowed us to image the retina on 1×1 mm field of view with an homogeneous SNR. I also validated experimentally the aberrations theory proposed by Victor Barolle [Barolle, 2019] using a custom built AO-FFOCT setup with an adaptive lens and a Shack-Hartmann wavefront sensor. I then transferred the AO part in our retinal imaging setup and implemented and studied several wavefront sensorless optimisation schemes to achieve real-time near diffraction limited imaging of the human retina in vivo. I could image and resolve photoreceptors as close as 0.5° from the fovea and image reliably the retinal fiber layer at different depths. I also adapted motion tracking algorithms for D-FFOCT to study the wound healing process in cornea and for FFOCT to quantitatively measure blood flow in the human limbus in vivo. These achievements are of great importance as they highlights the multimodal capability of (D-)FFOCT imaging and its ability to capture important and meaningful information. Finally, I investigated several machine learning and deep learning approaches to successfully perform retinal cell classification and breast cancer screening using D-FFOCT signals.

Considering the potential of (D-)FFOCT, its future seems bright and I hope that the clinical translation will take place for eye imaging but also for microscopy for organoids developmental studies and biopsies screening now that this technique is reliable and consistent. From a more fundamental point of view, there are still some leads that I have not had the time to investigate but which could be interesting for further developments. These ideas are briefly discussed below.

Computational aberrations correction

Recent work [Borycki et al., 2019] showed that computational aberrations correction can work for phase decorrelated swept-source FFOCT even when the spatial coherence of the

source is destroyed. This technique was successfully applied for in vivo cornea [Auksorius et al., 2020] and retina [Auksorius et al., 2019] imaging and briefly explained section 1.4.2. Benefits of performing computational aberrations correction include better signal to noise ratio, diffraction limited resolution and enhanced depth of field (especially useful for techniques that record the whole sample depth at each acquisition) while keeping the same experimental setup. In our implementation of FFOCT (spatially incoherent and time domain), aberrated photons are partly filtered out because they can't interfere with the reference. Computational aberrations correction would therefore lead to minimal improvements. My idea is to introduce a defocus in the reference arm so that aberrated photons could still interfere with the reference. By looking at the energy in the FFOCT image for various amount of defocus it should be possible to monitor the proportion of photons interfering. Then, by adding defocus in the reference we should observe more aberrations on the FFOCT image as the model for FFOCT image formation presented section 4.3.2 would not hold anymore. However these aberrations could be corrected in post-processing using previously developed approaches [Borycki et al., 2019, Hillmann et al., 2016] and could potentially remove the need for using an adaptive lens.

D-FFOCT on phase and amplitude only

As explained section 2.2 it is not possible to compute local physical properties of scatterers from raw D-FFOCT signals. This is partly due to the mixing of amplitude and phase fluctuations. Using the 10 phases triangular demodulation which exhibits a low degree of error regarding phase un-mixing and presented section 1.3.2 it should be possible to compute both phase and amplitude D-FFOCT images distinctly. This could lead to new biological insights depending on the type of fluctuations. A recent work [Münter et al., 2020] showed the possibility of doing dynamic measurements using a SD-OCT. The authors constructed dynamic image by computing the fluctuations on the amplitude of the OCT signals but they could potentially compute the same for the phase. Dynamic SD-OCT could therefore help understand the origin of dynamic signals because it naturally records amplitude and phase at the same time in the Fourier domain. In addition, by reducing the sensor size on the camera we could acquire with an higher frame rate. And by acquiring more images (typically tens of thousands) we could use the same approach as fluorescence correlation spectroscopy [Elson, 2011] in order to extract local physical properties of scatterers.

Phase retrieval approach for single shot FFOCT

Computational aberrations correction and amplitude and phase un-mixing could both benefit from phase retrieval algorithms. Adapting currently used algorithms [Yeh et al., 2015] to better separate the phase and amplitude of the light field should allow to image faster by acquiring FFOCT images in a single shot and allow for better computational aberrations correction if it can reduce reconstruction artifacts.

Dark Field D-FFOCT

Dark Field FFOCT was first proposed in [Auksorius and Boccara, 2015] and then applied for sub-surface fingerprint imaging [Auksorius and Boccara, 2020]. It relies on blocking specular reflections by adding a mask in the pupil plane of the system. In order for the reference to propagate back to the camera, the reference mirror therefore needs to be tilted or replaced by a grating. Combined with a light efficient beamsplitter, Fourier Domain Dark Field FFOCT can lead to a 4-fold improvement in SNR [Auksorius, 2020] in addition

to removing specular reflections which again allow to send more power and obtain an even better SNR. Dark Field D-FFOCT could therefore improve the penetration depth by a large amount. The difficulty being that the pupil plane of high NA objectives is usually physically inside the housing so that implementing Dark Field D-FFOCT would require to add a 4-f telescope to relay the pupil plane in each arm. This configuration will lead to bigger and more cumbersome systems but the expected gain is probably worth the risk.

Appendix A

Building a custom computer for D-FFOCT experiments

At the beginning of my PhD I was given the chance to build a computer especially designed for D-FFOCT computation with a high throughput. Several points were of great importance when choosing the parts:

- The motherboard should have as many PCIe ports as possible because each camera has a framegrabber that needs one. The digital to analog converter to drive the piezo also needs one. I was planning to have 2 graphics processing unit (GPU) to speed up the computation of D-FFOCT images, so 2 more PCIe express. Finally one or two spare ports needs to be considered in case we want to upgrade the setup.

- GPU with as many memory as possible to be able to compute D-FFOCT images on the biggest cube of data possible. I asked a grant to NVidia and I was offered a NVidia Titan V which was the best GPU at the time, so finally we did not need two GPUs.

- The hard drive must be fast enough to be able to store the data coming from the cameras for raw acquisitions without any data loss.

- The system must have enough random access memory (RAM) to store raw data for computation on the central processing unit (CPU) when using scripting programming language[1].

- The system must have a great cooling system in order to manage the heat under strong solicitations.

- The computer must be able to power itself plus several cameras (Adimec cameras are powered by the framegrabber) so the power supply must be powerful enough to power everything adequately.

Considering the previous requirements, the final build is the following:

---

[1]Scripting languages like Python allow rapid prototyping of experiments. Performances are generally lower than with C++/Cuda implementations but are a lot faster to develop.

Part	Name
Motherboard	Asus Sage x299 (7 PCIe)
Cooling system	Corsair Hydro H60 (water cooling)
CPU	Intel i7-7820X
GPU	Nvidia Titan V (12Go)
RAM	Crucial 2666 MHz 128Go
Hard drive (1)	Samsung NVMe 970 pro (fastest available SSD at the time)
Hard drive (2)	Samsung 860 pro (1To) + Mechanical disks (8To) for data storage.
Cooling system	CORSAIR HX1200I 1200W

Fig. A.1: Final computer build after mounting all the parts.

Appendix B

HSV image processing for 4D data representation on 2D image

Data representation and display is very important in research. Indeed, when showing results in conferences or publishing an article, researchers usually start by looking at figures. If you happen to have very interesting results but display them poorly, then your research impact will probably be considerably lower. Printed and screen format imposes major constrains when it comes to displaying data, especially in 3D. During my PhD I often needed to display 3D and 4D data on a 2D figure. Rather than using traditional volume display[1]. I developed a color approach using Hue Saturation and Value (HSV) colorspace that works very well for displaying physical parameters on images. This approach was used to construct D-FFOCT images chapter 2 and section 5.1.1, but also to display corneal blood flow section 5.1.2 and photoreceptor density section 4.2. This HSV approach is shown and compared with another display approach Fig. B.1 for organoid dynamic imaging. Although their resolution is lower in [Yang et al., 2020], the way the information is displayed is harder to interpret because natural images do not look like this in nature. The human brain is train to distinguish color and contrast, but perfoms poorly when superimposing shapes with different sizes and colors on an image. The result is a non appealing figure which is very hard to interpret Fig. B.1(B-D). On the contrary, the HSV approach creates *natural looking* images that are visually pleasing and easier to interpret. Comparing both approaches, our brightness corresponds to the motility metric M (or metabolic index), our colors corresponds to their α and our saturation is somehow similar to their R^2 as it measures something similar to noise.

Colored HSV images are constructed with the following steps:

1. 2 or 3 images must be created and be already displayable with satisfactory contrast[2]. These images must have the same *dtype* (e.g. unint16, float64).

2. Three matrices are created: H, S and V. The matrix V contains the image brighness (e.g. the protoreceptors acquired in FFOCT). The matrix H contains the physical property to be displayed in color (e.g. photoreceptor density). The matrix S contains the physical property to be coded as saturation on the image. It can be a mask to limit the color in certain area (e.g. the capillaries for the blood flow); or a constant matrix if only 2 physical properties are of interest.

---

[1]2D isocurves are also popular.

[2]Typically histograms are shrinked to saturate 0.1% of the lowest and highest values. Also, spatial filters can be applied for smoothing or denoising to improve the final aspect.

3. H, S and V are stacked in order to obtain a 3D tensor u_{HSV} with shape $(x, y, 3)$.

4. u_{HSV} is transformed[3] from HSV to RGB colorspace for display purposes.
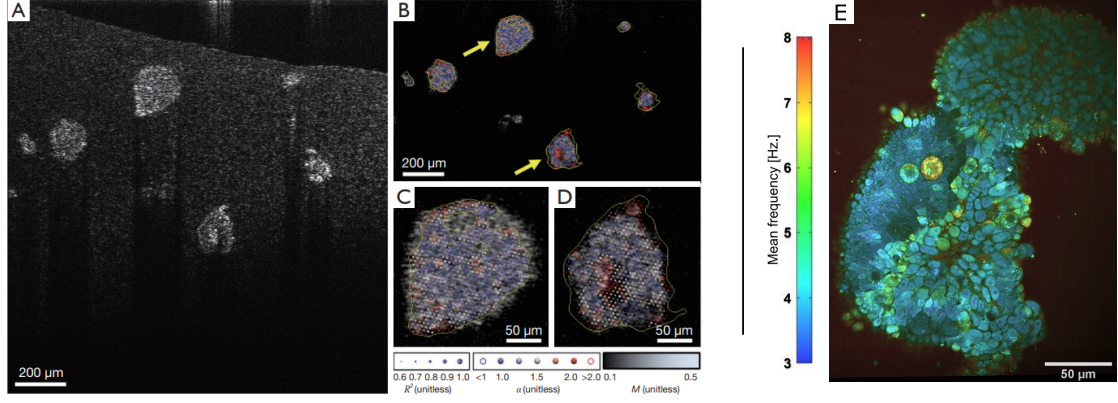
Fig. B.1: Comparison of display. (A-D) Figures representing D-FFOCT data from [Yang et al., 2020] (A) A representative cross-sectional OCT image of 6 live organoids **(B)** visualization of motility metrics on **(A)**, where two of the organoids (yellow arrows) are enlarged in **(C)** and **(D)**. The background gray-scale image indicates M at each pixel, and the yellow contour lines indicate the ROIs determined from a semi-automated segmentation. α is overlaid in each ROI as spherical glyphs with different colors and sizes. The color of the glyph indicates the value of α, while the size of the glyph represents R^2 from the power-law fitting. **E** Retinal organoid displayed using the proposed HSV methods.

---

[3]For many libraries, the functions requires the input to be scaled between 0 and 1, thus being of *float* type

Appendix C

Characterisation and calibration of the Adaptive Lens

Before mounting the lens in the AO-FFOCT setup I wanted to investigate its performances and properties. In order to characterise the lens I built the setup presented in Fig. C.1. The laser beam is expanded and collimated using a 4x microscope objective and a lens conjugated in its focal plane. The AL is conjugated through a telescope ($\gamma = \frac{1}{2.5}$) on the WFS.
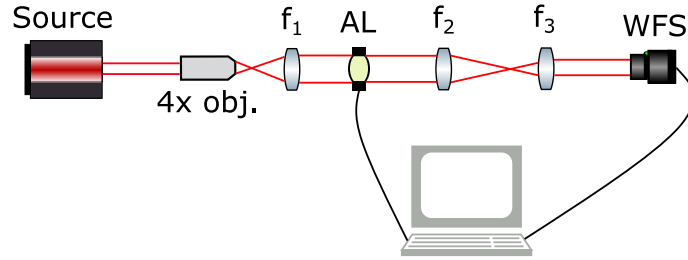
Fig. C.1: **Experimental setup for lens characterisation.** Source: 633nm laser - $f_1 = 100\ mm$ - $f_2 = 150\ mm$ - $f_1 = 60\ mm$ - WFS: Shack-Hartmann wavefront sensor.

Initial aberrations due to the AL computed on the 15 firsts Zernike modes was approximately 1.7λ RMS[1] almost exclusively defocus. Only the 15 firsts Zernike polynomials were considered because the lens can only correct for those [Bonora et al., 2015] and also because most of eye aberrations are low order modes [Guirao et al., 2002]. The first step in using the AL is to calibrate it by measuring the influence function, i.e. link the voltage applied to each actuator to the resulting wavefront modification which are measured using a Shack-Hartmann WFS (SH-WFS).

The AL is imaged onto a SH-WFS: an array of micro-lenses focused on a camera, see Fig. C.2. When there are no aberrations, the wavefront is plane. This results in a regular array of spots being formed on the camera placed at the focal length of the lenslet array. When the wavefront is aberrated however, the spots will shift their location according to the local tilt of the wavefront across each lenslet. The slopes $S_i(u, v)$ of the wavefront in

---

[1]Initial aberrations greatly vary with the lens. At the end of my PhD I used a second one which had less initial aberrations ($\sim 0.6\lambda$ RMS).

both transverse direction is computed for each lenslet as:

$$S_i(u, v) = \frac{r_0 - r_a}{f} \tag{C.1}$$

where r_0 is the position of the centroid of the focal spot i without aberrations, r_a is the position of the centroid of the focal spot i with aberration and f is the focal length of the lenslet. The spot location r_a is determined by a center of mass algorithm where the center position is determined as the barycenter of the spot intensity, resulting in a subpixel localisation accuracy.
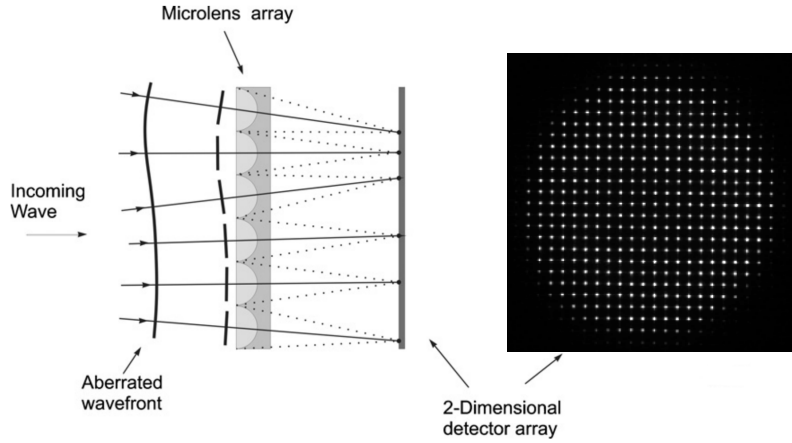
Fig. C.2: Shack-Hartmann WFS principle. A 2D array of lenselets with the same focal length is focusing the incoming beam onto a camera. Any phase aberration can be approximated by a set of local discrete tilts that are measured by the focal shift. By sampling the wavefront on the whole lenselet array it can be reconstructed with good accuracy.

The AL is composed of two 150 μm glass windows, upon which is mounted a piezoelectric actuator ring, see Fig. C.3. The space in between the windows is filled with a transparent mineral oil. The first window is mainly used to generate even wavefront distortion (e.g. defocus and astigmatism) while the second one mainly generates odd wavefront distortions (e.g. coma and trefoil). Piezoelectric actuators have an external diameter of 25 mm and an internal diameter of 10 mm with a thickness of 200 μm resulting in a annular shape. Each ring is divided into 9 independent actuators leading to 18 degrees of freedom. Application of a voltage on one of the actuator generates a bending of the glass window leading to a varying oil thickness, therefore introducing phase modifications. Actuators are controlled by a high voltage ($\pm 125\ V$) driver.
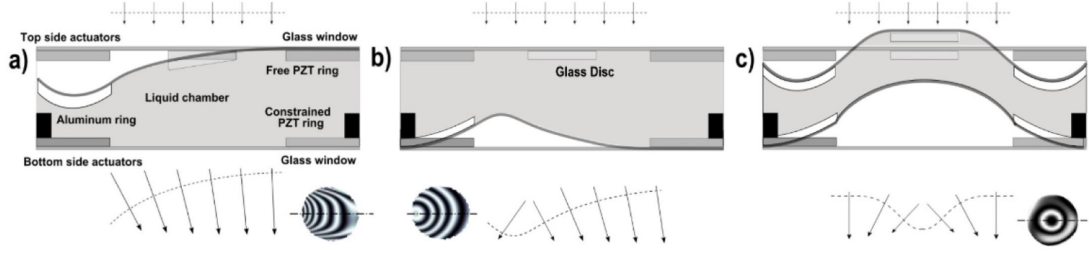
Fig. C.3: Adaptive lens principle. (a-c) Show the measured wavefront deformations (arrows) and the interferograms relative to the actuation of the AL in three different configurations: **(a)** one actuator on the top window, **(b)** one actuator on the bottom window, **(c)** all actuators fed with the same voltage. Figure adapted from [Bonora et al., 2015].

The idea is then to calibrate the AL in order to compute the influence function for each actuator and find an optimisation basis suitable for aberrations correction. If we suppose that the adaptive lens operates in a linear fashion, i.e. the voltages applied on different actuators lead to several wavefront modifications that can be added independently, then measuring the influence function entirely characterise our system. In order to measure the influence matrix we apply a positive and negative voltage for each actuator[2] and measure the associated Zernike aberration coefficients per unit control voltage. For each actuator we obtain a column in the influence matrix which corresponds to the wavefront distortion decomposed on the Zernike polynomials basis $(c)_{i \in [0,14]}$[3]:

$$a(n_{actuator}, n_{Zernike}) = \frac{c_{n_{Zernike}}^{+V} - c_{n_{Zernike}}^{-V}}{2V} \tag{C.2}$$

where $n_{Zernike}$ is the $n-th$ Zernike polynomials, $n_{actuator}$ is the $n-th$ actuator and V is the control voltage. Then the influence matrix is computed as:

$$\mathcal{I} = \begin{pmatrix} a_1^1 & a_1^2 & . & . & a_1^{N_{actuator}} \\ a_2^1 & & . & & . \\ . & & . & & . \\ . & & & . & . \\ a_{N_{Zernike}}^1 & . & . & . & a_{N_{Zernike}}^{N_{actuator}} \end{pmatrix} \tag{C.3}$$

where $N_{actuator} = 18$ and $N_{Zernike} = 15$. Then, given a wavefront error W measured with the SH-WFS (decomposed on the Zernike basis), the control voltage V that needs to be applied to correct the wavefront distortions are:

$$V = \mathcal{I}^{-1}W \tag{C.4}$$

In order to evaluate $\mathcal{I}^{-1}$ I compute the SVD of $\mathcal{I}$:

$$\mathcal{I} = U\Sigma V^T \tag{C.5}$$

where the rows of V^T represents each AL singular modes in the actuator space which can be used to perform the wavefront correction, see Fig. C.4, while the columns of U

---

[2]In practice I acquire the influence matrix by using a set of Hadamar control voltages rather than single actuator excitation in order to improve the signal to noise ratio of the measurement.

[3]The basis is composed of the 15-th firsts Zernike polynomials.

represent the modes in the sensor space. Finally, the singular values in Σ link the modes together. The influence matrix $\mathcal{I}$ is then inverted:

$$\mathcal{I}^{-1} = V\Sigma^{-1}U^T \tag{C.6}$$
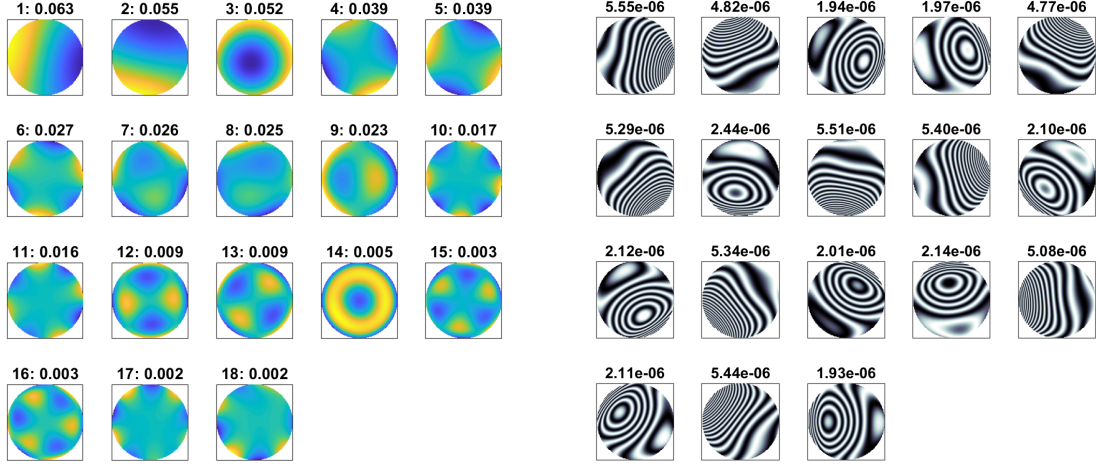
Fig. C.4: AL singular modes and influence matrix. On the left are displayed the reshaped rows of V^T with the associated singular values σ_i in title. The singular modes looks like Zernike polynomials. On the right the influence function of each actuator are displayed with the peak to valley wavefront deformation in title.

The wavefront can then be corrected in a closed loop fashion using a proportional–integral controller:

$$V_{t+1} = V_t + \mathcal{I}^{-1}\left(K_P W_t + K_I \sum_t W_t\right) \tag{C.7}$$

where V_{t+1} are the new control voltages, V_t are the previous control voltages, K_P and K_I are non-negative and denote the coefficients for the proportional and integral terms respectively which should be set to quickly converge and ensure stability. The first step when adding the lens is to calibrate the control voltage that are required to flatten it, i.e. to remove the introduced aberrations. After flattening, the residual AL aberrations are well below Marechal criterion $\sim 0.04\lambda$ RMS ($K_D = 1$ and $K_I = 0.1$).

Up to now I described how I calibrated and used the lens with a wavefront sensor and using a closed loop control. In practice, for retinal imaging, we use a wavefront sensorless approach to keep both complexity and cost down. The calibration step was nonetheless required in order to find the flattening control voltages and the modal decomposition:

1. For each experiment we start with a flat lens in order to limit the introduced aberrations.

2. Knowing the modal decomposition we can pre-compensate for known aberrations (given by the prescription glasses) in an open-loop fashion.

3. We can use a modal sensorless approach to correct for eye aberrations.

Appendix D

Cell and tissue classification

In this appendix I explore different approaches to process and treat dynamic signals to perform automatic classifications. With D-FFOCT I purposely performed dimensionality reduction and projected temporal signals on 3 dimensions (colored images) or 1 dimension (grayscale images) so that humans can visualize and interpret dynamic images. For algorithms however, higher dimensions are not a problem and the full dimension of dynamic signals can be considered to train machine learning algorithms, e.g. to distinguish between different cell types. I tested several approaches at various scale to test whether it was possible to classify cells or tissues based on the dynamic signals alone. Results suggests that biological information such as the cell type can be detected at the cell scale by computing the right features and aggregating them on each segmented cells, leading to more than 97% accuracy for retinal cell classification. Training deep neural networks when cells are not easily segmentable can also lead to accurate segmentation maps. In the preprint below, I also show that using information at the mesoscale ($1.2 \times 1.2\ mm$) it is possible to detect tumoral tissue in breast cancer biopsies. Finally, I tried to perform clustering with a non-supervised strategy at the pixel scale to see if there was meaningful information to probe on single pixel. Unfortunately it seems that without spatial knowledge and local dynamic variations it is not possible to gather much information.

Dynamic Full-Field OCT as tool for tissue and cell classification.

JULES SCHOLLER,[1,*] MARIE DARCHE,[2] EMILIE BENOIT A LA GUILLAUME,[3] CLAUDE BOCCARA,[1] KATE GRIEVE[2,4] AND OLIVIER THOUVENIN[1]

[1]*Institut Langevin, ESPCI Paris, CNRS, PSL University, 1 rue Jussieu, 75005 Paris, France*
[2]*Quinze-Vingts National Eye Hospital, 28 Rue de Charenton, Paris, 75012, France*
[3]*LLTech, 29 Rue du Faubourg Saint-Jacques, Pepiniere Paris Santé Cochin, 75014 Paris*
[4]*Institut de la Vision, Sorbonne Université, INSERM, CNRS, F-75012, Paris, France*
[*]*jules.scholler@espci.fr*
https://www.jscholler.com

Abstract: Classification of cells and tissues using dynamic full field OCT signals are demonstrated for various scales. At the tissue scale we were able to classify breast cancer tissue from healthy ones with an accuracy of 100% when aggregating results. At the cell scale we were able to classify retinal cells in 4 categories with more than 97% and proposed a method to perform cell classification even when cells can't be segmented. Finally we show that at the pixel scale, there is a lack of information to perform classification suggesting that spatial information is needed to gain insight on the underlying biology.

1. Introduction

Optical coherence tomography (OCT) is an interferometric imaging technique used for 3D imaging of microstructures in tissues and 3D cell cultures [1]. Especially used for imaging of the retina, OCT has revolutionized the clinical practice of ophthalmology [2]. OCT contrast arises from the endogenous backscattering contrast [3,4] and is therefore completely label-free. Time domain Full-field optical coherence tomography (FFOCT) is an *en face*, high transverse resolution version of OCT [5,6]. Using a megapixel camera and a spatially incoherent LED source, FFOCT acquires *en face* cross-sections of the sample at a given depth and has been used for biology studies and rapid histology applications [7,8]. Using the same experimental setup, a novel contrast has been exploited owing to FFOCT high throughput by measuring temporal fluctuations of the interferograms in a technique called Dynamic Full-Field OCT (D-FFOCT) [9]. Such dynamic contrasts have also been recently succesfully reported with scanning Fourier domain OCT [10]. In ex vivo fresh tissues, these dynamic measurements reveal living cells that are very weak backscatterers [11]. The high spatial resolution of FFOCT together with the high number of frames used to generate dynamic images makes D-FFOCT sensitive to intracellular motility signals and produces a contrast that reveals living cells in the retina [12,13]. Recently, phase fluctuations measurement in the human retina in vivo was applied for functional imaging with a swept source OCT [14] and allowed to see the shift in the information transduction in the retina. Imaging 3D live tissue samples is important in disease modeling applications, and non invasive methods such as D-FFOCT hold promise for removing the need for complex and invasive fluorescent labeling. However in order for non invasive methods to offer an effective alternative to fluorescent labeling, identification of specific cell types is an essential step. This study aims to use machine learning to achieve this goal through different approaches. First, we consider the dynamic signal directly at the mesoscale (intermediate scale between cell-scale and tissue-scale) and successfully performed classification using transfer learning on VGG16 convolutional neural network [15] for retinal cells classification and breast cancer detection on

biopsies. Secondly, we developed a cell-scale framework which consider the full dynamic signal to improve the classification performance when cells can be segmented. We used it to classify retinal cells in an explanted 100 μm thick live retinal tissue from primate: given the experimental data, cells are automatically segmented and classified given their depth and a data-set containing 4 different cell types is built. Classifiers are then trained using only the dynamic dimension of the signal, disregarding any information on the shape, structure, etc. leading in classifying retinal cells with 95% accuracy. We followed a similar approach to achieve 100% accuracy on breast cancer detection by computing cell and fibers features on dynamic images. Finally, we present a pixel-scale blind classification using clustering methods where we demonstrate that neglecting dynamic spatial distribution by considering only single pixel lead to poor classification performances and suggesting that single pixel dynamic does not carry much information when considered alone.

2. Acquisition protocol and signal processing

In this study we used two different FFOCT setups. The first one used for retinal samples imaging is a laboratory setup which consists of a Linnik interferometer where both arms contain identical microscope objectives (Olympus UPlanSApo 30×), see Fig. 1(a). Both sample and reference arms are mounted on translation stages (X-NA08A25, Zaber Technologies) for optical path length matching and axial scanning, respectively. In addition, the reference mirror is mounted on a piezoelectric translation stage (STr-25, Piezomechanik) for phase-shifting. Indeed, in order to construct an FFOCT image, at least two frames are acquired with different phase modulations and appropriate phase-shifting algorithms are used to build the final image [13, 16]. For D-FFOCT experiments the mirror position is not modulated, fluctuations arise by scatterers motions inside the coherence volume. This setup is purposely built in an inverted configuration where the sample is directly placed on top of a coverslip and imaged from beneath with high-numerical-aperture oil-immersed objectives. In this configuration the sample is held motionless by gravity and is naturally flattened against the coverslip. The second setup, used for breast biopsy imaging, is a LightCT commercial setup manufactured by LLTech SAS. The characteristics of both of these setups are summarized in Table 1.
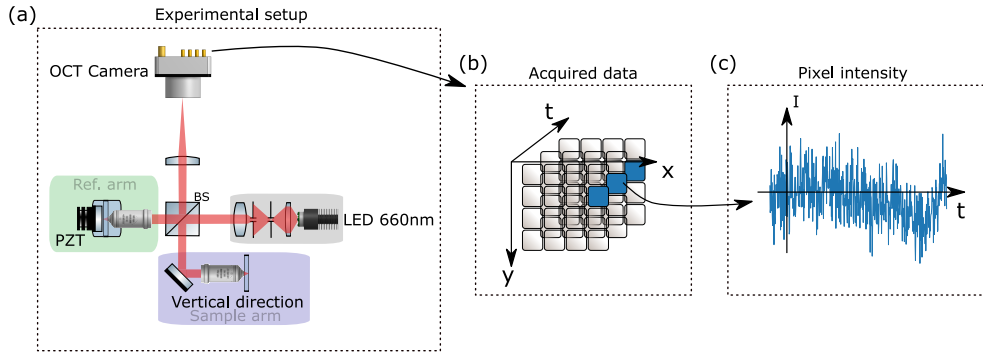
Fig. 1. PZT: piezoelectric translation - BS: Beam splitter. Experimental D-FFOCT setup in an inverted configuration optimized for tissue imaging. 512 images are acquired by the CMOS camera (a). The resulting $(1440, 1440, 512)$ 3D tensor (b) is then processed independently for each pixel (c).

In order to construct a D-FFOCT image, a stack of 512 direct images (1440×1440 pixels) is acquired (Fig. 1(b)) using a custom software [17] where each pixel are processed independently

(Fig. 1(c)). In the first report on D-FFOCT, grayscale dynamic images were computed using a running standard deviation averaged over the whole acquisition [9]. Computing the intensity standard deviation in time removes the signals from highly scattering stationary structures such as collagen and myelin fibers and enhance signals arising from cells. Recently, the cumulative sum was proposed to improve the signal to noise ratio together with Singular Value Decomposition (SVD) filtering to remove vibration artifacts [18]. Prior to classifications, each stack was denoised using SVD filtering. Segmentations and classification were performed using the dynamic images computed with the cumulative sum:

$$I'_{dyn}(\boldsymbol{r}) = \frac{1}{N} \sum_i max \left(|CumSum \left(I(\boldsymbol{r}, t_{[i,i+\tau]}) - \bar{I}(\boldsymbol{r}, t_{[i,i+\tau]}) \right) | \right) \tag{1}$$

where $CumSum$ is the cumulative sum operator, N is the total number of sub-windows, τ is the sub-windows length so that $t_{[i,i+\tau]}$ is the time corresponding to one sub-window and $\bar{I}(\boldsymbol{r}, t_{[i,i+\tau]})$ is the signal mean on the sub-window. Images were computed with $\tau = 16$.

Table 1. **Setups characteristics.**

Setup	Lab. setup Fig. 1(a)	LightCT (LLTech SAS)
Transverse resolution [μm]	0.4	1.5
Axial resolution [μm]	1	1
Field of view [$\mu m \times \mu m$]	390×390	1260×1260
Framerate [Hz]	150	150

3. Mesoscale classification with D-FFOCT images

This first mesoscale approach used for cell classification can be applied on all types of samples and do not require segmentation. Indeed, depending on the tissue properties it is not always possible to segment single cells. Moreover, cell segmentation is a hard task in itself, which is not in the scope of this paper. A straightforward approach is therefore presented in this section which avoid the need for segmentation and lead to fast classification by directly considering D-FFOCT images as a whole.

3.1. Thumbnail image classification on mouse retina

5 different mouse retinas were imaged with D-FFOCT and a training set was created on a single mouse retina Fig. 2(a) by manually annotating 395 random thumbnail images in 5 classes:

1. Ganglion Cell Layer (GCL)

2. Inner Plexiform Layer (IPL)

3. Inner Nuclear Layer (INL)

4. Outter Nuclear Layer (ONL)

5. Photoreceptors: inner segments and outter segments (PR)

The test set was created by manually annotating 292 random thumbnail images on a second retina in order to avoid over-fitting a single retina and validate that the model could generalize to another sample.
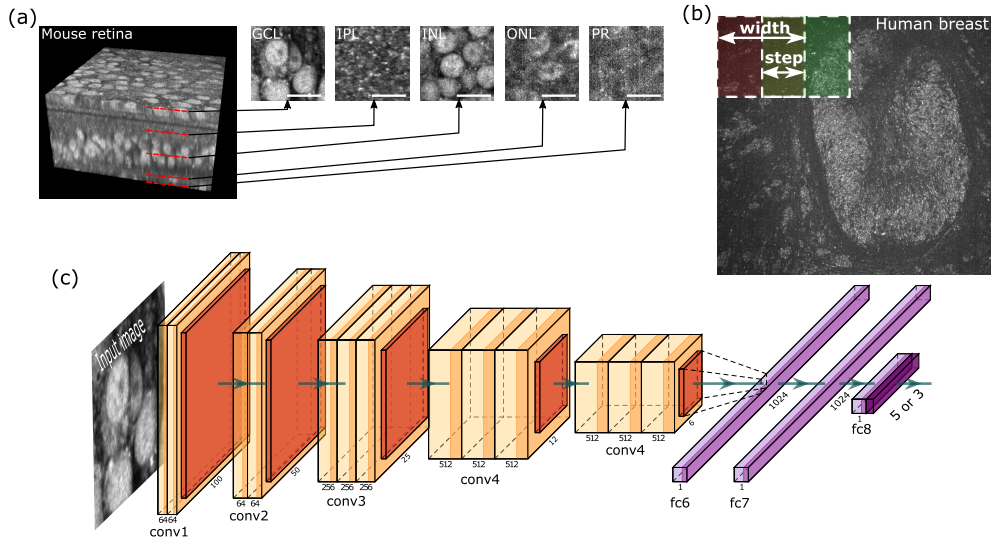
Fig. 2. (a) 3D stack of mouse retina on 80 μm depth. 697 thumbnail images of 100×100 pixels (corresponding to 27×27 μm) were randomly selected and manually classified on a single retina in 5 different classes: GCL, IPL, INL, ONL and PR. (b) For breast cancer classification each FOV is split in thumbnail images of size 224×224 pixels (corresponding to 196×196 μm) with an overlap of 112 pixels (50%). For each field we obtain 121 thumbnail images with a label corresponding to the original FOV label. (c) Neural network architecture based on VGG16 used for classifying thumbnail images in 5 different classes (mouse retina) or 3 different classes (breast cancer). Only the lasts fully connected layers (depicted in purple) were trained. Scale bar: 25 μm.

3.1.1. Transfer learning using convolutional neural network

In order to perform both feature extraction and classification the VGG16 network was used and adapted to this problem. The input size was changed so that it accepts $100 \times 100 \times 3$ thumbnail images (we duplicated the D-FFOCT in each channel, giving a grayscale image). The convolutional part, depicted in orange Fig. 2(c) was not retrained so that weights corresponds to the VGG16 network trained on ImageNet data-set [15]. To perform the classification, 2 fully-connected layers of size 1024 were added with a Rectified Linear Unit (ReLU) activation followed by a fully connected layer of size 5 with a SoftMax activation. These last layers were trained using dropout with a rate of 0.5. The final model consists of 20.5 millions parameters of which 5.8 millions are trainable. Data augmentation was used to generate more training data by using translation, rotations, mirror flips and small amount of shear (maximal shear angle was 10°), hence improving the generalization. The network was trained with 30 epochs with a batch size of 32 images and a total of 5000 images per epoch using a categorical cross-entropy loss and a RMSProp optimizer [19] which adapts the learning rate using a running average of the past gradients magnitudes.

3.1.2. Results

(a) GCL IPL INL ONL PR

(b) Confusion matrix

(c)
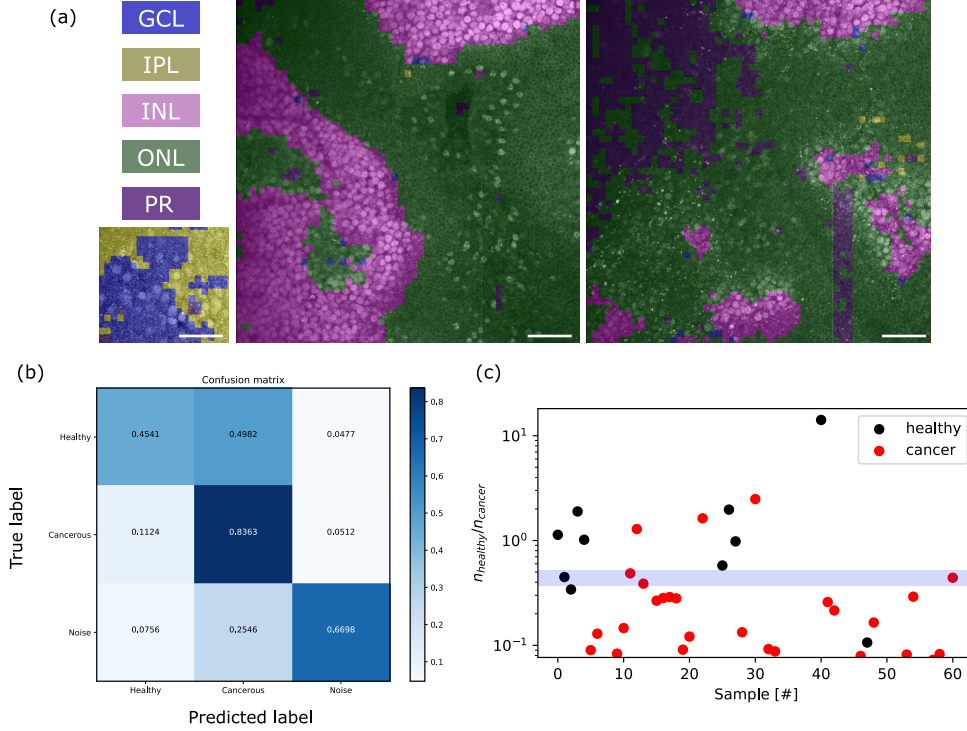
Fig. 3. (a) **Classification results for mouse retina.** Segmentation results for 3 held out retinas (that were not used during training and testing). The prediction accuracy is 92%, the neural networks mostly failing in boundary and low signal areas. (b,c) **Classification results for breast cancer.** (b) Confusion matrix for the held out set. (c) Ratio of thumbnail images classified as healthy and cancer $n_{healthy}/n_{cancer}$. The low opacity blue area highlights the ideal threshold to separate healthy samples from cancerous samples. Scale bar: 50 μm.

In order to test the trained network the 3 lasts retinas were used, especially on folded areas were several layers appear on each image. To do so, the input image was cropped in 100×100 pixels thumbnail images with an overlap of 75 pixels in order to obtain a 25×25 pixel resolution for the final classification map. Each thumbnail image was then classified using the trained neural network resulting in a coarse classification of the inputs image Fig. 3(a). The generalization was good as the accuracy reached 92% on the 3 held out retinas (that were not used during training and testing), the neural networks failed to make a good prediction mostly in boundaries between layers and in low signals area. These results suggests that using spatial information on dynamic signals also allows to predict the cell type.

3.2. Breast cancer detection using D-FFOCT images

Following the same scheme, the classification between cancerous and healthy samples from breast biopsies was performed on D-FFOCT images taken on a LightCT FFOCT commercial device from LLTech SAS.

3.2.1. Data set

The data set is composed of 650 field of view (FOV) taken on n samples from m patients. 517 FOV were from cancerous samples and 133 FOV were from healthy samples. Note that it may happen that cancerous FOV were in fact from healthy area, meaning that the data-set is possibly noisy in that regard.

3.2.2. Training framework

For each FOV thumbnail images of size 224×224 with an overlap of 50% were computed, see Fig. 2(b). The label assigned for each thumbnail image is the same as the label of the full FOV except for thumbnail images with low signals which are labeled as a third category corresponding to noisy thumbnail. This is to help the network focusing on interesting thumbnails rather than trying to classify noise when it is clearly not possible because no actual dynamic signals are in the thumbnail. The classifier part of the neural network was trained in the same fashion as in Section 3.1 with three category: healthy, cancerous and noise. During the training, adaptive sampling was used so that the neural network saw the same number of examples for each category.

3.2.3. Results

10% of the thumbnail images were held out for final accuracy testing (these thumbnail images were selected among the same FOV, so that one FOV is not split across training, validation and testing sets). The network performed reasonably well with an overall accuracy of 76,41%, see Table 2. The classifier tends to over predict cancer even-though adaptive sampling was used. Plotting the ratio between thumbnails classified as healthy and thumbnails classified as cancerous allows to separate most of the FOV, except for 3 false negatives and 1 false positive (which after investigation has in fact fibrosis which present similar features as breast cancer).

Table 2. **Accuracy results on breast cancer classification.**

	Accuracy on held out set
Healthy	45.41%
Cancerous	83.63%
Noise	66.98%
Total	76.41%

3.2.4. Class activation map for locating important features

Deep neural models based on Convolutional Neural Networks (CNNs) have lead to important breakthroughs in many computer vision tasks especially for image classification. While these models enable superior performance, their lack of decomposability into intuitive components makes them hard to interpret. Investigating signals and images for clinical purpose is particularly useful if there is knowledge to be extracted and this is why interpretability matters, i.e. we need models that have the ability to explain why they predict what they predict. In CNN, convolutional layers naturally retain spatial information whereas fully-connected layers usually present at the end of the NN performing the classification task does not. In order to locate the image area that triggered the CNN to decide in which category the image belongs the Grad-CAM [20] technique was used. Grad-CAM uses the gradient information flowing into the last convolutional layer of the CNN to assign importance values to each neuron for a particular class. In our case, this results in a coarse heatmap of the same size as the convolutional feature maps (14×14). Then, $max(0, heatmap(x, y))$ is taken to remove negative values because only features that have

positive influence on the class are interesting, i.e. pixels whose intensity should be increased in order to increase the class probability. This coarse heatmap is then interpolated and added as hue component to generate a thumbnail image with colored information corresponding to activation strength, see Fig. 4(a). Then, full FOV can be reconstructed by stitching (the maximum activation is taken on each overlapping area) the thumbnail images, see Fig.4(b). The trained CNN mainly focus on packed cell areas to make the prediction for healthy and cancerous classes, whereas focuses on low signal area for the last class. Interestingly, the same locations are triggering the CNN for both healthy and cancerous class suggesting that features of interest for detecting either if the sample is healthy or cancerous are the same, or at least located at the same spot.
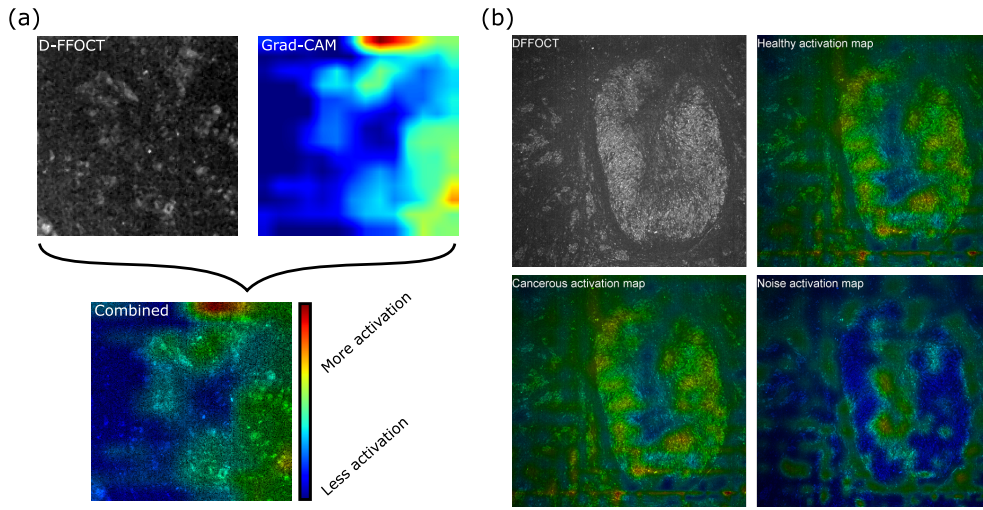
Fig. 4. (a) Grad-CAM computation. For an input D-FFOCT thumbnail image a heatmap is generated using Grad-CAM [20], the final image is generated by setting the activation level in the Hue channel and the D-FFOCT channel in the V channel and keeping the saturation constant. (b) Grad-CAM applied on a full FOV for a healthy breast sample.

4. Cell scale classification

4.1. Individual retinal cell classification

Current imaging modalities for cell cultures and tissues mainly fall in immunohistochemistry methods. Immunohistology rely on staining which adds specific color contrast and where the sample is mechanically sliced to provide sectioning, whereas immunofluorescence rely on targeted dyes where various techniques such as confocal illumination/detection and light-sheet illumination can provide optical sectioning. These techniques all require slicing, fixation or clearing steps which preclude the study of the same sample during its development. Furthermore, as these techniques depend on exogenous contrasts for imaging it greatly limits what can be seen in samples. Immunohistochemistry methods however can provide interpretable images with a diffraction limited resolution. Indeed, numerous research have been carried out using these methods and nowadays thousands of targeted dyes are commercially available. On the other hand, D-FFOCT is the only imaging technique that combines high spatial and temporal resolution, which already make it valuable, but it is also non-destructive which opens up the possibility to follow the development of the same cell in a bulk tissue throughout its cycles or for drug screening. The retina is a complex tissue made of several layers each of which containing different type of cells involved in the photo-transduction processes that ultimately lead to vision.

Because this tissue is highly structured it is possible to annotate cells based on the layer they are in, rather than on their real type. We acquired a stack on a macaque retina up to 100 μm depth with 1 μm steps where cells are clearly seperated and identifiable on 4 differents layer Fig. 5(a-c) (Ganglion cells on the Ganglion Cell Layer (GCL), bipolar cells on the Inner Nuclear Layer (INL), photoreceptor nuclei on the Outer Nuclear Layer (ONL) and Photoreceptors (PR)).
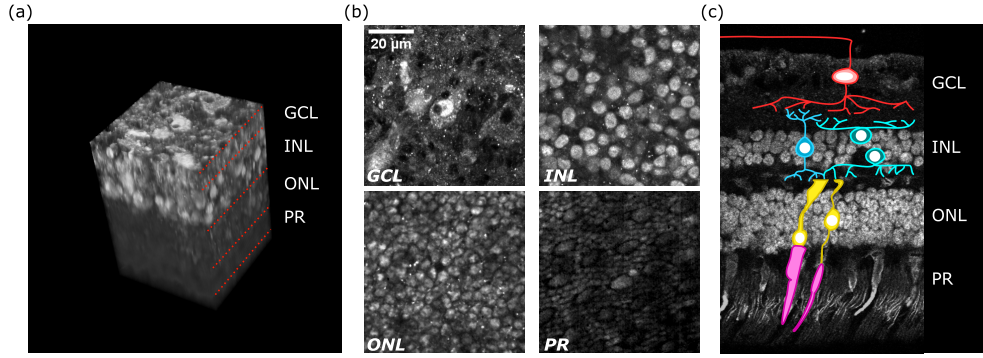
Fig. 5. (a) 3D dynamic stack of a macaque retina. (b) en face cross-sections are shown for the 4 layers where cells were classified: GCL, INL, ONL and PR. (c) Immunohistochemistry of a Macaque (Macaca fascicularis) retina, stained for nuclei (DAPI) and cones photoreceptors (Cone arrestin), courtesy of Dr. Anna Verschueren, highlighting the different layer and cell connections.

4.1.1. Cell segmentation

In order to build a data-set the first step is to segment as many cells as possible from the 4 aforementioned layers. To do so we developed two strategies; the first one based on active contours where the seeds are given by a coarse hierarchical K-means [21] segmentation and the second one based on pixel classification using different filtered version of the input image fed to a random forest classifier. The first methods performed better for sparse layers (GCL) whereas the latter performed better for packed cells, see Fig. 6(a-f). For the GCL segmentation with hierarchical K-means a 10-class thresholding based on a K-Means classification of the input image histogram was performed and then the contour of objects containing between 500 and 3000 pixels was used as input for an active contour algorithm [22] in order to refine the detection. For the other dense layers a pixel based approach where the task is to assign a class (cell, membrane and background) for each pixel was adopted. We manually segmented 10 cells for each layer. For each pixel a set of features listed in Table 3 was computed. A random forest classification algorithm was then trained with the manual segmentation and applied on the whole image. The probability map for the cell class was then thresholded at 0.6 followed by a morphological opening. A data-set of the detected cell was then constructed by considering all the different connected sets. Finally, outliers are filtered out based on high level features (size and shape).

4.1.2. Features computation

At this step pixels coordinates are known for each cell. The corresponding raw signals are then gathered for each detected cell and a set of features is computed in order to get the same number of descriptor for each cell, see Fig. 6(g). In this approach we purposely chose to disregard any information regarding the shape and size of each cell and consider only the measured dynamic and its statistics to make predictions. In order to get some insight on the importance of features, classifiers were trained using features based either on the amplitude of fluctuations, the temporal statistics of the fluctuations or both:
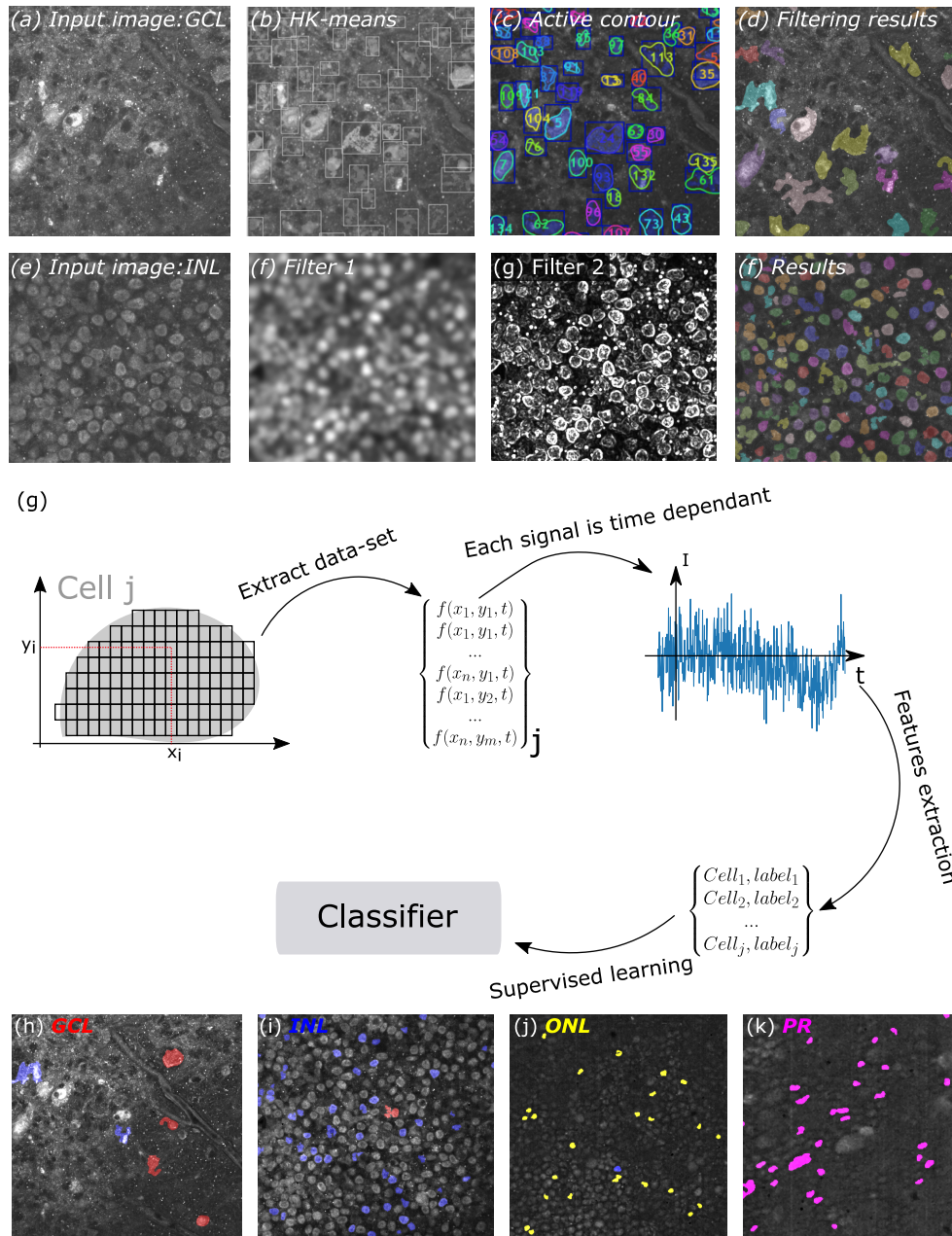
Fig. 6. Cell segmentation with two different strategies. For sparse cell distribution (a) in the GCL. Coarse segmentations are obtained with hierarchical K-means [21] (b) which serve as seeds input for an active contour (c) algorithm which further refines cells detection. Finally outliers are automatically filtered based on their size and shape (d). For dense distribution (e) different filtered version of the image (f,g) are computed and a random forest classifier is trained on a few examples (manual segmentation of 10 cells). (g) Learning framework. Raw temporal signal extracted from direct images are gathered for each cells, then features are computed on these signals. Classification results (zoomed on errors) on held out validation set (which represent 15% of the total segmented cells) for (h) GCL, (i) INL, (j) ONL and (k) PR. Cells classified as belonging to the GCL are depicted in red, belonging to the INL in blue, belonging to the ONL in yellow an belonging to the PR in pink. These colors match the retina cross-section Fig. 5.

Table 3. **Features used for feature based cells segmentation.**

Pixel feature	Dimension	Description
Intensity	1	Pixel value
Gaussian blur	5	Gaussian blur with $\sigma = [1, 2, 5, 10, 20]$ *pixel*
Anisotropic diffusion	10	Anisotropic diffusion filtering
Sobel filter	5	Sobel filtering perfomed for each blurred image
Hessian	48	Module, trace, orientation, eigenvalue, determinant of pixel Hessian matrix performed for each blurred image
Entropy	12	Histogram entropy of pixel vicinity
Difference of Gaussian	10	Differences of Gaussian blured images

- *Amplitude of fluctuations:* for each cell, the dynamic level was computed with Eq. 1 for each pixel included in the cell. Then, the mean, standard deviation and normalized histogram on 5 bins of dynamic level was computed for each cell.

- *Statistics of fluctuations:* for each cell, the decorrelation time was computed as the width at half maximum of the signal autocorrelation for each pixel included in the cell volume. Then, the mean, standard deviation and normalized histogram on 5 bins of decorrelation time was computed for each cell.

4.1.3. Training and performances

The data-set is split into a training/validation set (85%) and a testing held out set (15%). Classifiers including support vector machine [23], Gaussian processes, nearest neighbors and gradient tree boosting [24] were trained using 5-folds cross-validation on the training/validation set. The latter performing the better with an accuracy of 97.7% when all features are considered (chances are 25% for a 4 classes classification), see Table 4. Hyper-parameters have been optimized using a grid search strategy. Classification is obviously helped when the dynamic amplitude is considered, probably because the signal to noise ratio is lower at higher depth, nonetheless the accuracy remains very good when the decorrelation times (which do not depend on the signal to noise ratio) only are considered. Classification results on the held out validation set are shown Fig. 6(h-k). Classification error are mainly between the GCL and INL, by looking closely at the INL cell classified as belonging to the GCL (red overlay Fig. 6(i)) it seems that it was in fact a displaced ganglion cell. This experiment show that D-FFOCT raw signals contain metabolic information that can be useful at cellular level to gain information e.g. on the cell type here.

Table 4. Accuracy results for mouse retinal cell classification.

Training strategy	Accuracy on held out set
Amplitude of fluctuations	0.956
Statistics of fluctuation	0.886
Combined	0.977

4.2. Multi-scale cancer classification

Using D-FFOCT images, and comparison with histological diagnosis, two breast pathologists were able to distinguish normal/benign tissue from tumorous with a sensitivity of 92% and specificity of 94%. Although the results of the manual diagnosis are promising, they required training and time from expert histopathologists. There is an important need for efficient automatic diagnosis to reduce processing time and allow surgeons to operate with minimal protocol changes. A second approach was to define features of interest that will be measured automatically in our data set via image analysis. These features should help segmenting the acquired individual images as being part of a tumoral sample or not. We first selected a subpart of the original data set in order to obtain more homogeneous data. We selected only the images that have a corresponding static FFOCT and dynamic FFOCT image from the same field of view (Figure 7A1 and B1), and we imposed to have at least 5 field of views for each sample. It results in selecting 496 field of views (496 static FFOCT and 496 D-FFOCT images) from 39 samples (31 cancerous and 8 healthy). To analyze these images, we defined 44 features that were previously characterized as potential cancer biomarkers (REFS). These features can be sorted into 4 categories, including cell-based features, extracellular matrix features, mesoscale features and fat content (see supplementary for detailed description and specific references).

In order to measure these features for each image, two random forest classifiers were trained to segment individual cells and fibers using *ILastik* free software [25]. A first classifier was trained on all channels of 8 D-FFOCT images and was applied to all other images to segment cells in D-FFOCT images (Figure 7B2). A second classifier was trained on 8 FFOCT images and applied to all other FFOCT images to segment fibers, cell regions, and fat regions (respectively red, green, and blue -Figure 7A2). These classifiers were evaluated by manual inspection and are rather imprecise, but, because many cells and fibers can be found in each image, we believe the errors can be averaged out. Besides, the segmented images were then analyzed using a second filtering step to exclude some misclassified pixels. We also calculated mesoscale features, by segmenting regions of high-fiber, or high-cell, densities (Figure 7A3, B3).

The histological diagnosis of the sample was attributed to all the field of views acquired in this sample. This *ground truth* is rather imprecise because healthy regions can be found in cancerous samples. Nonetheless, We trained a linear SVM to classify each field of view (Figure 7C). We used a 5-fold cross validation and penalized by a factor 3 the possibility of having false positives (healthy samples found as cancerous) to balance the datas et inhomogeneity. Also, if healthy regions can be found in cancerous samples, the opposite should not be found, so that our *ground truth* is inhomogenous as well. An accuracy of 89% (89% sensitivity, 88% specificity) was found. This classification was used to calculate the ratio of field of views classified as normal versus all field of views for each sample (Figure 7D). Segmenting samples with such ratio above 0.5 results in a 100% accuracy segmentation between healthy and cancerous samples. Because the histological validation is made on the entire sample, it makes sense that the best level of prediction of our algorithm is the tissue scale. Note that, because the number of samples, especially healthy samples, is limited, we directly used the results from the test set applied to the SVM, although the k-fold cross validation ensures that none of the data was seen by the classifier before being predicted. To confirm these results, we performed a double k-fold cross validation, one at the image level, and a second one at the sample level. For each run, we kept the images from one healthy sample and four cancerous samples unused to serve as the validation set. The images from the other samples are used to train and test the SVM, which was applied to the kept images. Within height runs, all samples were evaluated separately, and we also obtained a 100% accuracy, although the accuracy at the image level is slightly worse. We could also mention that, using a quadratic SVM instead of a linear, we could obtain an accuracy of 97% at the image level (See supplementary) and of 100% at the sample level, but the validation procedure of double cross

validation did not give perfect predictions, suggesting that the quadratic SVM was more prone to overfitting. A larger and more balanced data set might give higher prediction scores at the image level.
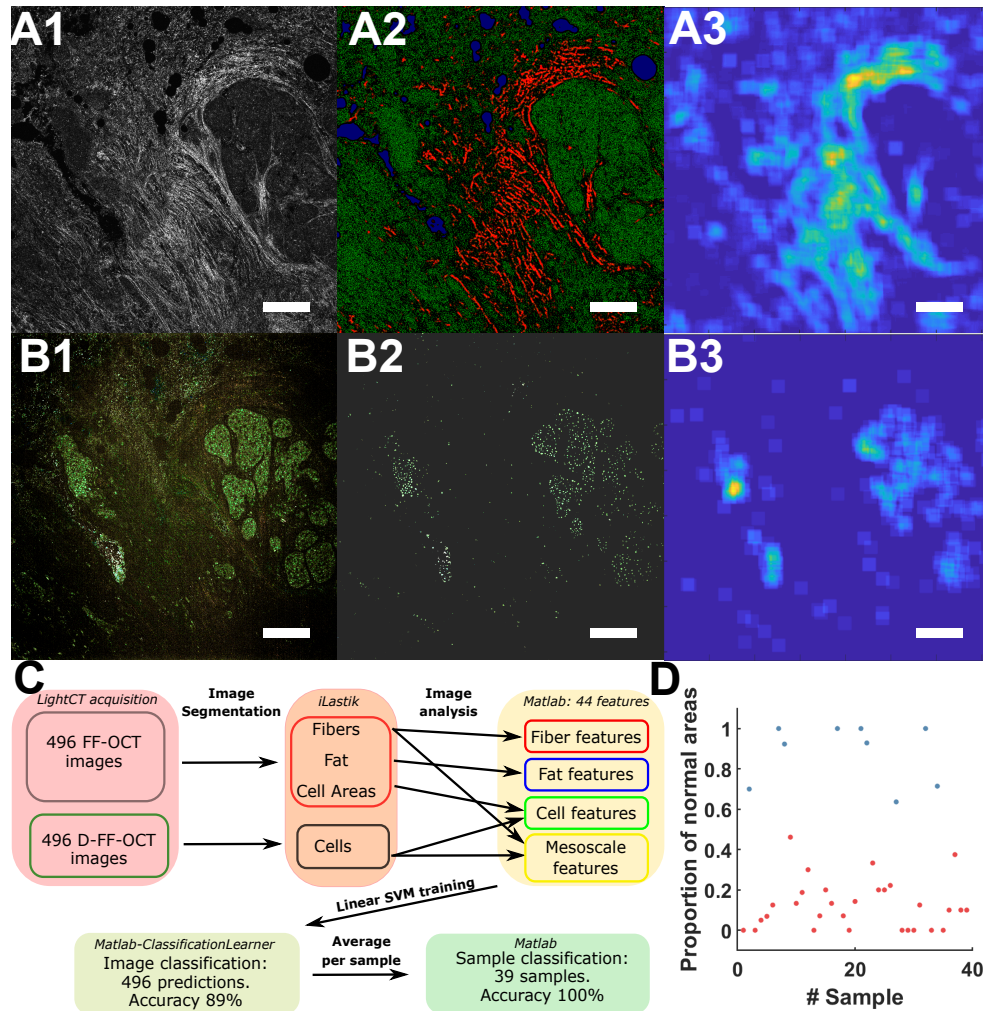
Fig. 7. **Feature engineering and SVM classification of breast cancer D-FFOCT images.** Static (A1) and dynamic (B1) FFOCT images of a cancerous breast sample are analyzed using two random forest classifiers (A2,B2). FFOCT image are segmented (A2) into fibers (red), cells (green), and fat/holes (blue). D-FFOCT image are segmented (B2) in cells. These segmented images, as well as mesoscale images (A3,B3), are used to compute engineered features. Mesoscale fiber regions (A3) describes the region of high fiber density in the FFOCT image. Mesoscale cell regions (B3) describes regions of high cell density in the D-FFOCT image. (C) Chart summarizing the processing of FFOCT and D-FFOCT images in order to classify each image and each sample using SVM. (D) Proportion of normal areas found for each healthy (blue) and cancerous (sample) showing 100% separability between the two classes. Scale bars: $200 \, \mu m$.

In total, once the random forests and SVM were trained, the acquisition of about 10 field of

views, as well as the prediction for a sample only took a few minutes, and was shown to be very powerful to distinguish healthy from cancerous samples. Nonetheless, the accuracy per field of view is not so high, which would make it complicated to use to find tumor margins within a sample. Also, this approach was only successful here, because the field of views acquired with D-FFOCT were chosen as being representative of the sample, but this requires training with FFOCT imaging. Finally, SVM are known to become computationally intensive when multiple classes (outputs) are used, which may add complexity if tumor phenotyping is to be achieved.

5. Pixel scale blind classification using clustering
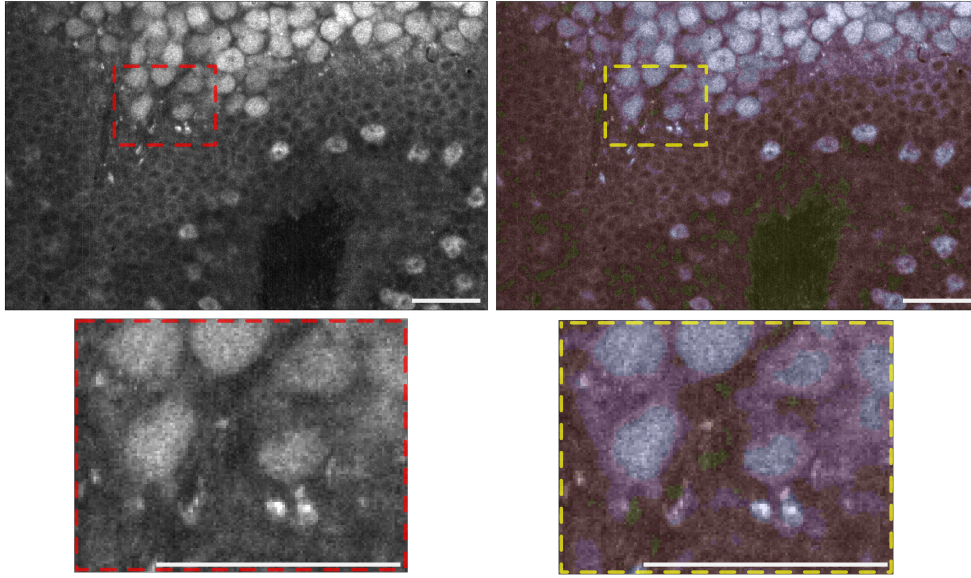
Fig. 8. Clustering results using GMM on a 10 dimensions feature space for each pixel on a mouse retina. Scale bar: 25 μm.

Finally, a pixel scale approach was developed with a non-supervised strategy. The bottleneck in the development of machine learning and neural networks is often data annotation which is both cumbersome and time consuming. It is interesting to see whether non-supervised algorithms could identify and cluster dynamic patterns without prior knowledge. To do so, dynamic features were extracted on each pixel. For each pixel, the power spectrum density was computed using Welch method with 16 samples per segment giving 9 features. The decorrelation time computed as the width at half maximum of the auto-correlation was added as 10th feature. The feature space was then clustered using Gaussian Mixtures Models (GMM) with 4 classes (arbitrary choice corresponding to the number of cell types present in the FOV). A local spatial filter was applied to take advantage of the spatial information and to smooth the class map which was noisy. For a given pixel, the final class was the most predicted class in a neighborhood corresponding to a disk of radius 4 pixels. The resulting clustering mainly follows the image intensity because the power spectrum density carries the energy information of fluctuations. With this approach it is possible to segment cell if membranes exhibit high contrast but it is really not a straightforward and fast method. These results suggest that D-FFOCT signals at the pixel scale do not carry much information without considering the spatial distribution of these fluctuations.

6. Conclusion

In this paper, we show that using the information contained in the dynamic signal allow for tissue and cell classification. We successfully classified retinal cells with 97.7% accuracy and breast healthy and cancerous tissues with 100% accuracy when aggregating results. We also demonstrated that dynamic images can be treated directly, disregarding most of the dynamic information by considering only its amplitude (motility index), and performed classification on thumbnail images using convolutional neural networks. Using the Grad-CAM technique we were able to exhibit the spatial location that led to a given classification and validated that the neural network learnt to discriminate between cancerous and healthy cell packing. Finally we shown that considering the dynamic at the single pixel scale does not carry much information and that the spatial distribution of the probed dynamics is important to gain insight on the tissue and cells.

Disclosures

Claude Boccara is one of the LLtech founders and is a shareholder. None for all other authors.

References

1. A. W. Browne, C. Arnesano, N. Harutyunyan, T. Khuu, J. C. Martinez, H. A. Pollack, D. S. Koos, T. C. Lee, S. E. Fraser, R. A. Moats, J. G. Aparicio, and D. Cobrinik, "Structural and Functional Characterization of Human Stem-Cell-Derived Retinal Organoids by Live Imaging," Investig. Ophthalmol. & Vis. Sci. **58**, 3311–3318 (2017).
2. M. Adhi and J. S. Duker, "Optical coherence tomography – current and future applications:," Curr. Opin. Ophthalmol. **24**, 213–221 (2013).
3. D. Huang, E. Swanson, C. Lin, J. Schuman, W. Stinson, W. Chang, M. Hee, T. Flotte, K. Gregory, C. Puliafito *et al.*, "Optical coherence tomography," Science **254**, 1178–1181 (1991).
4. W. Drexler and J. G. Fujimoto, eds., *Optical coherence tomography: technology and applications* (Springer, 2015), 2nd ed.
5. E. Beaurepaire, A. C. Boccara, M. Lebec, L. Blanchot, and H. Saint-Jalmes, "Full-field optical coherence microscopy," Opt. Lett. **23**, 244–246 (1998).
6. A. Dubois, K. Grieve, G. Moneron, R. Lecaque, L. Vabre, and C. Boccara, "Ultrahigh-resolution full-field optical coherence tomography," Appl. Opt. **43**, 2874–2883 (2004).
7. M. Jain, N. Shukla, M. Manzoor, S. Nadolny, and S. Mukherjee, "Modified full-field optical coherence tomography: A novel tool for rapid histology of tissues," J. Pathol. Informatics **2**, 28 (2011).
8. J. Ben Arous, J. Binding, J.-F. Léger, M. Casado, P. Topilko, S. Gigan, A. C. Boccara, and L. Bourdieu, "Single myelin fiber imaging in living rodents without labeling by deep optical coherence microscopy." Journal of Biomedical Optics **16**, 116012 (2011).
9. C. Apelian, F. Harms, O. Thouvenin, and A. C. Boccara, "Dynamic full field optical coherence tomography: subcellular metabolic contrast revealed in tissues by interferometric signals temporal analysis," Biomed. Opt. Express **7**, 1511–1524 (2016).
10. M. Münter, M. vom Endt, M. Pieper, M. Casper, M. Ahrens, T. Kohlfaerber, R. Rahmanzadeh, P. König, G. Hüttmann, and H. Schulz-Hildebrandt, "Dynamic contrast in scanning microscopic OCT," arXiv e-prints arXiv:2003.00006 (2020).
11. C.-E. Leroux, F. Bertillot, O. Thouvenin, and A.-C. Boccara, "Intracellular dynamics measurements with full field optical coherence tomography suggest hindering effect of actomyosin contractility on organelle transport," Biomed. Opt. Express **7**, 4501–4513 (2016).
12. O. Thouvenin, C. Boccara, M. Fink, J. Sahel, M. Pâques, and K. Grieve, "Cell motility as contrast agent in retinal explant imaging with full-field optical coherence tomography," Investig. Opthalmology & Vis. Sci. **58**, 4605 (2017).
13. J. Scholler, V. Mazlin, O. Thouvenin, K. Groux, P. Xiao, J.-A. Sahel, M. Fink, C. Boccara, and K. Grieve, "Probing dynamic processes in the eye at multiple spatial and temporal scales with multimodal full field OCT," Biomed. Opt. Express **10**, 731–746 (2019).

14. C. Pfäffle, H. Spahr, L. Kutzner, S. Burhan, F. Hilge, Y. Miura, G. Hüttmann, and D. Hillmann, "Simultaneous functional imaging of neuronal and photoreceptor layers in living human retina," Opt. Lett. **44**, 5671–5674 (2019).
15. K. Simonyan and A. Zisserman, "Very deep convolutional networks for large-scale image recognition," (2014).
16. A. Dubois, K. Grieve, G. Moneron, R. Lecaque, L. Vabre, and C. Boccara, "Ultrahigh-resolution full-field optical coherence tomography," Appl. Opt. **43**, 2874–2883 (2004).
17. J. Scholler, "FFOCT control and acquisition software," (2019). https://doi.org/10.5281/zenodo.3137245.
18. J. Scholler, "Motion artifact removal and signal enhancement to achieve in vivo dynamic full field oct," Opt. Express **27**, 19562–19572 (2019).
19. G. Hinton, "Overview of mini-batch gradient descent," http://www.cs.toronto.edu/~tijmen/csc321/slides/lecture_slides_lec6.pdf (2016). Accessed: 2019-11-26.
20. R. R. Selvaraju, M. Cogswell, A. Das, R. Vedantam, D. Parikh, and D. Batra, "Grad-cam: Visual explanations from deep networks via gradient-based localization," Int. J. Comput. Vis. (2019).
21. A. Dufour, V. Meas-Yedid, A. Grassart, and J. . Olivo-Marin, "Automated quantification of cell endocytosis using active contours and wavelets," in *2008 19th International Conference on Pattern Recognition,* (2008), pp. 1–4.
22. M. Kass, A. Witkin, and D. Terzopoulos, "Snakes: Active contour models," Int. J. Comput. Vis. **1**, 321–331 (1988).
23. J. C. Platt, "Probabilistic outputs for support vector machines and comparisons to regularized likelihood methods," in *Advances in large margin classifiers,* (MIT Press, 1999), pp. 61–74.
24. T. Chen and C. Guestrin, "XGBoost," Proc. 22nd ACM SIGKDD Int. Conf. on Knowl. Discov. Data Min. (2016).
25. C. Sommer, C. Straehle, U. Koethe, and F. A. Hamprecht, "Ilastik: Interactive learning and segmentation toolkit," in *2011 IEEE international symposium on biomedical imaging: From nano to macro,* (IEEE, 2011), pp. 230–233.

Appendix E

Scientific contributions

Publications

J. Scholler, V. Mazlin, O. Thouvenin, K. Groux, P. Xiao, J. Sahel, M. Fink, C. Boccara, and K. Grieve, *"Probing dynamic processes in the eye at multiple spatial and temporal scales with multimodal full field OCT,"* Biomed. Opt. Express 10, 731-746 (2019)

J. Scholler, *"Motion artifact removal and signal enhancement to achieve in vivo dynamic full field OCT,"* Opt. Express 27, 19562-19572 (2019)

J. Scholler, K. Groux, O. Goureau, J. Sahel, M. Fink, S. Reichman, C. Boccara and K. Grieve. *"Dynamic full-field optical coherence tomography: 3D live-imaging of retinal organoids."* Light Sci Appl 9, 140 (2020).

J. Scholler, K. Groux, K. Grieve, C. Boccara and P. Mecê *"Adaptive-glasses wavefront sensorless full-field OCT for high-resolution retinal imaging over a wide field-of-view"* arXiv:2007.04986 (2020).

P. Mecê, **J. Scholler**, K. Groux, and C. Boccara, *"High-resolution in-vivo human retinal imaging using full-field OCT with optical stabilization of axial motion,"* Biomed. Opt. Express 11, 492-504 (2020).

P. Mecê, K. Groux, **J. Scholler**, O. Thouvenin, M. Fink, K. Grieve and C. Boccara *""Coherence gate shaping for wide field high-resolution in vivo retinal imaging with full-field OCT,"* Biomed. Opt. Express 11, 4928-4941 (2020).

V. Mazlin, P. Xiao, **J. Scholler**, K. Irsch, K. Grieve, M. Fink and C. Boccara. *"Real-time, non-contact, cellular imaging and angiography of human cornea and limbus with common-path Full-field/SDOCT."* Nat Commun 11, 1868 (2020).

Proceedings and conference papers

2020

J. Scholler, P. Mecê, K. Groux, V. Mazlin, C. Boccara and K. Grieve *"Motion artifact removal and signal enhancement to achieve in vivo dynamic full field OCT (Conference*

Presentation)", Proc. SPIE 11228, Optical Coherence Tomography and Coherence Domain Optical Methods in Biomedicine XXIV, 112281N (9 March 2020)

J. Scholler, O. Thouvenin, E. Benoit a la Guillaume and C. Boccara *"One hundred percent successful automatic breast cancer diagnosis using static and dynamic FFOCT images (Conference Presentation)"*, Proc. SPIE 11222, Molecular-Guided Surgery: Molecules, Devices, and Applications VI, 1122206 (10 March 2020)

K. Groux, **J. Scholler**, P. Mecê, S. Reichman, V. Fradot, M. Pâques, C. Boccara and Kate Grieve *"Stress and repair in retinal pigmented epithelium cell culture imaged with dynamic full-field OCT (Conference Presentation)"*, Proc. SPIE 11239, Dynamics and Fluctuations in Biomedical Photonics XVII, 112390O (9 March 2020)

P. Mecê, **J. Scholler**, K. Groux, M. Fink, K. Grieve and C. Boccara *"Adaptive glasses-assisted Full-Field OCT for SNR enhanced 3D high-resolution retinal imaging (Conference Presentation)"*, Proc. SPIE 11228, Optical Coherence Tomography and Coherence Domain Optical Methods in Biomedicine XXIV, 112281O (9 March 2020)

P. Mecê, K. Groux, J. Scholler, M. Fink, K. Grieve and C. Boccara *"Increased field-of-view full-field OCT for 3D high-resolution retinal imaging (Conference Presentation)"*, Proc. SPIE 11218, Ophthalmic Technologies XXX, 112180S (9 March 2020)

S. Khare, R. Malpani, H. Lee, V. Gorti, K. Khaksari, **J. Scholler**, E. Benoit, C. Boccara, D. Sackett and A. Gandjbakhche *"D-FFOCT as a tool to assess oxygenation induced changes in cellular metabolism (Conference Presentation)"*, Proc. SPIE 11228, Optical Coherence Tomography and Coherence Domain Optical Methods in Biomedicine XXIV, 112281R (9 March 2020)

2019

J. Scholler, K. Groux, M. Fink, C. Boccara and K. Grieve; *Label free retinal cell imaging with dynamic full-field OCT.* Invest. Ophthalmol. Vis. Sci. 2019;60(11):009

J. Scholler, K. Groux, J. Sahel, M. Fink, C. Boccara and K. Grieve; *Real time dynamic imaging of retinal samples with full field OCT.* Invest. Ophthalmol. Vis. Sci. 2019;60(9):1265.

J. Scholler, K. Groux, S. Reichman, M. Pâques, O. Goureau, J. Sahel, M. Fink, C. Boccara, and K. Grieve *"Subcellular quantitative dynamic imaging: from metabolic activity to cell tracking of retinal and corneal structure (Conference Presentation)"*, Proc. SPIE 10867, Optical Coherence Tomography and Coherence Domain Optical Methods in Biomedicine XXIII, 108670E (4 March 2019);

K. Groux, **J. Scholler**, Sacha Reichman, M. Paques, O. Goureau, J. Sahel, M. Fink, C. Boccara and K. Grieve, *Imaging retinal organoid subcellular dynamics non invasively with Full-Field OCT.* Invest. Ophthalmol. Vis. Sci. 2019;60(9):3337.

V. Mazlin, **J. Scholler**, P. XIAO, K. Irsch, K. Grieve, J. Sahel, M. Fink and C. Boccara, *Central and peripheral cornea, limbal palisades of Vogt and blood flow visualized*

with cell-resolution non-contract en face full-field OCT. Invest. Ophthalmol. Vis. Sci. 2019;60(9):2125.

V. Mazlin, P. Xiao, **J. Scholler**, P. Mecê, K. Grieve, K. Irsch, M. Fink and C. Boccara, *Non-contact cell-detail real-time full-field OCT: capabilities and potential clinical applications of the novel anterior eye imaging tool.* Invest. Ophthalmol. Vis. Sci. 2019;60(11):008.

P. Mecê, V. Mazlin, **J. Scholler**, P. Xiao, J. Sahel, K. Grieve, M. Fink and C. Boccara, *Real-time axial retinal motion tracking and correction for consistent high-resolution retinal imaging with Full-Field Time-Domain Optical Coherence Tomography (FFOCT).* Invest. Ophthalmol. Vis. Sci. 2019;60(11):022.

P. Mecê, P. Xiao, V. Mazlin, **J. Scholler**, K. Grieve, J. Sahel, M. Fink and C. Boccara, *"Towards lens-based wavefront sensorless adaptive optics full-field OCT for in-vivo retinal imaging (Conference Presentation),"* Proc. SPIE 10867, Optical Coherence Tomography and Coherence Domain Optical Methods in Biomedicine XXIII, 1086722 (4 March 2019)

2018

K. Grieve, **J. Scholler**, P. Xiao, V. Mazlin, O. Thouvenin, M. Fink, J. Alain Sahel, M. Paques and C. Boccara; (2018), *Structural and functional imaging of ocular tissues with full-field OCT.* Acta Ophthalmol, 96: 48-48.

O. Thouvenin, **J. Scholler**, C. Boccara, M. Paques, J. Sahel, M. Fink and K. Grieve *"Ultrahigh resolution imaging of cellular dynamics in explanted corneas and retinas with ocular pathologies using dynamic full-field OCT (Conference Presentation)"*, Proc. SPIE 10474, Ophthalmic Technologies XXVIII, 104740T (14 March 2018)

V. Mazlin, P. Xiao, **J. Scholler**, K. Grieve, K. Irsch, J. Sahel, M. Fink, and C. Boccara, *"Ultra-High Resolution Full-Field OCT (FFOCT) for Cornea and Retina,"* in Imaging and Applied Optics 2018 (3D, AO, AIO, COSI, DH, IS, LACSEA, LS&C, MATH, pcAOP), OSA Technical Digest (Optical Society of America, 2018), paper IM3B.1.

P. Xiao, V. Mazlin, **J. Scholler**, M. Fink and C. Boccara, *"Adaptive Optics and Full-field OCT: the expected gain,"* in Imaging and Applied Optics 2018 (3D, AO, AIO, COSI, DH, IS, LACSEA, LS&C, MATH, pcAOP), OSA Technical Digest (Optical Society of America, 2018), paper OTh4C.1.

V. Mazlin, P. Xiao, **J. Scholler**, K. Grieve, J. Sahel, M. Fink and C. Boccara; (2018), *In vivo retinal cells visible without adaptive optics using a novel full-field OCT*. Acta Ophthalmol, 96: 82-82.

Softwares

J. Scholler. (2019, May 20). J.Scholler/FFOCT: FFOCT_v0.1 (Version v0.1). Zenodo. http://doi.org/10.5281/zenodo.3137246

Appendix F

Résumé en français

F.1 Introduction

Cette thèse s'inscrit dans le thème de l'imagerie optique, qui vise à sonder des objets et à produire des images claires et agrandies de ceux-ci. En clinique, l'imagerie précise du corps humain peut aider à fournir de meilleurs diagnostics; en recherche, elle peut apporter des connaissances biologiques importantes ou une meilleure compréhension de l'univers en imageant le ciel. Même si la propagation de la lumière peut être extrêmement complexe et que les images peuvent contenir une quantité d'informations démesurée, les systèmes optiques sont naturellement privilégiés par les humains, car c'est en partie de cette manière que nous interagissons avec le monde par l'intermédiaire de l'un des systèmes optiques les plus évolué : l'œil. La détection de la lumière présente de nombreux avantages par rapport à d'autres ondes. Tout d'abord, nous disposons d'une source de lumière gratuite qui éclaire notre monde. De plus, la lumière se propage si vite que, dans la plupart des cas, notre cerveau peut simplement négliger la propagation de celle-ci et traiter la scène comme si la vitesse de la lumière était infinie. Enfin, la lumière peut propager efficacement des informations provenant de structures plus petites que nos autres sens, ce qui nous donne un pouvoir de résolution supérieur.

L'imagerie optique est un domaine vaste et dynamique dans lequel de nombreux groupes et chercheurs s'investissent et développent des idées brillantes pour repousser toujours plus loin les limites de l'imagerie. Les systèmes d'imagerie optique peuvent être regroupés en différentes catégories, ce qui permet de les classer et de les comprendre. Ils peuvent d'abord être séparés en dispositifs fonctionnant en transmission ou en réflexion[1]. Dans les systèmes en transmission, l'illumination est du côté opposé à la détection, tandis que dans les systèmes en réflexion, l'illumination et la détection sont effectués du même côté de l'objet. Bien que la configuration en transmission puisse être intéressante (par exemple pour mesurer l'absorption des rayons X), elle serait invasive pour la plupart des applications de microscopie[2] de sorte que les systèmes fonctionnant en réflexion sont généralement préférés pour l'imagerie en limite de diffraction. Les systèmes optiques peuvent ensuite être classés en détection cohérente et incohérente en fonction de la façon dont le champ lumineux est mesuré. Les systèmes cohérents présentent des propriétés très intéressantes car ils permettent d'accéder à la nature complexe du champ lumineux, c'est-à-dire de mesurer

---

[1]Il existe également des systèmes hybrides où l'éclairage peut être orthogonal à la détection, comme la microscopie à feuille de lumière.

[2]L'endoscopie en transmission serait terriblement invasive car elle nécessiterait d'encastrer le détecteur dans le tissu du patient

à la fois l'amplitude et la phase. Les informations sur la phase sont utiles, par exemple, pour mesurer les déplacements axiaux avec une précision bien meilleure que la longueur d'onde ou pour propager le champ afin d'accéder à d'autres plans. Enfin, les systèmes peuvent être subdivisés en mesures directes et indirectes selon la façon dont les signaux sont sondés. En effet, certains systèmes d'imagerie tels que l'IRM, l'imagerie par diffraction des rayons X ou la spectroscopie par transformée de Fourier n'acquièrent pas de signaux dans le domaine direct (c'est-à-dire dans l'espace ou le temps) mais dans le domaine de Fourier (fréquence). Bien que les mesures indirectes présentent souvent des propriétés intéressantes, elles présentent généralement le même inconvénient, à savoir qu'il faut mesurer tout le domaine avant de pouvoir récupérer l'image en passant de l'espace sondé à l'espace direct. L'objectif commun de tous ces systèmes d'imagerie est de mesurer les propriétés optiques d'un objet avec la meilleure qualité et la meilleure résolution d'image possible. Les microscopistes ont de nombreux ennemis physiques[3] qui détériorent les performances d'imagerie. Ils s'efforcent de les surmonter en imaginant et concevant des méthodes innovantes qui permettent de récupérer et de filtrer les informations même lorsqu'elles sont supposées avoir été perdues. Ces méthodes comprennent le filtrage des photons balistiques des photons diffusés, les approches matricielles et l'utilisation de systèmes multimodaux qui combinent les ondes électromagnétiques et acoustiques. Toutes ces méthodes sont actuellement étudiées et développées dans notre laboratoire dans un environnement très stimulant.

Dans le cadre de cette thèse, j'ai surtout été impliqué dans la construction et l'utilisation des systèmes de tomographie optique cohérente (OCT) qui fonctionnent en réflexion, avec comme son nom l'indique une détection cohérente et à mesure directe[4]. Une propriété très intéressante de l'OCT est sa capacité à rejeter les photons diffusés ainsi que sa capacité de sectionnement optique qui permettent d'obtenir des images 3D. L'OCT est similaire à l'holographie, la différence étant que l'holographie utilise un éclairage monochromatique alors que l'OCT utilise des sources à large bande, de sorte que l'holographie n'a pas de capacité de sectionnement optique direct. Toutefois, pour les objets faiblement diffusants, la microscopie holographique numérique[5] peut reconstruire la structure de l'objet en 3D en utilisant des modèles de propagation de la lumière qui échouent généralement lorsque l'objet contient plus que quelques cellules d'épaisseur. Au cours de mon doctorat, j'ai essayé de combiner l'OCT avec l'imagerie de fluorescence dans une configuration en réflexion. La fluorescence est une mesure directe qui entre toujours dans la catégorie incohérente car la fluorescence est un processus non cohérent même si l'éclairage utilisé pour générer la fluorescence est cohérent. La nature incohérente de la fluorescence a conduit à de nombreuses tentatives[6] pour apporter une capacité de sectionnement optique avec des approches d'illumination et de détection intelligents.

Ce manuscrit est divisé en cinq chapitres. Le premier chapitre présente les concepts et les défis de l'imagerie dans les milieux diffusants. À cette fin, une brève introduction sur la propagation de la lumière dans ces milieux est donnée. Ensuite, les concepts généraux de filtrage des photons diffusés sont discutés et le filtrage ou fenêtrage temporel est introduit

---

[3]La diffraction, le bruit de photons, les aberrations, la diffusion et bien d'autres encore !

[4]Il existe également des systèmes OCT indirects qui fonctionnent dans le domaine de Fourier.

[5]Parfois appelée tomographie par diffraction optique.

[6]Telles que la microscopie confocale de fluorescence qui est basée sur un filtrage spatial des photons diffusés par illumination et détection à travers un sténopé, la microscopie à feuille de lumière où seule une fine tranche axiale de l'échantillon est illuminée et la fluorescence multi-photons qui est basée sur des processus non linéaires.

avec l'OCT. La première implémentation de l'OCT[7] est présentée avec les mains avant de dériver les concepts et équations mathématiques qui conduisent à la formation d'images sur le détecteur. Ces modèles mathématiques sont appliqués à la fois sur l'OCT temporel et de Fourier afin de montrer qu'ils mesurent tous deux la même quantité physique. Je voulais introduire ces concepts parce que je pense qu'ils sont importants pour quiconque veut construire un système d'OCT, car même s'ils semblent simples, les systèmes d'OCT présentent de nombreux pièges et subtilités. De plus, ces concepts sont fondamentaux pour comprendre les dernières recherches et avancées en OCT avec ses nombreuses branches. Ensuite, avec la description complète de l'OCT, je déduis les performances et les limites de l'OCT à balayage avant d'introduire l'OCT plein champ (FFOCT) où la mesure est parallélisée par l'utilisation d'une caméra plutôt que d'une photo-diode, et ne nécessite donc aucun balayage. De nombreux aspects du FFOCT sont décrits afin de donner au lecteur une vue d'ensemble des différents paramètres et de fournir un guide d'utilisation à tous ceux qui pourraient vouloir construire un tel système. Enfin, je compare notre approche FFOCT, qui est dans le domaine temporel et incohérent spatialement, avec les approches OCT plein champ qui me semble les plus prometteuses.

Le deuxième chapitre présente les mesures dynamiques que l'on peut faire avec le FFOCT en analysant les fluctuations temporelles du signal interférométrique. Dans ce chapitre, je soutiens l'idée que le FFOCT dynamique (D-FFOCT) n'est pas adapté pour mesurer les propriétés physiques locales des diffuseurs mais peut être utilisé pour générer des images quantitatives où les cellules sont révélées avec un excellent contraste et où l'étude de leur profil dynamique peut conduire à observer d'intéressants phénomènes biologiques. Une application du D-FFOCT est montrée avec l'imagerie d'organoïdes de rétine dans un article intégré à ce manuscrit [Scholler et al., 2020].

Le troisième chapitre rassemble les méthodes de post-traitement que j'ai développées au cours mon doctorat afin d'améliorer les images (D-)FFOCT. Une section particulièrement intéressantes est celle concernant la suppression des artefacts de mouvement des acquisitions D-FFOCT. Comme le D-FFOCT est sensible à la phase, de minuscules déplacements axiaux créent de grands signaux artefactuels qui masquent le signal d'intérêt et empêchent l'acquisition d'images D-FFOCT in vivo. L'élimination de ces artefacts a été une étape importante dans le développement du D-FFOCT et la méthode est expliquée en détail dans un article intégré à ce manuscrit qui a été publié en 2019 [Scholler, 2019b]. Dans ce même article, une méthode différente de calcul des images dynamiques qui a amélioré le rapport signal sur bruit est aussi présentée, permettant ainsi d'obtenir des images plus en profondeur des tissus.

Le quatrième chapitre rassemble les modifications ainsi que les améliorations matériel des système expérimentaux que j'ai développés pour la microscopie et l'imagerie in vivo de la rétine chez l'homme. En ce qui concerne l'imagerie de la rétine, le travail présenté est un effort commun avec Pedro Mecê pour faire du FFOCT un appareil robuste, à haute résolution et répétable pour imager la rétine. La première étape a consisté à combiner le FFOCT avec un dispositif de suivi axial afin de traquer la rétine pour faire correspondre automatiquement la longueur du chemin optique entre la couche de rétine imagée et le miroir de référence; condition nécessaire à l'obtention d'une image. Ensuite, la deuxième étape a consisté à manipuler le front d'onde afin de maintenir une symétrie optique entre l'œil et le bras de référence. Sans cette symétrie, les images FFOCT ne pouvaient être

---

[7]Qui est appelée OCT à balayage.

acquises que sur une petite zone plutôt que sur l'ensemble du champ imagé. Enfin, la dernière étape a consisté à corriger les aberrations oculaires par une approche efficace et peu coûteuse utilisant une lentille adaptative afin d'améliorer le rapport signal sur bruit et la répétabilité des acquisitions. Pour réussir cette dernière étape, un grand effort de compréhension sur la théorie de la manifestation des aberrations en FFOCT a été mené par Victor Barolle pendant son doctorat, puis démontré expérimentalement dans cette thèse.

Enfin, le cinquième chapitre rassemble les nombreuses applications du (D-)FFOCT qui ont été réalisées avec succès pendant ma thèse. Le suivi de mouvement a été utilisé pour surveiller la cicatrisation des blessures à l'aide d'images D-FFOCT et a fait l'objet d'un article publié en 2019 [Scholler et al., 2019]. Le suivi de mouvement a également été appliqué pour calculer des cartes d'angiographie du flux sanguin dans la conjonctive et limbe sclérocornéen chez l'homme in vivo dans un article publié en 2020 [Mazlin et al., 2020]. Ensuite, des stratégies visant à combiner le (D-)FFOCT avec l'imagerie par fluorescence sont décrites afin de mieux comprendre les signaux dynamiques (par exemple, différencier les mitochondries des vésicules), ce qui sera utile pour les futurs développements et applications biologiques du D-FFOCT[8]. Enfin, l'apprentissage machine et l'apprentissage profond pour la classification des cellules de la rétine et le dépistage du cancer du sein sont présentés à l'aide de mesures de (D-)FFOCT en appendice D.

F.2 Chapitre 1: imagerie 3D des milieux diffusants

Pendant de nombreuses années, l'imagerie optique a été l'outil le plus important de la recherche biomédicale pour observer les spécimens avec une résolution submicronique et un caractère invasif minimal [Hajdu, 2002]. Cependant, les conditions requises pour imager en limite de diffraction sont rarement réunies car la résolution et le contraste diminuent lorsque la profondeur d'imagerie augmente à l'intérieur d'un tissu biologique. Ce phénomène est une conséquence des variations spatiales de l'indice de réfraction du spécimen observé qui créent des distorsions du front d'onde. Lorsque ces variations présentent de faibles fréquences spatiales, ces distorsions sont appelées *aberrations* et sont généralement décrites à l'aide de polynômes orthogonaux. En revanche, lorsque ces variations sont de fréquences plus élevées, ces distorsions sont appelées *diffusion*[9]. Les aberrations et la diffusion limitent l'utilisation de la microscopie conventionnelle à de faibles profondeurs ou à des spécimens presque transparents. L'imagerie plus profonde, et donc l'imagerie 3D, nécessite de contrecarrer ces phénomènes nuisibles, de sorte que pour l'imagerie profonde, un mécanisme de sélection est généralement utilisé pour rejeter les photons diffusés et ne capturer que la lumière dite balistique. La lumière balistique est atténuée de façon exponentielle dans les tissus biologiques [Akkermans and Montambaux, 2007], ce qui signifie que plus on veut obtenir des images profondes, plus le signal balistique mesuré est faible et plus le bruit est élevé.

Une des grandeurs d'intérêt pour caractériser et comparer les systèmes d'imagerie 3D est le libre parcours moyen de *diffusion*. Le libre parcours moyen de diffusion l_s est la distance moyenne que parcours un photon entre deux évènements de diffusions. Un

---

[8]Ces aspects sont actuellement étudiés par Kassandra Groux dans notre équipe, en particulier sur les échantillons rétiniens.

[9]Le terme diffusion renvoie ici au *scattering* et non à la diffusion qui régie le transport de chaleur ou de particule. Malheureusement en français les deux principes physiques portent le même nom.

système d'imagerie classique permet d'imager un objet jusqu'à une profondeur de l'ordre du l_s, ensuite les photons diffusés rendent l'image trop floue et le contraste insuffisant pour reconstruire l'objet [Badon et al., 2017]. Un moyen pour imager à des profondeurs plus importantes est de filtrer les photons diffusées des photons balistiques. Ce filtrage peut être spatial comme en microscopie confocale [Minsky, 1988] où l'illumination et la détection sont filtrées à l'aide d'un sténopé. Ce filtrage peut aussi être temporel, en focalisant un pulse de lumière dans l'échantillon on peut trier les photons en fonction de leur temps d'arrivée et garder seulement ceux dont le temps de vol correspond à la profondeur à imager. Malheureusement la vitesse de l'électronique qu'il faudrait pour obtenir une résolution temporelle suffisante est plusieurs ordres de grandeurs supérieurs à ce dont nous disposons. Si, au lieu de mesurer le temps de vol des photons on les compare avec un pulse de référence qui a parcouru une distance connue alors les photons qui arrivent en même temps que les photons de référence vont donner lieu à des interférences. En mesurant ces interférence il est possible de séparer les photons diffusés des autres, c'est le principe de l'OCT [Huang et al., 1991] présenté Fig. 1.2. La résolution axiale δ_z en OCT dépend des propriétés spectrales de la source lumineuse utilisée [Goodman, 1985] et vaut:

$$\delta_z = \frac{l_\gamma}{2} = \frac{2ln(2)}{\pi}\frac{\lambda_c^2}{\Delta\lambda} \tag{F.1}$$

où l_γ est la longueur de cohérence de l'illumination, $\Delta\lambda$ est la largeur à mi-hauteur de la densité spectrale de puissance de la source et λ_c est la longueur d'onde centrale. La résolution transverse $\delta_{x,y}$ est limitée par la diffraction et vaut:

$$\delta_{x,y} = \frac{2\sqrt{ln(2)}}{\pi}\frac{\lambda_c}{NA} \tag{F.2}$$

où NA est l'ouverture numérique du système d'imagerie. La profondeur de champ (DOF) de l'OCT est liée à la longueur de Rayleigh et vaut:

$$DOF = \frac{\pi}{4}\frac{\delta_{x,y}^2}{\lambda_c} = \frac{ln(2)}{\pi}\frac{\lambda_c}{NA^2} \tag{F.3}$$

Étant donné que la profondeur de champ diminue lorsque la résolution transverse augmente, il est clair qu'il y a un compromis à trouver pour l'OCT à balayage. En effet, en améliorant la résolution latérale et en diminuant ainsi $\delta_{x,y}$ dans Eq. F.2, alors la DOF diminuera fortement. Dans les tissus biologiques, l'OCT permet d'acquérir des signaux jusqu'à une profondeur de 1 mm, de sorte que la DOF devrait être supérieur à 0.5 mm, ce qui conduit à une résolution transverse maximale de $\delta_{x,y} = 20$ μm, ce qui correspond à $NA = 0.015$. Par rapport aux techniques classiques de microscopie où le NA peut atteindre 1.5, ce résultat pour les OCT limitait son utilisation extensive en microscopie. Néanmoins, comme la résolution axiale était découplée du NA et de l'ordre de $\delta_z = 1$ μm l'OCT a rapidement trouvé des applications en ophtalmologie pour l'imagerie de la rétine où les couches rétiniennes sont séparées de quelques microns, l'OCT a donc pu résoudre les différentes couches de la rétine pour le diagnostic clinique. Afin de palier à ces défauts, l'OCT plein champ à été proposé, améliorant ainsi la résolution transverse et la vitesse d'acquisition. Contrairement à son homologue à balayage le FFOCT est très sensible à la cohérence spatiale de la source. En effet, comme les mesures sont parallélisées sur tout un plan, les interférences entre des pixels voisins peuvent donner des artefacts. Dans notre approche du FFOCT nous utilisons une LED qui est une source spatialement incohérente,

c'est à dire que deux points voisins de la source ne peuvent produire d'interférence et permet ainsi d'obtenir des images sans artefacts. D'autres approches de l'OCT plein champ existent notamment une approche hors-axe [Hillmann et al., 2016, Hillmann et al., 2017] qui permet de séparer spatialement les interférences intra-échantillons des interférences échantillon référence, ainsi qu'une approche utilisant une source spatialement cohérente conjuguée à une membrane vibrante [Auksorius et al., 2019] qui vient faire décorrélée la phase pendant le temps de la mesure, cassant ainsi la cohérence spatiale de la source.

F.3 Chapitre 2: nouveau contraste pour l'imagerie des cellules et tissus vivant avec le D-FFOCT

L'OCT plein champ dynamique (D-FFOCT) a été proposée pour la première fois par Clément Apelian [Apelian et al., 2016] comme une nouvelle technique permettant d'imager la dynamique intracellulaire des cellules vivantes dans des tissus frais ex vivo. L'idée première était de révéler les cellules à l'intérieur des tissus. En effet, les cellules sont pour la plupart transparentes et homogènes, ce qui les rend difficiles à imager, surtout dans les tissus où elles sont mélangées à des fibres de collagène très réfléchissantes. Les cellules sont essentiellement des objets de phase et Zernike a proposé en 1942 [Zernike, 1942] l'imagerie par contraste de phase pour améliorer le contraste des cellules, quasiment invisible en imagerie classique jusqu'alors. En utilisant la même idée, le D-FFOCT se base sur l'interférométrie pour sonder les changements de phase afin d'améliorer le contraste cellulaire et permettre de mesurer la motilité intracellulaire. Pour ce faire, on acquière un film de plusieurs centaines d'images (typiquement 512) sans introduire de décalage de phase, les décalages étant introduit par le mouvement des diffuseurs dans l'échantillon. A partir de ce film on construit une image dynamique en étudiant les fluctuations temporelles pour chaque pixel. L'indice métabolique a d'abord été proposé en étant calculé comme l'écart type glissant moyenné sur la totalité du signal pour chaque pixel [Apelian et al., 2016, Thouvenin et al., 2017a]. Plusieurs caractéristiques peuvent être calculées en plus de l'indice métabolique afin de générer des images colorées. Ces caractéristiques portent des informations physiques limitées sur les propriétés physique des diffuseurs locaux mais permettent de différencier les cellules en examinant leur profil dynamique. Une application de l'imagerie D-FFOCT pour les organoïdes de rétines est présenté avec une publication [Scholler et al., 2020] page 28 de ce manuscrit.

F.4 Chapitre 3: développements logiciels pour le (D-)FFOCT

Dans ce chapitre je montre que la partie de traitement des signaux est très importante dans la fabrication des images dynamiques. En effet, les mouvements axiaux de l'échantillon durant l'acquisition (qui dure plusieurs secondes) créent des changements de phase très important et masques les changements de phase lié aux diffuseurs locaux et donc à la motilité cellulaire. Une méthode de séparation des artefacts de mouvements est proposé utilisant la décomposition en valeur singulière. Cette méthode a permis pour la première fois d'obtenir des images D-FFOCT in vivo sur un foie de souris. Cette méthode est détaillée dans un article publié en 2019 [Scholler, 2019b] intégré page 42 de ce manuscrit avec un nouvel opérateur pour calculer l'index métabolique qui permet de multiplier le rapport signal sur bruit au moins par deux. Cet opérateur utilisant la somme cumulée permet d'amplifier les non-stationnarités dans les signaux dynamiques afin de les amplifier par

rapport au bruit. Ensuite, j'explique comment nous avons pu utiliser Holovibes[10] [Atlan, M. et al., 2009] et le modifier pour calculer des images dynamiques beaucoup plus rapidement et en évitant de devoir sauvegarder les données brutes qui peuvent peser jusque 4 *Go* par seconde d'acquisition. Grâce à l'utilisation d'Holovibes nous avons pu atteindre une résolution temporelle de 20 *ms* sur plusieurs heures, contre 30 *s* auparavant. Enfin, dans ce chapitre je présente deux autres méthodes. La première permet de stabiliser le plan d'imagerie pour rester plusieurs heures dans le même plan d'un échantillon en compensant ainsi les dérives mécaniques. La seconde permet de retirer les artefactes liés aux imperfections du miroir de référence sur les images FFOCT en les détectant automatiquement et en reconstruisant le signal FFOCT sous-jacent en propageant l'information sur les bords en utilisant l'équation de Navier-Stokes.

F.5 Chapitre 4: développements matériels: vers le D-FFOCT in vivo.

Dans ce chapitre je traite les nombreux développement matériels que j'ai mis en oeuvre pendant ma thèse pour l'imagerie de la rétine. La première étape a été de développer un dispositif de tracking de la rétine pour compenser les mouvement de l'oeil et ainsi obtenir des images FFOCT de la rétine avec une meilleure consistance et a fait l'object d'une publication [Mecê et al., 2020b]. Pour ce faire nous utilisons un SD-OCT pour acquérir des B-Scans de la rétine et ainsi déterminer sa position axiale au cours du temps. Lorsqu'un mouvement de la rétine est détecté, une commande numérique est envoyée à un moteur à bobine mobile qui contrôle la position du miroir de référence afin de conserver la même différence de chemin optique entre la couche de la rétine que l'on souhaite imager et le bras de référence, et ce même lorsque le sujet bouge. Ensuite nous avons observés que chez certain sujet et pour imager certaines excentricités de la rétine le champ de vue présentait des signaux en forme de bande. Le rapport signal sur bruit n'était pas constant sur le champ de vue à cause de l'asymétrie optique entre l'oeil et l'objectif de microscope dans le bras de référence. Les deux champs interférant sur la caméra n'étant plus co-planaire on observait des bandes de signaux (là où les champs étaient superposés). Pour résoudre ce problème nous avons proposé de contrôler la courbure du champ en ajoutant une lame de verre dans un des bras. Les points à l'extrémité du champ sortant avec un angle plus grand, ils traversent une plus grande épaisseur de verre entre la pupille de l'objectif ou de l'oeil et la lentille de tube. Ainsi on ajoute un retard ou une avance de phase différente selon la position transverse dans le champ de vue et on peut manipuler facilement la courbure du champ. Ce procédé simple et peu coûteux a fait l'objet d'une publication [Mecê et al., 2020a] qui est présenté dans la deuxième partie de ce chapitre. La troisième partie traite des aberrations et fera sûrement l'objet d'une publication dans un futur proche. Dans un premier temps je dérive les résultats connus sur la manifestation des aberrations dans un système optique conventionnel avant de dériver l'effet des aberrations en FFOCT qui a été découvert par Victor Barolle durant sa thèse [Barolle, 2019]. Ce modèle met en lumière plusieurs propriétés intéressantes du FFOCT grâce à la nature spatialement incohérente de l'illumination:

- Les aberrations symétriques ont une plus faible influence sur les images FFOCT que les images conventionnelles contrairement aux aberrations anti-symétriques.

---

[10]Holovibes est un logiciel développé par Michael Atlan et son équipe pour faire de la reconstruction d'hologramme sur GPU en temps réel.

- Le module de la fonction d'étalement du point est le même en FFOCT qu'en imagerie conventionnelle.

Dans le but de démontrer expérimentalement ce modèle j'ai construit un dispositif expérimental permettant de rajouter des aberrations de manière contrôlée à l'aide d'une lentille déformable et d'une mesure du front d'onde à l'aide d'un Shack-Hartmann. J'ai aussi mesuré les fonctions d'étalement du point à l'aide d'un gel de particules de TiO_2 conjointement en FFOCT et en imagerie conventionnel. A la lumière de ses résultats j'ai ensuite transféré la partie contrôle du front d'onde de l'expérience précédente sur notre banc d'imagerie rétinienne afin de corriger les aberrations oculaires pour l'imagerie. Différentes stratégies d'optimisation du front d'onde sont testés ainsi que différentes fonctions de coût. Finalement c'est l'algorithme DONE [Verstraete et al., 2017] combiné à une fonction de coût hybride calculée sur les B-Scans SD-OCT qui montre les meilleurs résultats. Grâce à la correction du front d'onde en temps réel nous avons pu obtenir des images proche de la limite de diffraction sur pupille dilatée[11], y compris sur des sujets présentant des aberrations de haut ordre (à cause de l'opération LASIK) et donc non imageable sans correction du front d'onde. En optimisant le signal sur la partie supérieure de la rétine nous avons pu obtenir pour la première en fois en FFOCT des image de la couche de fibre nerveuse à différentes profondeurs où l'on a pu deviner l'écoulement du sang dans un vaisseau. Grâce aux améliorations matérielles présentées dans ce chapitre nous avons bon espoir de pouvoir faire des mesures dynamiques in vivo dans la rétine.

F.6 Chapitre 5: des signaux aux diagnostiques

Le cinquième et dernier chapitre de ce manuscrit présente les différentes approches que j'ai développé pour extraire plus d'information des signaux dynamiques et aller vers le diagnostic. La première section regroupe les suivi de mouvements basés sur des films D-FFOCT et FFOCT. Le premier exemple est présentée dans un article [Scholler et al., 2019] et permet le suivi de la cicatrisation d'une blessure sur une cornée de macaque ex vivo. En traquant temporellement les cellules de l'epithelium grâce au calcul du flow optique j'ai pu extraire des cartes de déplacement et de vitesses et retrouver les valeurs typique de la littérature. Le second exemple est présenté dans un article [Mazlin et al., 2020] sur l'imagerie in vivo de la cornée. En analysant les films FFOCT du limbus j'ai pu mesurer quantitativement la vitesse du flux sanguin dans les capillaires du limbus. Pour ce faire j'ai traqué les globules rouges avec une approche par block-matching et reconstitué des carte angiographique du flux sanguin. Les propriétés du flux sanguin ainsi extrait ont été en accord avec la littérature et la théorie qui prédit un écoulement de type Poiseuille. La seconde section regroupe les étapes pour combiner le D-FFOCT et l'imagerie de fluorescence. L'imagerie de fluorescence est aujourd'hui la référence en biologie car elle permet par exemple de marquer des protéines, organelles, membranes et ainsi d'obtenir des images interprétable directement. Les images D-FFOCT sont elles très récentes et le manque de recul et de comparaison avec d'autres techniques font que nous ne pouvons pour l'instant pas interpréter toute l'information présente dans ces images. Le but de combiner l'imagerie de fluorescence au D-FFOCT est de pouvoir gagner en interprétabilité sur les images dynamiques et ainsi obtenir une méthode d'imagerie non-destructive et endogène. La difficulté que j'ai rencontré pour construire un système combiné est que l'imagerie de fluorescence ne présente pas de sectionnement optique en soi et il faut donc utiliser des méthodes d'illumination/détection évoluées pour ajouter ce sectionnement optique,

---

[11]Donc présentant un haut niveau d'aberrations.

nécessaire à l'imagerie en profondeur. J'ai utilisé pour cela la méthode HiLo, qui permet de rejeter les photons hors focus à partir de seulement deux images. Le problème est que cette technique fonctionne seulement à faible profondeur et ne permet pas de rivaliser avec le D-FFOCT en terme de pénétration. Une solution pourrait être de combiner le D-FFOCT avec un montage confocal mais l'implémentation n'est pas simple car le D-FFOCT est une technique plein champ alors que le confocal est une technique à balayage qui est de surcroît plus lente et nécessitant souvent la fixation des tissus et cellules. La dernière section traite de l'utilisation des signaux dynamiques pour faire de la classification de cellules et de la détection de cancer avec des approches d'apprentissage automatique et profond. En isolant des cellules de rétines par des techniques de segmentation et en utilisant les signaux brutes j'ai pu classifier ces cellules avec une précision de 97%. Pour la détection du cancer j'ai pu travailler sur des données d'une campagne de mesure sur la détection de cancer du sein et obtenir une précision de classification de 100%.

F.7   Conclusion et perspectives

Dans cette thèse, j'ai étudié les axes matériels et logiciels permettant de réaliser des acquisitions haute résolution en FFOCT dynamiques et statiques tout en conservant un dispositif expérimental peu complexe et très robuste. Pour la microscopie, j'ai appliqué le D-FFOCT pour l'imagerie des organoïdes rétiniens et j'ai démontré que cette technique peut apporter des connaissances biologiques intéressantes grâce à son contraste métabolique. J'ai trouvé une nouvelle méthode basée sur la décomposition en valeur singulière pour éliminer les artefacts provenant du mouvement axial de l'échantillon lors des acquisitions. J'ai également proposé un nouvel opérateur basé sur la somme cumulée pour calculer les images dynamiques. Cela a qui conduit à une amélioration du rapport signal sur bruit, nous permettant ainsi de pouvoir réaliser des images plus en profondeur dans les échantillons avec le D-FFOCT. Pour l'imagerie de la rétine, nous avons mis en œuvre un suivi et une compensation en temps réel de la position de la rétine qui fonctionne à 50 Hz et avec une erreur quadratique moyenne de $9,1\ \mu m$. Cela nous a permis d'obtenir des images de la rétine de manière fiable et répétable. Ensuite, nous avons étudié la courbure de champ due à l'asymétrie optique dans l'interféromètre de Linnik pour l'imagerie rétinienne et proposé une méthode pour trouver la compensation optimale afin de corriger à la fois la courbure de champ et la dispersion. Cela nous a permis d'imager la rétine sur un champ de vision de $1 \times 1\ mm$ avec un rapport signal sur bruit homogène sur tout le champ de vu. J'ai également validé expérimentalement la théorie des aberrations optiques proposée par Victor Barolle [Barolle, 2019] en utilisant une configuration AO-FFOCT construite à cette fin avec une lentille déformable et un capteur de front d'onde Shack-Hartmann. J'ai ensuite transféré la partie AO sur notre banc d'imagerie rétinienne et j'ai mis en œuvre et étudié plusieurs schémas d'optimisation sans capteur de front d'onde pour obtenir une image de la rétine humaine in vivo proche de la limite de diffraction en temps réel. J'ai pu imager et résoudre des photorécepteurs jusque 0,5 degré de la fovéa et imager de manière fiable la couche de fibre rétinienne à différentes profondeurs. J'ai également adapté des algorithmes de suivi de mouvement pour le D-FFOCT afin d'étudier le processus de cicatrisation des plaies de la cornée et pour le FFOCT afin de mesurer quantitativement le flux sanguin dans le limbe sclérocornéen in vivo chez l'humain. Ces accomplissements sont d'une grande importance car ils mettent en évidence la multimodalité de l'imagerie (D-)FFOCT et sa capacité à capturer des informations importantes et significatives. Enfin, j'ai étudié avec succès plusieurs approches d'apprentissage machine et d'apprentissage profond pour la classification des cellules de la rétine et la détection du cancer du sein à

l'aide des signaux D-FFOCT.

Compte tenu du potentiel du (D-)FFOCT, son avenir semble prometteur et j'espère que le transfert clinique pour l'imagerie de l'oeil mais aussi pour la microscopie avec l'étude du développement des organoides ainsi que le dépistage des biopsies aura lieu maintenant que cette technique est fiable et robuste. D'un point de vue plus fondamental, il existe encore certaines pistes que je n'ai pas eu le temps d'étudier mais qui pourraient être intéressantes pour de futurs développements. Ces idées sont brièvement discutées ci-dessous.

Correction numérique d'aberrations

Des travaux récents [Borycki et al., 2019] ont montré que la correction numérique des aberrations fonctionne aussi pour le FFOCT à transformée de Fourier même lorsque la cohérence spatiale de la source est détruite. Cette technique a récemment été appliquée avec succès pour l'imagerie in vivo de la cornée [Auksorius et al., 2020] et de la rétine [Auksorius et al., 2019] et a été brièvement expliquée dans la section 1.4.2. Les avantages de la correction numérique des aberrations sont notamment un meilleur rapport signal sur bruit, une résolution limitée par la diffraction et une profondeur de champ améliorée (particulièrement utile pour les techniques qui mesure axialement l'échantillon à chaque acquisition) sans nécéssité de modification du montage expérimental. Dans notre montage FFOCT (spatialement incohérent et dans le domaine temporel), les photons aberrés sont partiellement filtrés car ils ne peuvent pas interférer avec la référence. La correction numérique des aberrations n'entraînerait donc que des améliorations minimes. Mon idée est d'introduire une défocalisation dans le bras de référence afin que les photons aberrés puissent continuer à interférer avec la référence. En examinant l'énergie dans l'image FFOCT pour différentes niveaux de défocalisation, il devrait être possible de contrôler la proportion des photons abérrés interférant. Nous devrions observer davantage d'aberrations avec cette défocalisation car le modèle de formation d'images FFOCT présenté dans la section 4.3.2 ne tiendrait plus. Cependant, ces aberrations pourraient être corrigées en post-traitement en utilisant les approches développées précédemment [Borycki et al., 2019, Hillmann et al., 2016] et nous pourrions potentiellement nous passer de la lentille déformable.

D-FFOCT sur la phase et l'amplitude uniquement

Comme l'explique la section 2.2, il n'est pas possible de calculer les propriétés physiques locales des diffuseurs à partir des signaux D-FFOCT bruts. Cela est dû en partie au mélange des fluctuations d'amplitude et de phase. En utilisant la démodulation triangulaire à 10 phases qui a l'avantage de présenté un degré d'erreur faible sur la séparation de la phase et de l'amplitude présentée section 1.3.2, il devrait être possible de calculer distinctement les images D-FFOCT en phase et en amplitude. Cela pourrait conduire à de nouvelles connaissances en biologie selon le type de fluctuations. Un travail récent [Münter et al., 2020] a montré la possibilité de faire des mesures dynamiques en utilisant un SD-OCT. Les auteurs ont construit une image dynamique en mesurant les fluctuations de l'amplitude des signaux OCT, mais ils pourraient éventuellement calculer la même chose sur l'information de phase. Le SD-OCT dynamique pourrait ainsi aider à comprendre l'origine du signal dynamique. De plus, en réduisant la taille du capteur de la caméra, nous pourrions acquérir avec une fréquence d'images plus élevée. En acquérant plus d'images (des dizaines de milliers), nous pourrions utiliser la même approche que la spectroscopie de corrélation de fluorescence pour extraire les propriétés physiques locales des diffuseurs et ainsi extraire plus d'information quantitative sur les diffuseurs.

Phase retrieval pour le FFOCT

La correction numérique d'aberrations et le démélangeage d'amplitude et de phase pourraient tous deux bénéficier d'algorithmes de récupération de phase. L'adaptation des algorithmes actuellement utilisés [Yeh et al., 2015] pour le FFOCT pourrait permettre de mieux séparer la phase et l'amplitude du champ lumineux et ainsi d'obtenir des images plus rapidement et potentiellement en une seule prise. Cela pourrait aussi permettre une meilleure correction numérique d'aberrations en réduisant les artefacts de reconstruction.

D-FFOCT en champ sombre

Le FFOCT en champ sombre a d'abord été proposé dans [Auksorius and Boccara, 2015] puis appliqué à l'imagerie des empreintes digitales profondes [Auksorius and Boccara, 2020]. L'idée est de bloquer les réflexions spéculaires en ajoutant un masque dans le plan pupille du système d'imagerie. Pour que la référence puisse se propager vers la caméra, le miroir de référence doit donc être incliné ou remplacé par un réseau de diffraction. Combiné à un séparateur de faisceau efficace, le FFOCT par transformée de Fourier en champ sombre peut conduire à une amélioration par 4 du rapport signal sur bruit [Auksorius, 2020] en plus de supprimer les réflexions spéculaires qui permettent à nouveau d'envoyer plus de puissance et d'obtenir un signal encore meilleur. Le D-FFOCT en champ sombre pourrait donc améliorer considérablement la profondeur de pénétration. La difficulté étant que le plan de la pupille des objectifs à haute ouverture numérique est généralement physiquement à l'intérieur des objectifs, la mise en œuvre du D-FFOCT en champ sombre nécessiterait l'ajout d'un télescope pour relayer le plan de la pupille dans chaque bras. Cette configuration conduira à des systèmes plus grands et plus encombrants, mais le gain expecté en vaut probablement la peine.

Bibliography

[a la Guillaume et al., 2019] a la Guillaume, E. B., Groux, K., Scholler, J., Mandache, D., Yang, H., Wang, S., Meas-Yedid, V., and Boccara, C. (2019). Intracellular dynamics as a biomarker in tumor assessment using full-field optical coherence tomography (Conference Presentation). In Pogue, B. W. and Gioux, S., editors, *Molecular-Guided Surgery: Molecules, Devices, and Applications V*, volume 10862. International Society for Optics and Photonics, SPIE.

[Akkermans and Montambaux, 2007] Akkermans, E. and Montambaux, G. (2007). *Mesoscopic Physics of Electrons and Photons*. Cambridge University Press.

[Ammari et al., 2017] Ammari, H., Romero, F., and Shi, C. (2017). A signal separation technique for sub-cellular imaging using dynamic optical coherence tomography. *Multiscale Modeling & Simulation*, 15(3):1155–1175.

[Apelian et al., 2016] Apelian, C., Harms, F., Thouvenin, O., and Boccara, C. (2016). Dynamic full field optical coherence tomography: subcellular metabolic contrast revealed in tissues by interferometric signals temporal analysis. *Biomedical Optics Express*, 7(4):1511.

[Atlan, M. et al., 2009] Atlan, M. et al. (2009). Holovibes: hologram rendering software. http://holovibes.com.

[Auksorius, 2020] Auksorius, E. (2020). Light-efficient beamsplitter for fourier-domain full-field optical coherence tomography. *Optics Letters*, 45(5):1240.

[Auksorius and Boccara, 2015] Auksorius, E. and Boccara, A. C. (2015). Dark-field full-field optical coherence tomography. *Optics Letters*, 40(14):3272.

[Auksorius and Boccara, 2020] Auksorius, E. and Boccara, A. C. (2020). High-throughput dark-field full-field optical coherence tomography. *Optics Letters*, 45(2):455.

[Auksorius et al., 2020] Auksorius, E., Borycki, D., Stremplewski, P., Liżewski, K., Tomczewski, S., Niedźwiedziuk, P., Sikorski, B. L., and Wojtkowski, M. (2020). In vivo imaging of the human cornea with high-speed and high-resolution fourier-domain full-field optical coherence tomography. *Biomed. Opt. Express*, 11(5):2849–2865.

[Auksorius et al., 2019] Auksorius, E., Borycki, D., and Wojtkowski, M. (2019). Crosstalk-free volumetric in vivo imaging of a human retina with fourier-domain full-field optical coherence tomography. *Biomed. Opt. Express*, 10(12):6390–6407.

[Badon et al., 2017] Badon, A., Boccara, A. C., Lerosey, G., Fink, M., and Aubry, A. (2017). Multiple scattering limit in optical microscopy. *Opt. Express*, 25(23):28914–28934.

[Badon et al., 2016] Badon, A., Li, D., Lerosey, G., Boccara, A. C., Fink, M., and Aubry, A. (2016). Smart optical coherence tomography for ultra-deep imaging through highly scattering media. *Science Advances*, 2(11).

[Barolle, 2019] Barolle, V. (2019). Approche matricielle de la tomographie à cohérence optique.

[Beaurepaire et al., 1998] Beaurepaire, E., Boccara, A. C., Lebec, M., Blanchot, L., and Saint-Jalmes, H. (1998). Full-field optical coherence microscopy. *Opt. Lett.*, 23(4):244–246.

[Bedggood et al., 2008] Bedggood, P., Daaboul, M., Ashman, R., Smith, G., and Metha, A. (2008). Characteristics of the human isoplanatic patch and implications for adaptive optics retinal imaging. *Journal of Biomedical Optics*, 13(2):024008.

[Bertalmio et al., 2001] Bertalmio, M., Bertozzi, A. L., and Sapiro, G. (2001). Navier-stokes, fluid dynamics, and image and video inpainting. In *Computer Vision and Pattern Recognition, 2001. CVPR 2001. Proceedings of the 2001 IEEE Computer Society Conference on*, volume 1, pages I–I. IEEE.

[Binding et al., 2011] Binding, J., Arous, J. B., Léger, J.-F., Gigan, S., Boccara, C., and Bourdieu, L. (2011). Brain refractive index measured in vivo with high-na defocus-corrected full-field oct and consequences for two-photon microscopy. *Opt. Express*, 19(6):4833–4847.

[Bliek et al., 2018] Bliek, L., Verstraete, H. R. G. W., Verhaegen, M., and Wahls, S. (2018). Online Optimization With Costly and Noisy Measurements Using Random Fourier Expansions. *IEEE Transactions on Neural Networks and Learning Systems*, 29(1):167–182.

[Bonnans et al., 2006] Bonnans, J. F., Gilbert, J. C., Lemaréchal, C., and Sagastizábal, C. A. (2006). *Numerical Optimization*. Springer Berlin Heidelberg.

[Bonora et al., 2015] Bonora, S., Jian, Y., Zhang, P., Zam, A., Pugh, E. N., Zawadzki, R. J., and Sarunic, M. V. (2015). Wavefront correction and high-resolution in vivo oct imaging with an objective integrated multi-actuator adaptive lens. *Opt. Express*, 23(17):21931–21941.

[Booth et al., 2015] Booth, M., Andrade, D., Burke, D., Patton, B., and Zurauskas, M. (2015). Aberrations and adaptive optics in super-resolution microscopy. *Microscopy*, 64(4):251–261.

[Booth, 2007] Booth, M. J. (2007). Adaptive optics in microscopy. *Philosophical Transactions of the Royal Society A: Mathematical, Physical and Engineering Sciences*, 365(1861):2829–2843.

[Booth et al., 2002] Booth, M. J., Neil, M. A. A., Juskaitis, R., and Wilson, T. (2002). Adaptive aberration correction in a confocal microscope. *Proceedings of the National Academy of Sciences*, 99(9):5788–5792.

[Borycki et al., 2020] Borycki, D., Auksorius, E., Węgrzyn, P., and Wojtkowski, M. (2020). Computational aberration correction in spatiotemporal optical coherence (stoc) imaging. *Opt. Lett.*, 45(6):1293–1296.

[Borycki et al., 2019] Borycki, D., Hamkało, M., Nowakowski, M., Szkulmowski, M., and Wojtkowski, M. (2019). Spatiotemporal optical coherence (stoc) manipulation suppresses coherent cross-talk in full-field swept-source optical coherence tomography. *Biomed. Opt. Express*, 10(4):2032–2054.

[Bozinovic et al., 2008] Bozinovic, N., Ventalon, C., Ford, T., and Mertz, J. (2008). Fluorescence endomicroscopy with structured illumination. *Opt. Express*, 16(11):8016–8025.

[Chasles et al., 2007] Chasles, F., Dubertret, B., and Boccara, A. C. (2007). Optimization and characterization of a structured illumination microscope. *Opt. Express*, 15(24):16130–16140.

[Choi et al., 2012] Choi, W. J., Park, K. S., Eom, T. J., Oh, M.-K., and Lee, B. H. (2012). Tomographic imaging of a suspending single live cell using optical tweezer-combined full-field optical coherence tomography. *Opt. Lett.*, 37(14):2784–2786.

[Creath, 1988] Creath, K. (1988). V phase-measurement interferometry techniques. volume 26 of *Progress in Optics*, pages 349 – 393. Elsevier.

[Débarre et al., 2007] Débarre, D., Booth, M. J., and Wilson, T. (2007). Image based adaptive optics through optimisation of low spatial frequencies. *Opt. Express*, 15(13):8176–8190.

[Débarre et al., 2009] Débarre, D., Botcherby, E. J., Watanabe, T., Srinivas, S., Booth, M. J., and Wilson, T. (2009). Image-based adaptive optics for two-photon microscopy. *Opt. Lett.*, 34(16):2495–2497.

[Domínguez and Bérubé-Lauzière, 2013] Domínguez, J. B. and Bérubé-Lauzière, Y. (2013). Radiative transfer and optical imaging in biological media by low-order transport approximations: the simplified spherical harmonics (SP n) approach. In *Light Scattering Reviews 8*, pages 269–315. Springer Berlin Heidelberg.

[Drexler et al., 2014] Drexler, W., Liu, M., Kumar, A., Kamali, T., Unterhuber, A., and Leitgeb, R. A. (2014). Optical coherence tomography today: speed, contrast, and multimodality. *Journal of Biomedical Optics*, 19(7):071412.

[Dube, 2019] Dube, B. (2019). prysm: A python optics module. *Journal of Open Source Software*, 4(37):1352.

[Dubois et al., 2004] Dubois, A., Grieve, K., Moneron, G., Lecaque, R., Vabre, L., and Boccara, C. (2004). Ultrahigh-resolution full-field optical coherence tomography. *Applied Optics*, 43(14):2874–2883.

[Dubois et al., 2002] Dubois, A., Vabre, L., Boccara, A.-C., and Beaurepaire, E. (2002). High-resolution full-field optical coherence tomography with a linnik microscope. *Appl. Opt.*, 41(4):805–812.

[Elson, 2011] Elson, E. L. (2011). Fluorescence correlation spectroscopy: Past, present, future. *Biophysical Journal*, 101(12):2855–2870.

[Fercher et al., 1995] Fercher, A., Hitzenberger, C., Kamp, G., and El-Zaiat, S. (1995). Measurement of intraocular distances by backscattering spectral interferometry. *Optics Communications*, 117(1-2):43–48.

[Fischler and Bolles, 1987] Fischler, M. A. and Bolles, R. C. (1987). Random sample consensus: a paradigm for model fitting with applications to image analysis and automated cartography. In *Readings in computer vision*, pages 726–740. Elsevier.

[Fuji et al., 1997] Fuji, T., Miyata, M., Kawato, S., Hattori, T., and Nakatsuka, H. (1997). Linear propagation of light investigated with a white-light michelson interferometer. *J. Opt. Soc. Am. B*, 14(5):1074–1078.

[Ginner et al., 2017] Ginner, L., Kumar, A., Fechtig, D., Wurster, L. M., Salas, M., Pircher, M., and Leitgeb, R. A. (2017). Noniterative digital aberration correction for cellular resolution retinal optical coherence tomography in vivo. *Optica*, 4(8):924–931.

[Goodman, 1985] Goodman, J. (1985). *Statistical Optics*. A Wiley-Interscience publication. Wiley.

[Goodman, 2005] Goodman, J. W. (2005). Introduction to fourier optics. *Introduction to Fourier optics, 3rd ed., by JW Goodman. Englewood, CO: Roberts & Co. Publishers, 2005*, 1.

[Guirao et al., 2002] Guirao, A., Porter, J., Williams, D. R., and Cox, I. G. (2002). Calculated impact of higher-order monochromatic aberrations on retinal image quality in a population of human eyes. *J. Opt. Soc. Am. A*, 19(1):1–9.

[Guizar-Sicairos et al., 2008] Guizar-Sicairos, M., Thurman, S. T., and Fienup, J. R. (2008). Efficient subpixel image registration algorithms. *Optics letters*, 33(2):156–158.

[Hajdu, 2002] Hajdu, S. I. (2002). The First Use of the Microscope in Medicine. *Annals of Clinical & Laboratory Science*, 32(3):309–310.

[Han et al., 2018] Han, G., Cao, Z., Mu, Q., Wang, Y., Li, D., Wang, S., Xu, Z., Wu, D., Hu, L., and Xuan, L. (2018). Isoplanatic patch of the human eye for arbitrary wavelengths. *Optics Communications*, 410:811–816.

[Hermann et al., 2004] Hermann, B., Fernández, E. J., Unterhuber, A., Sattmann, H., Fercher, A. F., Drexler, W., Prieto, P. M., and Artal, P. (2004). Adaptive-optics ultrahigh-resolution optical coherence tomography. *Opt. Lett.*, 29(18):2142–2144.

[Hillmann et al., 2016] Hillmann, D., Spahr, H., Hain, C., Sudkamp, H., Franke, G., Pfäffle, C., Winter, C., and Hüttmann, G. (2016). Aberration-free volumetric high-speed imaging of in vivo retina. *Scientific Reports*, 6(1):35209.

[Hillmann et al., 2017] Hillmann, D., Spahr, H., Sudkamp, H., Hain, C., Hinkel, L., Franke, G., and Hüttmann, G. (2017). Off-axis reference beam for full-field swept-source oct and holoscopy. *Opt. Express*, 25(22):27770–27784.

[Horn and Schunck, 1981] Horn, B. K. and Schunck, B. G. (1981). Determining optical flow. *Artificial Intelligence*, 17(1):185 – 203.

[Horstmeyer et al., 2016] Horstmeyer, R., Heintzmann, R., Popescu, G., Waller, L., and Yang, C. (2016). Standardizing the resolution claims for coherent microscopy. *Nature Photonics*, 10:68–71.

[Huang et al., 1991] Huang, D., Swanson, E. A., Lin, C. P., Schuman, J. S., Stinson, W. G., Chang, W., Hee, M. R., Flotte, T., Gregory, K., Puliafito, C. A., and Et, A. (1991). Optical coherence tomography. *Science*, 254(5035):1178–1181.

[Ilina et al., 2020] Ilina, E., Nyman, M., Mondal, T., Kaivola, M., Setälä, T., and Shevchenko, A. (2020). Interferometric imaging of reflective micro-objects in the presence of strong aberrations. *Optics Express*, 28(2):1817.

[Jacques, 2013] Jacques, S. L. (2013). Optical properties of biological tissues: a review. *Physics in Medicine and Biology*, 58(11):R37–R61.

[Jarosz et al., 2017] Jarosz, J., Mecê, P., Conan, J.-M., Petit, C., Paques, M., and Meimon, S. (2017). High temporal resolution aberrometry in a 50-eye population and implications for adaptive optics error budget. *Biomed. Opt. Express*, 8(4):2088–2105.

[Jian et al., 2014] Jian, Y., Xu, J., Gradowski, M. A., Bonora, S., Zawadzki, R. J., and Sarunic, M. V. (2014). Wavefront sensorless adaptive optics optical coherence tomography for in vivo retinal imaging in mice. *Biomed. Opt. Express*, 5(2):547–559.

[Karamata et al., 2005a] Karamata, B., Laubscher, M., Leutenegger, M., Bourquin, S., Lasser, T., and Lambelet, P. (2005a). Multiple scattering in optical coherence tomography. i. investigation and modeling. *J. Opt. Soc. Am. A*, 22(7):1369–1379.

[Karamata et al., 2005b] Karamata, B., Leutenegger, M., Laubscher, M., Bourquin, S., Lasser, T., and Lambelet, P. (2005b). Multiple scattering in optical coherence tomography. ii. experimental and theoretical investigation of cross talk in wide-field optical coherence tomography. *J. Opt. Soc. Am. A*, 22(7):1380–1388.

[Kim, 2010] Kim, M. K. (2010). Principles and techniques of digital holographic microscopy. *SPIE Reviews*, 1(1):1 – 51.

[Kishi, 2016] Kishi, S. (2016). Impact of swept source optical coherence tomography on ophthalmology. *Taiwan Journal of Ophthalmology*, 6(2):58–68.

[Labiau et al., 2009] Labiau, S., David, G., Gigan, S., and Boccara, A. C. (2009). Defocus test and defocus correction in full-field optical coherence tomography. *Opt. Lett.*, 34(10):1576–1578.

[Larkin, 1996] Larkin, K. G. (1996). Efficient nonlinear algorithm for envelope detection in white light interferometry. *Journal of the Optical Society of America A*, 13(4):832.

[Laslandes et al., 2017] Laslandes, M., Salas, M., Hitzenberger, C. K., and Pircher, M. (2017). Increasing the field of view of adaptive optics scanning laser ophthalmoscopy. *Biomed. Opt. Express*, 8(11):4811–4826.

[Leitgeb et al., 2006] Leitgeb, R. A., Villiger, M., Bachmann, A. H., Steinmann, L., and Lasser, T. (2006). Extended focus depth for fourier domain optical coherence microscopy. *Opt. Lett.*, 31(16):2450–2452.

[Leith and Upatnieks, 1962] Leith, E. N. and Upatnieks, J. (1962). Reconstructed wavefronts and communication theory∗. *J. Opt. Soc. Am.*, 52(10):1123–1130.

[Lim et al., 2008] Lim, D., Chu, K. K., and Mertz, J. (2008). Wide-field fluorescence sectioning with hybrid speckle and uniform-illumination microscopy. *Opt. Lett.*, 33(16):1819–1821.

[Maguen et al., 2004] Maguen, E., Wong, J., Schlanger, J., and Salz, J. J. (2004). Relationship between total aberrations (RMS) and pupil size in ametropic eyes with the

LADARWAVE system. In Manns, F., Soderberg, P. G., and Ho, A., editors, *Ophthalmic Technologies XIV*, volume 5314, pages 206 – 208. International Society for Optics and Photonics, SPIE.

[Matungka et al., 2009] Matungka, R., Zheng, Y., and Ewing, R. (2009). Image Registration Using Adaptive Polar Transform. *IEEE Transactions on Image Processing*, 18(10):2340–2354.

[Mazlin et al., 2020] Mazlin, V., Xiao, P., Scholler, J., Irsch, K., Grieve, K., Fink, M., and Boccara, A. C. (2020). Real-time non-contact cellular imaging and angiography of human cornea and limbus with common-path full-field/SD OCT. *Nature Communications*, 11(1).

[Mecê et al., 2020a] Mecê, P., Groux, K., Scholler, J., Thouvenin, O., Fink, M., Grieve, K., and Boccara, C. (2020a). Coherence gate shaping for wide field high-resolution in vivo retinal imaging with full-field oct. *Biomed. Opt. Express*, 11(9):4928–4941.

[Mecê et al., 2018] Mecê, P., Jarosz, J., Conan, J.-M., Petit, C., Grieve, K., Paques, M., and Meimon, S. (2018). Fixational eye movement: a negligible source of dynamic aberration. *Biomed. Opt. Express*, 9(2):717–727.

[Mecê et al., 2020b] Mecê, P., Scholler, J., Groux, K., and Boccara, C. (2020b). High-resolution in-vivo human retinal imaging using full-field oct with optical stabilization of axial motion. *Biomed. Opt. Express*, 11(1):492–504.

[Mecê et al., 2020] Mecê, P., Gofas-Salas, E., Paques, M., Grieve, K., and Meimon, S. (2020). Optical incoherence tomography: a method to generate tomographic retinal cross-sections with non-interferometric imaging systems.

[Mehrotra, 1992] Mehrotra, S. (1992). On the implementation of a primal-dual interior point method. *SIAM Journal on Optimization*, 2(4):575–601.

[Mertz, 2011] Mertz, J. (2011). Optical sectioning microscopy with planar or structured illumination. *Nature Methods*, 8:811.

[Mertz, 2019] Mertz, J. (2019). *Optical Coherence Tomography*, page 238–262. Cambridge University Press, 2 edition.

[Mertz et al., 2015] Mertz, J., Paudel, H., and Bifano, T. G. (2015). Field of view advantage of conjugate adaptive optics in microscopy applications. *Applied Optics*, 54(11):3498.

[Minsky, 1988] Minsky, M. (1988). Memoir on inventing the confocal scanning microscope. *Scanning*, 10(4):128–138.

[Moisan, 2011] Moisan, L. (2011). Periodic Plus Smooth Image Decomposition. *Journal of Mathematical Imaging and Vision*, 39(2):161–179.

[Munson et al., 2006] Munson, B. R., Young, D. F., Okiishi, T. H., and Huebsch, W. W. (2006). Fundamentals of fluid mechanics. hoboken. *John Wiley & Sons, Inc*, 69:520.

[Münter et al., 2020] Münter, M., vom Endt, M., Pieper, M., Casper, M., Ahrens, M., Kohlfaerber, T., Rahmanzadeh, R., König, P., Hüttmann, G., and Schulz-Hildebrandt, H. (2020). Dynamic contrast in scanning microscopic OCT. *arXiv e-prints*, page arXiv:2003.00006.

[Nahas et al., 2013a] Nahas, A., Bauer, M., Roux, S., and Boccara, A. C. (2013a). 3d static elastography at the micrometer scale using full field oct. *Biomed. Opt. Express*, 4(10):2138–2149.

[Nahas et al., 2013b] Nahas, A., Tanter, M., Nguyen, T.-M., Chassot, J.-M., Fink, M., and Boccara, A. C. (2013b). From supersonic shear wave imaging to full-field optical coherence shear wave elastography. *Journal of Biomedical Optics*, 18(12):1 – 9.

[Neil et al., 2000] Neil, M. A. A., Booth, M. J., and Wilson, T. (2000). Closed-loop aberration correction by use of a modal zernike wave-front sensor. *Opt. Lett.*, 25(15):1083–1085.

[Ntziachristos, 2010] Ntziachristos, V. (2010). Going deeper than microscopy: the optical imaging frontier in biology. *Nature Methods*, 7(8):603–614.

[Oyallon and Rabin, 2015] Oyallon, E. and Rabin, J. (2015). An Analysis of the SURF Method. *Image Processing On Line*, 5:176–218.

[Pfäffle et al., 2019] Pfäffle, C., Spahr, H., Kutzner, L., Burhan, S., Hilge, F., Miura, Y., Hüttmann, G., and Hillmann, D. (2019). Simultaneous functional imaging of neuronal and photoreceptor layers in living human retina. *Opt. Lett.*, 44(23):5671–5674.

[Pianykh, 2011] Pianykh, O. S. (2011). Improving digital signal interpolation: L2-optimal kernels with kernel-invariant interpolation speed.

[Porter et al., 2001] Porter, J., Guirao, A., Cox, I. G., and Williams, D. R. (2001). Monochromatic aberrations of the human eye in a large population. *J. Opt. Soc. Am. A*, 18(8):1793–1803.

[Považay et al., 2006] Považay, B., Unterhuber, A., Hermann, B., Sattmann, H., Arthaber, H., and Drexler, W. (2006). Full-field time-encoded frequency-domain optical coherence tomography. *Opt. Express*, 14(17):7661–7669.

[Richards et al., 1959] Richards, B., Wolf, E., and Gabor, D. (1959). Electromagnetic diffraction in optical systems, ii. structure of the image field in an aplanatic system. *Proceedings of the Royal Society of London. Series A. Mathematical and Physical Sciences*, 253(1274):358–379.

[Richardson and Lichtman, 2015] Richardson, D. S. and Lichtman, J. W. (2015). Clarifying tissue clearing. *Cell*, 162(2):246 – 257.

[Santi, 2011] Santi, P. A. (2011). Light sheet fluorescence microscopy: A review. *Journal of Histochemistry & Cytochemistry*, 59(2):129–138. PMID: 21339178.

[Sarunic et al., 2006] Sarunic, M. V., Weinberg, S., and Izatt, J. A. (2006). Full-field swept-source phase microscopy. *Opt. Lett.*, 31(10):1462–1464.

[Saunter et al., 2009] Saunter, C. D., Perng, M. D., Love, G. D., and Quinlan, R. A. (2009). Stochastically determined directed movement explains the dominant small-scale mitochondrial movements within non-neuronal tissue culture cells. *FEBS Letters*, 583(8):1267–1273.

[Schnars and Jüptner, 2002] Schnars, U. and Jüptner, W. P. O. (2002). Digital recording and numerical reconstruction of holograms. *Measurement Science and Technology*, 13(9):R85–R101.

[Scholler, 2019a] Scholler, J. (2019a). FFOCT control and acquisition software. https://doi.org/10.5281/zenodo.3137245.

[Scholler, 2019b] Scholler, J. (2019b). Motion artifact removal and signal enhancement to achieve in vivo dynamic full field oct. *Opt. Express*, 27(14):19562–19572.

[Scholler et al., 2020] Scholler, J., Groux, K., Goureau, O., Sahel, J.-A., Fink, M., Reichman, S., Boccara, C., and Grieve, K. (2020). Dynamic full-field optical coherence tomography: 3D live-imaging of retinal organoids. *Light: Science & Applications*, 9(140).

[Scholler et al., 2019] Scholler, J., Mazlin, V., Thouvenin, O., Groux, K., Xiao, P., Sahel, J.-A., Fink, M., Boccara, C., and Grieve, K. (2019). Probing dynamic processes in the eye at multiple spatial and temporal scales with multimodal full field OCT. *Biomedical Optics Express*, 10(2):731–746.

[Sheppard, 1988] Sheppard, C. (1988). Super-resolution in confocal imaging. *Optik - International Journal for Light and Electron Optics*, 80:53.

[Sheppard and Wilson, 1981] Sheppard, C. J. R. and Wilson, T. (1981). The theory of the direct-view confocal microscope. *Journal of Microscopy*, 124(2):107–117.

[Stremplewski et al., 2019] Stremplewski, P., Auksorius, E., Wnuk, P., Kozoń, Ł., Garstecki, P., and Wojtkowski, M. (2019). In vivo volumetric imaging by crosstalk-free full-field oct. *Optica*, 6(5):608–617.

[Sudkamp et al., 2018] Sudkamp, H., Hillmann, D., Koch, P., vom Endt, M., Spahr, H., Münst, M., Pfäffle, C., Birngruber, R., and Hüttmann, G. (2018). Simple approach for aberration-corrected oct imaging of the human retina. *Opt. Lett.*, 43(17):4224–4227.

[Sudkamp et al., 2016] Sudkamp, H., Koch, P., Spahr, H., Hillmann, D., Franke, G., Münst, M., Reinholz, F., Birngruber, R., and Hüttmann, G. (2016). In-vivo retinal imaging with off-axis full-field time-domain optical coherence tomography. *Opt. Lett.*, 41(21):4987–4990.

[Thaung et al., 2009] Thaung, J., Knutsson, P., Popovic, Z., and Owner-Petersen, M. (2009). Dual-conjugate adaptive optics for wide-field high-resolution retinal imaging. *Opt. Express*, 17(6):4454–4467.

[Thibos et al., 2002] Thibos, L. N., Hong, X., Bradley, A., and Cheng, X. (2002). Statistical variation of aberration structure and image quality in a normal population of healthy eyes. *J. Opt. Soc. Am. A*, 19(12):2329–2348.

[Thouvenin et al., 2017a] Thouvenin, O., Boccara, C., Fink, M., Sahel, J.-A., Paques, M., and Grieve, K. (2017a). Cell motility as contrast agent in retinal explant imaging with full-field optical coherence tomography. *Investigative Ophtalmology & Visual Science*, 58(11):4605.

[Thouvenin et al., 2017b] Thouvenin, O., Fink, M., and Boccara, C. (2017b). Dynamic multimodal full-field optical coherence tomography and fluorescence structured illumination microscopy. *Journal of Biomedical Optics*, 22(2):026004.

[Tricoli and Carminati, 2019] Tricoli, U. and Carminati, R. (2019). Modeling of full-field optical coherence tomography in scattering media. *J. Opt. Soc. Am. A*, 36(11):C122–C129.

[Verstraete et al., 2017] Verstraete, H. R. G. W., Heisler, M., Ju, M. J., Wahl, D., Bliek, L., Kalkman, J., Bonora, S., Jian, Y., Verhaegen, M., and Sarunic, M. V. (2017). Wavefront sensorless adaptive optics oct with the done algorithm for in vivo human retinal imaging. *Biomed. Opt. Express*, 8(4):2261–2275.

[Verstraete et al., 2015] Verstraete, H. R. G. W., Wahls, S., Kalkman, J., and Verhaegen, M. (2015). Model-based sensor-less wavefront aberration correction in optical coherence tomography. *Opt. Lett.*, 40(24):5722–5725.

[Xiao et al., 2016] Xiao, P., Fink, M., and Boccara, A. C. (2016). Full-field spatially incoherent illumination interferometry: a spatial resolution almost insensitive to aberrations. *Opt. Lett.*, 41(17):3920–3923.

[Xiao et al., 2018] Xiao, P., Mazlin, V., Grieve, K., Sahel, J.-A., Fink, M., and Boccara, A. C. (2018). In vivo high-resolution human retinal imaging with wavefront-correctionless full-field oct. *Optica*, 5(4):409–412.

[Yaakob et al., 2013] Yaakob, R., Aryanfar, A., Halin, A. A., and Sulaiman, N. (2013). A comparison of different block matching algorithms for motion estimation. *Procedia Technology*, 11:199 – 205. 4th International Conference on Electrical Engineering and Informatics, ICEEI 2013.

[Yang et al., 2020] Yang, L., Yu, X., Fuller, A. M., Troester, M. A., and Oldenburg, A. L. (2020). Characterizing optical coherence tomography speckle fluctuation spectra of mammary organoids during suppression of intracellular motility. *Quantitative Imaging in Medicine and Surgery*, 10(1):76–85.

[Yeh et al., 2015] Yeh, L.-H., Dong, J., Zhong, J., Tian, L., Chen, M., Tang, G., Soltanolkotabi, M., and Waller, L. (2015). Experimental robustness of fourier ptychography phase retrieval algorithms. *Opt. Express*, 23(26):33214–33240.

[Yoko and Yukio, 2016] Yoko, H. M. and Yukio, Y. (2016). Overview of diffuse optical tomography and its clinical applications. *Journal of Biomedical Optics*, 21(9):1 – 11.

[Yoo et al., 1990] Yoo, K. M., Liu, F., and Alfano, R. R. (1990). When does the diffusion approximation fail to describe photon transport in random media? *Physical Review Letters*, 64(22):2647–2650.

[Yoon et al., 2020] Yoon, S., Kim, M., Jang, M., Choi, Y., Choi, W., Kang, S., and Choi, W. (2020). Deep optical imaging within complex scattering media. *Nature Reviews Physics*.

[Zernike, 1942] Zernike, F. (1942). Phase contrast, a new method for the microscopic observation of transparent objects. *Physica*, 9(7):686 – 698.

RÉSUMÉ

Cette thèse vise à appliquer et combiner des méthodes numériques et optiques pour repousser les limites de la tomographie optique cohérente plein champ (FFOCT) statique et dynamique pour la microscopie et l'imagerie médicale.

Des méthodes de post-traitement utilisant la décomposition en valeurs singulières ont permis pour la première fois l'acquisition d'images dynamiques in vivo tandis que l'utilisation des signaux non stationnaires a permis d'obtenir des images avec un meilleur rapport signal sur bruit, soit la possibilité d'imager plus profondément les échantillons. L'application de l'imagerie dynamique est présentée sur des organoïdes rétiniens où nous montrons que notre méthode est capable de fournir de nouvelles informations biologiques intéressantes qui ne sont possibles avec aucune autre méthode.

Des développements matériel pour compenser les aberrations optiques ont été menés avec succès, ce qui a permis une mise en œuvre peu complexe et peu coûteuse permettant d'acquérir de manière fiable des images de la rétine avec une résolution proche de la limite de diffraction. La compréhension de la manifestation des aberrations optiques en FFOCT validée expérimentalement nous a permis de concevoir et de simuler les performances du système proposé.

Enfin, les applications cliniques potentielles du FFOCT dynamique et statique pour l'angiographie de l'œil humain in vivo, la cicatrisation ex vivo, la classification des cellules de la rétine et le dépistage du cancer du sein par des méthodes d'apprentissage automatique ont été démontrées avec succès.

MOTS CLÉS

Tomographie optique cohérente - Microscopie - Imagerie dynamique - Traitements spatio-temporels - Imagerie de la rétine - Optique adaptative - Apprentissage automatique.

ABSTRACT

This PhD project aims at combining numerical and optical methods to apply and push the limits of static and dynamic full-field optical coherent tomography (FFOCT) for microscopy and medical imaging.

Post-processing methods using singular value decomposition allowed the acquisition of dynamic images in vivo for the first time while the use of the signals non-stationarities allowed to image with a better signal to noise ratio, hence deeper inside samples. Application of dynamic imaging is presented on retinal organoids where we show that our method is able to provide new interesting biological insights that are not possible with any other methods.

Hardware developments to counteracts optical aberrations were successfully conducted leading to low complexity and cost efficient implementation which can reliably acquire retinal images with a resolution close to the diffraction limit. The understanding and demonstration of the particular aberrations manifestation in FFOCT allowed us to design and simulate the performances of the proposed system.

Finally, potential clinical applications of dynamic and static FFOCT for angiography in the human eye in vivo, wound healing ex vivo, retinal cell classification and breast cancer screening using machine learning methods are successfully demonstrated.

KEYWORDS

Optical coherence tomography - Microscopy - Dynamic imaging - Spatio-temporal processing - Retinal imaging - Adaptive optics - Machine learning.